

**A microwell array  
coated with dopaminergic cell adhesive film  
for single cell analysis in drug discovery**

Dissertation  
zur Erlangung des Grades  
des Doktors der Ingenieurwissenschaften  
der Naturwissenschaftlich-Technischen Fakultät II  
- Physik und Mechatronik -  
der Universität des Saarlandes

von  
**Jihwang Park**

Saarbrücken

2013

Tag des Kolloquiums: 07.08.2013

Dekan: Univ.-Prof. Dr. Christian Wagner

Gutachter: Univ.-Prof. Dr.-Ing. habil. Stefan Seelecke

Univ.-Prof. Dr. rer. nat. Helmut Seidel

Prof. Dr. Andreas Manz

Dr.-Ing. Björn Martin

## Abstract

Drug discovery requires prompt decision-making to identify which new chemical entities constitute viable new drug candidates and have a high likelihood of market success. Conventional *in vitro* cell-based screens sometimes provide misleading data that may not represent *in vivo* responses. We developed an array of microcellular platforms to provide a uniform environment for single-cell suspension, mimic *in vivo* functions, and demonstrate the biological effects of a drug on the chemistry of a single cell at the molecular level. Dopaminergic mesoporous inorganic-organic hybrid resin (HR4-DOPA) was used to coat the wells of 200-microwell plates fabricated for these experiments. The biocompatibility of HR4-DOPA was demonstrated by cell adhesion and viability assays. HeLa cell adhesion to the HR4-DOPA film was comparable to the controls: mesoporous inorganic-organic hybrid resin (HR4), ECM proteins (fibronectin and collagen IV), and glass. HeLa cell viability on HR4-DOPA was 86.1%, indicating insignificant growth inhibition. We also investigated the optimal microwell depth and cell concentration for HeLa single-cell occupancy: 25- $\mu\text{m}$ -deep microwells at  $1.0 \times 10^6$  cells/ml demonstrated 67.5% single-cell occupancy while providing sufficient cell-adhesive surface area for long-term cell culture ( $\geq 3000 \mu\text{m}^2$ ). We obtained singly occupied microwells with only 5.9% array-to-array variation, thus providing adequate throughput for accurate quantification in advanced single-cell analyses. Arrays of HR4-DOPA-coated microwells can be used for high-throughput single-cell-based assays for drug discovery as a “bio-cell processor.” Given that the microwell arrays are integrated in a microfluidic biochip, they can mimic the *in vivo* microenvironment; we can thus predict *in vivo* responses through high-throughput, isolated single-cell analysis to assess cellular chemistry at the molecular level.

**Keywords:** drug discovery, high-throughput screening, single-cell-based assay, dopaminergic mesoporous inorganic-organic hybrid resin (HR4-DOPA), HeLa cells, microwell, single-cell occupancy

## Zusammenfassung

In der Medikamentenforschung ist eine schnelle Entscheidungsfindung erforderlich, um neue chemische Stoffe aus einem Kandidaten-Pool möglicher neuer Medikamente zu finden, die eine Chance auf Markteinführung haben. Konventionelle, *in vitro*, zell-basierte Methoden liefern oft irreführende Ergebnisse, die nicht der *in vivo* Antwort entsprechen. Wir haben ein Einzelzell Array in einer mikrofluidischen Plattform entwickelt, das ein gleichförmiges Millieu für die Zellen bereit stellt, *in vivo* Funktionalität imitieren kann und biologische Effekte eines Medikaments auf die Chemie einer einzelnen Zelle auf molekularer Ebene demonstrieren kann. Ein dopaminerges, mesopores, inorganisches/organisches Harz (HR4-DOPA) wurde benutzt um die Microwells einer 200-Microwell-Platte zu beschichten. Die Biokompatibilität dieses Harzes wurde durch Zell-Adhäsions- und Viabilitäts-Experimente nachgewiesen. Die Anlagerung von HeLa Zellen an HR4-DOPA war vergleichbar mit der an den Vergleichssubstanzen: mit HR4 (Hybrides, mesoporöses, inorganisches/organisches Harz), mit Proteinen der extrazellulären Matrix (Fibronectin, Collagen IV) und mit biologischem Glas. Die Viabilität der HeLa Zellen auf HR4-DOPA lag dabei bei 86,1%, was auf eine geringe Wachstumshemmung hindeutet. Die optimale Tiefe der Wells und die optimal Anzahl der Zellen wurden ebenfalls untersucht, wobei eine Zellzahl von  $1,0 \times 10^6$  Zellen/ml und eine Tiefe der Microwells von 25  $\mu\text{m}$  die besten Ergebnisse lieferten mit einer Einzel-Zell Belegung der Wells von 67,5% und eine genügend große Fläche ( $\geq 3000 \mu\text{m}^2$ ) für die Zellanlagerung und Langzeit-Kultivierung bereit stellt. Die Reproduzierbarkeit der Ergebnisse war dabei hoch, lediglich 5,9% Abweichung wurde festgestellt. Somit liefert dieser Ansatz eine geeignete Methode für die exakte Bestimmung und Quantifizierung verschiedener zellulärer Prozesse bei der state-of-the-art Einzel-Zell Analyse. Anordnungen von HR4-DOPA beschichteten Microwells können für Hochdurchsatz Untersuchungen in der Medikamentenforschung als „Bio-Zell Prozessor“ verwendet werden. Vorausgesetzt die Microwells sind integriert in einen mikrofluidischen Biochip, können diese eine *in vivo* ähnliche Mikroumgebung bereit stellen für weiterführende Versuche. Somit wird es möglich, *in vivo* Reaktionen akkurat und in einem Hochdurchsatz Verfahren voraus zu sagen und zelluläre Reaktionen auf der molekularen Ebene zu testen.

# Table of Contents

List of Figures

List of Tables

CHAPTER 1. INTRODUCTION .....	1
1.1. New Drug Application .....	1
1.1.1 Aim of a new drug application .....	1
1.1.2 Process of a new drug application .....	1
1.1.3 Importance of cell-based screening assays during preclinical trials in an new drug application .....	3
1.2. Microelectromechanical systems .....	3
1.3. Single-cell Analysis for drug discovery .....	4
1.3.1 Misleading results from conventional in vitro cell-based screening .....	4
1.3.2 Need for a single-cell isolation system for drug discovery .....	4
1.4. Single-cell isolation system .....	5
1.4.1 Single-cell isolation techniques .....	5
1.4.2 Limitations of previous single-cell isolation system .....	6
1.5. Research objective .....	7
1.6. Scope of this work .....	7
1.6.1 HeLa cells for microengineering (Chapter 3) .....	7
1.6.2 Dopaminergic mesoporous inorganic-organic hybrid resin (Chapter 4) .....	8
1.6.3 HeLa cell adhesion assay and viability on HR-DOPA (Chapter 5) .....	9
1.6.4 Micro single-cell array coated with HR-DOPA (Chapter 6) .....	9
CHAPTER 2. STATE OF THE ART .....	1 1
2.1. Introduction .....	1 1
2.2. Single cell isolation techniques .....	1 2
2.3. Microfluidic techniques .....	1 2
2.3.1 Semipermeable microstructures .....	1 3
2.3.2 Microfluidic ports .....	1 4
2.3.3 Pipette-like microfluidic systems .....	1 5
2.3.4 Droplet-based microfluidic systems for single cell encapsulation .....	1 5

2.4. Array-based single cell isolation techniques .....	1 7
2.4.1 Two-dimensional cell adhesive patterns .....	1 7
2.4.2 Holographic optical tweezers .....	2 2
2.4.3 Magnetophoretic techniques .....	2 4
2.4.4 Dielectrophoretic techniques .....	2 4
2.5. Microwells .....	2 5
2.5.1 Geometry and substrates of microwells .....	3 8
2.5.2 Cell types and seeding conditions .....	4 0
2.5.3 System integration .....	4 1
2.5.4 Differences and significance of the previously presented microwells .....	4 2
CHAPTER 3. HELa CELLS FOR MICROENGINEERING .....	4 5
3.1. Introduction .....	4 5
3.1.1 Human cancer cell lines .....	4 5
3.1.2 Human cancerous cervical epithelial HeLa cells .....	4 7
3.1.3 Physical properties of HeLa cells for microengineering .....	4 8
3.2. Materials and methods .....	4 9
3.2.1 Culture of HeLa cells .....	4 9
3.2.2 Measurement of cell diameter and volume .....	5 0
3.2.3 Measurement of cell Stokes velocity .....	5 1
3.3. Results .....	5 3
3.3.1 Culture of HeLa cells .....	5 3
3.3.2 Physical properties of HeLa cells .....	5 4
3.3.3 Stokes velocity of HeLa cell settling .....	5 6
3.3.4 Settling time of HeLa cells in cell adhesion assays .....	7 2
3.4. Discussion .....	7 3
3.4.1 Physical properties of HeLa cells .....	7 3
3.4.2 Stokes velocity of HeLa cells .....	7 5
3.5. Conclusion .....	8 0
CHAPTER 4. DOPAMINERGIC MESOPOROUS INORGANIC-ORGANIC HYBRID RESIN .....	8 3
4.1. Introduction .....	8 3
4.1.1 Development of new biomaterials and novel technologies .....	8 3

4.1.2	Significance of cell adhesion to biomaterials .....	8 3
4.1.3	Method for promoting cell adhesion by surface engineering .....	8 3
4.1.4	Wettability control for promoting cell adhesion .....	8 5
4.1.5	Mesoporous inorganic-organic hybrid resin .....	8 5
4.1.6	Dopamine .....	8 5
4.1.7	Dopaminergic mesoporous inorganic-organic hybrid resin .....	8 6
4.2.	Material and Methods .....	8 6
4.2.1	Dopaminergic mesoporous inorganic-organic hybrid resin .....	8 6
4.2.2	Preparation of HR4-DOPA film .....	8 8
4.2.3	Measurement of surface roughness .....	9 0
4.2.4	Water contact angle goniometry of HR4-DOPA film .....	9 1
4.3.	Results .....	9 1
4.3.1	Surface roughness .....	9 1
4.3.2	Water contact angle of HR4-DOPA film .....	9 3
4.3.3	Long-term stability of HR4-DOPA .....	9 4
4.4.	Discussion .....	9 4
4.4.1	Surface roughness of HR4-DOPA .....	9 4
4.4.2	Long-term stability of HR4-DOPA .....	9 5
4.5.	Conclusion .....	9 5
 CHAPTER 5. BIOCOMPATIBILITY OF DOPAMINERGIC INORGANIC-ORGANIC HYBRID RESIN		
	FILM .....	9 7
5.1.	Introduction .....	9 7
5.1.1	Cell adhesion assay .....	9 7
5.1.2	Cell viability assay .....	1 0 2
5.1.3	Biocompatibility of dopaminergic inorganic-organic hybrid resin films .....	1 0 3
5.2.	Materials and Methods .....	1 0 3
5.2.1	Culture of HeLa cells .....	1 0 3
5.2.2	Preparation of HR4-DOPA and HR4 film .....	1 0 3
5.2.3	Cell adhesion assay .....	1 0 4
5.2.4	Statistical analysis .....	1 0 6
5.3.	Results .....	1 0 6
5.3.1	HeLa cell adhesion assay .....	1 0 6

5.3.2 HeLa cell viability assay .....	1	1	1
5.4. Discussion .....	1	1	2
5.4.1 HeLa cell adhesion assay .....	1	1	2
5.4.2 HeLa cell viability assay .....	1	1	8
5.5. Conclusion .....	1	1	8
 CHAPTER 6. A MICROWELL ARRAY COATED BY DOPAMINERGIC MESOPOROUS			
INORGANIC-ORGANIC HYBRID RESIN FILM .....			
	1	2	1
6.1. Introduction .....	1	2	1
6.1.1 Requirement of a microwell array for drug discovery .....	1	2	1
6.1.2 Limitations of the previous microwell arrays .....	1	2	2
6.1.3 Dopaminergic mesoporous inorganic-organic hybrid resin .....	1	2	3
6.1.4 A microwell array coated by dopaminergic inorganic-organic hybrid resin film .....	1	2	3
6.2. Materials and methods .....	1	2	4
6.2.1 Fabrication of a replica-micromolding master for soft lithography .....	1	2	4
6.2.2 Fabrication of a microwell coated by dopaminergic mesoporous inorganic- organic hybrid resin .....	1	2	6
6.2.3 Culture of HeLa cells .....	1	2	8
6.2.4 HeLa cell occupancy of a microwell array .....	1	2	9
6.3. Results .....	1	3	0
6.3.1 Design of a microwell array .....	1	3	0
6.3.2 Fabrication of a microwell array .....	1	3	1
6.3.3 HeLa cell adhesion on the controls .....	1	3	5
6.3.4 HeLa cell occupancy of a microwell array .....	1	3	6
6.4. Discussion .....	1	4	2
6.4.1 Physical dimension of the microwell array .....	1	4	2
6.4.2 Cell conditions .....	1	4	4
6.5. Conclusion .....	1	4	7
 CHAPTER 7. DISCUSSION .....			
	1	4	9
7.1. Biological conditions used in the cellular experiments .....	1	4	9
7.1.1 HeLa cells .....	1	4	9
7.1.2 FBS concentration in the medium .....	1	5	1
7.2. Dopaminergic mesoporous inorganic-organic hybrid resin .....	1	5	1

7.2.1 HeLa cell adhesion on HR4-DOPA .....	1	5	1
7.2.2 HeLa cell viability of HR4-DOPA .....	1	5	2
7.3. Physical dimensions of the microwell array .....	1	5	2
7.3.1 Physical dimensions of the microwell .....	1	5	2
7.3.2 Physical dimensions of the microwell array for single-cell occupancy .....	1	5	3
7.4. System integration .....	1	5	3
7.4.1 Microfluidic biochip .....	1	5	3
7.4.2 Cell-based biosensors .....	1	5	3
CHAPTER 8. CONCLUSION .....	1	5	5
CHAPTER 9. FUTURE WORK .....	1	5	9
9.1. Integration of cell-based biosensors in microwells .....	1	5	9
9.2. Mimic <i>in vivo</i> microenvironments .....	1	5	9
REFERENCES .....	1	6	1
ABBREVIATIONS .....	1	8	7
REMARKS .....	1	9	1
VIA .....	1	9	3
ACKNOWLEDGEMENTS .....	1	9	5



## List of Figures

Figure 1.1: New drug application (NDA). .....	2
Figure 1.2: Schematic drawing of a bio-cell processor for drug discovery. ....	8
Figure 2.1: Semipermeable microstructures for capturing or paring cells. ....	1 3
Figure 2.2: Cell trapping mechanism by changing flow conditions using microfluidic ports. ...	1 4
Figure 2.3: Pipette-like microfluidic devices to entrap single cells in an array. ....	1 5
Figure 2.4: Microfluidic droplet-generation devices for isolating single cells .....	1 6
Figure 2.5: Effect of spreading on cell growth and apoptosis [72]. ....	1 8
Figure 2.6: A conceptual model of the behavior of fibronectin and albumin adsorbed to surfaces with different wettability [90-92]. ....	2 1
Figure 2.7: Proposed mechanisms for substrate topographic regulation of cellular motility on ligand-modified substrates [95]. ....	2 2
Figure 2.8: Holographic optical tweezers for single cell isolation. ....	2 3
Figure 2.9: Magnetophoretic single cell isolation techniques. ....	2 4
Figure 2.10: Dielectrophoretic single cell isolation techniques. ....	2 5
Figure 2.11: Optimization study of PDMS microwell dimensions and cell seeding parameters for NIH3T3 and RBL-1 [38]. ....	2 7
Figure 2.12: Adjacent rough cone-shaped cell retainers (CRs) [110]. ....	2 8
Figure 2.13: Arrays of microwells with different geometries (circle, square, triangle, rectangle and spindle) for 3D shape control of single cells [111]. ....	2 9
Figure 2.14: A microwell-based single cell lysis method [112]. ....	3 0
Figure 2.15: A microwell array measuring oxygen consumption rate (OCR) [113]. ....	3 1
Figure 2.16: A single cell array of PDMS microwells chemically modified by a self- assembled monolayer (SAM) [70]. ....	3 2
Figure 2.17: A rounded bottom microwell array (MA) of PDMS by molding a monolayer of highly ordered polystyrene (PS) microspheres [114]. ....	3 3
Figure 2.18: An array of microwells composed of wall of polymer and bottom of commercially available porous membranes to use vacuum-assisted cell seeding [115]. ....	3 4
Figure 2.19: Flow method to find the effective shape of microwells for single cell trapping in a microfluidic channel [116]. ....	3 5
Figure 2.20: 3D polyurethane-based microwell cell culture arrays selectively functionalized inside the wells to promote cell adhesion and on the plateau of wells to resist cell adhesion [71]. ....	3 6
Figure 2.21: A simple, low-cost microarray platform of PDMS that can trap tens of thousands of mammalian cells for dynamic single-cell analysis using the elasticity of PDMS [117]. ....	3 7

Figure 2.22: Microfluidic chips with arrays of microwells were developed for single-cell chemical lysis [118].	3	8
Figure 3.1: CASY cell counter and the principles used to measure cell size.	5	0
Figure 3.2: Analysis of the settling velocity of cells.	5	1
Figure 3.3: Boltzmann sigmoidal curve using the following parameters: initial value ( $A1$ ), final value ( $A2$ ), center ( $x0$ ), and time constant ( $dx$ ).	5	2
Figure 3.4: Size distribution of HeLa cells. Debris measured less than 7 $\mu\text{m}$ , dead HeLa cells measured from 7 to 12 $\mu\text{m}$ , and viable HeLa cells measured from 12 to 30 $\mu\text{m}$ .	5	5
Figure 3.5: Forces acting on a settling cell in liquid.	5	6
Figure 3.6: Photographs of settling HeLa cells in PBS (2 ml volume, $2.2 \times 10^6$ cells/ml) in a PS cuvette with inner dimensions of $10 \times 10 \text{ mm}^2$ .	6	3
Figure 3.7: Surface plot profile of the grayness values of the HeLa cell suspension.	6	4
Figure 3.8: Line plot profile of HeLa cells every 3 min for 45 min. The plot for each increasing time point was separated by an offset of 20 in order to distinguish between plots.	6	5
Figure 3.9: Polynomial curve fits of the line plot profile of the HeLa cell suspension at 0 min.	6	6
Figure 3.10: Line plot profiles at 0 min (black) and at the final measuring time of 45 min (red) for HeLa cells in the suspension.	6	6
Figure 3.11: Modified line plot profiles of HeLa cells. Photographs were taken every 3 min for 45 min. The modified line plot profiles indicate relative values of the original data to the 9th-degree polynomial fit of the plot at 0 min. The plot for each increasing time point was separated by an offset of $-20$ in order to distinguish between plots.	6	7
Figure 3.12: Heights of the HeLa cell suspension as determined by comparing the neighboring measured times the neighbor modified line plot profiles. The arrows indicate the height of the HeLa cells in the suspension, and the arrow color corresponds to the color of the line.	6	8
Figure 3.13: Boltzmann sigmoid of the height of HeLa cells in the suspension over time. The Boltzmann sigmoid was characterized by the following parameters: center ( $x0$ ) of 20.20 min, initial value ( $A1$ ) of $-0.369$ mm, final value ( $A2$ ) of 18.94 mm, and time constant ( $dx$ ) of 6.49 min.	6	9
Figure 3.14: Linear fits of the standard Boltzmann sigmoid with various time constants, ranging from $1/4$ to 3.	7	1
Figure 3.15: Different types of well plates for cell adhesion assays: (a) a 6-well plate with a well diameter of 34.80 mm, (b) a 12-well plate with a well diameter of 22.11 mm, and (c) a 24-well plate with a well diameter of 15.62 mm.	7	2
Figure 3.16: Images of a HeLa cell and the cell division process.	7	3
Figure 3.17: Spheroidal shape of the HeLa cell. The lengths are (a) for the two minor axes and (b) for the major axis.	7	4
Figure 3.18: Increase in the settling velocity of HeLa cells during the initial phase of settling (in PBS, at $23^\circ\text{C}$ and $37^\circ\text{C}$ ).	7	7

Figure 3.19: Large-scale fluctuations of particles occur when heavy, large particles (blue) settle to the bottom and light, small particles (red) raise to the top of the suspension [156]. The timescale is based on the Stokes time ( $t_S$ ) of particles. ....	7 8
Figure 3.20: Effects of particle concentration on particle-particle interactions [157]. ....	7 9
Figure 4.1: Synthesis of dopaminergic mesoporous inorganic-organic hybrid resins (HR-DOPAs). ....	8 7
Figure 4.2: Fabrication process for HR4-DOPA film on glass slides. The glass slides were 22 mm in diameter. ....	8 9
Figure 4.3: Resonance frequency of the cantilever with a single crystal silicon tip (PPP-NCLR-10). ....	9 0
Figure 4.4: AFM images of pure white glass coverslips. The measured area was $1 \times 1 \mu\text{m}^2$ in tapping and noncontact mode. The average ( $\pm$ SD) surface roughness was $446.00 \pm 128.06$ pm. ....	9 2
Figure 4.5: AFM images of the HR4-DOPA film on the glass coverslip. ....	9 3
Figure 4.6: The water contact angle (sessile drop) of HR4-DOPA was $62.08^\circ \pm 1.90^\circ$ at room temperature. The water volume was 10 $\mu\text{l}$ . ....	9 3
Figure 4.7: Comparison of the stability of MPTMS in HR4 and HR4-DOPA over time. Both resins were kept in vials at $8^\circ\text{C}$ for two years after synthesis without being opened. The formation of cross-linked silane aggregates – islands – was observed in HR4 (left), while HR4-DOPA remained clear and stable for a long period of time. ....	9 4
Figure 5.1: Structure of the cell membrane. The cell membrane is composed of a phospholipid bilayer, which is embedded with a large number of receptors, channels, and cell adhesion molecules. This depiction of the cell membrane was adapted from Wikipedia. ....	9 8
Figure 5.2: Integrin-mediated focal cell adhesion to the extracellular matrix (ECM) [204]. ....	9 9
Figure 5.3: Schematic showing the major components of hemidesmosomes in epithelial cells [209]. ....	1 0 1
Figure 5.4: Integrin-mediated cell spreading and migration. ....	1 0 2
Figure 5.5: Procedure for the HeLa cell adhesion assay. ....	1 0 5
Figure 5.6: Observation points for the HeLa cell adhesion assay. The adhered HeLa cells were manually counted in 3 different view fields ( $0.48 \text{ mm}^2$ ) from each sample using the grid function. The left/right observing point is 11 mm away from the center of the sample. ....	1 0 5
Figure 5.7: The number of adhered HeLa cells at various incubation times on dopaminergic mesoporous inorganic-organic hybrid resin (HR4-DOPA), mesoporous inorganic-organic hybrid resin (HR4), ECM protein layers (collagen IV and fibronectin), and glass. ....	1 1 0
Figure 5.8: Morphological features of BHK-21 cells after treatment with various concentrations of dopamine [224]. ....	1 1 4
Figure 5.9: Adsorption of fibronectin from serum solutions in relation with cell-spreading activity and cell adhesion [165]. In all the experiments, pairs of tissue culture dishes were treated with human serum at the concentrations indicated in the	

buffers shown, for 10 min at 22°C. At the end of the incubations, the dishes were rinsed and fixed. ....	1	1	5
Figure 6.1: Fabrication process for the SU-8 micromolding master for soft-lithography. ....	1	2	4
Figure 6.2: Fabrication process for the PDMS microwell array. ....	1	2	7
Figure 6.3: Fabrication process for the PDMS microwell array coated with cell-adhesive HR4-DOPA on the inner surface of the microwells. ....	1	2	8
Figure 6.4: The HeLa cell occupancy experiment in the microwell array. ....	1	2	9
Figure 6.5: Microwell arrays in an area of $2 \times 2 \text{ mm}^2$ . This area contained a total of 8 arrays, and each array (area, $500 \times 500 \mu\text{m}^2$ ) contained 200 microwells (size, $25 \times 25 \mu\text{m}^2$ each). ....	1	3	1
Figure 6.6: Detached SU-8 microstructures on the MCC primer 80/20-coated silicon substrate after development. Red circles show the locations of SU-8 microstructure detachment, which occurred despite their size ( $100 \times 100 \mu\text{m}^2$ ). ....	1	3	2
Figure 6.7: Scanning electron microscope images of the fabricated replica-micromolding master containing the array of 25- $\mu\text{m}$ -high SU-8 structures shaped in $25 \times 25 \mu\text{m}^2$ squares. ....	1	3	2
Figure 6.8: Pattern transfer failure of the liquid PDMS layer (thickness, 5 $\mu\text{m}$ ). ....	1	3	3
Figure 6.9: Thickness of the PDMS films at various concentrations of PDMS in tert-butyl alcohol (TBA) as a function of spin speed [238]. All substrates were spun for 5 min. ....	1	3	4
Figure 6.10: The fabricated microwell array coated with dopaminergic inorganic-organic hybrid resin (HR4-DOPA) on the inner surface of the microwells. The plateaus of the microwells were passivated by the cytophobic PDMS layer using microcontact printing. ....	1	3	5
Figure 6.11: HeLa cell adhesion on the control surfaces. HeLa cells were cultured for 3 h at an initial seeding concentration of $1.0 \times 10^6$ cell/ml. The cells were stained green with 5(6)-carboxyfluorescein diacetate n-succinimidyl ester (CFSE). All images depict overlapped fluorescent photomicrographs. ....	1	3	6
Figure 6.12: HeLa cell occupancy in 6 microwell arrays under two different experimental conditions: cell concentration and microwell depth. ....	1	4	1
Figure 6.13: Microwells containing 2 or more HeLa cells at the seeding cell concentration of $2.0 \times 10^6$ cells/ml. ....	1	4	3
Figure 6.14: Different morphologies of adherent (anchorage-dependent) and nonadherent (anchorage-independent) cells. ....	1	4	6
Figure 9.1: Microbiochip for mimicking <i>in vivo</i> microenvironments in a bio-cell processor for application to high-throughput drug screening with cellular analysis. ....	1	6	0

## LIST of Table

Table 2.1: Comparison of time and costs for the complete screen using traditional robot system and in microfluidic emulsions [65].	1 6
Table 2.2: Correlation between the extent of cell adhesion and the subsequent cell behavior [45].	1 8
Table 2.3: Comparison of well-defined terminal functional groups such as hydroxyl (OH), carboxyl (COOH), amine (NH <sub>2</sub> ) and methyl (CH <sub>3</sub> ) referring to water contact angle and surface charge related to cell adhesion and protein adsorption.	1 9
Table 2.4: Comparison and significance of the previous single cell arrays of microwells.	4 3
Table 3.1: Panels of human cancer cell lines and xenografts for <i>in vitro</i> assays in Europe [132], the USA [133], and Japan [134]. Numbers in parenthesis are the total number of cell lines available.	4 6
Table 3.2: Growth rate of HeLa cells at various incubation times.	5 4
Table 3.3: Density and dynamic viscosity of pure water at different temperatures [152].	5 9
Table 3.4: Components of phosphate buffered saline (PBS).	6 0
Table 3.5: Densities and dynamic viscosities of 4 different liquids: pure water, PBS, RPMI 1640, and Opti-MEM at 23°C (RT).	6 0
Table 3.6: Densities and dynamic viscosities of 4 different liquids: pure water, PBS, RPMI 1640, and Opti-MEM at 37°C.	6 0
Table 3.7: Calculated Stokes velocities of HeLa cells in 4 different liquids: pure water, PBS, RPMI 1640, and Opti-MEM at 23°C and 37°C using the measured diameter.	6 1
Table 3.8: Reynolds numbers of settling HeLa cells in 4 different liquids: pure water, PBS, RPMI 1640, and Opti-MEM at 23°C and 37°C.	6 1
Table 3.9: Calculated Stokes velocities of HeLa cells in 4 different liquids: pure water, PBS, RPMI 1640, and Opti-MEM at 23°C and 37°C using the measured diameter and volume (n = 15).	6 2
Table 3.10: The heights and settling velocities of the HeLa cell suspension at various times. The velocity at each time point is shown as the mean velocity from the previous time to the indicated time.	6 8
Table 3.11: The range of the x-axis from -1 to 1 in terms of various time constants for the standard Boltzmann sigmoid.	7 0
Table 3.12: Theoretical and experimental Stokes velocities of HeLa cells in PBS at 23°C.	7 1
Table 3.13: Heights of liquids with the different working volumes in 6-, 12-, and 24-well plates	7 2
Table 3.14: Settling time of HeLa cells in PBS according to working volume in 6-, 12-, or 24-well plates at 23°C and 37°C.	7 3
Table 4.1: Chemical compositions of various dopaminergic mesoporous inorganic-organic hybrid resins.	8 8
Table 4.2: Properties of a single crystal silicon tip (PPP-NCLR-10).	9 0

Table 4.3: Measured surface roughness (RMS) in a $1 \times 1 \mu\text{m}^2$ area of the glass slide. ....	9 2
Table 4.4: Measured surface roughness (RMS) in a $1 \times 1 \mu\text{m}^2$ area of the HR4-DOPA film. ...	9 2
Table 5.1: Morphological features of the adhered HeLa cells on HR4-DOPA. The grid size is $100 \times 100 \mu\text{m}^2$ . ....	1 0 8
Table 5.2: Morphological features of HeLa cell adhered on the control substrates. The grid size is $100 \times 10 \mu\text{m}^2$ . ....	1 0 9
Table 5.3: The number of HeLa cells per millimeter square adhering to the various substrates. The values indicate the mean $\pm$ SEM values from the 3 different view fields on the sample (n = 3). ....	1 1 0
Table 5.4: Light absorbance of the XTT reagent for HeLa cell viability for HR4-DOPA and HR4. The blank contained XTT reagent alone, without any cells in the well. The positive control consisted of XTT reagent plus HeLa cells cultured in medium without substrate. ....	1 1 2
Table 5.5: Effect of the serum in the medium on the adhesion and proliferation of RIN-5F cells on various ECM proteins by comparing two different culture conditions: in serum-free medium (RPMI 1640) or in serum medium (RPMI 1640 with 10% FBS). The cells were cultured for 8 h at $37^\circ\text{C}$ and 5% $\text{CO}_2$ . ....	1 1 6
Table 6.1: Fabrication specifications for construction of negative SU-8 photoresists with various thicknesses. ....	1 2 5
Table 6.2: Microwell arrays (size, $25 \times 25 \mu\text{m}^2$ ; depth, $10 \mu\text{m}$ ) coated with the HR4-DOPA film for assaying HeLa cell occupancy of microwells. ....	1 3 7
Table 6.3: The number of microwells (depth, $10 \mu\text{m}$ ) occupied by different numbers of HeLa cells at various cell concentrations. The microwells measured $25 \times 25 \mu\text{m}^2$ in size and were coated with the HR4-DOPA film. The initial seeding cell concentrations were $0.5 \times 10^6$ , $1.0 \times 10^6$ , and $2.0 \times 10^6$ cells/ml. The values indicate means $\pm$ SDs. ....	1 3 8
Table 6.4: Microwell arrays (size, $25 \times 25 \mu\text{m}^2$ ; depth, $25 \mu\text{m}$ ) coated with the HR4-DOPA film for assaying HeLa cell occupancy of microwells. ....	1 3 8
Table 6.5: The number of microwells (depth, $25 \mu\text{m}$ ) occupied by different numbers of HeLa cells at various cell concentrations. The microwells measured $25 \times 25 \mu\text{m}^2$ in size and were coated with the HR4-DOPA film. The initial seeding cell concentrations were $0.5 \times 10^6$ , $1.0 \times 10^6$ , and $2.0 \times 10^6$ cells/ml. The values indicate means $\pm$ SDs. ....	1 3 9
Table 6.6: Microwell arrays (size, $25 \times 25 \mu\text{m}^2$ ; depth, $40 \mu\text{m}$ ) coated with the HR4-DOPA film for assaying HeLa cell occupancy. ....	1 4 0
Table 6.7: The number of microwells (depth, $40 \mu\text{m}$ ) occupied with different numbers of HeLa cells at various cell concentrations. The microwells measured $25 \times 25 \mu\text{m}^2$ and were coated with the HR4-DOPA film. The initial seeding cell concentrations were $0.5 \times 10^6$ , $1.0 \times 10^6$ , and $2.0 \times 10^6$ cells/ml. The values indicate means $\pm$ SDs. ....	1 4 0

# Chapter 1. Introduction

## 1.1. New Drug Application

### 1.1.1 Aim of a new drug application

The pharmaceutical industry has expanded the development of new drug therapies in response to increasing healthcare demands from the global population. The mission of pharmaceutical research companies is to understand a prevalent or an emerging disease, to research and develop new therapies, and to bring a safe and effective new treatment to patients. The most recent trend in pharmaceutical research is to pursue drug development for the treatment of chronic diseases, for example, the 3 leading causes of death, that is, cardiovascular disease (CVD), cancer, and stroke. Among these 3 chronic conditions, CVD is the biggest killer [1]. According to an estimate by the Centers for Disease Control and Prevention (CDC, USA), in the United States alone, the cost of treating CVD was US \$444 billion in 2010, and more than 1 in 3 (83 million) American adults have some form of CVD.

### 1.1.2 Process of a new drug application

The process of new drug application (NDA) demands time and major investments of financial, human and technological resources. A new medicine must conform to strict regulations regarding testing and manufacturing standards. In most cases, it takes approximately 10–15 years to develop one new drug from the time of discovery to the time it is available for treating patients. The average cost for research and development for each successful medicine is estimated to be between US \$0.8 billion and 1 billion, which includes the cost of thousands of failed attempts . Out of approximately 5,000–10,000 candidate drugs, ultimately only one single drug will receive approval through the NDA process, as shown in **Figure 1.1**. During the NDA process, researchers work to

- validate drug targets identified from basic causes of disease at the level of genes, proteins, and cells,
- discover the correct molecule (potential drug) to interact with the chosen target,
- examine the new compound in both the laboratory and clinical settings for safety and efficacy,
- gain approval and market the new drug for use in the general population [1, 3-5].

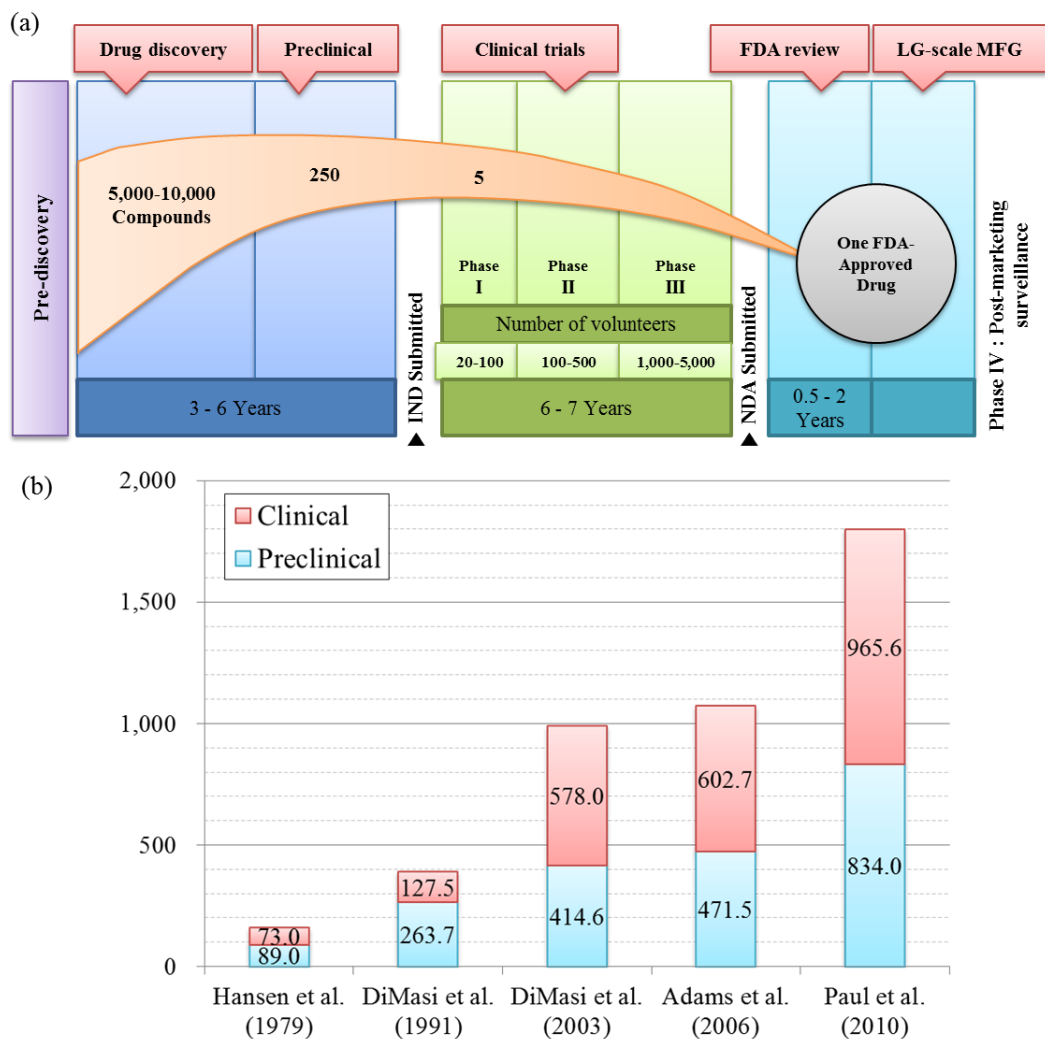


**Figure 1.1:** New drug application (NDA).

- (a) Overview of the NDA process and timeline, including the estimated number of drug candidates in preclinical trials and the number of volunteers needed during each phase of clinical trials for a single new drug [2].
- (b) Trend in capitalized preclinical, clinical, and total costs per approved drug, in terms of millions of US dollars (year 2009) [3]; IND: Investigational New Drug, FDA: Food and Drug Administration, LG-scale MFG: Large-scale manufacturing.

### **1.1.3 Importance of cell-based screening assays during preclinical trials in a new drug application**

A new bottleneck emerges at the point of drug discovery in the early phases of an NDA [6]. Drug discovery obviously requires prompt decision-making to identify from an enormous number of potential compounds, which kind of new chemical entities (NCEs) would constitute viable new drug candidates and have a high probability of becoming marketable [1, 6]. To reduce the risk to pharmaceutical firms, promising screening approaches have included a series of toxicity and *in vitro* cell-based assays that are performed at an intermediate stage after gene- or protein-based studies but before early *in vivo* animal testing [1, 6-8].

## **1.2. Microelectromechanical systems**

Microelectromechanical systems (MEMS) constitute a technology that can be used to miniaturize mechanical and electromechanical elements (i.e., devices and structures) in the analytical sciences. Commonly, miniaturized elements are fabricated using silicon, glass, or, more recently, different polymer types. Over the last several decades, MEMS researchers have developed an extremely large number of microsensors for chemical species, inertial forces, temperature, pressure, magnetic or electric fields, etc [9]. Many of these micromachined sensors have shown better performance than their macroscale counterparts [10]. Miniaturized sensors and actuators with microelectronic integrated circuits are added to develop complete systems-on-a-chip and to increase the numerous commercial market opportunities [11]. Among various MEMS applications, biochips or “lab-on-a-chip” have been widely adopted in the fields of analytical chemistry and the biomedical sciences, with integration of nano- or microfluidics, photonics, electronics, and chemistry for biomedical research [12-14]. With the help of these biochips, biological matter can be manipulated to analyze and measure its activity in a chip. Today, microbiochips are being extensively used in

the drug discovery process because of their capability for rapid high-throughput multiplexed analysis using low volumes of sample and reagent as well as a convenient and cost-effective approach for various analytical processes in biomedical research [15-17].

### **1.3. Single-cell Analysis for drug discovery**

#### **1.3.1 Misleading results from conventional *in vitro* cell-based screening**

Cell models in conventional *in vitro* cell-based screening continue to provide misleading data that are not necessarily representative of *in vivo* responses. Widely divergent phenotypes can arise even within the same cells in a short time scale because of slightly different cellular environments in the assay, such as temperature gradients or different chemical compound densities [8, 18-21]. Therefore, cell population analysis does not demonstrate a consistent response distribution, even when the same experiment is performed multiple times [22]. This behavior makes repetitive experiments and statistical analyses yielding average values and standard error of the mean (SEM) mandatory for the development of mathematical descriptions of cellular behavior [23]. To increase the reliability of an analysis of cellular responses and to benefit from economies of scale, uniform environmental conditions are required for cells in the early discovery process [8, 19].

In addition, multiplex and complicated cell-to-cell contact and communications within a single population of cells can conceal direct and accurate correlations between cells and stimuli [24]. Several types of cell-to-cell communication exist, including neurotransmitters recognized in the synapse, antigens that trigger antibody responses, and target cells that respond to specific hormones [25].

#### **1.3.2 Need for a single-cell isolation system for drug discovery**

In order to overcome the disadvantages associated with cell population analysis, a new technology that can not only provide uniform cellular environments during drug screening

but can also allow analysis of the direct effects of a drug on a single isolated cell is required in clinical diagnostics [26, 27]. In addition, because each cell can express a phenotype more or less different from other cells, even within the same cell type, an array of isolated single cells is required to produce regular cellular responses from individual cells in a quantitative manner [27, 28].

To allow highly accurate measurement of cellular response to a drug, researchers have used microfabrication techniques to create cell culture models [4, 8, 27]. These microcellular platforms can provide a uniform cellular environment and can mimic *in vivo* functions [19, 29, 30]. Moreover, an array of individual living cells can contribute to the elucidation of the biological effects of a drug on a single cell and can provide remarkable information regarding cellular chemistry at the molecular level [20, 27].

## **1.4. Single-cell isolation system**

### **1.4.1 Single-cell isolation techniques**

Single-cell isolation systems have been developed to provide various aspects of environmental control, measurements on fast timescales, image processing, and isolation of secreted biomolecules. Single-cell isolation methods have been developed in two ways: (1) microfluidic techniques and (2) array-based techniques [27, 31].

Microfluidic systems provide dynamic control of cells as well as reagents via fluid perfusion and pressure gradients. Hydrodynamic systems trap single cells by using (1) microfluidic ports, (2) semipermeable microstructure, or (3) microfluidic pipette-like channels that are smaller than the diameter of the cell. Continuous flow is required to maintain the cell in the correct position. Single-cell encapsulation systems are prevalent because an enclosed chamber surrounding individual cells can biologically and physically isolate a single cell from the environment. This system has high-throughput potential because

many cells can be encapsulated if a microfluidic droplet generator is used [32, 33].

Other methods such as array-based techniques have been developed to isolate single cells in uniform environments without integration into a microfluidic platform. Common methods for creating arrays are based on (1) physical trapping, (2) chemical modification, (3) physical modification, (4) holographic optical tweezers, or (5) dielectrophoretic techniques.

#### **1.4.2 Limitations of previous single-cell isolation system**

Polydimethylsiloxane (PDMS) is commonly used in hydrodynamic systems designed to trap single cells. PDMS enables numerous replications at both micro- or nanometer scales with high-precision from a micro- or nanofabricated mold. However, the inherent properties of PDMS do not allow for cellular adhesion, which, due to the absence of supporting cells, an extracellular matrix and growth factors, could affect the natural behavior of anchor-dependent cells that can survive only when they adhere to substrates.

Almost all micro single-cell arrays are developed in 2D culture systems using planar patterns of a cell adhesive, although conventional 2D cultures usually suffer from contact inhibition and a loss of native cell morphology and functionality [34, 35]. Compared to 2D cultures, 3D *in vitro* cell models provide a more realistic cellular environment and can reproduce *in vivo* cellular metabolism and function, including morphogenesis, gene expression, and differentiation [36, 37]. However, a 3D cell culture array must be multilayered, which makes it difficult to fabricate the array and to use it in high-throughput toxicological tests. The native 3D cellular morphology of the microwells on the plate is maintained, thereby providing a novel approach for 3D *in vitro* cell models that are suited for population statistics analysis from individual cell measurements. In addition, the cell adhesive surface of a microwell can support native cellular functionality by supporting cells, extracellular matrices, or growth factors [38].

## 1.5. Research objective

The main objective of this study is to introduce single-cell arrays for 3D *in vitro* cell models into high-throughput drug discovery and screening by developing a platform with an array of microwells coated with cell adhesive material to control the 3D shape of cells and to maintain native cell morphology and functionality.

## 1.6. Scope of this work

A potential application for this research, illustrated in **Figure 1.2**, is a bio-cell processor that can be used for drug discovery and can be integrated with novel platforms such as microfluidic chips and biochips. Microfluidic chips are designed for the introduction of nutrient cell media and drugs by using microvalves and mixers. Biochips are designed for immobilizing single cells, for mimicking the *in vivo* microenvironment, and for application to high-throughput drug screening with cellular analysis. A single-cell array is essential with regard to the bio-cell processor in order to maintain the native morphology and functionality of experimental cells and to provide results that better predict *in vivo* responses during the drug discovery process.

### 1.6.1 HeLa cells for microengineering (Chapter 3)

Depending on the type of cell, cellular behaviors differ widely. Surface treatment techniques using chemical or physical methods were determined to optimize cellular immobilization. The cell line used for experiments should be carefully chosen with respect to significance for clinical diagnosis and application to a microplatform for single cell analysis. HeLa, a cervical cancer cell line, was used in this study on the basis of previous literature, because of its biological value for cancer treatment and good adherent behavior on hydrophilic surfaces [39-42]. Despite many different descriptions of the biological characteristics of HeLa cells, few physical properties of HeLa cells have been reported.

Therefore, this study included collection and reanalysis of the physical properties of HeLa cells as well as measurement of cell diameter to provide technical specifications for the physical dimensions of the microwells intended for cells from the HeLa cell line.

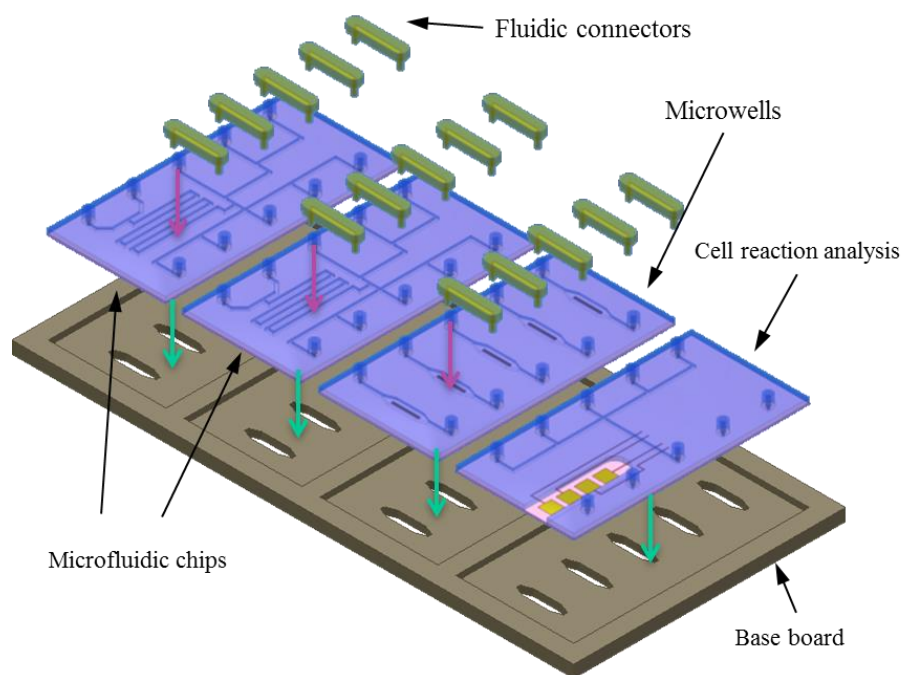


**Figure 1.2:** Schematic drawing of a bio-cell processor for drug discovery.

The bio-cell processor was composed of microfluidic chips and biochips. Microfluidic chips are designed for introducing both nutrient cell media and drugs by using microvalves and mixers. Biochips are designed for immobilizing single cells and mimicking the *in vivo* microenvironment and for application to high-throughput drug screening with cellular analysis.

### 1.6.2 Dopaminergic mesoporous inorganic-organic hybrid resin (Chapter 4)

New biological materials and novel technologies for surface engineering have been developed for a wide range of biological studies and applications, including medicine, pharmacology, and bioengineering [43-45]. An ideal biological material should be amenable to molecular design for a biologic purpose and easily synthesized [44]. Moreover, for application in microfabrication, a new biologic material should enable easy fabrication to exacting specifications and should be highly stable against water and organic solvents. Dopaminergic mesoporous inorganic-organic hybrid resin (HR-DOPA), one of the various materials available for promotion of cell adhesion, was used in this study. It was modified

from mesoporous inorganic-organic hybrid resin (HR) by substituting dopamine for catechol salt. HR films have demonstrated good adhesion strength to various substrates, high stability against organic solvents, and good biocompatibility [46, 47]. However, HR films were only stable for short periods because of silane coupling agents. The stability of HR films is guaranteed for only 3 weeks after synthesis, and HR films can therefore not be used after this period.

### **1.6.3 HeLa cell adhesion assay and viability on HR-DOPA (Chapter 5)**

Analysis of cell adhesion is an essential part of cell biology. Cell adhesion is the first step in a cascade of events, including cell survival by proliferation and migration and cell communication through cell-cell or cell-matrix interactions, which are dominated by the chemical or physical properties of substrates and media [48-50]. Cell adhesion assays commonly quantify cell adhesion by manually counting adherent cells per unit area [49, 51]. Moreover, biocompatibility of a new material should be proven by cell adhesion assays [52, 53]. Therefore, HeLa cell adhesion assay and viability experiments were performed to verify the biologic functions of HR-DOPA for microcellular applications.

### **1.6.4 Micro single-cell array coated with HR-DOPA (Chapter 6)**

The native cellular morphology and function of microwells coated with a cell adhesive surface are maintained, thereby providing a novel approach to 3D *in vitro* cell models that is suited for population statistics analysis from individual cell measurements [34-37]. In this study, microwells for micro single-cell arrays were (1) designed according to the physical dimensions of HeLa cells, (2) fabricated by soft lithography and microcontact printing, and (3) examined for HeLa cell occupancy of microwells after staining living cells.



## Chapter 2. State of The Art

### 2.1. Introduction

Single mammalian cells are fragile and small and therefore strictly require a particular microenvironment, such as one with moderate cell density, oxygen level, temperature, and nutrition level, to keep them viable and healthy [54]. Much of the research effort underway in the field of microtechnology pertains to miniaturizing biochips and mimicking the natural properties of single cells with *in vivo* functions, which involves provision of appropriate and uniform microenvironmental conditions for the cells [26, 27].

The use of microtechniques for analyzing isolated single cells, otherwise referred to as “single cells on chip,” has increased over the last decade because these methods can be used to clearly elucidate the effects of a specific stimulus on a single cell. In particular, these techniques can help elucidate cellular chemistry at the molecular level while minimizing cell-cell communications, stochastic biological noise, temperature gradients, and non-uniform densities of chemical compounds [8, 18-21, 24, 54]. In order to achieve significant results for cell reactions to external stimuli, a large number of single cells must be investigated to acquire adequate sets of data, which can be used to reasonably determine the distribution of responses and thereby to safely draw conclusions taking into consideration cellular heterogeneity [23, 27, 28]. Conventionally, 10,000 cells are considered the standard number for single-cell analysis [54]. However, some single-cell analysis techniques have assessed 1,000 single cells to provide adequate sets of data [55]. In general, analytical single-cell techniques are developed with the aims of being time-efficient and accurate, as well as the considerations of instrument compatibility, cell accessibility/manipulation, gentle cell handling, stable and robust cell tracking, continuous cell monitoring, and mimicking of *in vivo* conditions [27].

In this chapter, single-cell isolation techniques for microplatforms have been classified and explained in terms of their features and applications, and a detailed review of some representative papers is given. Furthermore, the significance of previous studies involving an array of microwells has been interpreted by comparing the geometry of microwells (size and shape), their material, the cell conditions, and the integration of microfluidics or sensors in these studies.

## **2.2. Single cell isolation techniques**

Single-cell isolation systems have been developed by the combined use of microengineering, chemistry, physics, and microfluidic techniques. Therefore, designing and constructing an analytical microplatform for isolated single cells requires comprehensive knowledge of several disciplines: (1) microengineering, for fabricating and integrating the device; (2) chemistry, for modifying the device's surface and analyzing its chemical characteristics; (3) physics, for analyzing phenomena at the nano- or microscale and for detecting and manipulating cell behaviors; and (4) fluidics, for controlling the flow and carrying cells; as well as (5) biology, for identifying and testing hypotheses concerning cell behavior.

The methods for single-cell isolation are largely categorized as microfluidic techniques or array-based techniques. Microfluidic techniques are used for perfusion cell cultures, where nutrient solutions are continuously fed to the bioreactor and the spent medium is constantly removed. Array-based techniques for static cell culture are used for conventional static cell culture.

## **2.3. Microfluidic techniques**

When designing microfluidic systems, it is important to recognize some unique physical principles at the micrometer scale, as well as general physical principles at the macro scale.

Generally, microfluidic channels with low Reynolds numbers (1 or below) assure laminar flow conditions, and mass transport of reagents and cells is highly controlled by fluid diffusion and pressure gradients [56].

Hydrodynamic systems designed to trap single cells are mainly divided into (1) semipermeable microstructures for changing flow direction by altering the shape of the microstructures after trapping cells, (2) microfluidic ports using pressure drops between 2 microfluidic channels with different length and/or size, (3) microfluidic pipette-like channels trapping single cells by negative pressure, and (4) droplet-based microfluidic systems encapsulating a single cell in an aqueous droplet within the oil phase.

### 2.3.1 Semipermeable microstructures

An array of semipermeable microstructures is used in microfluidic chips with the aim of constructing large-scale perfusion systems that recirculate media. This can be used for large quantities of reagents and enables analysis of large groups of individual cells in a uniform microenvironment [57].

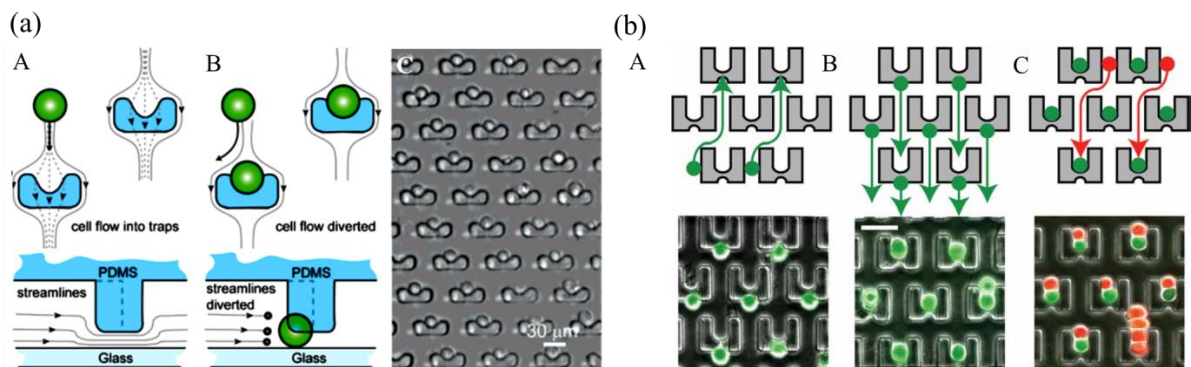


**Figure 2.1:** Semipermeable microstructures for capturing or paring cells.

- (a) The mechanism of cell trapping using flow-through arrayed suspended obstacles [57]. The cup-shaped PDMS trapping sites allow a fraction of fluid streamlines to enter the traps. After a cell is trapped, the fraction of streamlines through the barred trap decreases, leading to the self-sealing quality of the traps and a high quantity of single-cell isolates.
- (b) Three-step cell-loading protocol [58]. [A] Cells are first loaded ‘up’ toward the smaller back-side capture cup. [B] The direction of the flow is reversed, and the cells are transferred ‘down’ into the larger front-side capture cup two rows below. [C] The second cell type is loaded in from the top, and cells are captured in front of the first cell type.

Semipermeable microstructures are shaped like a pocket and are alternately arrayed such that intact cells can be easily transported into the micropockets [57-59]. Once a single cell enters a micropocket, the shape of the micropocket changes. The changed shape of the microstructure results in a diversion of flow direction and therefore the subsequent cells are transferred to the vacant pockets. Using this technique, most cells are loaded in an array in a short period (e.g., < 30 s) [57].

### 2.3.2 Microfluidic ports

In a hydrodynamic single-cell array of microfluidic ports using differential fluidic resistance, individual single cells are sequentially confined in a trapping site composed of a short channel and a narrow channel [60-62].

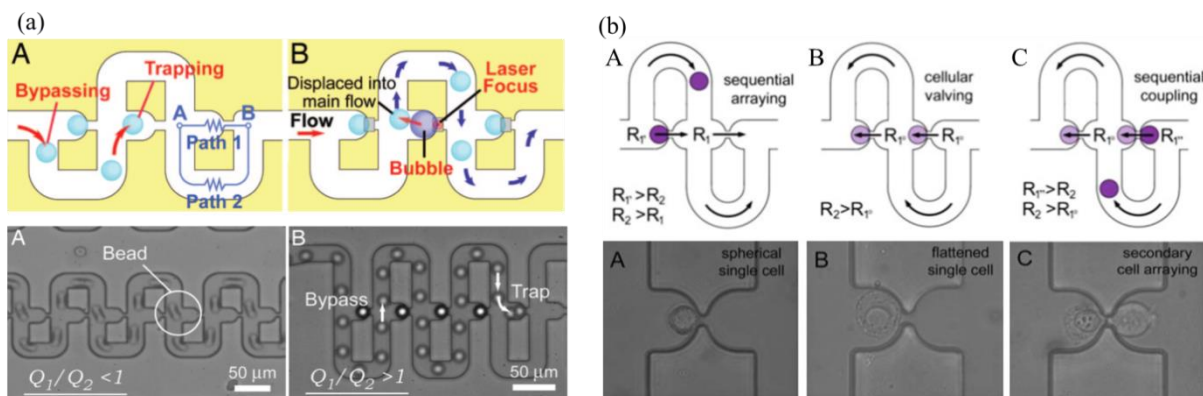


**Figure 2.2:** Cell trapping mechanism by changing flow conditions using microfluidic ports.

- (a) Schematic diagram of the fluidic cell trap [61]. [A] When the trap is empty, flow resistance along the straight channel is lower than that of the loop channel, and the main stream carries a cell into the trap if it is empty (trapping mode). [B] Cells will be carried along the loop channel if the trap is filled, bypassing the occupied trap (bypassing mode).
- (b) Hydrodynamic homotypic and heterotypic single cell co-culturing array [62]. [A] Loading of a spherical single cell (purple) reverses the fluidic resistance ratio, acting to divert subsequent cells ( $R_1 > R_2$ ) for sequential ( $R_2 > R_1$ ) single cell arraying. [B] Viable cells adhere and flatten, restoring the  $Q_1 > Q_2$  condition (i.e.,  $R_2 > R_1$ ). [C] Flow reversal is used for introducing a second spherical cell type and sequential single cell coupling ( $R_1' > R_2$ ;  $R_2 > R_1$ ).

Pressure force used to trap individual cells is generated by the different lengths [60] and sizes [61, 62] of the trapping and bypassing channels. To create the required pressure drops in

the microchannels varying with respect to the trapping state and the bypassing state, fluidic simulations and calculations are strongly required.

### 2.3.3 Pipette-like microfluidic systems

Pipette-like microfluidic systems use negative pressure driven by an exterior micropump to trap single cells, while the pressure required for trapping cells in microfluidic ports is spontaneously generated by differential pressure drops, as previously described [60-62]. Large groups of individual cells have been arrayed at a high density by using array-based single-cell isolation systems for static cell culture, but in a relatively short period with the help of the lower pressure. By using a micropump instead of complicated schemes of pressure drop generation, designing single-cell isolation systems using pipette-like microfluidics is easier than using microfluidic ports.

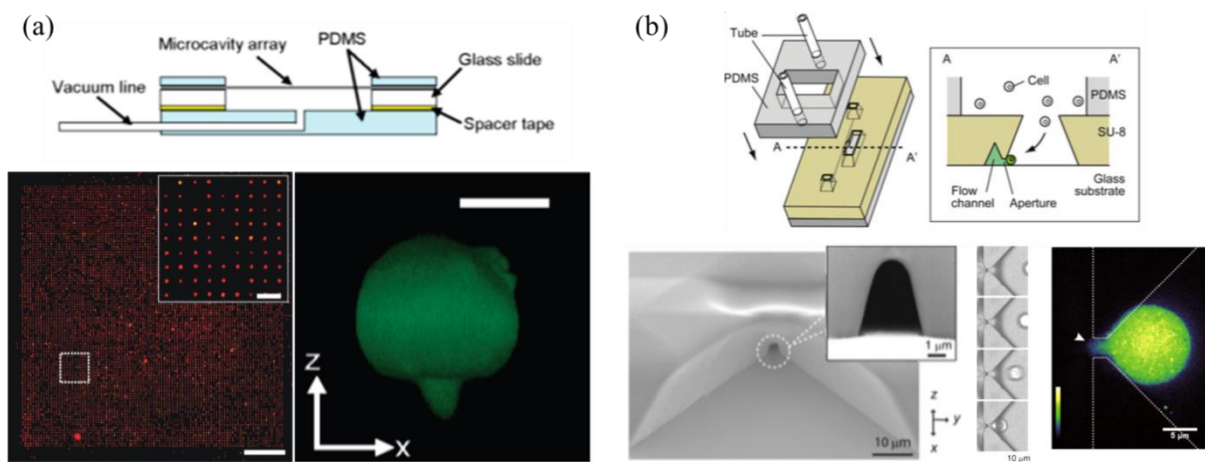


**Figure 2.3:** Pipette-like microfluidic devices to entrap single cells in an array. (a) High-density microcavity array for cell entrapment [63], (b) A pipette-like microfluidic device to visualize intercellular events of trapped single cell by space- and time-resolution [64].

### 2.3.4 Droplet-based microfluidic systems for single cell encapsulation

Recently, ultrahigh-throughput screening platforms using drop-based microfluidics have been rapidly developed because of their ability to overcome the scale and speed limitations of conventional robotic screening systems [65]. Aqueous droplets of picoliter volume dispersed

in oil are amenable to ultrahigh-throughput screening speeds (thousands of reactions per second) for biochemical analysis. Compared to conventional robotic screening systems, microfluidic droplets can be used for screening with a ~1000-fold increase in speed and a ~1-million-fold reduction in cost (**Table 2.1**) [65]. Microfluidic systems to sequentially generate droplets, for encapsulating and isolating single cells from the nozzle, at upstream of the microchannels symmetrically joining of two oil phase channels and an aqueous phase channel (**Figure 2.4**) [66-68].

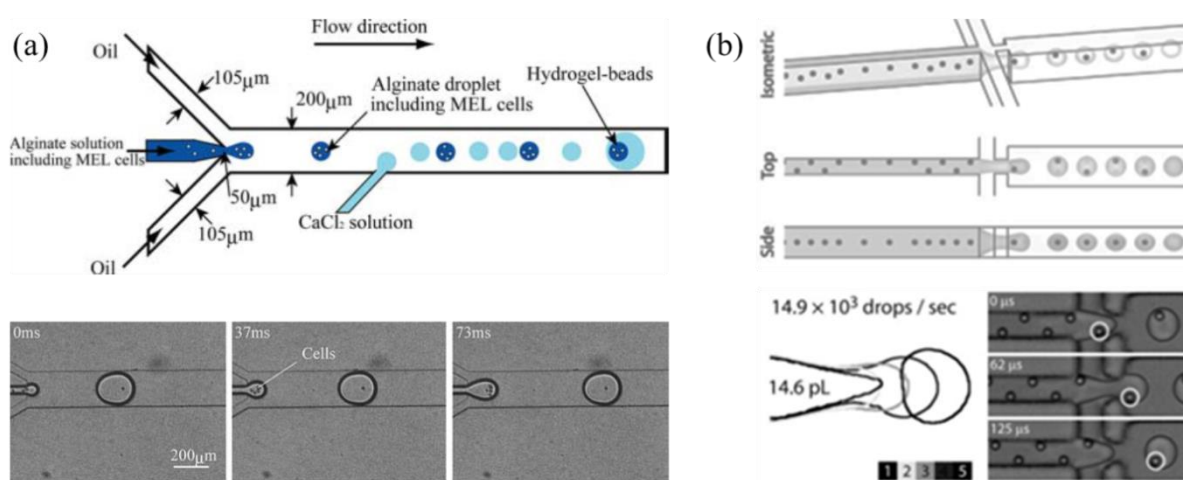


**Figure 2.4:** Microfluidic droplet-generation devices for isolating single cells  
 (a) A microfluidic droplet-generation device to produce hydrogel beads containing single living cells [66]. (b) Ordered single cell encapsulation in aqueous droplets [67].

**Table 2.1:** Comparison of time and costs for the complete screen using traditional robot system and in microfluidic emulsions [65].

	Robot	Microfluidic droplets
Total reactions	$5 \times 10^7$	$5 \times 10^7$
Reaction volume	100 $\mu$ l	6 pL
Total volume	5,000 l	150 $\mu$ l
Reactions per day	73,000	$1 \times 10^8$
Total time	~2 years	~7 h
Number of plates or devices	260,000	2
Cost of tips	\$ 520,000	\$ 1.00
Amortized cost of instruments	\$ 10 million	\$ 0.30
Substrate	\$ 4.75 million	\$ 0.25
Total cost	\$ 15.81 million	\$ 2.50

General materials of aqueous droplet were cross-linked hydrogel constraining cell motility and making the encapsulated cells incubated in suspension [66, 67]. However, microdroplets are only useful for anchorage-independent cells because the anchorage-dependent cells in suspension are induced to undergo apoptosis by losing their natural morphology and functions [69].

## **2.4. Array-based single cell isolation techniques**

Array-based single-cell isolation systems are fabricated for static cell cultures. They rely on specific chemical or physical properties of the surface to promote cell adhesion and immobilization. Array-based single-cell isolation systems are categorized into (1) two-dimensional cell adhesive patterns created chemically or physically, (2) dielectrophoretic electrodes, (3) magnetophoresis for immobilizing cells bound to magnetic particles coated with immunochemical molecules, (4) optical tweezers forcing cells to be trapped by the highest light intensity, and (5) microwells into which cells settle by gravity or flow via micro-channels.

### **2.4.1 Two-dimensional cell adhesive patterns**

The chemical and physical properties of cell-repellent and cell-adhesive biocompatible materials have been developed and analyzed with a focus on the interaction between cells and the surface. A surface treatment that promotes or prevents cell adhesion is applicable to the specification of other single-cell isolation techniques [8, 62, 70, 71]. Recently, surface chemistry analysis of biomaterials has assisted in the development of planar single or multiple cell-patterning methods using microtechnology.

The size of micropatterned cell-adhesive islands strongly regulates cell behavior such as cell growth, migration, proliferation, and viability (**Table 2.2**) [45, 72]. When the cell attaches on the surface with small cell-material contact area, the cell usually cannot survive

shaping round without formation of focal contacts and spreading. At middle-sized adhesion area, the cells are most active in proliferation and migration. If the contact area is very large with well-developed focal adhesion sites, the cells tend to be in differentiation phase rather than proliferation and migration [45]. Chen *et al.* [72] showed that apoptosis of single human or bovine endothelial cells adhering to a cell-adhesive pattern progressively declined as the island size was increased from 75 to 3000  $\mu\text{m}^2$ . Cell-adhesive patterns covering an area larger than 3,000  $\mu\text{m}^2$  were suggested for long-term cell culture (see **Figure 2.5**). Micro single-cell arrays are commonly developed in 2D culture systems by using planar cell-adhesive patterns. However, conventional 2D cultures may often be subject to contact inhibition and exhibit loss of native cell morphological features and functionality [34, 35].

**Table 2.2:** Correlation between the extent of cell adhesion and the subsequent cell behavior [45].

Cell spread	viability	migration	proliferation	differentiation
small	↓	↓	↓	↓
medium	↑	↑	↑	↓
high	↑	↓	↓	↑

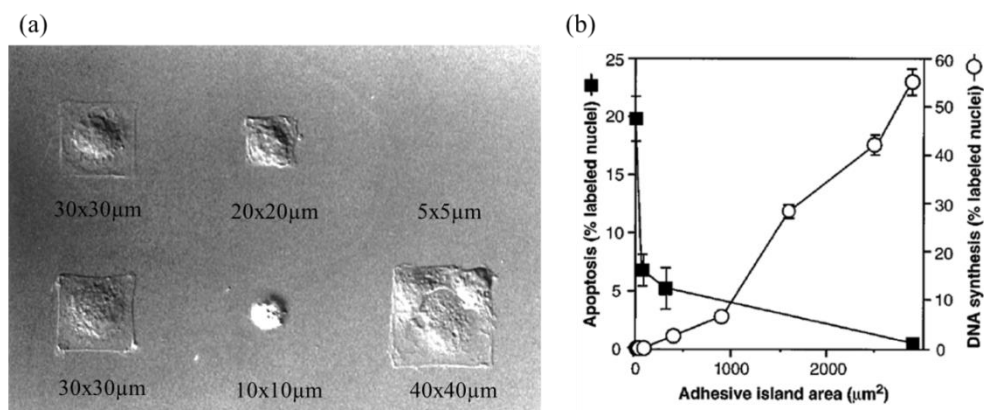


**Figure 2.5:** Effect of spreading on cell growth and apoptosis [72].

- (a) Nomarski images of the final shapes of bovine adrenal capillary endothelial cells adherent to the fabricated substrate.
- (b) Apoptotic index (percentage of cells exhibiting positive TUNEL staining) and DNA synthesis index (percentage of nuclei labeled with 5-bromodeoxyuridine) after 24 h, plotted as a function of the projected cell area. Data were obtained only from islands that contained single adherent cells; similar results were obtained with circular or square islands and with human or bovine endothelial cells.

### 2.4.1.1 Self-assembled monolayers

The interactions of cells with polymers are very difficult to measure because polymers have various chemical functional groups [51]. Therefore, self-assembled monolayers (SAMs) have been used as a surface chemical model to interpret the interactions of proteins and cells with artificial surfaces. SAMs are composed of a head group, tail, and functional group. The substrate materials depend on head groups. Alkanethiols, which contain an S–H head group, are the most commonly used molecules for attachment of noble metals such as gold (Au) and platinum (Pt). Silanes ( $\text{Si}_n\text{H}_{2n+2}$  or  $\text{SiR}_3$ ) are generally used on nonmetallic oxide surfaces such as glass and silicon dioxide. Phosphonic acids ( $-\text{PO}(\text{OH})_2$ ) are used on surfaces coated with metal oxides such as  $\text{Al}_2\text{O}_3$ ,  $\text{Ta}_2\text{O}_5$ ,  $\text{NbO}_5$ ,  $\text{ZrO}_2$ , and  $\text{TiO}_2$  [73, 74].

**Table 2.3:** Comparison of well-defined terminal functional groups such as hydroxyl (OH), carboxyl (COOH), amine ( $\text{NH}_2$ ) and methyl ( $\text{CH}_3$ ) referring to water contact angle and surface charge related to cell adhesion and protein adsorption.

Functional Group	hydroxyl (OH)	carboxyl (COOH)	amine ( $\text{NH}_2$ )	methyl ( $\text{CH}_3$ )
Chemical Structure	$\begin{array}{c} \text{H} \\   \\ -\text{C}-\text{OH} \\   \\ \text{H} \end{array}$	$\begin{array}{c} \text{O} \\ // \\ -\text{C} \\ \backslash \\ \text{OH} \end{array}$	$\begin{array}{c} \text{H} \\ / \\ -\text{N} \\ \backslash \\ \text{H} \end{array}$	$\begin{array}{c} \text{H} \\   \\ -\text{C}-\text{H} \\   \\ \text{H} \end{array}$
Water contact angle [75]	$29.0 \pm 0.6^\circ$ (hydrophilic)	$22.7 \pm 0.9^\circ$ (hydrophilic)	$52.9 \pm 2.3^\circ$ (hydrophilic)	$108.6 \pm 0.3^\circ$ (hydrophobic)
Chemical Structure in medium (pH=7.4)	$\begin{array}{c} \text{H} \\   \\ -\text{C}-\text{OH} \\   \\ \text{H} \end{array}$	$\begin{array}{c} \text{O} \\ // \\ -\text{C} \\ \backslash \\ \text{O}^- \end{array}$	$\begin{array}{c} \text{H} \\   \\ -\text{N}^+ - \text{H} \\   \\ \text{H} \end{array}$	$\begin{array}{c} \text{H} \\   \\ -\text{C}-\text{H} \\   \\ \text{H} \end{array}$
Surface charge in culture medium	neutral	negative carboxylate anion	positive ammonium cation	neutral
Effect on cells [76]	increase osteoblast differentiation	increase osteoblast attachment	promotes myoblast and endothelial proliferation and osteoblast differentiation	promotes increased leukocyte adhesion and phagocyte migration

The well-defined terminal functional groups in SAMs are the hydroxyl (OH), carboxyl (COOH), amine (NH<sub>2</sub>), and methyl (CH<sub>3</sub>) groups [77]. The strength of cell adhesion to SAMs decreases in the following order: OH > COOH = NH<sub>2</sub> > CH<sub>3</sub> [78]. Four different functional groups of SAMs are involved in the surface charge and wettability of polymers related with cell adhesion as well as protein adsorption. **Table 2.3** shows the characteristics of the main functional groups of SAMs, focusing on water contact angle and surface charge in cell culture medium (pH = 7.4). The planar cell-adhesive micropatterns of SAMs were generally fabricated by photolithography or micro-contact printing ( $\mu$ CP) [79-81].

#### **2.4.1.2 Surface charge**

Nearly all cells (except for some bacteria) are covered with negatively charged functional groups at a neutral pH [82]. Therefore, the surface charge needed to immobilize cells is typically positive and is created by coating chemical components (i.e., amine functional groups) [83], by changing chemical composition and exposing to light [84], or by applying DC electrical fields to the electrodes for temporarily capturing cells (electrophoresis [EP]) [85]. Negatively charged surfaces are also utilized to immobilize cells on the surface; oxygen plasma treatment of polymers or hydrogels has been commonly used to increase negative charge by adding carbonyl groups or ester groups, thereby generating moderate wettability for cell adhesion [86, 87].

#### **2.4.1.3 Surface hydrophilicity/hydrophobicity**

Wettability has been commonly assessed to determine cell adhesion onto polymers, copolymers, and polymers treated by plasma, corona, or surface graft polymerization [51]. Measurement of the water contact angle is very simple and clearly indicates the comprehensive result from various chemical molecules and physical properties of the surface. Moderate wettability for cell adhesion is in the range of 40–70° of the water contact angle [51,

88]. Extreme hydrophobicity or hydrophilicity of the surface inhibits cell adhesion [89-91] as shown in **Figure 2.6**. A super-hydrophobic surface randomly binds to nonspecific proteins such as albumin, preventing cell adhesion. The albumin adsorbs onto hydrophobic surfaces 10–100 times more effectively than fibronectin and vitronectin (which promote cell adhesion), and thus the albumin layer interferes with cell-to-surface interactions [90]. Water molecules are strongly attached on super-hydrophilic surfaces. Cell-adhesive ECM molecules such as fibronectin and vitronectin bind too weakly to detach water molecules on super-hydrophilic surfaces and are not subsequently adsorbed onto the surface. Therefore, cells are poorly attached to super-hydrophilic surfaces [91, 92]. Micropatterns for cell adhesion as well as protein adsorption in terms of wettability have been fabricated by coating the mixed SMAs with different well-defined functional groups [51] or by chemically modifying the surface using plasma treatment [93].

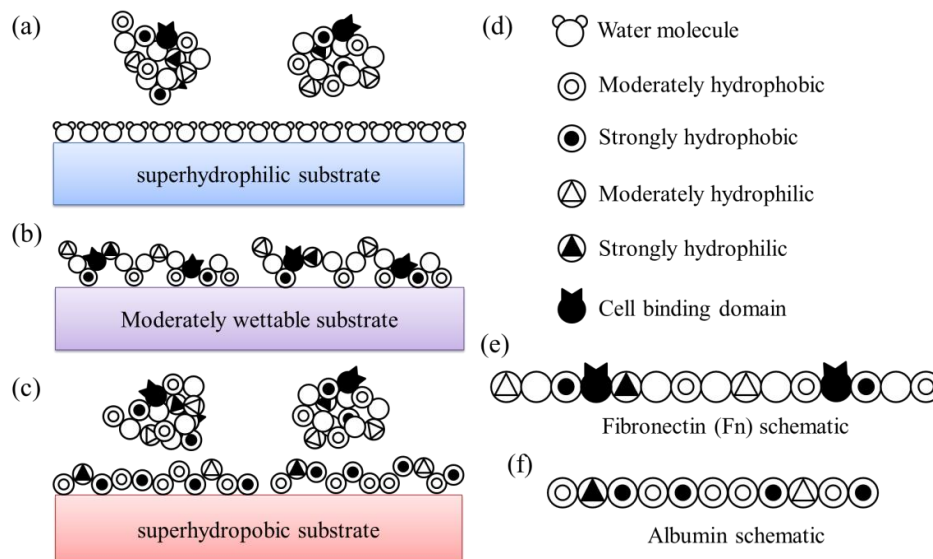


**Figure 2.6:** A conceptual model of the behavior of fibronectin and albumin adsorbed to surfaces with different wettability [90-92].

- (a) On superhydrophilic substrates, water molecules are strongly attached, preventing any cell-adhesive ECM molecule such as fibronectin (Fn) or vitronectin (Vn).
- (b) On moderately wettable substrates (water contact angle: 40–70°) Fn and Vn are adsorbed on the surface and help cell adhesion.
- (c) A superhydrophobic surface is randomly bound to non-specific proteins such as albumin without cell binding domains. The albumin adsorbs on hydrophobic surfaces 10–100-fold higher than Fn and Vn.

### 2.4.1.4 Surface roughness

Mechanistic investigations indicate that substrate microtopography can alter the establishment and organization of cell membrane-based focal adhesion complexes and can therefore invoke specific signaling pathways that may regulate cellular phenotypes and functions [94, 95]. Although microtopography affects cell behavior, cells exist in interfaces with topography closer to the nanometer scale [96]. Ranucci and Moghe [95] reported a cellular focal adhesion mechanism for substrate topographic regulation of cellular motility on ligand-modified polymer substrates, as shown in **Figure 2.7**.

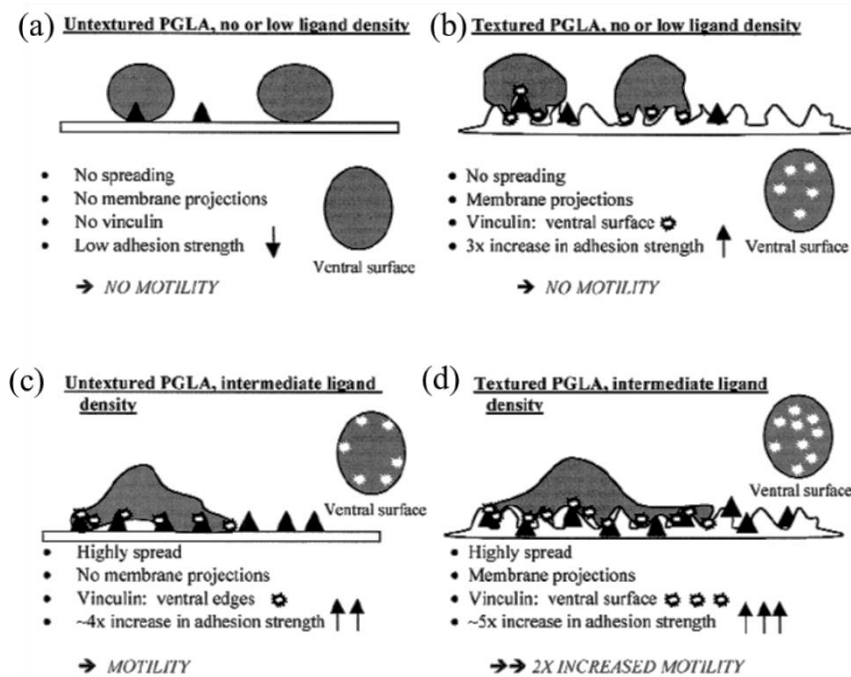


**Figure 2.7:** Proposed mechanisms for substrate topographic regulation of cellular motility on ligand-modified substrates [95].

(a) In the absence of binding ligands and substrate microtexture. (b) The incorporation of substrate microtexture in the form of micropores. (c) Increased cellular adhesion to the untextured substrate by adsorbing adhesive ligands to the polymer. (d) Distinct mechanical and biochemical modes of cellular adhesion during the formation of focal adhesion complexes.

### 2.4.2 Holographic optical tweezers

Holographic optical tweezers are considered essential tools for manipulating single cells and for performing sophisticated biophysical/biomechanical characterizations. The trapping

forces depend on the intensity of laser power, the size and shape of the trapped particles, and on the index of refraction of the trapped particles relative to the surrounding medium. Optical tweezers can be used to transport foreign materials into single cells, to deliver cells to specific locations, and to sort cells in microfluidic systems [97]. For single-cell trapping, optical tweezers are used to apply non-contact force to cells, using well-defined geometries with accurate force resolution and amenability to liquid medium environments. The cellular microarray by using an optical tweezer enables to separate and immobilize single cells with the precise control of the cell number and density within the measurement region [98, 99]. However, cells can be damaged by high-intensity light and elevated temperatures [97].

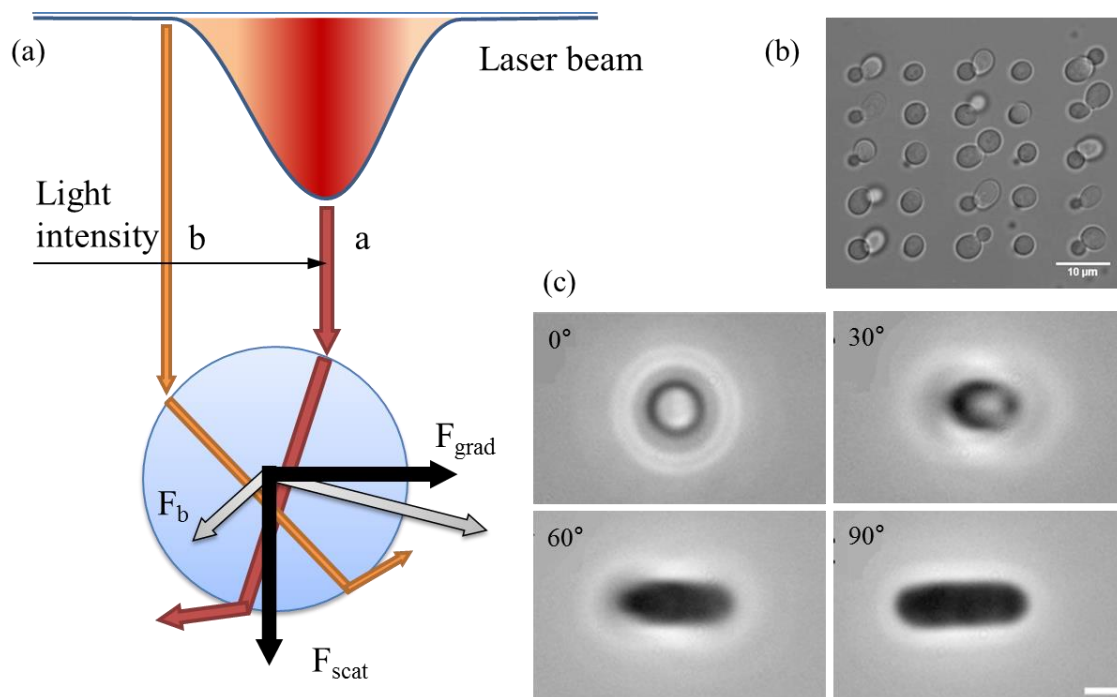


**Figure 2.8:** Holographic optical tweezers for single cell isolation.

- (a) Principle of optical tweezer [97]. The scattering ( $F_{\text{scat}}$ ) and gradient ( $F_{\text{grad}}$ ) components of optical forces on a dielectric sphere due to a Gaussian laser beam (light intensity increases from b to a).
- (b) Cellular microarray in microfluidic chip combined with optical tweezers enabling precise control of the cell density [98].
- (c) Controlled tilt-angle of rod-shaped *E. coli* by adjusting torque by varying the amplitude of the highly focused linear polarized Gaussian beam [100].

### 2.4.3 Magnetophoretic techniques

The migration of a particle under a magnetic field is termed magnetophoresis. Magnetic separation of ferromagnetic nanoparticles in microfluidic devices is widely utilized in chemical and/or biological analyses [101-103]. Magnetophoresis using immunobinding and electromagnets is applicable to a wide range of single-cell analyses owing to the potential for specific sorting/immobilization of target cells in a short time and to the reversibility of immobilization/release of target cells by an on-and-off magnetic force [104, 105]. However, the range of the effective magnetic force is limited because the magnetic force dramatically decreases with the distance between the magnet and the beads.

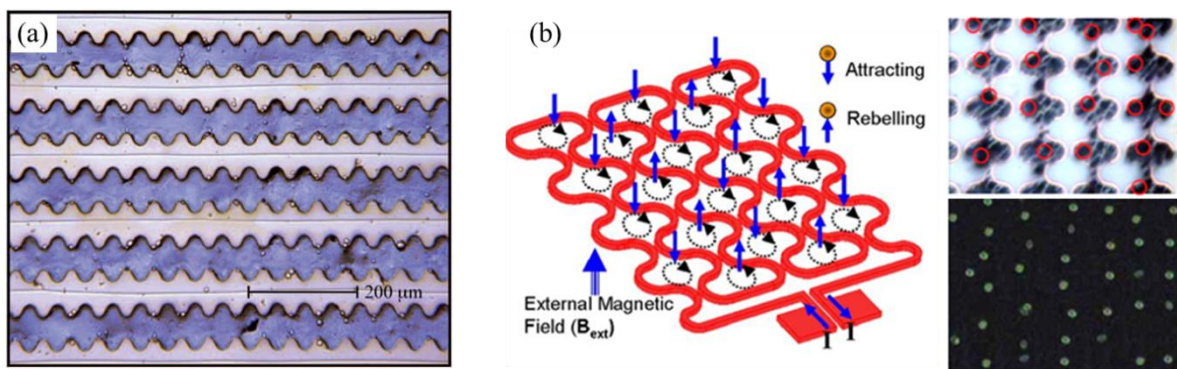


**Figure 2.9:** Magnetophoretic single cell isolation techniques.

- (a) Permalloy based magnetic single cell micro array (MSCMA) [104]. Yellow regions show the gold substrate and blue regions are the electroplated permalloy.
- (b) A reversible assembly of immunomagnetically labeled single cells in an array by CCCs creating a template periodically attracting and repelling zones [105].

### 2.4.4 Dielectrophoretic techniques

Dielectrophoresis (DEP) is a common approach for performing cellular manipulations by using the interactions of the dipole of particles or cells and the spatial gradient of the electric field. Typically, AC fields are used for DEP in order to minimize physiological impact on the cells and any electrochemical reactions at the electrodes. The dipolar rate of cells polarized by applied electric fields is predominantly due to the cell wall, cell membrane, and/or cytoplasmic electrical properties. The DEP force on particles or cells is strongly

dependent on the dipole constitution and magnitude. Free-charge dipoles of particles or cells dominate at low frequencies whereas polarization-charge dipoles dominate at high frequencies. Dielectrophoretic microarrays simultaneously and actively trap thousands of single mammalian cells in alignment with a planar or microstructured microelectrode array [106-109]. However, known undesired effects of electric fields on cells are induced thermal heat caused by electric currents and the electric fields imposed within the cell membrane or the cytoplasm [82].

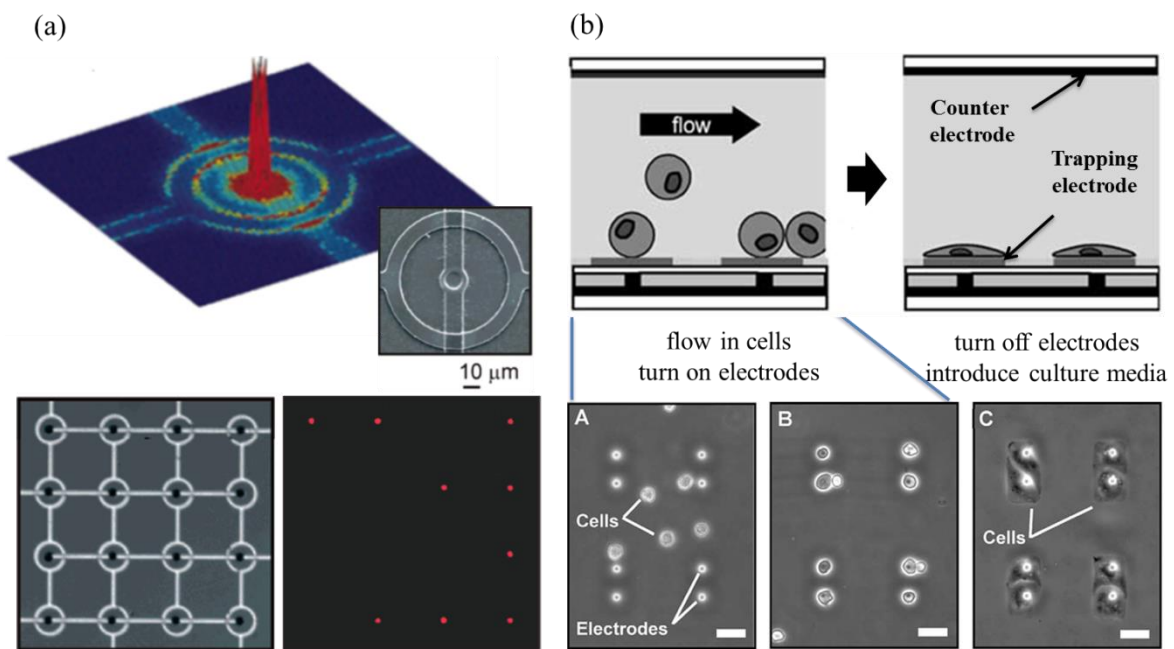


**Figure 2.10:** Dielectrophoretic single cell isolation techniques.

- (a) Addressable positive dielectrophoretic (p-DEP) trapping array with a passive, scalable architecture (“ring-dot” geometry) [106].
- (b) A dielectrophoretic microarray to simultaneously and actively trap thousands of single mammalian cells [107].

## 2.5. Microwells

Micro single-cell arrays are generally developed using planar cell adhesive patterns, although conventional 2D cultures are often subject to loss of native cell morphology and functionality [34, 35]. Compared to 2D cultures, 3D *in vitro* cell models provide a more realistic cellular environment and can reproduce *in vivo* cellular metabolism and function,

including morphogenesis, gene expression, and differentiation [36, 37]. However, a 3D cell culture array must be multilayered, which makes it difficult to fabricate the array and to use it in a high-throughput toxicological test. The native 3D cellular morphology of the microwells on the plate is maintained, thereby providing a novel approach for 3D *in vitro* cell models that are suitable for population statistics analysis from individual cell measurements. In addition, the cell adhesive surface of a microwell can support native cellular functionality by supporting cells, extracellular matrix, or growth factors [38].

By spatially arranging isolated cells in an array, a sufficient number of single cells can be quantitatively analyzed to draw valid conclusions, rather than interpreting individual cell variation as noise due to cell population heterogeneity [23, 27, 28, 54, 55]. Larger microwells generally facilitate long-term culture (days and weeks) while smaller microwells are designed for instant analysis (hours and days) because of the correlation between cell behavior and the size of the cell-adhesive area [45, 55, 72]. Nevertheless, there is a strong interest in using smaller microwells than larger ones for single cell analysis because the shorter distances and diffusion times of molecules and cells are more suitable for time-efficient and accurate analysis, especially in high-throughput applications [27, 55].

Rettig and Folch at the University of Washington, USA [38], reported an optimization study of microwell dimensions and cell-seeding parameters for mouse fibroblast cells (NIH3T3) and rat basophilic leukemia cells (RBL-1) as models of anchorage-dependent and anchorage-independent cells, respectively (**Figure 2.11**). Circular microwells of PDMS of different diameters (15, 20, 25, 30, 35, and 40  $\mu\text{m}$ ) and depths (16, 21, and 27  $\mu\text{m}$ ) were fabricated using soft lithography and were arrayed with 10- $\mu\text{m}$ -thick walls as a hexagonal honeycomb. An optimal ratio of depth to diameter for obtaining maximum single-cellular occupancy was  $\sim 1$  for both cell types. The maximum single-cell occupancy of NIH3T3 cells was  $84.5\% \pm 0.2\%$  in microwells with a depth of 27  $\mu\text{m}$  and a diameter of 25  $\mu\text{m}$ , whereas it

was  $92.2\% \pm 2.2\%$  in microwells with a depth of  $21\ \mu\text{m}$  and a diameter of  $20\ \mu\text{m}$  for RBL-1 cells after 40 min of settle time. Single-cell occupancy did not increase as the depth increased beyond the optimal diameter for both cells.

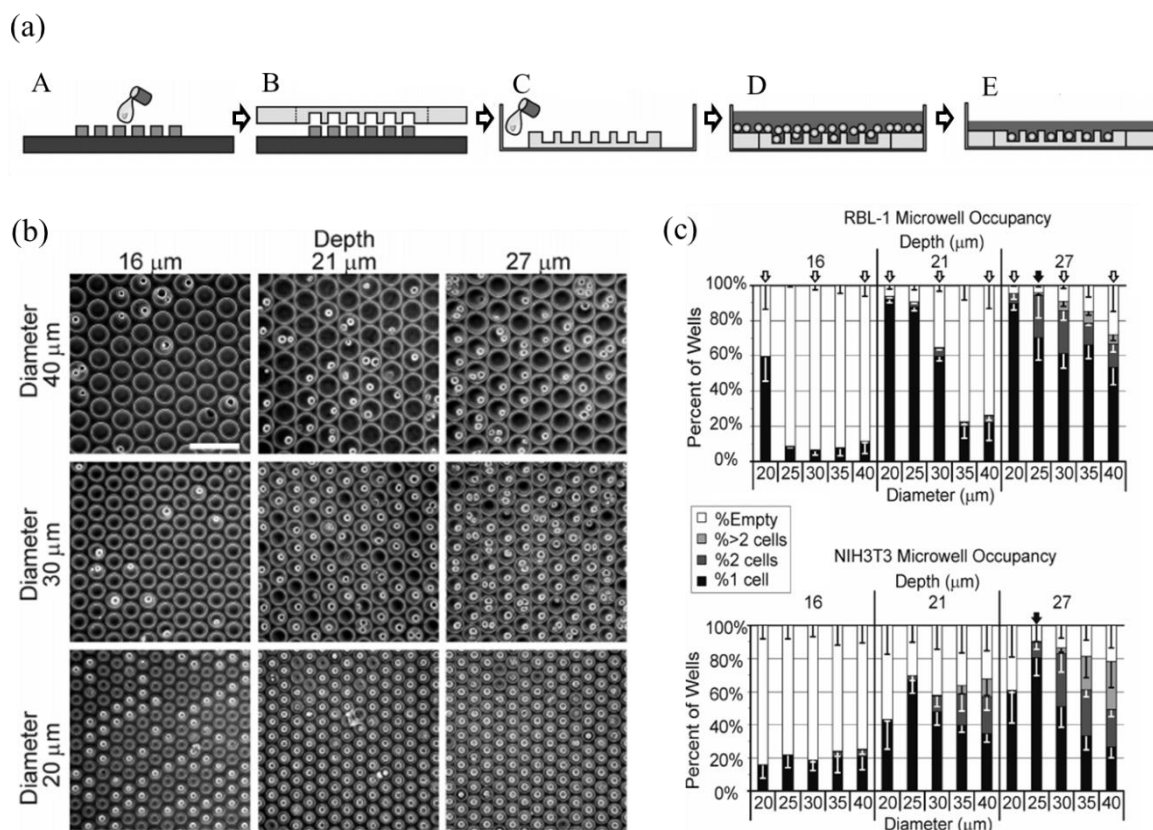


**Figure 2.11:** Optimization study of PDMS microwell dimensions and cell seeding parameters for NIH3T3 and RBL-1 [38].

- (a) Schematics of the fabrication and seeding procedure.  
 (b) Nine representative pictures of RBL-1 cells in microwells for all the combinations of 3 different diameters with range of  $20\text{--}40\ \mu\text{m}$  and three different depths with range of  $16\text{--}27\ \mu\text{m}$ . Scale bar is  $100\ \mu\text{m}$ .  
 (c) Cellular occupancy as a function of microwell dimensions. Each vertical bar depicts the percentage of microwells occupied by a single cell (black segment), 2 cells (dark gray), more than 2 cells (light gray), or no cells (white).

Deutsch and co-workers at Bar Ilan University, Israel [110], fabricated adjacent rough cone-shaped cell retainers (CR) used for high-content correlative multi-parametric measurements of living individual anchorage-independent cells within a population (**Figure 2.12**). The CRs made of glass were wet-etched by hydrofluoric acid (HF, 48%) with a

densely packed 2D arrangement of  $\sim 8\text{-}\mu\text{m}$ -deep hexagonal picoliter wells (PWs) with a  $20\text{-}\mu\text{m}$ -pitched honeycomb-like pattern. Cellular occupancy, retention, and apoptosis were investigated using 4 different human acute T lymphoblastic leukemia cell lines: MOLT-4, U937, Jurkat, and K-562. The percentage of occupied PWs was  $81\% \pm 4.2\%$  from 7,000 loaded cells, and the single-cell occupancy rate was  $93\% \pm 2.8\%$  of all the cells located in the PWs.

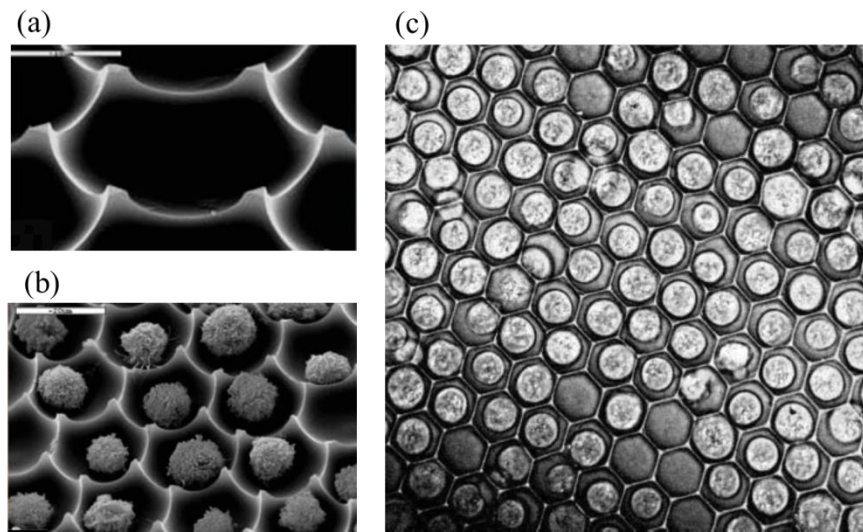


**Figure 2.12:** Adjacent rough cone-shaped cell retainers (CRs) [110].

(a) SEM micrograph of the CR structure. Scale bar is  $10\ \mu\text{m}$ .

(b) Post-fixation observations of Jurkat T cells by SEM image. Scale bar:  $20\ \mu\text{m}$ .

(c) Highly dense loading of K-562 myelogenous leukemia cells in CRs.

Ochsner and co-workers at the Swiss Federal Institute of Technology (ETH), Zurich, Switzerland, [111] fabricated arrays of microwells with different geometries (circle, square, triangle, rectangle, or spindle) and a depth of  $10\ \mu\text{m}$  to control the 3D shape of single cells (**Figure 2.13**). Adherence of HUVECs was limited to the inside of microwells by passivation of the microwell plateau by using inverted microcontact printing. The cell-repellent polymer on the plateau was PLL-g-PEG, and the surface of the microwell was air-plasma-treated PDMS coated with specific adhesive proteins (fibronectin) or lipid bilayers (1,2-dioleoyl-sn-glycero-3-phosphocholine [DOPC]). Adequately controlled 3D shape of the cells was seen in

fluorescent confocal images of cell nuclei and actin cytoskeletal networks, stained by ethidium homodimer (blue) and Alexa 488-phalloidin (green), respectively (**Figure 2.13**).

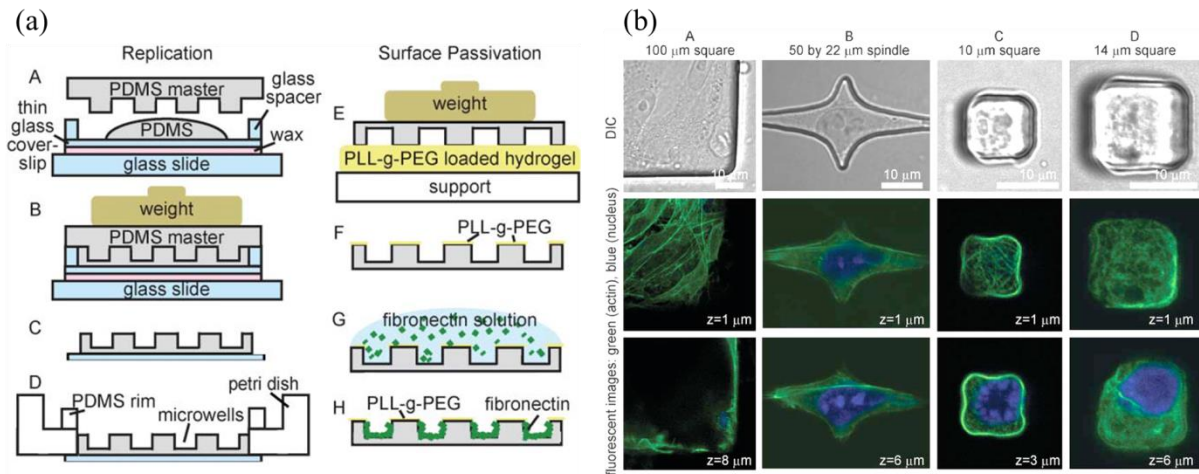


**Figure 2.13:** Arrays of microwells with different geometries (circle, square, triangle, rectangle and spindle) for 3D shape control of single cells [111].  
 (a) Schematics of the fabrication procedure.  
 (b) DIC and fluorescent confocal images are shown of cell nuclei (blue) and actin cytoskeletal networks (green). HUVECs were cultured for 24 h.

Sasuga and co-workers at the Tokyo Metropolitan Institute of Medical Science, Japan [112], developed a microwell-based single-cell lysis method by using a dense array of microwells with 10–30 pl volume (**Figure 2.14**). Cuboidal microwells of PDMS with different sizes ( $20 \times 20$ ,  $30 \times 30$  or  $40 \times 40 \mu\text{m}^2$ ) and a uniform depth of  $20 \mu\text{m}$  were fabricated by soft lithography and arrayed on a  $24 \times 32\text{-mm}^2$  coverslip with a well-to-well spacing of  $30 \mu\text{m}$ . Single-cell analysis of rat pheochromocytoma cells (PC12) was performed in 3 steps: (1) cell trapping in an array of picoliter-scale microwells; (2) chemical lysis in the closed microwell; and (3) fluorescent detection of immunosignals or enzymatic activities in the microwell. Using this device, enzymatic activities of a single PC12 cell in each well were continuously monitored under several different conditions.

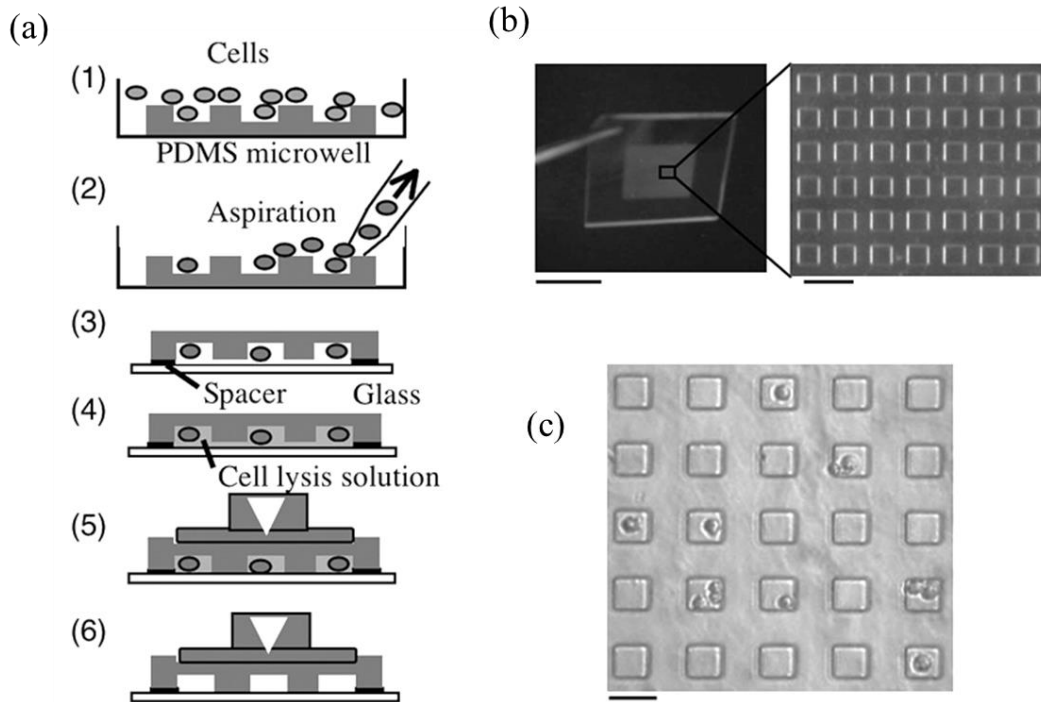


**Figure 2.14:** A microwell-based single cell lysis method [112].

(a) Schematic drawing of the single-cell lysis procedures.

(b) An overview of the PDMS sheet (scale bar, 10 mm) and a microscopic image of the microwells (scale bar, 100  $\mu\text{m}$ ).

(c) A microscopic image of a PC12 cell-trapped microwell.

Molter and co-workers at the University of Washington, USA [113], developed an MA device capable of measuring cellular parameters and single-cell oxygen consumption rates (OCRs) in each well while minimizing the disruption of normal cell function (**Figure 2.15**). The rounded-cylindrical glass microwells had a diameter of approximately 65  $\mu\text{m}$ , a depth of 25  $\mu\text{m}$ , and a volume of 80 pl and were arrayed with a center-to-center space of 300  $\mu\text{m}$ . Phosphorescent oxygen sensors were integrated inside each microwell by sintering FluoSpheres<sup>®</sup> Platinum carboxylate-modified microspheres adhering to the plasma-treated surface of the microwell on a 120°C hot plate for 10 min. Oxygen consumption in the murine macrophage cell line (RAW264.7), human epithelial lung cancer cell line (A549), and human Barrett's esophagus cell line (CP-D) in each sealed microwell was measured by optimized rapid lifetime determination (ORLD) methods. An OCR experiment performed on the array

showed different oxygen-concentration depletion rates inside microwells containing 0, 1, or 2 cells and different oxygen consumptions according to cell types, that is, 0.61, 0.91, and 1.32 fmol/min for RAW264.7, A549, and CP-D cells, respectively.

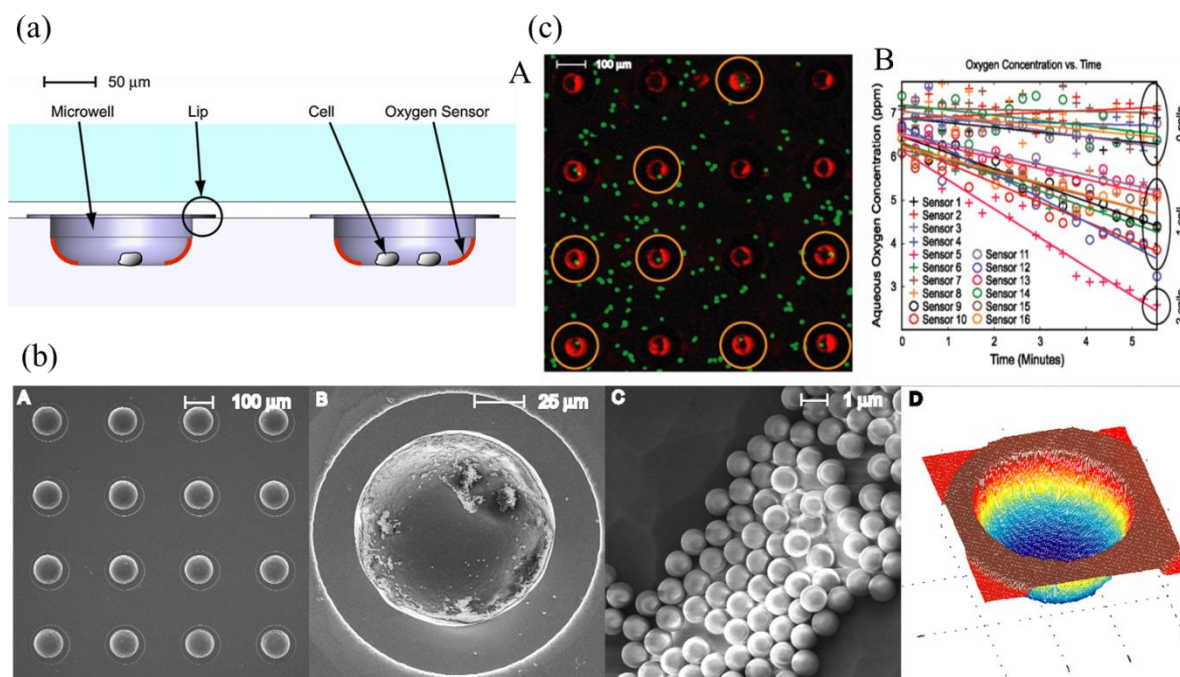


**Figure 2.15:** A microwell array measuring oxygen consumption rate (OCR) [113].

The cells residing in the 100- $\mu\text{m}$ -in-diameter and 30- $\mu\text{m}$ -deep microwells with the oxygen sensor are diffusionally sealed from the external surroundings. Polystyrene beads (diameter, 1  $\mu\text{m}$ ) tend to clump and attach to the microwell in areas other than the side wall. An OCR experiment performed on the array yields a plot of oxygen concentration versus time for each sealed microwell in the array after a lid has been lowered.

Leong and co-workers at the University of Washington, USA [70], fabricated a single-cell array of PDMS microwells chemically modified by a SAM (**Figure 2.16**). The bottom of the microwells was sputtered with a 25-nm-thick gold layer, functionalized by a SAM of (10-mercaptopomethyl-9-anthyl)(4-aldehydephenyl)acetylene (MMAAPA), and then coated with collagen, an adhesion receptor ligand, covalently bound to the SAM by using Schiff chemistry. Collagen is a long fibrous structural protein that enhances the attachment and proliferation of various cells, including endothelial cells, fibroblasts, hepatocytes, and epithelial cells. Optimal microwell geometry in an array for single mouse pituitary tumor

cells (AtT-20; diameter,  $\sim 15 \mu\text{m}$ ) was a diameter of  $20 \mu\text{m}$  and interstitial spacing of  $250 \mu\text{m}$ , with ranges of  $10\text{--}50 \mu\text{m}$  and  $20\text{--}250 \mu\text{m}$ , respectively.

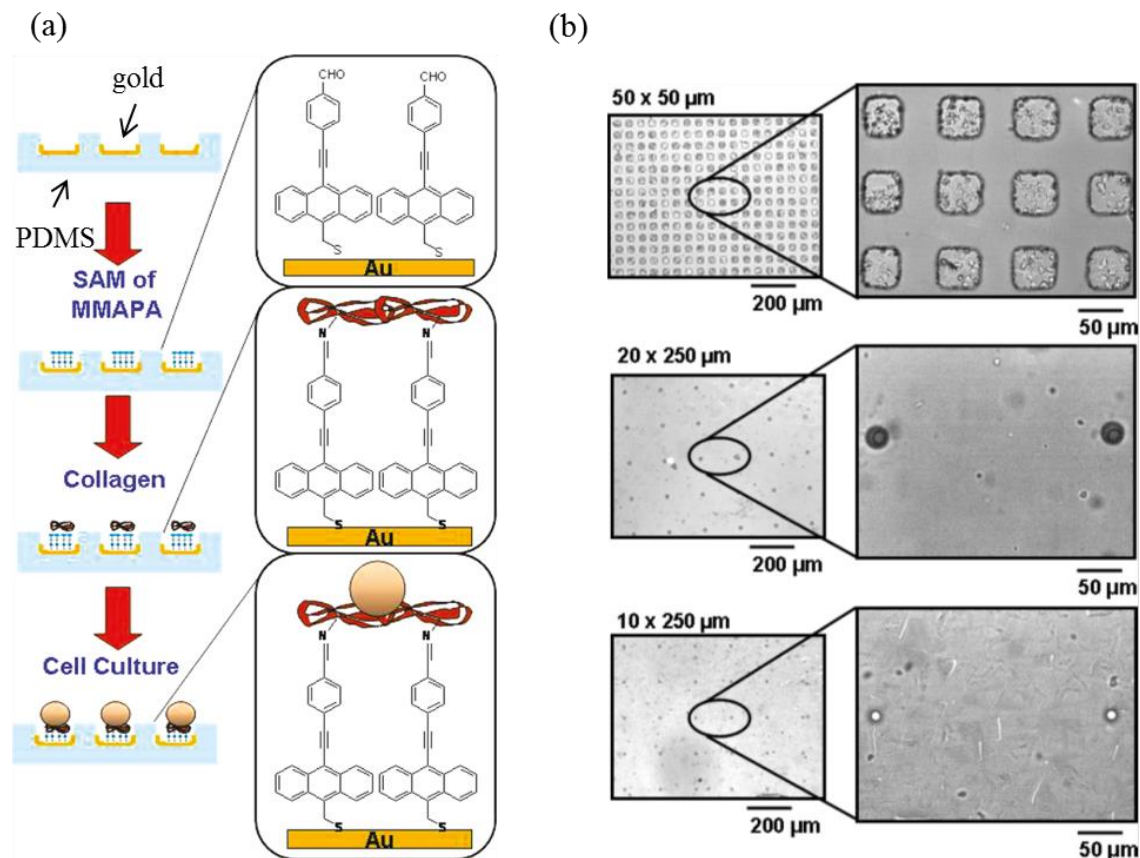


**Figure 2.16:** A single cell array of PDMS microwells chemically modified by a self-assembled monolayer (SAM) [70].

Liu and co-workers at Tsinghua University, China [114], reported a fabrication method for rounded-bottom MAs (**Figure 2.17**), shaped like those of Deutsch *et al.* [110] (see **Figure 2.12**). PS microspheres were self-assembled on a glass slide and were partially melted at  $240^\circ\text{C}$  for 3 min on a hot plate to increase the adhesive force with the substrate. The array of PDMS microwells was fabricated by soft lithography, and the microwell depth was  $8.1 \mu\text{m}$  for highly ordered microspheres with a diameter of  $20 \mu\text{m}$ . The rate of cellular occupancy in each well for Ramos cells (Burkitt's lymphoma; human B-lymphoblast) was  $90\% \pm 1\%$  and  $84\% \pm 3\%$  for single cells seeded at cell densities of  $1 \times 10^6 \text{ cells/ml}$  and  $1 \times 10^5 \text{ cells/ml}$ , respectively.

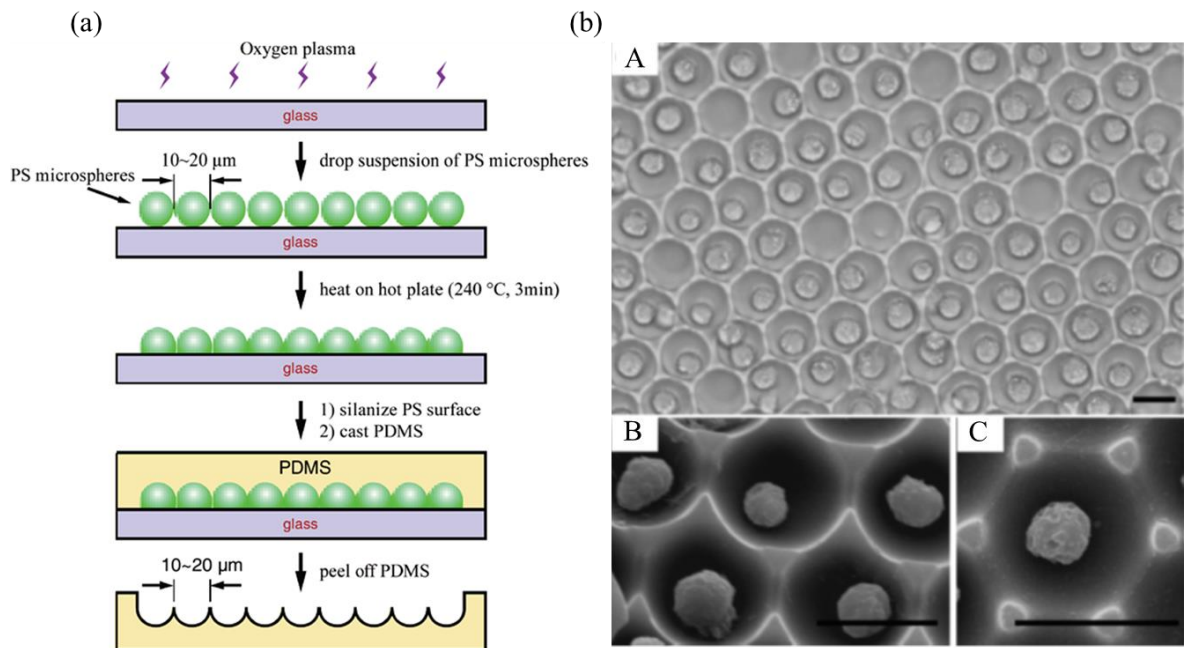


**Figure 2.17:** A rounded bottom microwell array (MA) of PDMS by molding a monolayer of highly ordered polystyrene (PS) microspheres [114].

(a) Schematic fabrication of PDMS microwell arrays.

(b) Cell arrays on the microwells. [A] Micrograph of dense trapping of Ramos cells. [B, C] The SEM images of Ramos cells located in microwells. Scale bars are 20  $\mu\text{m}$ .

Ferrell and co-workers at Ohio State University, USA [115], fabricated an array of microwells composed of a polymer (PMMA or PS) wall and a bottom made of commercially-available porous membranes, allowing the use of vacuum-assisted cell seeding (similar to the pipette-like microfluidic technique) (**Figure 2.18**). Three different porous membranes were used: track-etched polycarbonate membranes, anodized alumina membranes, and polyester membranes. Cell suspensions of fibroblasts (NIH3T3), pancreatic ductal epithelial-like cells (PANC-1), and monocytic leukemia cells (THP-1) were placed in a vacuum filtration apparatus to suck culture medium through the microdevice. The cells were trapped in the microwells by applying vacuum for 0.5–5 min and sucking the cell culture medium through the membrane. The cellular occupancy of each cell line was determined for different geometries of cylindrical microwells (diameter of 15, 20, or 50  $\mu\text{m}$ ) at various cell densities (300, 400, or 600 cells/ $\text{mm}^2$ ). Single cells of NIH3T3 and THP-1 were isolated in microwells

with a diameter of 20  $\mu\text{m}$  and 15  $\mu\text{m}$ , respectively. The cellular occupancy of NIH3T3 in 20- $\mu\text{m}$  microwells was  $\sim 45\%$  that of single cells, but the microwells were  $\sim 41\%$  empty at the cell density of 300 cells/ $\text{mm}^2$ . The occupancy for THP-1 cells was  $\sim 50\%$  that of single cells, but was  $\sim 35\%$  that of 2 cells at the cell density of 300 cells/ $\text{mm}^2$ .

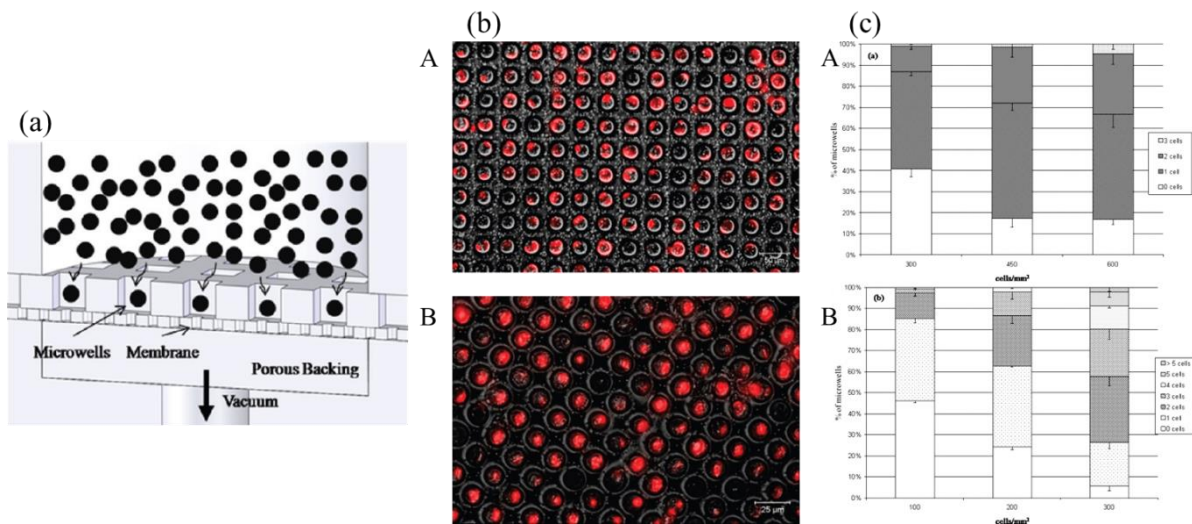


**Figure 2.18:** An array of microwells composed of wall of polymer and bottom of commercially available porous membranes to use vacuum-assisted cell seeding [115].

- (a) Schematic illustration of experimental setup for cell isolation.
- (b) Fluorescence/phase contrast merged images. [A] NIH 3T3 cells were in 20- $\mu\text{m}$ -diameter wells. [B] THP-1 cells were in 15  $\mu\text{m}$  diameter wells.
- (c) Number of NIH 3T3 cells per microwell as a percentage of the total number of microwells: [A] Cells seeded at 300, 450, and 600 cells/ $\text{mm}^2$  in the circular microwells (diameter, 20  $\mu\text{m}$ ); [B] Cells seeded at 100, 200, and 300 cells/ $\text{mm}^2$  in the circular microwells (diameter, 50  $\mu\text{m}$ ).

Park and co-workers at the University of Michigan, USA [116], investigated the optimal geometry of microwells in a microfluidic channel by a flow method designed to trap single cells (**Figure 2.19**). All the microwells were constrained to a side length of 50  $\mu\text{m}$  and depth of 20  $\mu\text{m}$  to allow sufficient attachment and differentiation of captured cells. The microwells were arrayed with a spacing of 50  $\mu\text{m}$  to provide a total of  $\sim 10,000$  microwells in a microchannel with a height of 200  $\mu\text{m}$ , width of 5 mm, and length of 15 mm. Among various shapes (triangle, square, circle, diamond, and cone), triangular microwells were the most efficient for single-cell trapping because of a strong flow recirculation, efficiently trapping

cells inside the microwell. The presence of a single cell in the microwell changed the flow pattern, thereby preventing the trapping of subsequent cells. In this device, cellular occupancy of single human prostate cancer cells (PC3) in triangular microwells was ~62% after a 20-min loading procedure.

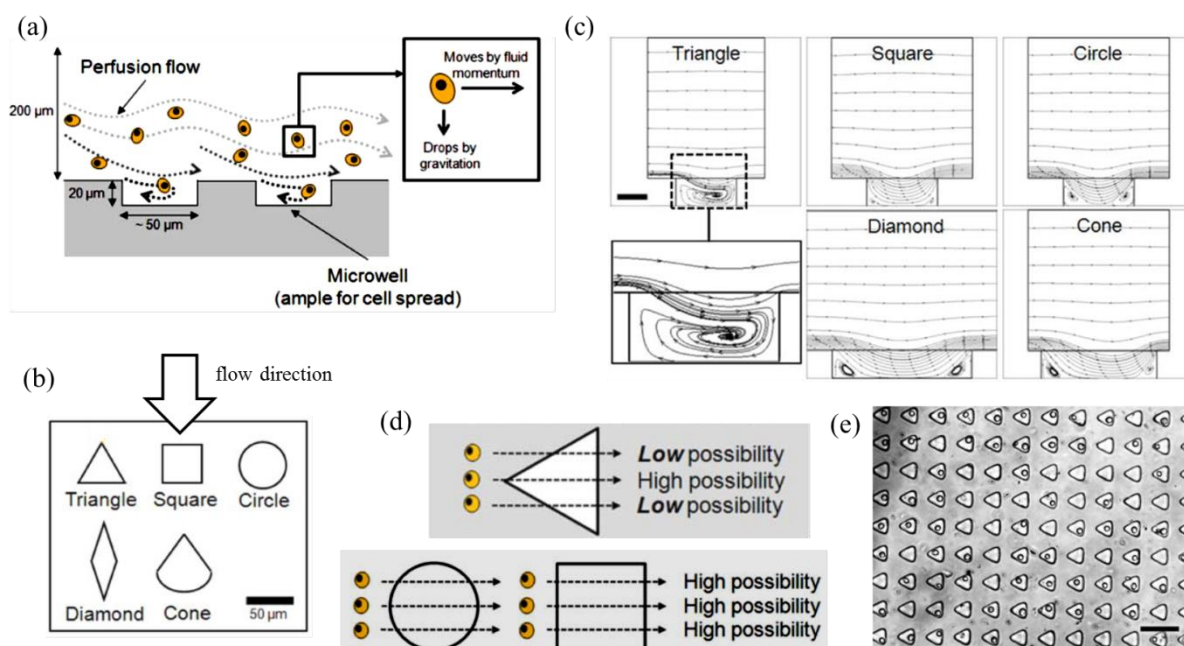


**Figure 2.19:** Flow method to find the effective shape of microwells for single cell trapping in a microfluidic channel [116].

The geometry of microwells affects the trapping rate; The triangular well provides different trapping possibilities when the cell travels through the middle path and side paths. A capture rate of 62% was observed for PC3 cells with less than 6% of multiple cells trapping. Scale bar is 100  $\mu\text{m}$ .

Broderick and co-workers at the University of Wisconsin in Madison, USA [71], fabricated 3D polyurethane-based microwell cell culture arrays selectively functionalized inside the wells to promote cell adhesion and on the plateau of wells to resist cell adhesion (**Figure 2.20**). The interior of the cuboidal microwells (size,  $300 \times 300 \mu\text{m}^2$ ; depth,  $120 \mu\text{m}$ ) was coated with a layer-by-layer assembly of multilayers by using branched polyethyleneimine (BPEI) and the azlactone-functionalized polymer poly(2-vinyl-4,40-dimethylazlactone) (PVDMA), while the exterior of microwells was coated by amine-functionalized

molecules by using the micro-contact printing method. Cellular patterns of African green monkey kidney fibroblasts (COS-7 cells) were determined for up to 28 d.

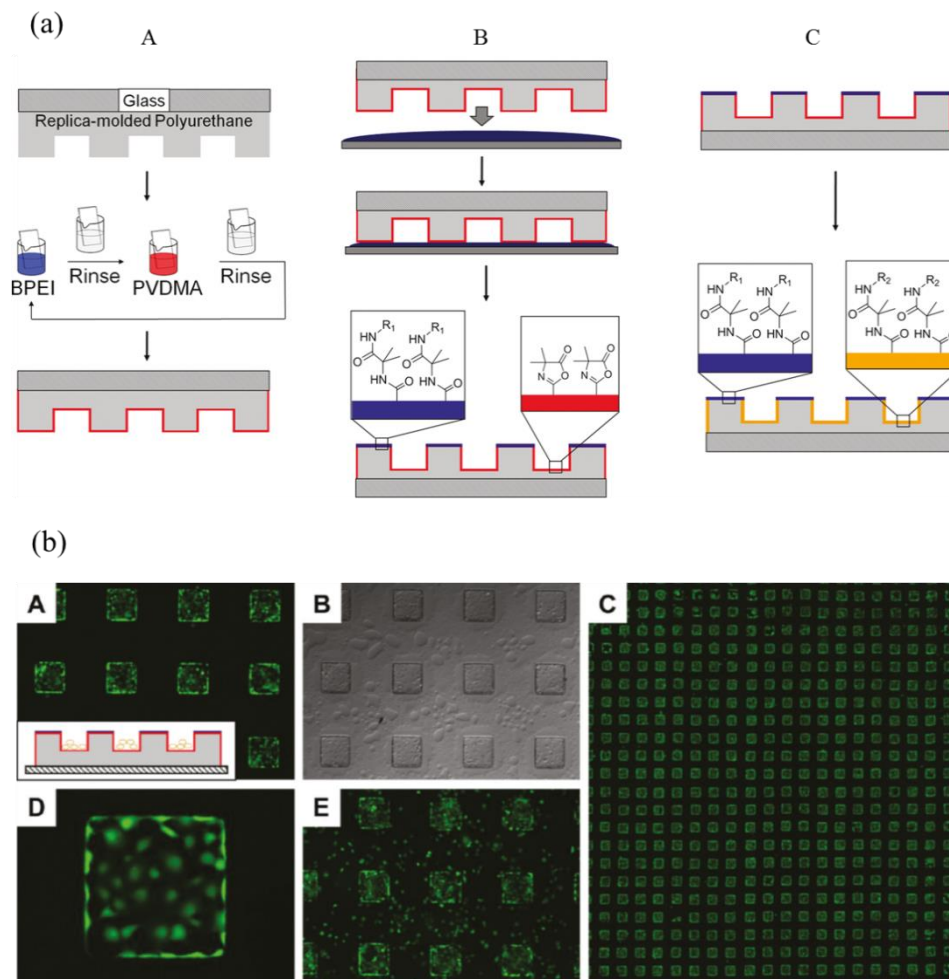


**Figure 2.20:** 3D polyurethane-based microwell cell culture arrays selectively functionalized inside the wells to promote cell adhesion and on the plateau of wells to resist cell adhesion [71].

(a) Schematic fabrication of PDMS microwell arrays.

(b) Representative phase contrast and fluorescence micrographs of COS-7 cells on film-coated microwell arrays. [A–D] Arrays functionalized selectively to introduce glucamine in areas between the microwells prior to cell seeding result in preferential attachment and growth of cells inside the microwells. Microwell dimensions are 300  $\mu\text{m}$  on each side.

Wang and co-workers at the University of North Carolina, USA [117], presented a simple low-cost microarray PDMS platform that can trap tens of thousands of mammalian cells for dynamic single-cell analysis by using the elasticity of PDMS (**Figure 2.21**). After seeding and then allowing murine hematopoietic (Ba/F3) cells to settle for 5 min, the

diameters of individual microwells (depth, 15  $\mu\text{m}$ ) were expanded from 12 to 20  $\mu\text{m}$  at  $\sim 1$  Hz to assist settling into the microwells; then, the tension was slowly released. For Ba/F3 cells with an average diameter of 14.1  $\mu\text{m}$ , the cell trapping efficiency was  $65.3\% \pm 7.6\%$  ( $n = 3$ ) at a cell density of  $1.25 \times 10^6$  cells/ $\text{cm}^2$ . Using this device, trapped cells were subjected to multicolor analysis and individual cells were analyzed by measuring real-time calcium flux after exposure to the calcium ionophore ionomycin.

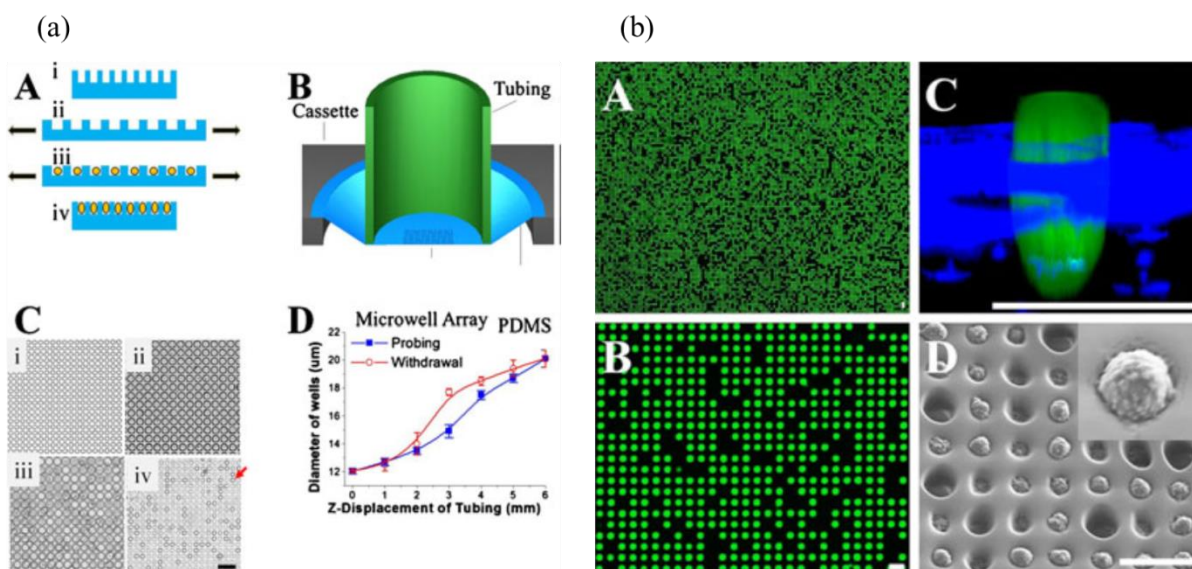


**Figure 2.21:** A simple, low-cost microarray platform of PDMS that can trap tens of thousands of mammalian cells for dynamic single-cell analysis using the elasticity of PDMS [117].  
 (a) Reversible stretching of PDMS microwells and loading of cells on the array.  
 (b) High-density, single-cell array on the stretchable traps. Scale bar is 20  $\mu\text{m}$ .

Jen and co-workers at National Chung Cheng University, Taiwan [118], fabricated microfluidic chips with arrays of microwells that were developed for single-cell chemical lysis (**Figure 2.22**). The main fluidic channel was 15 mm wide, 160  $\mu\text{m}$  high, and 65 mm long, and microwells with a diameter of 20  $\mu\text{m}$  or 30  $\mu\text{m}$  and a depth of 20  $\mu\text{m}$  were arrayed ( $10 \times 10$ ) at 15 sites on the bottom layer. Human cancerous cervix epithelial cells (HeLa) at a cell density of  $1 \times 10^7$  cells/ml were loaded into the microfluidic channel at injection flow rates varying from 2.8 to 4.0  $\mu\text{l}/\text{min}$ . At an injection flow rate of 2.8  $\mu\text{l}/\text{min}$ , the HeLa cellular occupancy rate was maximized. The cellular occupancy was 91.45% and 83.19% in

microwells with a diameter of 30 and 20  $\mu\text{m}$ , respectively. Most 20- $\mu\text{m}$  microwells and 85% of the 30- $\mu\text{m}$  microwells were occupied by single cells.

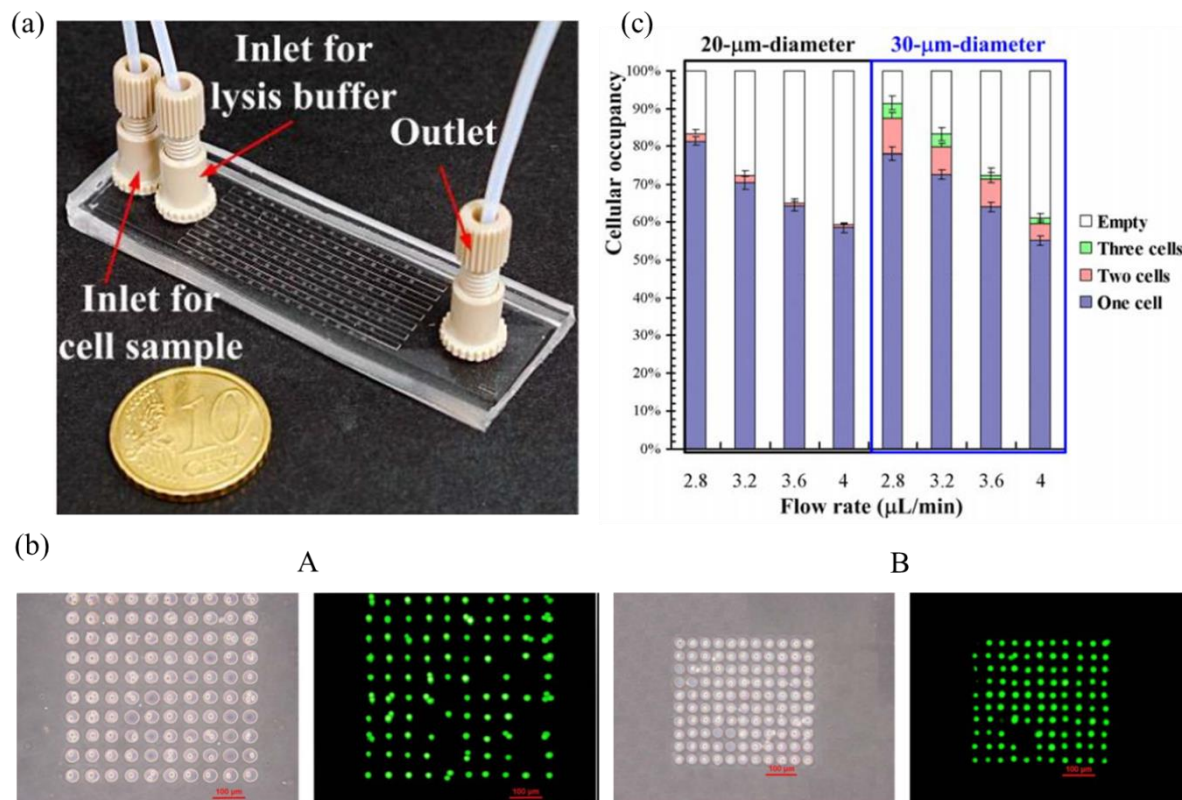


**Figure 2.22:** Microfluidic chips with arrays of microwells were developed for single-cell chemical lysis [118].

- (a) Photograph of the completed microfluidic chip with tubing.
- (b) Bright and fluorescence images of micropatterned HeLa cells in microwells with diameters of [A] 30  $\mu\text{m}$  and [B] 20  $\mu\text{m}$ . The injection flow rate of the cell sample is 2.8  $\mu\text{L}/\text{min}$ .
- (c) Distributions of cellular occupancy of HeLa cells in the microwells with diameter of 20  $\mu\text{m}$  and 30  $\mu\text{m}$  at various injection flow rates. The experimental data are based on manual counts of cells in three arrays of 10  $\times$  10 microwells. Error bar is standard error of the mean (SEM).

### 2.5.1 Geometry and substrates of microwells

Both geometry and substrate of microwells play a crucial role in retaining a single target cell per microwell and maintaining cells with native 3D cellular morphology by supporting cells, by an extracellular matrix, or by growth factors and thereby *in vivo* cellular metabolism and function, including morphogenesis, gene expression, and differentiation [36-38].

Single-cell occupancy depends strongly on the geometry of microwells, such as size,

depth, and shape, according to the target cell and whether the cells were seeded by gravity or flow. The optimal size of microwells is slightly bigger than the diameter of the target cell, that is, by  $\sim 5\text{--}15\ \mu\text{m}$ . For example, the highest single-cell occupancy of RBL-1 ( $7.74\ \mu\text{m}$ ) and AtT-20 ( $\sim 15\ \mu\text{m}$ ) is in  $20\text{-}\mu\text{m}$  microwells, NIH3T3 ( $16\text{--}20\ \mu\text{m}$ ) in  $25\text{-}\mu\text{m}$  microwells, and HeLa ( $21 \pm 4.4\ \mu\text{m}$ ) in  $30\text{-}\mu\text{m}$  microwells [38, 70, 80, 118-120].

Rettig and Folch [38] showed that the optimal ratio of size and depth was  $\sim 1$ , from analysis of single-cell occupancy among various sizes and depths of cylindrical microwells. Single-cell occupancy dramatically increased as the ratio of size and depth increased up to  $\sim 1$ , and then slightly decreased. Considering that the optimal size of the microwell was similar to that of the cell, microwell depth was also similar to the target cell. Wang *et al.* [117] also used  $15\text{-}\mu\text{m}$ -deep microwells to match the size of Ba/F3 cells (diameter,  $14.1 \pm 1.4\ \mu\text{m}$ ) and achieve high single-cell occupancy.

Microwell shape is not a consideration when seeding target cells with uniform shape (i.e., cylindrical [38, 113, 115, 117], cuboidal [112], or hemispherical [110, 114]) in the microwells by gravity. Park *et al.* [116] described the effect of microwell shape (constant size) by flow simulation when the cells were seeded by flow in a microchannel. The triangular shape was found to be most efficient for single-cell trapping because of strong flow recirculation, which efficiently trapped cells inside the microwell.

Polydimethylsiloxane (PDMS) is commonly used in the fabrication of microwells to trap single cells [38, 112, 114, 117, 118]. PDMS enables numerous replications at both micro- or nanometer scale from a micro- or nanofabricated mold with high precision. However, the inherent properties of PDMS do not allow for cellular adhesion, which, due to the absence of supporting cells, extracellular matrix, and growth factors, could affect the natural behavior of anchorage-dependent cells that can survive only when they adhere to substrates. Therefore, the significant function of microwells with respect to maintaining the native 3D morphology

of anchorage-dependent cells is feasible only when the inner surface of the microwell is conducive for cell adhesion. Ochsner *et al.* [111] fabricated a cell-adhesive surface inside microwells in order to control 3D cellular shape by using various shapes of microwells, including squares and spindles. The surface was plasma-treated PDMS adsorbed with cell-adhesive fibronectin. Leong *et al.* [70] fabricated microwells containing a cell-adhesive SAM. However, SAM was located on the bottom, not including the wall, and was not predicted to provide native 3D cellular morphology.

### 2.5.2 Cell types and seeding conditions

Interactions between cells placed in a microwell and the surface of the microwell are strongly dependent on the characteristics of cells, whether adherent or non-adherent. Given a cell-adhesive microwell surface, adherent cells firmly adhere to the microwell while non-adherent cells are just mechanically trapped inside the microwell. Higher single-cell occupancy is expected for adherent cells rather than nonadherent cells.

However, single-cell occupancy of non-adherent cells is often higher than that of adherent cells [38, 114, 118]. The single-cell occupancy of non-adherent RBL-1 and Ramos cells reached 92.2% and 90% [114], respectively. In the case of adherent cells, NIH3T3 and HeLa cells showed single-cell occupancy of 84.5% [38] and 83.19% [118], respectively. The disparate single-cell occupancy between adherent and non-adherent cells might be due to the different shapes of both cell types.

A seeding cell concentration of  $\sim 1.0 \times 10^6$  cells/ml is commonly used for static culture [70, 110, 114, 116, 117]. Liu *et al.* [114] showed the effect of cell concentration on single-cell occupancy by varying cell concentrations from  $1 \times 10^5$  to  $1 \times 10^7$  cells/ml. The single-cell occupancy of Ramos cells was found to be  $90\% \pm 1\%$  and  $84\% \pm 3\%$  at cell densities of  $1 \times 10^6$  and  $1 \times 10^5$  cells/ml, respectively. Higher cell seeding densities (exceeding  $1 \times 10^6$  cells/ml) do not have an obvious effect on cell occupancy. The results indicate that

$1.0 \times 10^6$  cells/ml of cell density is an optimal concentration for an isolated single cell array.

When seeding cells by flow in a microchannel, the flow rate is a dominant parameter for single cell loading in the microwells. Park *et al.* [116] determined that the optimal flow rate for cell trapping in triangular microwells located in a microchannel was 0.05–0.15 ml/h (14–42  $\mu\text{m/s}$ ) among various flow rates. Jen *et al.* [118] showed that the highest single-cell occupancy in a 15-mm-high and 160- $\mu\text{m}$ -wide microchannel was achieved at a flow rate of 2.8  $\mu\text{l/min}$ , which had been calculated on the basis of flow velocity in the microchannel, that is, 19.4  $\mu\text{m/s}$  (calculated on the basis of the dimensions of the microchannel).

### **2.5.3 System integration**

Arrays of microwells for single-cell isolation were integrated by material properties [117], microfluidics [115, 116, 118], or biosensors [113]. Wang *et al.* [117] used the elasticity of soft PDMS to mechanically grasp the cells by changing the size of microwells from 20  $\mu\text{m}$  to 12  $\mu\text{m}$  after seeding cells. Loading cells into microwells by using the flow in microchannels is more effective than the conventional method, which involves the use of gravity for this purpose, with respect to loading time and cellular occupancy. The flow necessary to carry target cells is controlled by microwell geometry [116, 118] or vacuum pump [115]. The microwell shape and flow rate are dominant factors for increasing single-cell occupancy when an array of microwells is integrated by a microfluidic system [116, 118]. Molter *et al.* [113] fabricated an oxygen sensor integrated in microwells for measuring and analyzing oxygen consumption rate according to cell type and the number of cells per well. Although the microwells were bigger than the ideal size for a single cell per well, the capability of individual single-cell analysis was shown by integration of the oxygen sensor.

Microfluidic applications must account for the fundamental elements of the cellular environment at the microscale level for cell culture in an array. In a microchannel, replenishment of nutrient media components to arrayed single cells is necessary whether

static or perfusion culture techniques are being used. An effective culture time (ECT) is a proper feeding interval for static cell culture and is mathematically calculated by the ratio of the height of medium in a microchannel and in a conventional petri dish. For example, the medium (height, 1.2 mm) in a petri dish is generally replaced every 48 h, and thus, medium in a 200- $\mu\text{m}$ -high microchannel should be replenished every 8 h, since the expected ECT is reduced by a factor of  $\sim 6$ . In the case of perfusion culture, an appropriate perfusion rate (critical perfusion rate [CPR]) is determined by calculating the time required for chemical molecules to completely diffuse from the top to bottom of a microchannel during transit from the inlet to the site of the arrayed cells.

#### **2.5.4 Differences and significance of the previously presented microwells**

Depending on the intended application and system integration, a microwell device can be designed in numerous different ways by selecting different parameters, such as geometry, surface materials, the number of wells, cell density, and flow rate. In **Table 2.4**, the optimal parameters and unique features of the summarized papers are described in detail.

**Table 2.4:** Comparison and significance of the previous single cell arrays of microwells.

Author & Features	Geometry and material of microwell				Cells		Single-cellular occupancy of optimal conditions	
	Shape	Size (μm)	Depth (μm)	Material	Type	Diameter (μm)	Incubation time @ Initial seeding concentration	Occupancy (%) @ optimal size × depth (μm) of microwell
Rettig <i>et al.</i> [38] Seeding by gravity	Circle	15, 20, 25,30, 35, 40	16, 21, 27	PDMS	NIH3T3* RBL-1§	16–20 [80] 7.74 [120]	40 min @ 2500–6200 cells/mm <sup>2</sup>	84.5 ± 0.2 @ 25 × 27 92.2 ± 2.2 @ 20 × 21
Deutsch <i>et al.</i> [110] Seeding by gravity	Hemisphere	20	~ 8	Glass	MOLT-4§ U937§ Jurkat§ K-562§	11.4 ± 1.3 [121] 13.0 ± 1.8 [121] 10–15 [122] 14.3 ± 1.6 [121]	4 h @ 3.5 × 10 <sup>6</sup> cells/ml	~75.3
Ochsner <i>et al.</i> [111] 3D cell adhesion	Square Spindle	100, 14, 10 50 × 20	10	Plasma treated PDMS	HUVEC*	33.28 ± 0.85 [123]	—	—
Sasuga <i>et al.</i> [112]	Square	20, 30, 40	20	PDMS	PC12§	~14 [124]	12 h @ 2 × 10 <sup>7</sup> cells/ml	~40 (1–3 cells) @ 40 × 20
Molter <i>et al.</i> [113] Sensor integrated	Circle	65	25	glass	RAW264.7‡ A549* CP-D*	10–15 [125] ~40 [126] —	1 h @ 10,000 cells	~ 85 ± 25(SD) (n = 3)
Leong <i>et al.</i> [70] Cell adhesive bottom	Square Circle	50 20, 10	25	B : SAM W : PDMS	AtT-20*	~ 15	24 h @ 1.0 × 10 <sup>6</sup> cells/ml	~ 83
Liu <i>et al.</i> [114] Seeding by gravity	Hemisphere	20	8.1	PDMS	Ramos§ HeLa*	— 21±4.4 [119]	5-10 min @ 1 × 10 <sup>6</sup> cells/ml —	90 ± 1 —
Ferrell <i>et al.</i> [115] Vacuum assisting	Circle	15, 20, 50	—	B : porous PC, Alumina, PET W : PMMA, PS	NIH3T3* PANC-1* THP-1*	16–20 [80] 22.3 [127] 15 / 13.0 ± 1.8 [121]	1–2 h @ 600 cells/mm <sup>2</sup>	~50 @ 20 × —
Park <i>et al.</i> [116] Seeding by flow	Triangle, Square, Circle, Diamond, Cone	50	20	—	PC-3*	18 [128]	10 min @ 1.5 × 10 <sup>6</sup> cells/ml Flow rate: ~28 μm/s	62 ± 10 @ triangle 50 × 20
Broderick <i>et al.</i> [71] 3D cell adhesion	Square	300	120	BPEI/PVDMA	COS-7*	30–50 [129]	20 min @ 600 cells	—
Wang <i>et al.</i> [117] PDMS elasticity	Circle	20 → 12	15	PDMS	Ba/F3*	14.1 ± 1.4	— @ 1.25 × 10 <sup>6</sup> cells/cm <sup>2</sup>	65.3 ± 7.6
Jen <i>et al.</i> [118] Seeding by flow	Circle	20, 30	20	PDMS	HeLa*	21 ± 4.4 [119]	— @ 10 <sup>7</sup> cells/ml Flow rate: 2.8 μl/min	83.19 @ 20 × 20

Notes: (B) is surface of bottom. (W) is surface of wall. (\*) is an adherent (anchorage-dependent) cell. (§) is non-adherent (anchorage-independent) cell. (‡) is a semi-adherent cell. (—) is non-available.



## Chapter 3. HeLa Cells for Microengineering

### 3.1. Introduction

Cellular behaviors and phenotypes differ widely depending on cell type. In this study, surface treatment techniques for optimizing cellular immobilization were determined according to the target cell type using chemical and/or physical methods. Cell lines should be carefully chosen with respect to their potential biological significance for clinical diagnosis and applicability to microplatforms for single cell analysis.

#### 3.1.1 Human cancer cell lines

Although clinical trials in humans are essential for determining the efficacy of anticancer therapies, they are enormously expensive and difficult to perform for logistical, regulatory, legal, and ethical reasons. Therefore, *in vitro* cellular model systems are required to adequately explore the molecular basis of drug activities, despite the inability of this model system to accurately reflect many aspects of a drug's behavior in the human body [130]. Recently, large-scale resources for human cancerous cell lines (~1,000 unique cell lines) have become publicly available for use in *in vitro* assays; these cell line resources are described in the Cancer Cell Line Encyclopedia [131]. This type of public resource for all cancerous cell lines allows us to predict intrinsic cell sensitivity and resistance to various existing drugs or potential future drugs [130]. Panels of human cancer cell lines and xenografts were established in Europe in 1988 (40 cell lines) [132], in the USA in 1990 (60 cell lines) [133], and in Japan in 2003 (39 cell lines) [134], supporting the conduct of *in vitro* assays to efficiently evaluate test compounds for potential anticancer activity. Although these panels are limited in the number of available cell types, they have been used to test more than 100,000 chemically defined potential drugs and a larger number of natural-product extracts [130].

**Table 3.1:** Panels of human cancer cell lines and xenografts for *in vitro* assays in Europe [132], the USA [133], and Japan [134]. Numbers in parenthesis are the total number of cell lines available.

Organs	Europe (40)	USA (60)	Japan (39)
Brain			U251, SF-268, SF-295, SF-539, SNB-75, SNB-78
Breast	MAXF 401, MAXF 449, MAXF 583, MAXF 857	BT-549, MCF7, MDA-MB-231/ATCC, HS-578T, T-47D	HBC-4, BSY-1, HBC-5, MCF-7, MDA-MB-231
CNS		SF-268, SF-295, SF-539, SNB-19, SNB-75, U251	
Colon	CXF 158, CXF 233, CXF 243, CXF 280	COLO-205, HCC-2998, HCT-116, HCT-15, HT29, KM12, SW-620	HCC-2998, KM-12, HCT-116, HCT-15, HT-29
Head and Neck	HNX-Hep-2, HNX-LP, HNX-14A, HNX-14C, HNX-PI		
Kidney		786-0, A498, ACHN, CAKI-1, RXF-393, SN12C, TK-10, UO-31	
Leukemia		CCRF-CEM, HL-60(TB), K-562, MOLT-4, RPMI-8226, SR	
Lung	EVXOA, AHXOL, LXFE 397, LXFE 409, LXFL 529, LXFA 629, NXEE 002, CXEA 117 LBXOS, LSFS 538, LXFS 605, LSFS 638, LXFS 638, LXFS 650, NXES 004, WXES 322	A549/ATCC, EK VX, HOP-62, HOP-92, NCI-H226, NCI-H23, NCI-H322M, NCI-H460, NCI-H522	A549, DMS273, DMS114, NCI-H226, NCI-H23, NCI-H460, NCI-H522
Melanoma	THXO, FEMXO, MEXF 274, MEXF 394, MEXF 514	LOX-IMVI, MALME-3M, M14, SK-MEL-2, SK-MEL-28, SK-MEL-5, UACC-257, UACC-62	RXF-631L
Ovarian	Ov.Pe, Ov.He, FMa, Ov.G1, Ov.Ri, FKo	IGROV1, OVCAR-3, OVCAR-4, OVCAR-5, OVCAR-8, SK-OV-3	OVCAR-3, OVCAR-4, OVCAR-5, OVCAR-8, SK-OV-3
Prostate		DU-145, PC-3	DU-145, PC-3
Renal			LOX-IMVI, ACHN
Stomach			MKN-1, MKN-7, MKN-28, MKN-45, MKN-74, St-4
Uncertain		NCUIADR-RES * MDA-MB-435** MDA-N**	

Notes: \*, Formerly designated as breast, but its origin is now considered uncertain. \*\*, Formerly designated as breast, but our analysis shows that they are more like melanomas or at least have the activity and protein expression signatures of melanoma. CNS: central nervous system.

### **3.1.2 Human cancerous cervical epithelial HeLa cells**

#### **3.1.2.1 Significance of the HeLa cell line in biology**

Modern biomedical research relies heavily on experiments conducted using HeLa cells, derived from human cancerous cervical epithelium, despite of the absence of HeLa cells in representative panels of human cancer cell lines for *in vitro* assays [132-134]. HeLa cells are adherent and immortal, allowing them to divide continuously assuming the culture conditions permit cell survival.

The HeLa cell line has a complex and relevant history. Originally described in 1952, HeLa cells were established as the first immortal human cancer line [135]; they have been widely used to investigate almost every cellular pathway and process because, although they are cancer cells, HeLa cells share many characteristics with noncancerous cells. Therefore, HeLa cells are used as a universal human cell to study active biochemical pathways in both normal and diseased tissues [40]. Generally, aggressive cancers (e.g., that from which HeLa cells were derived) have unique phenotypes and genotypes [136], and some genetic drift and phenotypic changes may occur during cell growth and passaging within a laboratory [137, 138]. However, HeLa cells have been shown to remain relatively stable under standard laboratory culturing conditions. This stability, coupled with the similarities between HeLa cells and normal cells, make HeLa cells highly relevant in biomedical and basic research. Consequently, HeLa cells are also used to produce standardized nutrient media that can be employed during studies of the growth of other cell lines [139].

The first remarkable achievement involving the use of HeLa cells was the development of a vaccine against polio in 1953 [39]. A large number of HeLa cells were needed to begin large-scale production of the polio vaccine. Production facilities for HeLa cells were set up, and HeLa cells became the first cell line to be produced industrially. After this milestone, HeLa cells were distributed worldwide and became a general go-to laboratory model for

cancer cells [40]. HeLa cells were also used to create the first hybrid cell, heterokaryon cells [140]. Moreover, using HeLa cells, researchers developed viable cells from a fusion of human and animal cells [141], enabling the regulation of DNA synthesis to be more thoroughly investigated. HIV-infected HeLa cells have been used to support the development of new drugs and therapies against AIDS [142] and cancer [41].

### **3.1.2.2 Application of the HeLa cells in microengineering**

The development of microbiochips has enabled us to control the complete cellular microenvironment and to analyze single cells, leading to new questions and discoveries. Among the potential mammalian cell models for microengineering, HeLa cells were widely used because of their biological relevance to cancer treatment and their ability to adhere to hydrophilic surfaces controlled by microtechniques [39-42, 143]. The biological characteristics of HeLa cells have been well described in a range of studies [39-41, 135, 137-142]; however, few reports have adequately described the physical properties of HeLa cells as they related to the construction of a customized microplatform for single HeLa cell analysis [119, 144-147]. In the design and fabrication of microwells for single cell arrays, the physical properties of the cell may strictly limit the size of microwells. The optimal size for microwells is just slightly larger than the diameter of the target cell, i.e., by approximately 10  $\mu\text{m}$  [38, 70, 80, 118-120]. Moreover, in addition to cell diameter, successful integration of versatile microplatforms also requires more information on other cellular characteristics, such as shape, mass, volume, and settling velocity.

### **3.1.3 Physical properties of HeLa cells for microengineering**

In this study, we sought to define the relevant physical properties of HeLa cells for use in microengineering applications. We collected information describing the physical characteristics of HeLa cells from previously published papers and the technical

specifications provided by the cell vendor. Next, the diameter and volume of HeLa cells were measured using a CASY cell counter. The significance of the gathered information was analyzed to determine the correlation between the collected and measured values. Settling velocity of HeLa cells at room temperature (RT, 23°C) was theoretically analyzed and measured at the cell population level in time-lapse format for application to cell adhesion assays. Additionally, in this analysis, the density and viscosity of various liquids used in biological experiments, including phosphate buffered saline (PBS), RPMI 1640 supplemented with fetal calf serum (FCS), and Opti-MEM, were determined, based on the properties of pure water. Settling velocity was analyzed by curve fitting of the line plot profile. Using these analyzed data and estimations, the settling velocity of HeLa cells at 37°C and the settling time of HeLa cells in 6-, 12-, or 24-well plates were also determined for applicability to cell adhesion assays.

## **3.2. Materials and methods**

### **3.2.1 Culture of HeLa cells**

HeLa cells (Deutsche Sammlung für Mikroorganismen und Zellkulturen GmbH [DSMZ], Germany) were cultivated in an incubator at 37°C and 5% CO<sub>2</sub>. In all experiments, we used RPMI 1640 medium (PAN Biotech GmbH, Germany) supplemented with 10% fetal bovine serum (FBS, Sigma-Aldrich) and 2% penicillin/streptomycin (Sigma-Aldrich) without phenol red. Confluent cultures of HeLa cells were passaged by 1:3 (v/v) every 3 days using a trypsin/EDTA solution (Sigma-Aldrich) for 5 min in an incubator at 37°C and 5% CO<sub>2</sub>. Cells were washed 3 times with 400 µl PBS to remove trypsin after centrifugation for 3 min at 200 × g. HeLa cells were subsequently resuspended in growth medium to achieve a seeding concentration of 1 × 10<sup>6</sup> cells/80 cm<sup>2</sup>.

### 3.2.2 Measurement of cell diameter and volume

To measure the diameter and volume of HeLa cells, adhered HeLa cells were first detached using trypsin/EDTA. The HeLa cell suspension was then washed 3 times with 400  $\mu\text{l}$  PBS and diluted in PBS to achieve a concentration of  $5 \times 10^5$  cells/ml. The diameter and volume of HeLa cells were measured 3 times for each trial using a CASY cell counter (CASYton, Schärfe System GmbH, Germany).

The CASY cell counter utilizes electric current exclusion and pulse area analysis to count dead and viable cells in the cell suspension. Cell viability is determined by measuring the integrity of the plasma membrane for dead and viable cells (see **Figure 3.1**).

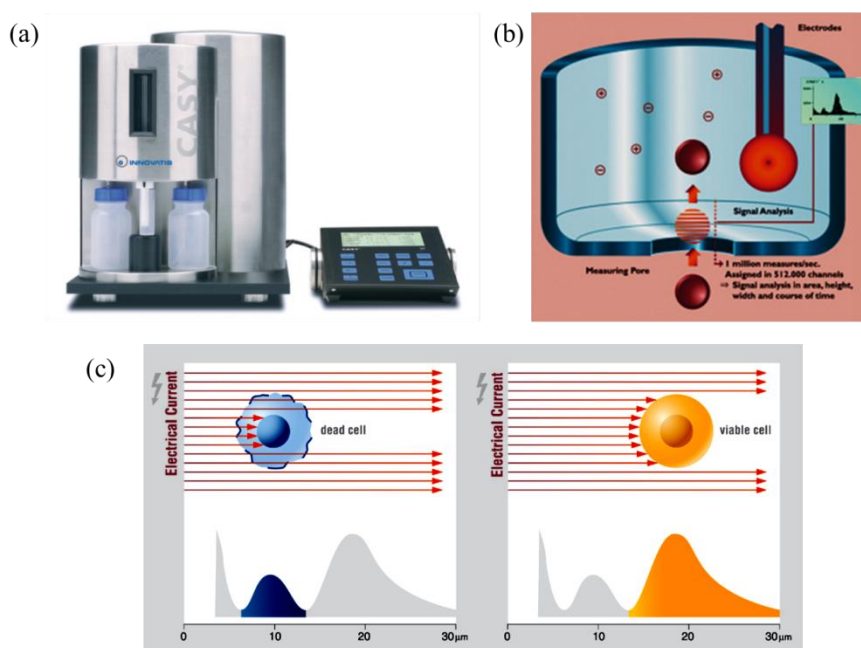


**Figure 3.1:** CASY cell counter and the principles used to measure cell size.

(a) CASY cell counter (DT model, Schärfe System GmbH, Germany).

(b) Principle of counting cells. The number and size of cells were measured when the cells passed through a measuring pore in a low-voltage field.

(c) Cell viability was measured by determining the difference in electrical current exclusion of the cell membrane between viable and dead cells.

When a low-voltage field is applied to viable cells, the electrical current cannot penetrate the intact membrane, which acts as an electric insulator. In contrast, the membrane of injured cells is often broken and contains pores, allowing the electrical field to penetrate

the membrane. In both viable and dead cells, the measured cell size cannot be smaller than the nucleus. Therefore, the criterion for determining whether cells are viable or dead was based on the size of the nucleus in the target cells.

### 3.2.3 Measurement of cell Stokes velocity

PS cuvettes (Plastibrand, Garlroth GmbH, Germany) with inner dimensions of  $10 \times 10 \times 42 \text{ mm}^3$  were sterilized by 95% ethanol for 5 min and dried at RT. On the backside of a cuvette, a black ruler with white grids was printed for determining the appearance of high-density HeLa cells, which are white and opaque enough to cover the white grids in the suspension. For measuring the settling velocity, HeLa cells were resuspended to a concentration of  $2.2 \times 10^6$  cells/ml in PBS. The HeLa cell suspension (2 ml) was then added to the marked cuvette at RT. Changes in the height of the HeLa cell suspension were recorded every 3 min for 45 min by photography. Grayness values of the cell suspension at each time point were obtained using ImageJ software (version 1.45; <http://rsbweb.nih.gov/ij/>) as a function of the surface plot profile (SPP) and line plot profile (LPP), as shown in **Figure 3.2**. The line for the LPP was perpendicularly located on the grids of the ruler for zero adjustment of the grayness values at each time point.

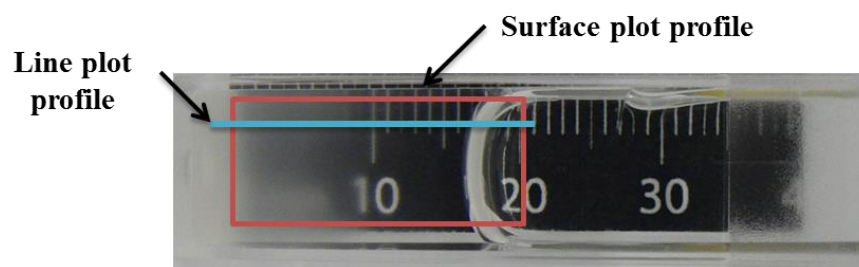


**Figure 3.2:** Analysis of the settling velocity of cells.

Surface and line plot profiles were used to measure grayness values from the height of settling HeLa cells over time. The grids of the ruler in the analyzed area or line were used for the zero adjustment of the grayness values at each time point.

Grayness values of HeLa cells over time were obtained by determining the LPP and were modified by polynomial curve fit of the value at 0 min to reduce the interference of

external lighting effects in the photos. The height of the HeLa cell suspension was determined by comparing 5 plots of the neighbor measuring times (e.g., 0–12, 12–24, 24–36, and 33–45 min). Settling velocities were calculated by determining the change in height of the HeLa cell suspension for each time interval. Ranges of the constant settling velocity (Stokes velocity) of HeLa cells were determined by Boltzmann sigmoidal curve fit of the heights of HeLa cell suspensions over time.

The Boltzmann sigmoid is a logistic function or curve that generally models growth for some populations that exhibit S-shaped behaviors [148]. The sigmoidal curve is used for modeling growth of tumors, neural networks, chemical reactions, etc. The sigmoidal curve is a function (**Equation 3.1**) of the initial value ( $A_1$ , bottom), final value ( $A_2$ , top), center ( $x_0$ ) – the half value between the bottom and top – and time constant ( $d_x$ ). From these parameters, the Boltzmann sigmoid becomes shaped as shown in **Figure 3.3**.

$$y = A_1 + \frac{A_2 - A_1}{1 + e^{\frac{x_0 - x}{d_x}}} \quad (3.1)$$

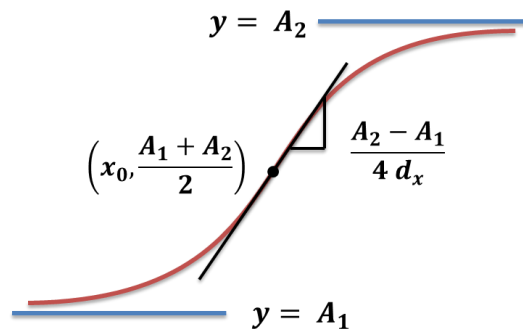


**Figure 3.3:** Boltzmann sigmoidal curve using the following parameters: initial value ( $A_1$ ), final value ( $A_2$ ), center ( $x_0$ ), and time constant ( $d_x$ ).

Using the analyzed settling velocity of HeLa cells at RT, the settling velocity of HeLa cells at 37°C (cell culture conditions) and settling time of HeLa cells in 6-, 12-, and 24-well plates were determined for application in cell adhesion assays.

### 3.3. Results

#### 3.3.1 Culture of HeLa cells

HeLa cells are epithelial-like cells that grow in monolayers on the surface of culture dishes. HeLa cells are generally grown in MEM (90%) with Earle's salts containing 10% FBS, 2 mM L-glutamine, and nonessential amino acids or RPMI 1640 (90–95%) containing 5–10% FBS. Confluent cultures should be passaged at 1:4 to 1:6 ratios every 3–5 days using trypsin/EDTA to achieve a seeding concentration of  $1\text{--}2 \times 10^6$  cells/80 cm<sup>2</sup>. When incubated at 37°C with 5% CO<sub>2</sub>, HeLa cells have a doubling time of ~48 h, and  $5\text{--}15 \times 10^6$  cells can be harvested from 175 cm<sup>2</sup> plates. This information on the growth and passaging of HeLa cells was found in a technical note from DSMZ (<http://www.dsmz.de>).

The growth rate in terms of incubation time was calculated using **Equation 3.2** and **Equation 3.3**, which are based on the doubling time (48 h) of the HeLa cell population.

$$GR_h = 2^{\frac{1}{DT_h}} = 2^{\frac{1}{48}} = \sqrt[48]{2}, \quad (3.2)$$

$$GR_{h,n} = 2^{n/48}. \quad (3.3)$$

$GR_h$  is the growth rate of the HeLa cell population every 1 h,  $DT_h$  is the doubling time of HeLa cells, and  $CR_{h,n}$  is the growth rate of HeLa cells over an  $n$ -h incubation. Cultivated HeLa cells are expected to increase in number by 1.5% during the first hour, 4.4% during a 3-h incubation, and 9.1% during a 6-h incubation.

Cell harvesting densities can be used to indicate the maximum number of cells that can be grown on the culture plate in order to keep the cells viable and healthy. The harvesting density for HeLa cells was between 285 and 857 cells/mm<sup>2</sup>, which was calculated based on the estimated cell density provided by the vendor ( $5\text{--}15 \times 10^6$  cells/175 cm<sup>2</sup>).

**Table 3.2:** Growth rate of HeLa cells at various incubation times.

Incubation time (h)	Growth rate (%)						
1	101.5	13	120.7	25	143.5	37	170.6
2	102.9	14	122.4	26	145.6	38	173.1
3	104.4	15	124.2	27	147.7	39	175.6
4	105.9	16	126.0	28	149.8	40	178.2
5	107.5	17	127.8	29	152.0	41	180.8
6	109.1	18	129.7	30	154.2	42	183.4
7	110.6	19	131.6	31	156.5	43	186.1
8	112.2	20	133.5	32	158.7	44	188.8
9	113.9	21	135.4	33	161.0	45	191.5
10	115.5	22	137.4	34	163.4	46	194.3
11	117.2	23	139.4	35	165.8	47	197.1
12	118.9	24	141.4	36	168.2	48	200.0

### 3.3.2 Physical properties of HeLa cells

#### 3.3.2.1 Diameter and volume of HeLa cells

The diameter and volume of HeLa cells were measured using a CASY cell counter ( $n = 15$ ). The criterional size used to distinguish between viable and dead HeLa cells was set at  $12 \mu\text{m}$ , which was calculated on the basis of the diameter of HeLa cell nuclei ( $\sim 11 \mu\text{m}$ ) calculated from the measured HeLa nucleus volume of  $690 \mu\text{m}^3$  [145]. **Figure 3.4** shows the size distribution of HeLa cells. The distribution of viable HeLa cells resembled a Gaussian curve. The size of cell debris ranged from 0 to  $7 \mu\text{m}$ , while the size of dead HeLa cells ranged from  $7$  to  $12 \mu\text{m}$  in diameter. The measured diameter and volume of viable HeLa cells were  $16.17 \pm 2.4 \mu\text{m}$  (range  $12$ – $30 \mu\text{m}$ ) and  $2,385 \pm 91 \mu\text{m}^3$  (mean  $\pm$  SD), respectively.

Calculation of cell volume using the measured diameter of HeLa cells did not directly correspond to the measured volume. Using the measured diameter ( $16.17 \mu\text{m}$ ), the calculated volume ( $2,225 \mu\text{m}^3$ ) was 6.7% less than the measured volume ( $2,385 \mu\text{m}^3$ ). Similarly, using the measured volume to calculate the diameter resulted in a calculated diameter ( $16.58 \mu\text{m}$ ) that was 2.5% larger than the actual measured diameter.

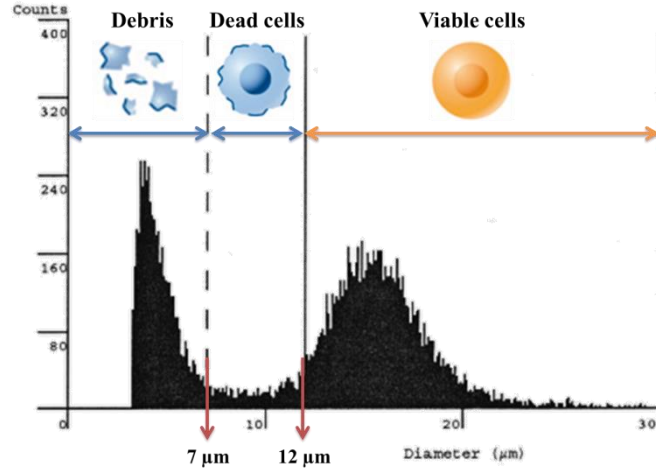


**Figure 3.4:** Size distribution of HeLa cells. Debris measured less than 7  $\mu\text{m}$ , dead HeLa cells measured from 7 to 12  $\mu\text{m}$ , and viable HeLa cells measured from 12 to 30  $\mu\text{m}$ .

### 3.3.2.2 Mass of HeLa cells

The density of HeLa cells has been reported to be  $1,060 \text{ kg/m}^3$  [149, 150]; using this reported density and **Equation 3.4**, the mass of a HeLa cell was calculated to be 2.359 ng based on the measured diameter and 2.528 ng based on the measured volume.  $V_h$  is the volume of a HeLa cell, and  $D_h$  is the diameter of a HeLa cell.

$$V_h = \frac{\pi D_h^3}{6}. \quad (3.4)$$

### 3.3.2.3 Spread area and concentration of HeLa cells

When HeLa cells adhere to the substrate, their spread area is  $1600 \pm 500 \mu\text{m}^2$  [146]; this indicates that the number of the adhered HeLa cells in an area of  $1 \text{ mm}^2$  would be approximately 625 cells, which falls in the range of the harvesting density (285–857 cells/ $\text{mm}^2$ ). In cell adhesions assays, the concentration of HeLa cells cannot exceed the harvesting density because over-proliferated cells are eliminated by self-destruction mechanisms, i.e., apoptosis, during which cells develop abnormal phenotypes [151].

### 3.3.3 Stokes velocity of HeLa cell settling

#### 3.3.3.1 Theoretical calculation of the Stokes velocity of a cell from the measured diameter

Stokes velocity can be used to describe the settling of a large number of dispersed HeLa cells with random positions through Newtonian fluid under gravitational laws. The calculation of cell settling velocity in liquid is based on Stokes' law under the following assumptions of cell behavior in a liquid:

- Laminar flow
- Spherical and rigid particles
- Homogeneous (uniform in composition) material
- Smooth surface
- Particles do not interfere with each other.

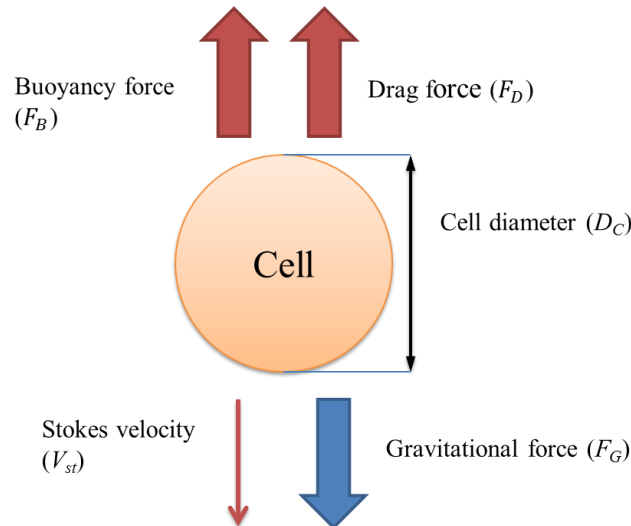


**Figure 3.5:** Forces acting on a settling cell in liquid.

Settling velocity varies until the net forces are equivalent: buoyancy force, gravitational force, and drag force. The terminal settling velocity is the Stokes velocity.

In particular, settling cells exhibit creep-flow movement in liquids, with a Reynolds number ( $Re$ ) of below 1. The settling of cells in a liquid is mainly governed by 3 forces: (1)

gravitational force, (2) buoyancy force, and (3) drag force (flow friction force). Brownian forces on the cells are ignored because they are considerably lower and act in random directions. A cell settles by gravitational force because it has a greater density than liquid. In contrast, buoyancy force acts upward on the cell, and drag force, a form of flow resistance, acts against the direction of a moving cell (**Figure 3.5**).

The gravity force of a cell ( $F_G$ ) is calculated by the equation

$$F_G = M_C g = \frac{\pi \rho_C g D_C^3}{6} \quad (3.5)$$

where  $M_C$  is the mass of the cell,  $g = 9.81 \text{ m/s}^2$  is the acceleration of gravity,  $\rho_C$  is the density of the cell, and  $D_C$  is the diameter of the cell. The buoyancy force ( $F_B$ ) of a cell is calculated by the equation

$$F_B = V_C \rho_L g = \frac{\pi \rho_L g D_C^3}{6} \quad (3.6)$$

where  $V_C$  is the volume of the cell as calculated by **Equation 3.4** and  $\rho_L$  is the density of the liquid. The drag force of a cell ( $F_D$ ) is calculated by Stokes' equation (**Equation 3.7**):

$$\begin{aligned} F_D &= \frac{1}{2} C_D \rho_L v_{st}^2 A_P = \frac{1}{2} \left( \frac{24 \mu_L}{\rho_L v_{st} D_C} \right) \rho_L v_{st}^2 \left( \frac{1}{4} D_C^2 \pi \right) \\ &= 3 \pi v_{st} \mu_L D_C \end{aligned} \quad (3.7)$$

where  $C_D$  is the drag coefficient from Stokes' law at  $Re < 1$  as calculated by **Equation 3.8**,  $v_{st}$  is the Stokes velocity (a terminal and constant settling velocity) of the cell,  $A_P$  is the projected area to the direction of a settling cell, and  $\mu_L$  is the dynamic viscosity of the liquid.

$$C_D = \frac{24}{Re_C} = \frac{24 \mu_L}{\rho_L v_{st} D_C} \quad (3.8)$$

$Re_C$ , the Reynolds number (Re) of a settling cell, is calculated by **Equation 3.9**:

$$Re_C = \frac{\rho_L v_{st} D_C}{\mu_L} \quad (3.9)$$

The projected area of HeLa cell ( $A_P$ ) is calculated by the equation

$$A_P = \frac{1}{4} D_C^2 \pi \quad (3.10)$$

The Stokes velocity of a cell is calculated by Stokes' equation in the equilibrium state of buoyancy, gravitational, and drag forces acting on a cell, according to **Equation 3.11** and **Equation 3.12**:

$$F_D = F_G - F_B \quad (3.11)$$

$$3 \pi v_{st} \mu_L D_C = \frac{\pi \rho_C g D_C^3}{6} - \frac{\pi \rho_L g D_C^3}{6} = \frac{\pi (\rho_C - \rho_L) g D_C^3}{6} \quad (3.12)$$

The Stokes velocity of a cell can be calculated as

$$v_{st} = \frac{(\rho_C - \rho_L) g D_C^2}{18 \mu_L} \quad (3.13)$$

Stokes velocity is proportional to the differences in density between cells and liquids and the square of diameter of a cell and is inversely proportional to the dynamic viscosity of the liquid.

### 3.3.3.2 Theoretical calculation of the Stokes velocity of a cell using the measured diameter and volume

While the measured diameter and volume of HeLa cells did not correspond mathematically, Stokes velocity was calculated by **Equation 3.15** based on the measured diameter and volume:

$$3 \pi v_{st} \mu_L D_C = V_C \rho_C g - V_C \rho_L g = V_C (\rho_C - \rho_L) g \quad (3.14)$$

$$v_{st} = \frac{V_C (\rho_C - \rho_L) g}{3 \pi \mu_L D_C} \quad (3.15)$$

### 3.3.3.3 Density and dynamic viscosity of various liquids

Liquid parameters, such as density and dynamic viscosity, are needed to calculate the Stokes velocity of a cell. The general types of liquids used in cellular experiments are PBS, RPMI 1640 supplemented with 10% FBS or FCS, and Opti-MEM (serum-free medium). The density and dynamic viscosity of these liquids are nearly identical to those of water and are dependent on temperature. **Table 3.3** indicates the density and dynamic viscosity of pure water at different temperatures [152]. The values at RT and 37°C were obtained by a linear interpolation method.

**Table 3.3:** Density and dynamic viscosity of pure water at different temperatures [152].

Temperature (°C)	Density, $\rho$ (kg/m <sup>3</sup> )	Viscosity, $\mu$ (mN·s/m <sup>2</sup> )	Temperature (°C)	Density, $\rho$ (g/cm <sup>3</sup> )	Viscosity, $\mu$ (mN·s/m <sup>2</sup> )
10	999.73	1.3069	37	993.34	0.6931
20	998.23	1.0020	40	992.25	0.6535
23	997.54	0.9350	45	990.24	0.5963
25	997.08	0.8903	50	998.07	0.5471
30	995.68	0.7975	60	983.24	0.4666
35	994.06	0.7195	70	977.81	0.4089

PBS is a buffer solution commonly used in biological research. It is a water-based salt solution containing sodium chloride, sodium phosphate, and, in some formulations, potassium chloride and potassium phosphate. The buffer's phosphate groups help to maintain a constant pH (i.e., 7.4). The osmolarity and ion concentrations of the solution usually match those of the human body (isotonic). The components in PBS are shown in **Table 3.** Although ionic components are found in PBS, the density and dynamic viscosity of PBS are generally similar to those of pure water.

**Table 3.4:** Components of phosphate buffered saline (PBS).

Chemicals	Proportion (wt%)	Density, $\rho$ (g/cm <sup>3</sup> )
Sodium chloride (NaCl)	0.80 %	2.165 g/cm <sup>3</sup>
Potassium dihydrogen phosphate (KH <sub>2</sub> PO <sub>4</sub> )	0.02 %	2.34 g/cm <sup>3</sup>
Disodium hydrogen phosphate (Na <sub>2</sub> HPO <sub>4</sub> )	0.10 %	0.5–1.2 g/cm <sup>3</sup>
Potassium chloride (KCl)	0.02 %	1.984 g/cm <sup>3</sup>
Water (H <sub>2</sub> O)	99.00 %	0.9975 g/cm <sup>3</sup>

The specific gravity of RPMI 1640 is 1.0004231667, as measured by the heat transfer experiment [153]. The dynamic viscosity of RPMI 1640 supplemented with 10% FCS and L-glutamine is similar to that of water [154]. The dynamic viscosity of Opti-MEM is 0.737 mN·s/m<sup>2</sup> at 37°C, as measured using a capillary viscometer [155]. From the collected data, the densities and dynamic viscosities of various liquids are summarized in **Table 3.5** at RT and in **Table 3.6** at 37°C.

**Table 3.5:** Densities and dynamic viscosities of 4 different liquids: pure water, PBS, RPMI 1640, and Opti-MEM at 23°C (RT).

Liquid type (at 23°C)	Density, $\rho$ (kg/m <sup>3</sup> )	Dynamic viscosity, $\mu$ (mN·s/m <sup>2</sup> )
Pure water	997.54 [152]	0.935 [152]
PBS	997.54	0.935
RPMI 1640	997.96 [153]	0.935 [154]
Opti-MEM	997.54	0.990

**Table 3.6:** Densities and dynamic viscosities of 4 different liquids: pure water, PBS, RPMI 1640, and Opti-MEM at 37°C.

Liquid type (at 37°C)	Density, $\rho$ (kg/m <sup>3</sup> )	Dynamic viscosity, $\mu$ (mN·s/m <sup>2</sup> )
Pure water	993.34 [152]	0.696 [152]
PBS	993.34	0.696
RPMI 1640	993.76	0.696 [154]
Opti-MEM	993.34	0.737 [155]

### 3.3.3.4 Calculation of the Stokes velocity of HeLa cells using the measured diameter

The Stokes velocity of HeLa cells at 23°C (RT) and 37°C (**Equation 3.13**) was calculated based on the measured diameter (16.17  $\mu$ m), as determined using a CASY cell

counter. The calculated Stokes velocity of HeLa cells in PBS was 9.52  $\mu\text{m/s}$  at 23°C and 13.65  $\mu\text{m/s}$  at 37°C. HeLa cells in RPMI 1640 settled at the Stokes velocity of 9.46  $\mu\text{m/s}$  at 23°C and 13.56  $\mu\text{m/s}$  at 37°C. The higher Stokes velocity at 37°C in both liquids was caused by the decreasing dynamic viscosity of the liquid as the temperature increased. The Stokes velocities of HeLa cells in various liquids at 23°C and 37°C are described in **Table 3.7**.

**Table 3.7:** Calculated Stokes velocities of HeLa cells in 4 different liquids: pure water, PBS, RPMI 1640, and Opti-MEM at 23°C and 37°C using the measured diameter.

HeLa	23°C		37°C	
	$v_{st}$ ( $\mu\text{m/s}$ )	$v_{st}$ ( $\mu\text{m/min}$ )	$v_{st}$ ( $\mu\text{m/s}$ )	$v_{st}$ ( $\mu\text{m/min}$ )
Water	9.52	571.2	13.65	818.9
PBS	9.52	571.2	13.65	818.9
RPMI 1640+10% FCS	9.46	567.3	13.56	813.7
Opti-MEM	8.99	539.4	12.89	773.3

From the calculated Stokes velocity of HeLa cells, the Reynolds number of HeLa cells ( $Re_H$ ) was  $1.45\text{--}3.18 \times 10^{-4}$ , supporting the assumption of Stokes' law ( $Re < 1$ ) for the drag coefficient ( $C_D$ ) (**Table 3.8**).

**Table 3.8:** Reynolds numbers of settling HeLa cells in 4 different liquids: pure water, PBS, RPMI 1640, and Opti-MEM at 23°C and 37°C.

Reynolds number of HeLa	Temperature	
	23°C	37°C
Water	$1.64 \times 10^{-4}$	$3.18 \times 10^{-4}$
PBS	$1.64 \times 10^{-4}$	$3.18 \times 10^{-4}$
RPMI 1640 + 10% FCS	$1.63 \times 10^{-4}$	$3.16 \times 10^{-4}$
Opti-MEM	$1.45 \times 10^{-4}$	$2.81 \times 10^{-4}$

### 3.3.3.5 Calculation of the Stokes velocity of HeLa cells using the measured diameter and volume

The Stokes velocity of HeLa cells, as calculated by using the measured diameter (16.17  $\mu\text{m}$ ) and volume (2,385  $\mu\text{m}^3$ ), is shown in **Table 3.9**. The Stokes velocity of HeLa cells in PBS was 10.26  $\mu\text{m/s}$  at 23°C and 14.70  $\mu\text{m/s}$  at 37°C. HeLa cells in RPMI 1640

settled at 10.19  $\mu\text{m/s}$  at 23°C and 14.61  $\mu\text{m/s}$  at 37°C. Using the measured diameter and volume, an increase in the Stokes velocity of HeLa cells (by 3.4%) was observed; this was because the measured volume (2,385  $\mu\text{m}^3$ ) was greater than the volume calculated from the measured diameter (2,225  $\mu\text{m}^3$ ).

**Table 3.9:** Calculated Stokes velocities of HeLa cells in 4 different liquids: pure water, PBS, RPMI 1640, and Opti-MEM at 23°C and 37°C using the measured diameter and volume (n = 15).

HeLa	23°C		37°C	
	$v_{st}$ ( $\mu\text{m/s}$ )	$v_{st}$ ( $\mu\text{m/min}$ )	$v_{st}$ ( $\mu\text{m/s}$ )	$v_{st}$ ( $\mu\text{m/min}$ )
Water	10.26	615.3	14.70	882.2
PBS	10.26	615.3	14.70	882.2
RPMI 1640 + 10% FCS	10.19	611.2	14.61	876.7
Opti-MEM	9.69	581.1	13.89	833.2

### 3.3.3.6 Experiments to demonstrate the Stokes velocity of HeLa cells

For the following experiments, the HeLa cell concentration was  $2.2 \times 10^6$  cells/ml, which was the maximum concentration we were able to obtain. The expected height of the HeLa cell suspension (volume, 2 ml) was 20 mm from the sectional area of a PS cuvette ( $10 \times 10 \text{ mm}^2$ ). However, the measured height of the cell suspension in the cuvette was 18.57 mm due to the concave meniscus of the suspension. All cells in PBS were assumed to have the same kinetic energy (settling velocity) and the initial settling velocity was assumed to be 0  $\mu\text{m/s}$ . Experiments were conducted at RT. The settling time – the time for the cells in the suspension to fully settle to the bottom of the cuvette – was expected to be 30.0 min for HeLa cells, as shown in **Table 3.9**. The thickness of the deposited HeLa cell population ( $T_{dH}$ ) was calculated as 104.9  $\mu\text{m}$  using the following equation

$$T_{dH} = \frac{V_H n_H}{A_c}, \quad (3.16)$$

where the volume of a HeLa cells ( $V_H$ ) was 2,385  $\mu\text{m}^3$ , the total number of HeLa cells in the

suspension ( $n_c$ ) was  $4.4 \times 10^6$ , and the cross sectional area of the cuvette ( $A_c$ ) was  $100 \text{ mm}^2$ .

The settling velocity of HeLa cells was measured over time. Photographs of settling HeLa cells in the PS cuvette were obtained every 3 min for 45 min, as shown in **Figure 3.6**. The clearness of the background ruler gives an indication as to how far the cells have settled in each frame. All images exhibited external interference from the bottom of the cuvette (0 mm) to 12 mm in height due to the reflection of light.

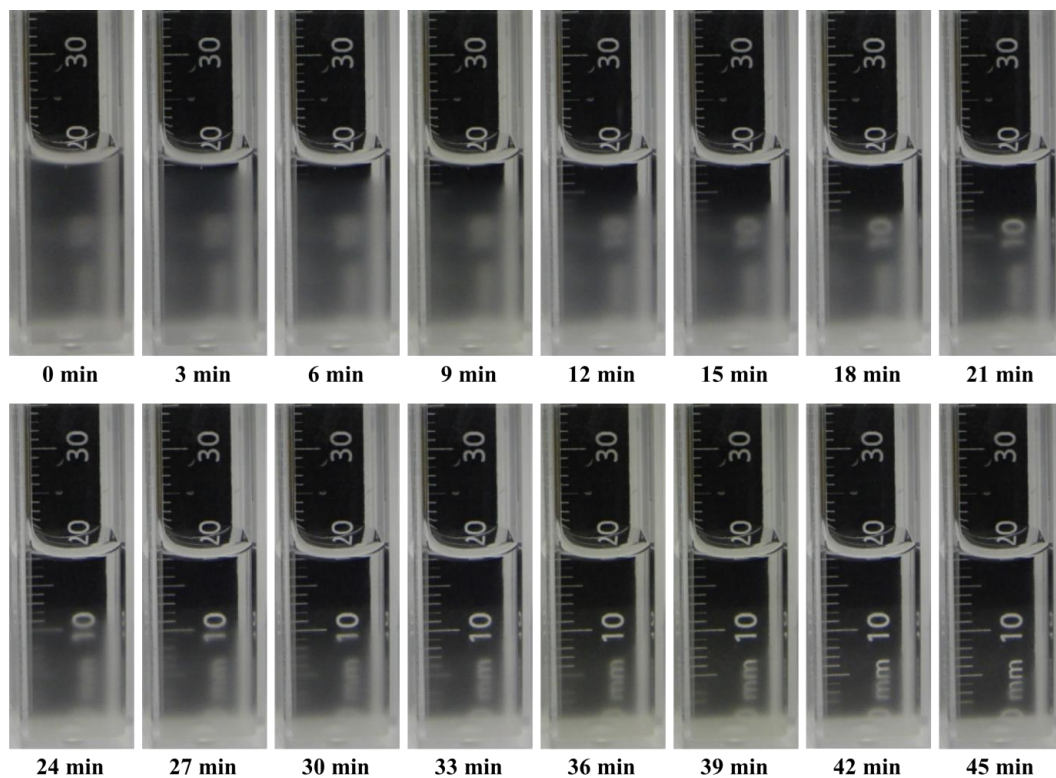


**Figure 3.6:** Photographs of settling HeLa cells in PBS (2 ml volume,  $2.2 \times 10^6$  cells/ml) in a PS cuvette with inner dimensions of  $10 \times 10 \text{ mm}^2$ .

Photographs were taken every 3 min for 45 min. From the meniscus of cell suspension, the maximal height of PBS was 18.57 mm. External interference was observed from the bottom of the cuvette to the 12-mm mark.

Grayness values for the HeLa cell suspension in SPP are shown in **Figure 3.7**. The highest and lowest grayness values were 256 (white) and 0 (black), respectively. The highest values, which resemble a wall at the rear of each graph, represent the white meniscus of the HeLa cell suspension. As HeLa cells settled, the white grids of the black ruler appeared from the top, and the range showing the grids extended from the top.



**Figure 3.7:** Surface plot profile of the grayness values of the HeLa cell suspension. The appearance of a wall at the rear of each graph represents the white meniscus of the cell suspension. The peaks indicate the white grids appearing from the top of the cell suspension, and the range showing the grids grew as the HeLa cells settled.

The LPP of settling HeLa cells at every time point is shown in **Figure 3.8**. The plot for each increasing time point was separated by an offset of 20 in order to distinguish between plots. The meniscus of the HeLa cell suspension located at 18–19 mm caused a dramatic increase in the grayness value. At 0 min, the HeLa cells were uniformly dispersed in the suspension and covered the entire range of white grids, with grayness values of 50–130. The

slopes of the LPPs were caused by the external interference observed in the photographs. As the HeLa cells settled, the white grids – peaks of LPPs – appeared from top, and the range showing the grids extended from the top.

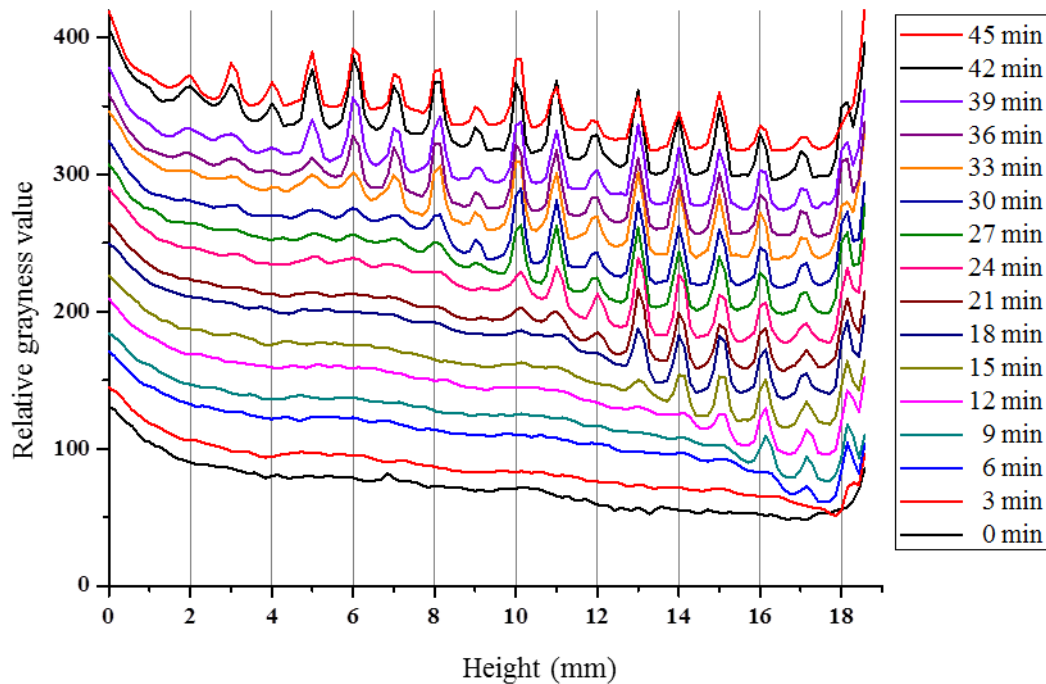


**Figure 3.8:** Line plot profile of HeLa cells every 3 min for 45 min. The plot for each increasing time point was separated by an offset of 20 in order to distinguish between plots.

To reduce the effects of external interference on the photographs (the slopes of the LPPs), the obtained LPPs for the time course experiment were modified by the polynomial curve fit of the LPP at 0 min. The degree of polynomial fitting was determined by comparing the original LPP and the polynomial fits of various degrees (e.g., 5, 7, 8, and 9). As shown in **Figure 3.9**, the 9th-degree polynomial fit most closely resembled the LPP at 0 min. This polynomial was

$$\begin{aligned}
 f(x) = & 73.51 + 34.01 x - 54.46 x^2 + 27.31 x^3 - 6.92 x^4 \\
 & + 1.00 x^5 - 8.71 \times 10^{-2} x^6 + 4.46 \times 10^{-3} x^7 - 1.25 \times 10^{-4} x^8 \\
 & + 1.47 \times 10^{-6} x^9
 \end{aligned}
 \tag{3.17}$$

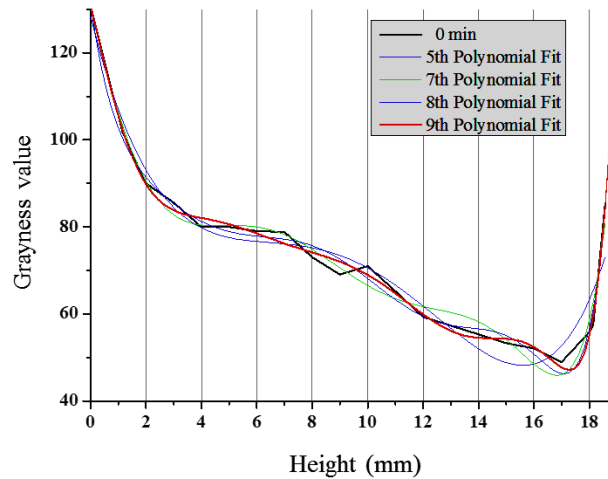


**Figure 3.9:** Polynomial curve fits of the line plot profile of the HeLa cell suspension at 0 min. Among various degrees of polynomials (e.g., 5, 7, 8, and 9), a 9th-degree polynomial fit most closely resembled the line plot profile at 0 min. The function of this polynomial fit was  $f(x) = 73.51 + 34.01x - 54.46x^2 + 27.31x^3 - 6.92x^4 + 1.00x^5 - 87.08 \times 10^{-2}x^6 + 4.46 \times 10^{-3}x^7 - 1.25 \times 10^{-4}x^8 + 1.47 \times 10^{-6}x^9$ .

The effect of the polynomial fit on reducing the interference of LPPs was demonstrated by the relative grayness values – subtraction the polynomial fit of the LPP at 0 min from that of the LPP at 45 min (**Figure 3.10**). The slope of the modified LPP at 0 min was almost flat, and all values were close to 0. The valleys of the modified LPP at 45 min were also positioned in a narrow range of variance ( $\sim 10$ ) from 0 to 18 mm.

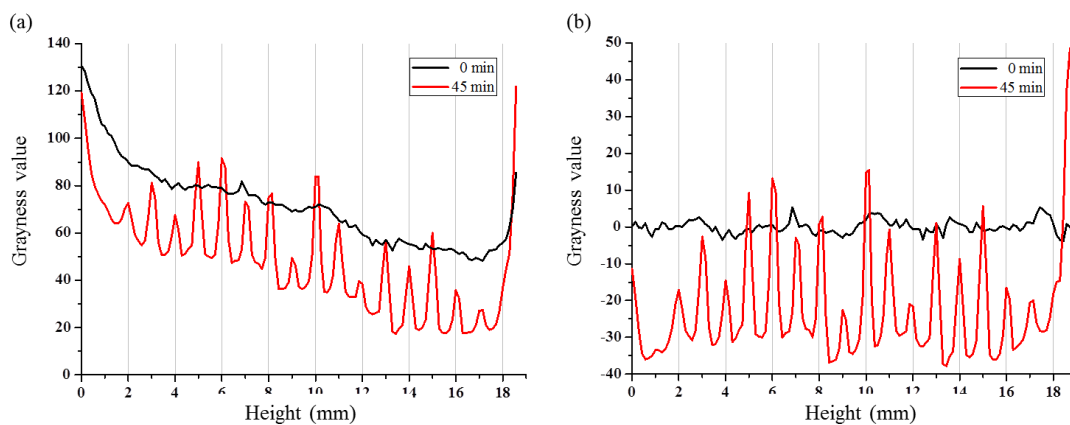


**Figure 3.10:** Line plot profiles at 0 min (black) and at the final measuring time of 45 min (red) for HeLa cells in the suspension.

- (a) Graph of the original line plot profile data. The slopes of both lines ranged from 0 to 12 mm and was caused by external interference.
- (b) Graph of the modified line plot profile by the 9th-degree polynomial fit.

The modified LPPs for HeLa cell settling over time are shown in **Figure 3.11**. The plot for each increasing time point was separated by an offset of  $-20$  in order to distinguish between plots.

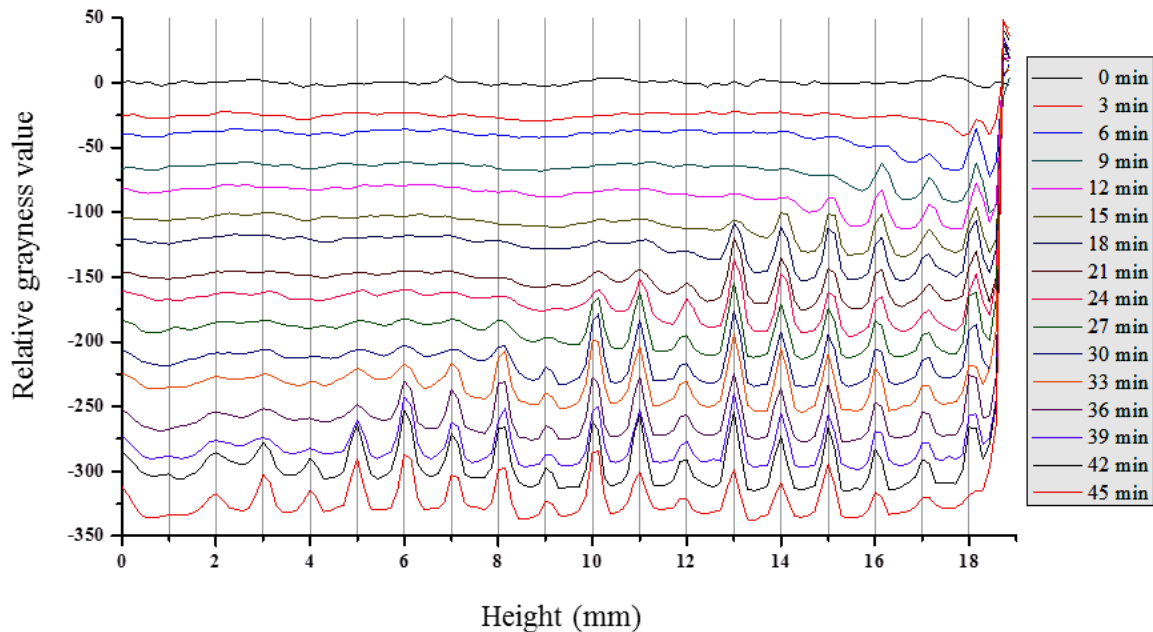


**Figure 3.11:** Modified line plot profiles of HeLa cells. Photographs were taken every 3 min for 45 min. The modified line plot profiles indicate relative values of the original data to the 9th-degree polynomial fit of the plot at 0 min. The plot for each increasing time point was separated by an offset of  $-20$  in order to distinguish between plots.

Heights of the HeLa cells were determined by comparing the 5 plots of the neighboring measured times (e.g., 0–12, 12–24, 24–36, and 33–45 min) by magnifying the range of the heights. In **Figure 3.12**, the magnified range of the height was 9–19 mm for 0–12 min (a), 5–15 mm for 12–24 min (b), 0–10 mm for 24–36 min (c), and 0–10 mm for 33–45 min (d).

The height of the HeLa cell suspension at each time point was determined by taking the minimum value below the appearance of the white grid (peak point), whether it was high or low. These measured heights are shown in **Table 3.10**.

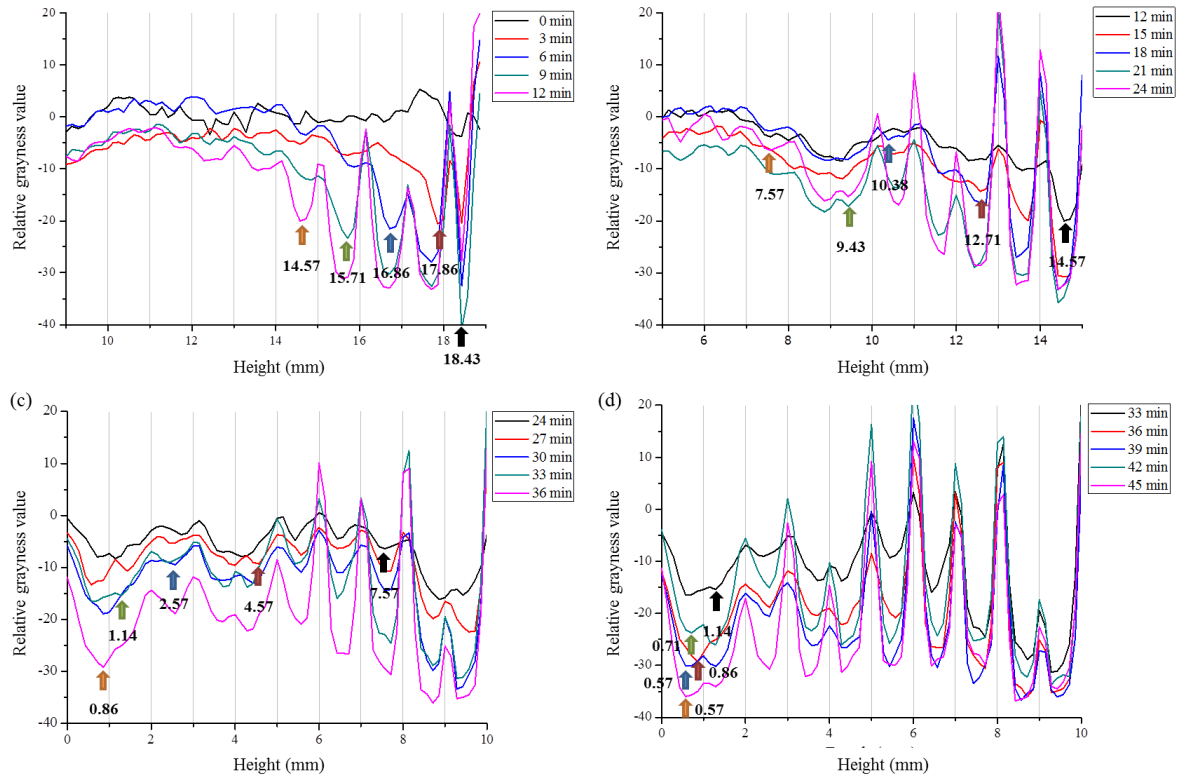


**Figure 3.12:** Heights of the HeLa cell suspension as determined by comparing the neighboring measured times the neighbor modified line plot profiles. The arrows indicate the height of the HeLa cells in the suspension, and the arrow color corresponds to the color of the line.

- (a) The modified LPPs at 0–12 min. The valley at 18.57 mm indicates the height of the HeLa suspension (2 ml) in the cuvette. The height of the HeLa cells was 18.57 mm at 0 min, 17.86 mm at 3 min, 16.86 mm at 6 min, 15.71 mm at 9 min, and 14.57 mm at 12 min.
- (b) The modified LPPs at 12–24 min. The height of the HeLa cells was 12.71 mm at 15 min, 10.38 mm at 18 min, 9.43 mm at 21 min, and 7.57 mm at 24 min.
- (c) The modified LPPs at 24–36 min. The height of the HeLa cells was 4.57 mm at 27 min, 2.57 mm at 30 min, 1.14 mm at 33 min, and 0.86 mm at 36 min.
- (d) The modified LPPs at 33–36 min. The height of the HeLa cells was 0.57 mm at 39 min, 0.71 mm at 42 min, and 0.57 mm at 45 min.

**Table 3.10:** The heights and settling velocities of the HeLa cell suspension at various times. The velocity at each time point is shown as the mean velocity from the previous time to the indicated time.

Measuring time (min)	Height (mm)	Settling velocity		Measuring time (min)	Height (mm)	Settling velocity	
		( $\mu\text{m}/\text{min}$ )	( $\mu\text{m}/\text{s}$ )			( $\mu\text{m}/\text{min}$ )	( $\mu\text{m}/\text{s}$ )
0	18.57	–	–	24	7.57	620.0	10.33
3	17.86	190.0	3.17	27	4.57	1,000.0	16.67
6	16.86	333.3	5.56	30	2.57	666.7	11.11
9	15.71	383.3	6.39	33	1.14	476.7	7.94
12	14.57	380.0	6.33	36	0.86	93.3	1.56
15	12.71	620.0	10.33	39	0.57	96.7	1.61
18	10.38	776.7	12.94	42	0.71	–46.7	–0.78
21	9.43	316.7	5.28	45	0.57	46.7	0.57

The settling velocity of HeLa was slow, but increased from its initial state until 9 min. After 9 min, the Stokes velocity of HeLa cells was  $11.11 \pm 2.46 \mu\text{m/s}$  from 12 to 30 min ( $n = 6$ ). After 30 min, the settling velocity dramatically decreased. The slow settling velocity of HeLa cells during the initial and final phases makes it difficult to measure the Stokes velocity of HeLa cells using the entire time range; thus, the settling time was postponed. The height of the HeLa cell suspension did not reach  $104.9 \mu\text{m}$  until 45 min, despite the fact that theoretical methods predicted a settling time of 30.0 min for these cells.

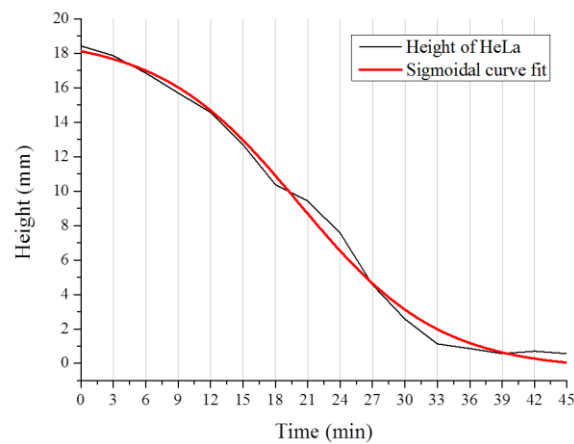


**Figure 3.13:** Boltzmann sigmoid of the height of HeLa cells in the suspension over time. The Boltzmann sigmoid was characterized by the following parameters: center ( $x_0$ ) of 20.20 min, initial value ( $A_1$ ) of  $-0.369$  mm, final value ( $A_2$ ) of 18.94 mm, and time constant ( $d_x$ ) of 6.49 min.

Because of the slow settling velocities in the initial and final phases of settling, the height of the HeLa cells in the suspension resembled an S-shaped Boltzmann sigmoid (**Figure 3.13**).

The sigmoid for the heights of HeLa cells in the suspension over time can be described by the equation

$$y = -0.37 + \frac{18.95 + 0.37}{1 + e^{\frac{x-20.2}{6.49}}} \quad (3.18)$$

Using this equation, the center ( $x_0$ ) was 20.2 min, the initial value ( $A_1$ ) was  $-0.37$  mm,

and the final value ( $A_2$ ) was 18.95 mm. The time constant ( $d_x$ ) was 6.49 min. According to this Boltzmann sigmoid, HeLa cells have a settling time of 44.1 min, the time required for the height of HeLa cells in the suspension to reach 104.9  $\mu\text{m}$ ; this time was 47.0% longer than the expected time of 30.0 min.

In our study of the settling velocity, the time range during which we could measure the Stokes velocity (12–30 min) was roughly assumed; however, it is necessary to define the optimal time range for determining the Stokes velocity of HeLa cells, i.e., the linear range of the Boltzmann sigmoidal fit of the heights over time. For this reason, the linear range of the Boltzmann sigmoid was analyzed by a standard Boltzmann sigmoid with different time constants ( $d_x$ ): 1/4, 1/3, 1/2, 2/3, 1, 3/2, 2, and 3, as shown in **Figure 3.14** (a). The x-axis ranged from  $-1$  to  $1$  and was inversely proportional to the time constant (**Table 3.11**). For example, when the time constant was 1/4, the range of the x-axis showed a 4-fold time constant, while the time constant of 3 had a range of  $-1/3$  to  $1/3$  of the time constant.

**Table 3.11:** The range of the x-axis from  $-1$  to  $1$  in terms of various time constants for the standard Boltzmann sigmoid.

Time constant ( $d_x$ )	Range of x-axis from $-1$ to $1$ in terms of time constant	Time constant ( $d_x$ )	Range of x-axis from $-1$ to $1$ in terms of time constant
1/4	$4 \times d_x$	1	$1 \times d_x$
1/3	$3 \times d_x$	3/2	$2/3 \times d_x$
1/2	$2 \times d_x$	2	$1/2 \times d_x$
2/3	$3/2 \times d_x$	3	$1/3 \times d_x$

The linear fits of the different Boltzmann sigmoidal curves overlapped, as shown in **Figure 3.14** (a). Errors of the linear fits to the different sigmoid functions are also shown in **Figure 3.14** (b). The error of the linear fits was less than 1% when the range of the x-axis was less than 1-fold the time constant ( $d_x \leq 1$ ) in the graph. Therefore, the optimal range for the constant differential value – the Stokes velocity – was from the  $-$  time constant to the  $+$  time constant, from the center of the sigmoid function (from  $x_0 - d_x$  to  $x_0 + d_x$ ).

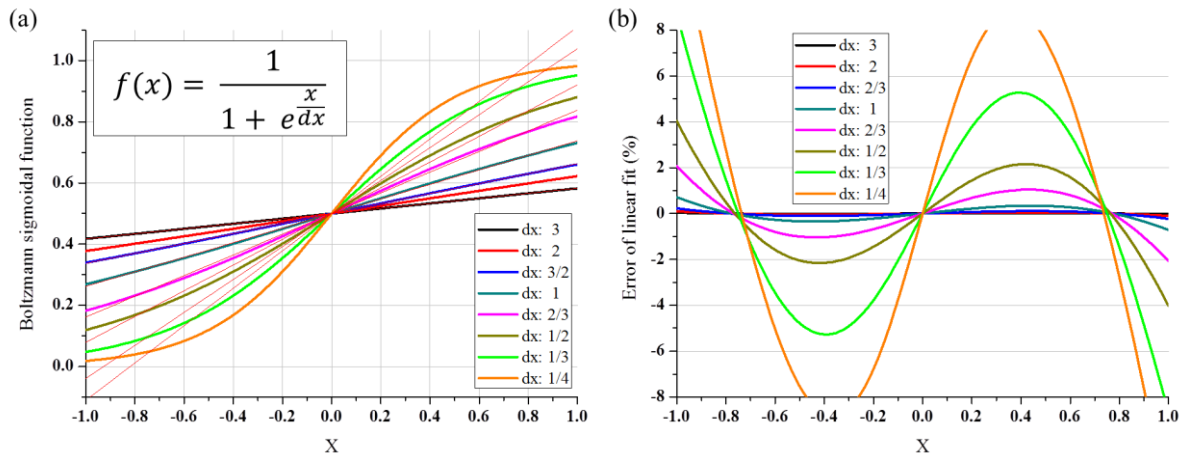


**Figure 3.14:** Linear fits of the standard Boltzmann sigmoid with various time constants, ranging from 1/4 to 3.

- (a) Boltzmann sigmoidal curves with various time constants ( $d_x$ ) (1/4, 1/3, 1/2, 2/3, 1, 3/2, 2, and 3) and their linear fits. The x-axis ranged from  $-1$  to  $+1$ ,  
 (b) Graph of the errors of linear fits to the Boltzmann sigmoid curves. The error of the linear fit was less than 1% when the x-axis ranged from  $-d_x$  to  $+d_x$ .

Boltzmann sigmoids of the heights of HeLa cells in suspension revealed a Stokes velocity of  $11.14 \mu\text{m/s}$  in the range of 13.71–26.69 min, with a center of 20.20 min and a time constant of 6.49 min. The theoretical and experimental Stokes velocities of HeLa cells are summarized in **Table 3.12**. Errors were based on the Stokes velocity calculated using the measured diameter and volume of HeLa cells. The error of the Stokes velocity using the Boltzmann sigmoid was 11.1%.

**Table 3.12:** Theoretical and experimental Stokes velocities of HeLa cells in PBS at 23°C.

Method in PBS at 23°C	Stokes velocity ( $\mu\text{m/s}$ )	Error (%)
Theory : measured diameter (16.17 $\mu\text{m}$ )	9.52	-7.2
Theory : measured diameter (16.17 $\mu\text{m}$ ) and volume (2,385 $\mu\text{m}^3$ )	10.26	—
Experiment : measured heights in 15–24 min	9.72	-5.2
Experiment : sigmoidal function in 13.71–26.69 min	11.14	11.1

### 3.3.4 Settling time of HeLa cells in cell adhesion assays

Cell adhesion assays are generally conducted in 6-, 12-, or 24-well plates (**Figure 3.15**) at RT or 37°C. The diameter of the cylindrical wells is 34.80 mm for 6-well plates, 22.11 mm for 12-well plates, and 15.62 mm for 24-well plates. Typical working volumes for liquids are 2.7–3.2 ml for 6-well plates, 1.4–2.3 ml for 12-well plates, and 0.7–0.9 ml for 24-well plates.

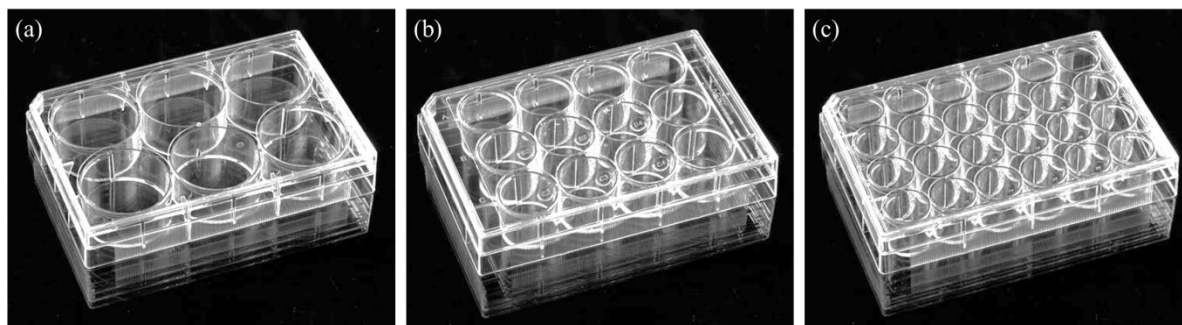


**Figure 3.15:** Different types of well plates for cell adhesion assays: (a) a 6-well plate with a well diameter of 34.80 mm, (b) a 12-well plate with a well diameter of 22.11 mm, and (c) a 24-well plate with a well diameter of 15.62 mm.

Different working volumes yield different liquid heights in wells of these plates (**Table 3.13**). For our analysis, we used working volumes of 0.7–0.9 ml for 24-well plates, 1.5–2.5 ml for 12-well plates, and 2.5–3.5 ml for 6-well plates.

**Table 3.13:** Heights of liquids with the different working volumes in 6-, 12-, and 24-well plates

Working Volume	0.7 ml	0.9 ml	1.5 ml	2.0 ml	2.5 ml	3.0 ml	3.5 ml
Height (mm) in 6-well plate	–	–	–	–	2.63	3.15	3.68
Height (mm) in 12-well plate	–	–	3.91	5.21	6.51	–	–
Height (mm) in 24-well plate	3.65	4.70	–	–	–	–	–

The settling times for HeLa cells in 6-, 12-, and 24-well plates were determined according to these different working volumes for cell adhesion assays, using the settling time calculated for the 18.57-mm HeLa cell suspension at RT by the Boltzmann sigmoid function (44.61 min). **Table 3.14** shows the settling times of HeLa cells in PBS for different working

volumes in 6-, 12-, or 24-well plates at RT and 37°C. The settling time of HeLa cells in RPMI 1640 supplemented with 10% FBS or FCS was similar to that in PBS (ratio, 0.994; **Table 3.7**).

**Table 3.14:** Settling time of HeLa cells in PBS according to working volume in 6-, 12-, or 24-well plates at 23°C and 37°C.

PBS		0.7 ml	0.9 ml	1.5 ml	2.0 ml	2.5 ml	3.0 ml	3.5 ml
Settle time (s) in a 6-well plate	23°C	–	–	–	–	379.1	454.0	530.4
	37°C	–	–	–	–	264.4	316.7	370.0
Settle time (s) in a 12-well plate	23°C	–	–	563.6	750.9	938.3	–	–
	37°C	–	–	393.1	523.7	654.4	–	–
Settle time (s) in a 24-well plate	23°C	526.1	677.4	–	–	–	–	–
	37°C	366.9	472.5	–	–	–	–	–

### 3.4. Discussion

#### 3.4.1 Physical properties of HeLa cells

In this study, we found that the measured diameter of HeLa cells could not be used to accurately predict the volume, and vice versa. One explanation for the larger measured volume may be the presence of long cilia on the surface of HeLa cells or the occurrence of cell division (**Figure 3.16**).

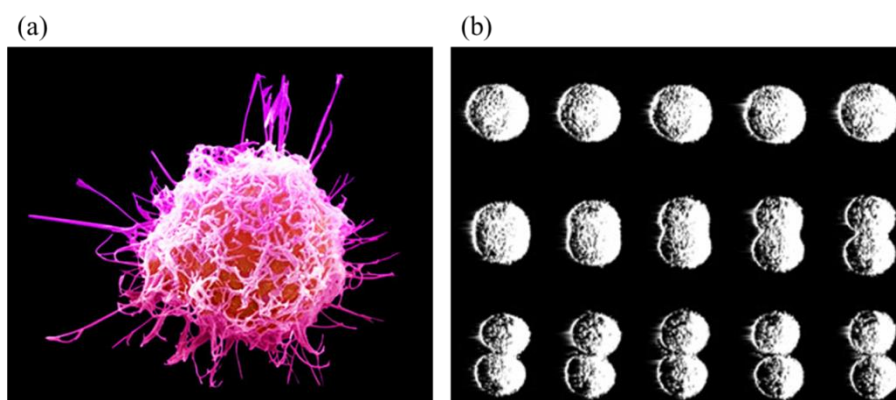


**Figure 3.16:** Images of a HeLa cell and the cell division process.

- (a) Scanning electron microscope image of a HeLa cell. HeLa cells have long, narrow cilia on their surface [<http://www.smithsonianmag.com>].
- (b) In cell division, spherical cells grow and elongate in one direction. In the final state of cell division, 2 small daughter cells appear (<http://www.davidicke.com>).

However, the effect of cilia on differences between the measured and calculated diameters and volumes would seem insignificant because the CASY cell counter measures the diameter and volume of HeLa cells spontaneously. The other possible cause is the spheroidal shape of HeLa cells during cell division [Figure 3.16 (b)], which occurs in normal HeLa cells undergoing mitosis. The shape of the HeLa cell was assumed to be spheroidal with two minor axes (a) and a major axis (b).

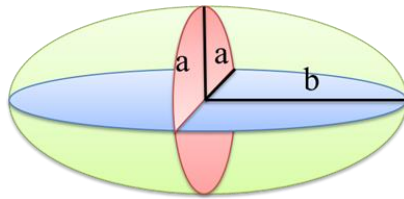


**Figure 3.17:** Spheroidal shape of the HeLa cell. The lengths are (a) for the two minor axes and (b) for the major axis.

The measured volume and radius were calculated using the length of the major (b) and minor (a) axes of the spheroid (**Equation 3.19** and **Equation 3.20**). The radius of a HeLa cell was calculated as the geometric mean of the minor axis (a) and major axis (b). From this, we found that the volume ( $V_H$ ) and radius ( $r_H$ ) of a HeLa cell were  $2,385 \mu\text{m}^3$  and  $8.09 \mu\text{m}$ , respectively.

$$V_H = \frac{4\pi}{3} a^2 b \quad (3.19)$$

$$r_H = \sqrt{ab} \quad (3.20)$$

Combining **Equation 3.19** and **Equation 3.20**, the length of the minor (a) and major (b) axes were  $7.51 \mu\text{m}$  and  $8.71 \mu\text{m}$ , respectively. The minor axis was less than the measured radius by  $0.58 \mu\text{m}$ , while the major axis was longer than the measured radius by  $0.62 \mu\text{m}$ . Using **Equation 3.21**, the eccentricity of HeLa cells ( $e_H$ ) was 0.507.

$$e_H = \sqrt{1 - \left(\frac{a}{b}\right)^2} \quad (3.21)$$

### 3.4.2 Stokes velocity of HeLa cells

Our mathematical model of settling HeLa cells was reasonable, with a maximum error of 11.4% ( **Table 3.12**), despite the presence of cilia on the surface of the cell (see **Figure 3.16**) and the spheroidal shape of HeLa cells (see **Figure 3.17**), which violate the assumptions of Stokes' law (spherical particles and a smooth surface). These violations may explain the slow development of the settling velocity during the initial phase of settling and the exponential decrease in the settling velocity during the final phase of settling (see **Figure 3.13**). According to the Boltzmann sigmoid, the settling velocity accelerated until 13.71 min during the initial phase and slowed beginning at 26.69 min during the final phase (**Table 3.11**).

#### 3.4.2.1 Development of the settling velocity of HeLa cells during the initial phase

To provide insight into the mechanisms mediating the initial phase of settling, developing time (i.e., the time required for HeLa cells to reach the Stokes velocity) was calculated. If the developing time was the same as that determined using the Boltzmann sigmoid (13.71 min), analysis of the slow settling velocity in the initial phase would not be required.

We calculated the developing time for HeLa cells using a differential equation. Before reaching the developing time, the settling velocity must increase until it reaches an equilibrium state where all forces (gravity, buoyancy, and drag) are equal (**Equation 3.22**), allowing cells to settle at the Stokes velocity of 10.26  $\mu\text{m/s}$ . The settling velocity of HeLa cells was calculated using **Equation 3.24**.

$$F_C = F_G - F_B - F_D \quad (3.22)$$

The acceleration of a settling cell ( $a_c$ ) is the time derivative of the settling velocity of a cell ( $v_c$ ), that is,  $a_c = dv_c/dt$ .

$$\rho_c V_c \frac{dv_c}{dt} = (\rho_c - \rho_L) V_c g - \left( \frac{1}{2} C_D \rho_L A_P \right) v_c^2 \quad (3.23)$$

$$\frac{dv_c}{dt} = \frac{(\rho_c - \rho_L)}{\rho_c} g - \left( \frac{C_D \rho_L A_P}{2 \rho_c V_c} \right) v_c^2 \quad (3.24)$$

By assumption, the initial velocity of a HeLa cell in a liquid ( $v_{c,0}$ ) is 0  $\mu\text{m/s}$  when the time ( $t$ ) is 0 s.

$$\frac{dv_c}{dt} = \frac{(\rho_c - \rho_L)}{\rho_c} g - \left( \frac{C_D \rho_L A_P}{2 \rho_c V_c} \right) v_c^2 \quad (3.25)$$

$$dv_c = -N (v_c^2 - K^2) dt \quad \left( N = \frac{C_D \rho_L A_P}{2 \rho_c V_c}, K^2 = \frac{2 (\rho_c - \rho_L) V_c}{C_D \rho_L A_P} g \right) \quad (3.26)$$

$K$  indicates the Stokes velocity (10.26  $\mu\text{m/s}$  for HeLa cells in PBS at 23°C and 14.17  $\mu\text{m/s}$  for HeLa cells in PBS at 37°C). In the following differential equation,  $K \geq v_c$  for the full time range and the constant ( $\tilde{C}$ ) is 0 because  $v_{c,0} = 0$ .

$$\int \frac{1}{v_c^2 - K^2} dv_c = - \int N dt \quad (3.27)$$

$$\frac{1}{2K} \ln \frac{K + v_c}{K - v_c} = Nt + \tilde{C} \quad (3.28)$$

$$v_c(t) = K \frac{1 - e^{-Pt}}{1 + e^{-Pt}}, (P = 2KN) \quad (3.29)$$

Time constant ( $P$ ) for HeLa cells in PBS was  $1.13 \times 10^5$  at 23°C and  $8.71 \times 10^4$  at 37°C. As shown in **Figure 3.18**, the developing time for the settling velocity of HeLa cells during

the initial phase was very short ( $< 100 \mu\text{s}$ , calculated using **Equation 3.29**). Therefore, the developing time estimated from the Boltzmann sigmoid (13.71 min) was affected by other factors.

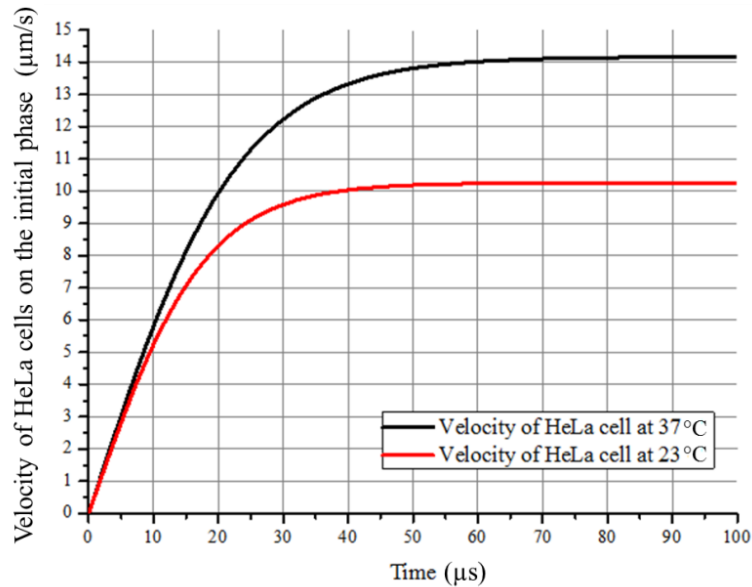


**Figure 3.18:** Increase in the settling velocity of HeLa cells during the initial phase of settling (in PBS, at 23°C and 37°C).

### 3.4.2.2 Slow developing time for the settling velocity of HeLa cells during the initial phase of settling

During the initial phase, the slow developing time for the settling velocity of HeLa cells was affected by dense debris in the HeLa cell suspension (**Figure 3.4**). The concentration of HeLa cells was  $1.024 \times 10^6$  cells/ml, with  $4.103 \times 10^5$  debris particles/ml. These two different sized particles (cells and debris) would result in differential sedimentation of the bidispersed suspension. The initial phase of differential sedimentation would be instable because of large-scale fluctuations in particle size, i.e., heavy, large particles – HeLa cells – would settle to the bottom, while light, small particles – debris – would rise to the top of the suspension (**Figure 3.19**) [156]. This suggests that HeLa cell suspensions should be allowed to settle for some time in order to reach a steady settling velocity.

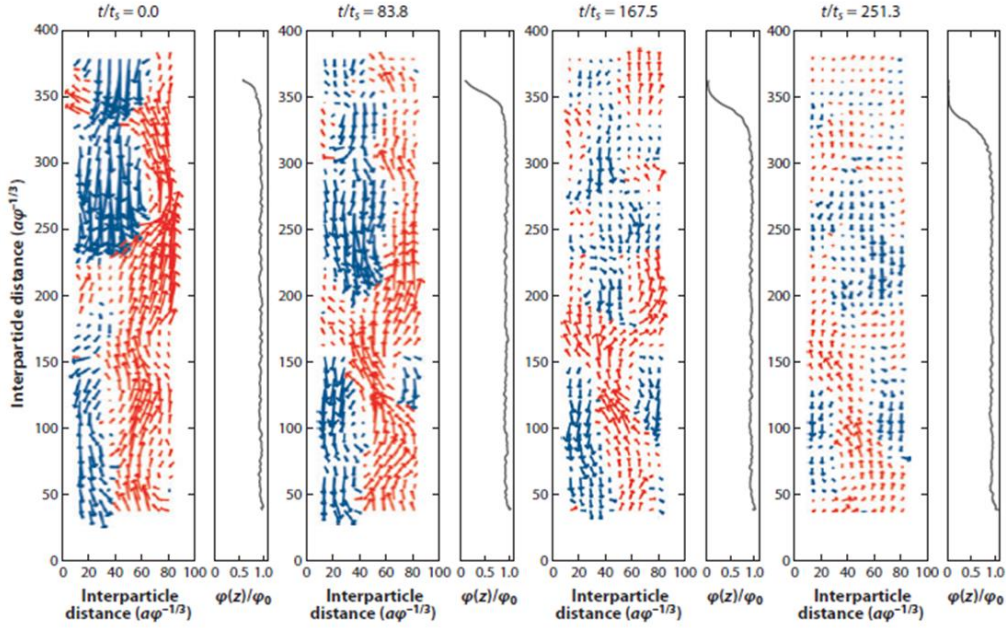


**Figure 3.19:** Large-scale fluctuations of particles occur when heavy, large particles (blue) settle to the bottom and light, small particles (red) raise to the top of the suspension [156]. The timescale is based on the Stokes time ( $t_s$ ) of particles.

The Stokes time ( $t_s$ ) is the time for an isolated sphere to sediment in terms of its radius ( $D_c/2$ ) [156]. The calculated Stokes time of a HeLa cell in PBS is 788.0 ms at 23°C and 592.3 ms at 37°C according to the equation

$$t_s = \frac{D_c}{2 v_{sd}} \quad (3.30)$$

Therefore, particles are still experiencing large-scale fluctuations at the maximal time (e.g., 3.3 min at 23°C and 2.5 min at 37°C for HeLa cells in PBS), based on the Stokes time ( $t/t_s = 251.3$ ), as shown in **Figure 3.19**.

### 3.4.2.3 Exponential decrease in the settling velocity of HeLa cells during the final phase

During the final phase, the decreased settling velocity of HeLa cells near the bottom of the cuvette was likely dependent on the concentration of HeLa cells in the suspension. This phase of settling was probably also affected by the strong cell-cell interactions between HeLa cells. HeLa cells, derived from epithelial cells, which are known to pack densely to form the

epithelium, interact and attach to each other [157]. These cell-cell interactions constitute another violation of the assumptions of Stokes' law (i.e., that particles do not interfere with each other). Marieb [157] demonstrated the effects of particle-particle interactions on the settling velocity of particles (**Figure 3.20**). When the concentration of interacting particles is increased, the settling velocity of particles decreases due to interaction between particles. Therefore, as the concentration of HeLa cells increased near the bottom of the cuvette, the settling velocity exponentially decreased, as shown in **Figure 3.20** (b).

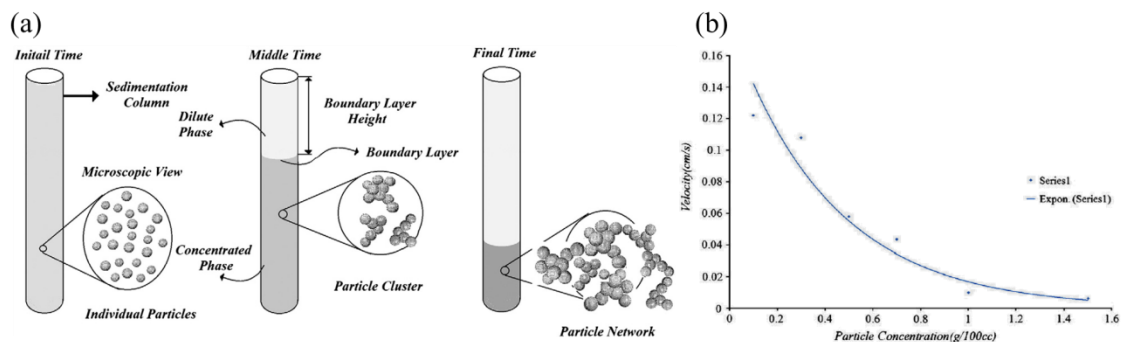


**Figure 3.20:** Effects of particle concentration on particle-particle interactions [157].

(a) Structure of particles in the suspension with time. (b) The effect of particle concentration on settling velocity.

#### 3.4.2.4 Conditions of the cell suspension for measuring settling velocity

The effects of the dense debris on the initial phase of settling and the effects of cell-cell interactions and cell concentration at the bottom of the cuvette on the final phase of settling should be further investigated, using different conditions for the cell suspension to measure the Stokes velocity. For the initial phase, the density of debris may be reduced by filtration, creating a homogeneously dispersed cell suspension to reduce the effects of large-scale fluctuations on the settling velocity. For the final phase, the decrease in settling velocity may be lessened by using a lower density of HeLa cells or by using nonadherent cells (i.e., T-lymphocytes or Jurkat cells) that do not exhibit cell-cell interactions. By reducing the density of cell debris and using nonadherent cells, the time range during which cells exhibit Stokes velocity can be extended.

### 3.5. Conclusion

This study demonstrated the physical properties of HeLa cells for potential application in microbiochips, which enable us to control the complete cellular microenvironment or to analyze single cells, leading to new questions and discoveries. Our results demonstrated that HeLa cell populations exhibited insignificant growth for the first 6 h of incubation, with only a 9% increase in the number of cells. The harvesting density of HeLa cells on the culture plate exhibited a maximum of 857 cells/mm<sup>2</sup>; this value is important to avoid causing apoptosis due to overproliferation. Moreover, the diameter and volume of HeLa cells were  $16.17 \pm 2.4 \mu\text{m}$  and  $2,385 \pm 91 \mu\text{m}^3$ , respectively. The spheroidal shape of HeLa cells during cell division may explain the mathematical discordance between the measured diameter and volume. Using the measured volume, the mass of a HeLa cell was estimated to be 2.528 ng, and the density of HeLa cells was 1,060 kg/m<sup>3</sup>.

The Stokes law in Newtonian fluid dynamics can be used to calculate the Stokes velocity – or constant settling velocity – of HeLa cells. The calculated settling velocity of HeLa cells in PBS was 10.26  $\mu\text{m/s}$  at 23°C and 14.70  $\mu\text{m/s}$  at 37°C using the measured diameter and volume. The higher Stokes velocity of HeLa cells at 37°C than at 23°C was caused by the lower dynamic viscosity of PBS at the higher temperature. Importantly, experiments to investigate the settling velocity of HeLa cells were performed for cell populations in a PS cuvette at 23°C. The 18.57-mm-deep cell suspension was based on the volume of PBS at a cell concentration of  $2.2 \times 10^6$  cells/ml, and the cell height was measured every 3 min for 45 min. This time study revealed that the settling velocity developed slowly during the initial phase and decreased exponentially during the final phase, leading to a Boltzmann sigmoid-shaped curve. The Stokes velocity of HeLa cells was 11.14  $\mu\text{m/s}$  from 13.71 to 26.69 min by Boltzmann sigmoidal fit. The slow development and exponential decrease of the settling velocity in HeLa cells delayed the settling time to 44.1 min, which

represented a 46.1% delay from the calculated settling time of 30.0 min by the Boltzmann sigmoid. The slow developing time for the settling velocity of HeLa cells was caused by large-scale fluctuations between HeLa cells and debris present in the cell suspension. The exponential decrease in the settling velocity was caused by the abundant cell-cell interactions and high density of HeLa cells near the bottom of the cuvette.

The assumptions of Stokes' law were violated by several conditions, including the presence of cilia on the surface of the cells, the spheroidal shape of HeLa cells, and cell-cell interactions between HeLa cells. However, the measured Stokes velocity exhibited 11.1% error compared to the theoretical velocity. The time range of the Stokes velocity may be extended by filtration of debris and beginning with a lower density of HeLa cells. Moreover, the use of nonadherent cells may reduce the decreased settling velocity during the final phase of settling by eliminating cell-cell interactions.

Finally, we applied these principles and measured the settling velocity and settling time of HeLa cells in typical well plates. This information on the expected settle time of HeLa cells will be useful for cell adhesion assays in time-course analyses.



# Chapter 4. Dopaminergic Mesoporous Inorganic-organic Hybrid Resin

## 4.1. Introduction

### 4.1.1 Development of new biomaterials and novel technologies

New biomaterials and novel technologies for surface engineering have been developed for a wide range of biological studies and applications, including medicine, pharmacology, and bioengineering [43-45]. An ideal biomaterial should be amenable to molecular design for biological purposes and easily synthesized [44]. Moreover, for application in micro-fabrication, a new biomaterial should enable easy fabrication to exacting specifications and should be highly stable in both water and organic solvents.

### 4.1.2 Significance of cell adhesion to biomaterials

The most frequently obtained cellular phenotypes on foreign materials are changes in cell morphology, adhesion, and proliferation during cultivation for anchorage-dependent cells [53, 158, 159]. Among these, cell adhesion is most essential because it is the first step in a cascade of events during which cellular interaction with the surface of the biomaterial occurs [49]. Cell adhesion also represents the *in vitro* simulation of physiologically relevant events, which may facilitate our understanding of cellular functions and realization of the feasibility of tissue engineering of bio-artificial solid organs and systems [160]. Recent adaptation of MEMS fabrications to control cell adhesion and micropatterning of cells using cell-surface interactions has been applied in cell culture models to better reproduce *in vivo* functions in the form of single cell arrays and coculture systems [27, 28, 30].

### 4.1.3 Method for promoting cell adhesion by surface engineering

The chemical and physical properties of cell-repellent and cell-adhesive biocompatible

materials have been developed and analyzed with a focus on the interactions between cells and the surface material. Generally, cells exhibit two distinct mechanisms that mediate cellular adhesion during the formation of focal adhesion complexes: (1) mechanical, through membrane projections; and (2) biochemical, induced through receptor-ligand binding. Both of these mechanisms are used when substrates are modified by both incorporation of surface microstructures and adsorption of adhesive ligands whereby maximum adhesion strength and motility responses were achieved, indicating the engagement of optimal tractional forces mediated by both structural and chemical cues.

Chemical methods for promoting cell adhesion include self-assembled monolayers (SAMs) [79-81], surface charge [83, 84, 87], and wettability [51, 93, 161]. SAMs have been used as surface chemical models to interpret the interactions of proteins and cells with artificial surfaces. The strength of cell adhesion to fibronectin (Fn)-coated SAMs decreases in the following order: OH > COOH = NH<sub>2</sub> > CH<sub>3</sub> [78]. The surface charge needed to immobilize cells is typically positive because nearly all cells are covered with negatively charged functional groups at a neutral pH [82]. A positively charged surface is created by coating chemical components (i.e., amine functional groups) [83, 87] or by applying DC electrical fields to the electrodes to temporarily capture cells (electrophoresis) [84]. Wettability has been commonly assessed to determine cell adhesion onto polymers, copolymers, and polymers treated by plasma, corona, or surface graft polymerization [51]. The representative physical method for promoting cell adhesion is surface roughness on the micro- [95, 162] or nanoscale [96].

Among the various cell adhesion methods, performance of cell adhesion on artificial surface decreases in the following order: wettability, surface charge, functional group, and surface roughness [49, 88, 92, 158, 159, 162-180].

#### **4.1.4 Wettability control for promoting cell adhesion**

The surface wettability of bio-artificial materials is one of the most important factors determining cell adhesion behavior. Surface hydrophilicity and hydrophobicity can be determined by measuring the water contact angle on the surface of the material. Measurement of the water contact angle is very simple and clearly indicates the comprehensive results for various chemical molecules and physical properties of the surface material. The water contact angle associate with moderate wettability for cell adhesion is in the range of 40–70° [51, 88], while extreme hydrophobicity or hydrophilicity of the surface inhibits cell adhesion [89-91].

#### **4.1.5 Mesoporous inorganic-organic hybrid resin**

Kim and colleagues [47, 158], recently reported a series of mesoporous inorganic-organic hybrid resins (HRs) that presented a good adhesion strength to various substrates, high stability against organic solvents, and good biocompatibility. HRs were synthesized for biocompatible poly(ethylene glycol)-dimethacrylate (PEG-DMA) to increase adhesion strength to various substrates with the help of silica-titania-based inorganic components. The wettability of HRs was adjusted by changing the molecular ratio of the inorganic components and the organic PEG-DMA component, which were combined with a silane coupling agent [158]. However, silane coupling agents are unstable in aqueous environments [181], and thus, the stability and function of HRs were guaranteed for just 3 weeks after synthesis.

#### **4.1.6 Dopamine**

For mussels (*Mytilus edulis*), permanent bio-adhesion to a surface in an aqueous environment is crucial for survival [see **Figure 4.1(a)**]. The byssus of the mussel, an adhesive organelle, consists of byssal thread and plaques (the distal adhesive pad). Byssal plaques firmly adhere to a surface and tether the organism to that surface. At least 5 specialized mussel adhesive protein (MAP) subtypes of byssal are known to contain the catecholic amino

acid DOPA (3,4-dihydroxy-L-phenylalanine, the precursor of dopamine) at concentrations ranging from a few mol% to 27 mol% [182, 183]. Polymers utilizing DOPA from MAPs demonstrated increasing adhesion strength of nanostructured pillars by 15-fold [184], good binding to organic polymers and various metal surfaces [185], and adhesive characteristics for even nonadherent cells [186].

#### **4.1.7 Dopaminergic mesoporous inorganic-organic hybrid resin**

In this study, a dopaminergic mesoporous inorganic-organic hybrid resin (HR-DOPA) was modified using dopamine from previous HRs [47, 158] for long-term stability and good cell adhesive characteristics. The surface roughness of HR-DOPA film was measured by atomic force microscopy (AFM) and determination of the water contact angle to verify the cell adhesion capabilities of the resin. HR-DOPA was also observed over a long-term period of two years.

## **4.2. Material and Methods**

### **4.2.1 Dopaminergic mesoporous inorganic-organic hybrid resin**

HR4-DOPA was kindly provided by Prof. Dong-Pyo Kim at Chungnam National University, South Korea. HR4-DOPA is one of a series of HR-DOPA materials created and is a derivative of HR4, made by replacing the catecholic salt with dopamine in chemical synthesis (**Table 4.1**). Among the various HR-DOPAs synthesized, HR4-DOPA was used in this study because it contained the largest amount of the organic compound (PEG-DMA), which lessens the brittleness of HR-DOPA and improves the microfabrication process. The chemical composition of HR-DOPA is shown in **Figure 4.1**.

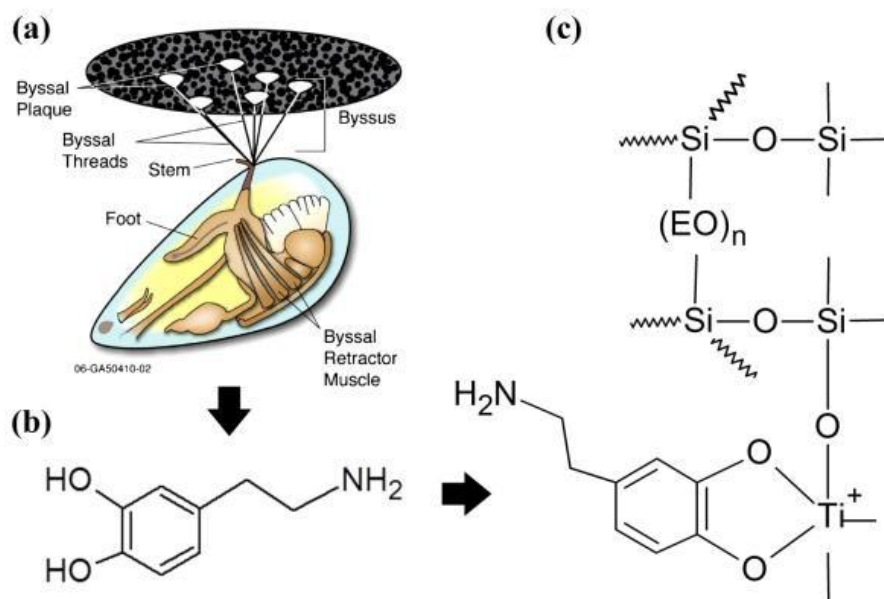


**Figure 4.1:** Synthesis of dopaminergic mesoporous inorganic-organic hybrid resins (HR-DOPAs).

- (a) Depiction of a mussel (*M. edulis*) attached by a byssus to various materials. Adapted from Springer Images.
- (b) Chemical structure of dopamine.
- (c) Chemical composition of the dopaminergic mesoporous inorganic-organic hybrid resin (HR-DOPA).

HR-DOPA synthesis was conducted as described by Chungnam National University as follows. Dopaminergic silica-titania ( $\text{SiO}_2\text{-TiO}_2$ ) hybrid materials were prepared by consecutive sol-gel-based reactions as follows. Tetraethylorthosilicate (TEOS) was prehydrolyzed in a 100:50 (v/v) ethanol:water solution containing HCl at  $60^\circ\text{C}$ . The nonionic triblock copolymer, Pluronic P123 ( $\text{EO}_{20}\text{PO}_{70}\text{EO}_{20}$ ), as a structure-directing agent, was dissolved in ethanol and added to the TEOS sols. Titania sols were prepared by mixing  $\text{TiCl}_4$  in an 80:20 (v/v) water:ethanol mixture at room temperature (RT). Inorganic silica-titania composite sols were prepared by mixing silica and titania sols at various ratios, followed by stirring for 2 h. As a hydrophilic, biocompatible generator, dopamine (4-(2-aminoethyl)benzene-1,2-diol), was subsequently added to the homogeneous silica-titania composite sol, and the solutions then instantly changed to a transparent orange color. Composite sols were composed at the TEOS: $\text{TiCl}_4$ :dopamine molar ratio of 1:0.1:0.05. For the preparation of

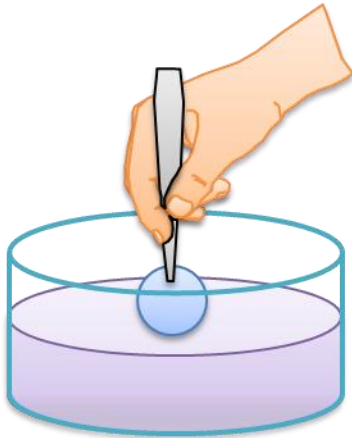
inorganic-organic hybrid resins, inorganic composite sols were mixed by stirring for 3 h with the desired amounts of 3-(methacryloyloxy) propyltrimethoxysilane (MPTMS; a silane coupling agent) and PEG-DMA (a hydrophilic component) as shown in **Table 4.1**.

**Table 4.1:** Chemical compositions of various dopaminergic mesoporous inorganic-organic hybrid resins.

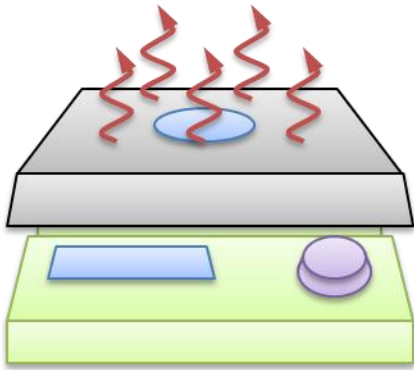
Samples	Molecular ratio HR-DOPA composition				
	TEOS	TiCl <sub>4</sub>	Dopamine	MPTMS	PEG-DMA
SR-DOPA	1	0.1	0.05	0	0
HR1-DOPA	1	0.1	0.05	0.08	0.042
HR2-DOPA	1	0.1	0.05	0.22	0.104
HR3-DOPA	1	0.1	0.05	0.44	0.208
HR4-DOPA	1	0.1	0.05	0.88	0.416

#### 4.2.2 Preparation of HR4-DOPA film

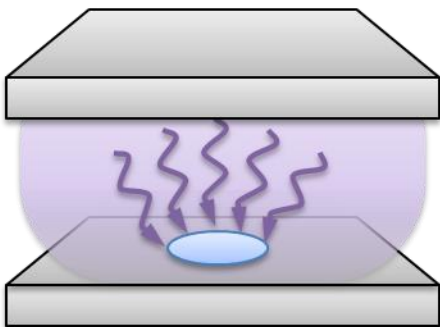
Borosilicate glass coverslips (Fisher Scientific, Germany; diameter, 22 mm) were cleaned by acetone and subsequently washed with ethanol and deionized (DI) water. The slides were then dried on a hotplate at 150°C for 10 min. HR4-DOPA was spun on the glass slide at 3000 rpm for 20 s using a spin-coater (BLE Laboratory Equipment GmbH, Germany) after oxygen plasma treatment at 200 W and 30 mbar for 25 s (Diener Electronic GmbH, Germany). These films were cured on a hotplate at 50°C for 5 h and subjected to postheat treatment at 100°C for 2 h, then immersed in ethanol for 2 h to remove the surfactants incorporated in the material [158] and dried at RT.



A. Cleaning Glass slide  
(Acetone → Ethanol → DI water).



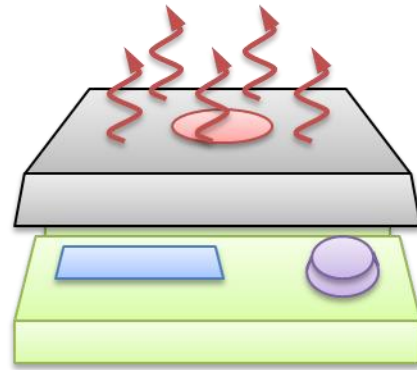
B. Dehydrating at 150°C for 10 min.



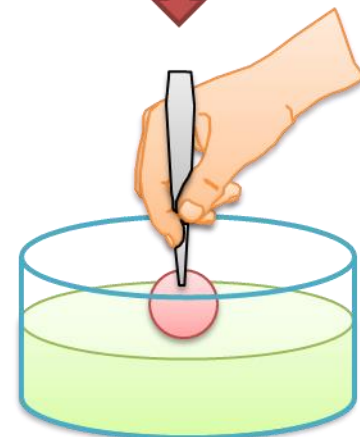
C. Oxygen plasma treatment at 200W  
and 30mbar for 25 s.



D. Spinning HR4-dopa at 3000 rpm  
for 20 s.



E. Thermal curing at 50°C for 5 h  
and 100°C for 2 h



F. Immersing HR4-dopa film in  
ethanol for 2 h

**Figure 4.2:** Fabrication process for HR4-DOPA film on glass slides. The glass slides were 22 mm in diameter.

### 4.2.3 Measurement of surface roughness

Surface roughness of the glass slides and the HR4-DOPA film were analyzed using an atomic force microscope (AFM; MobileS, Nanosurf AG, Switzerland). The substrates were probed in tapping and noncontact mode with a single crystal silicon tip (PPP-NCLR-10; Nanosensors AG, Switzerland) with a resonant frequency of approximately 155 kHz. The properties of the single crystal silicon chip are described in **Table 4.2**.

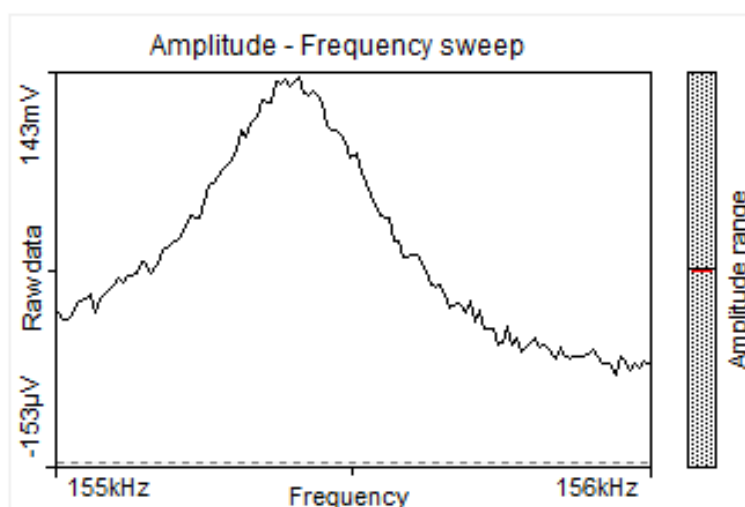


**Figure 4.3:** Resonance frequency of the cantilever with a single crystal silicon tip (PPP-NCLR-10).

**Table 4.2:** Properties of a single crystal silicon tip (PPP-NCLR-10).

Type	PPP-NCLR-10		
Product	POINTPROBE-PLUS <sup>®</sup> Silicon-SPM-Sensor		
Material	N*-Silicon (Resistivity: 0.01–0.02 Ω·cm)		
Cantilever dimension	Thickness	Length	Width
	7.1 ± 1 μm	225 ± 10 μm	38 ± 7.5 μm
Resonance Frequency	146 – 236 kHz		

Height and phase images (measured area, 1 × 1 μm<sup>2</sup>) of 3 different samples at 5 separate points were collected simultaneously (n = 15) and analyzed using Nanosurf MobileS software (version, 2.2.1.16). All roughness values, filtered by polynomial fit in this paper, referred to the root-mean square (RMS). The RMS of the surface was measured relative to the center

plane and was calculated by the following equation:

$$RMS = 1/L_x L_y \int_0^{L_y} \int_0^{L_x} [f(x,y)] dx dy \quad (4.1)$$

where  $f(x,y)$  was the surface relative to the center plane and  $L_x$  and  $L_y$  were the dimensions of the surface.

#### 4.2.4 Water contact angle goniometry of HR4-DOPA film

All sessile drop contact angle measurements were conducted at RT using a goniometer (DSA 10MK2, Krüss, Germany) equipped with a microliter syringe. The typical protocol involved using a constant drop volume (10 ml) of ultrapure water, which was gently deposited onto the surface and allowed to grow prior to slow needle retraction and image collection. Captured images were analyzed using Drop Shape Analysis (DSA1 V1.80, Krüss, Germany) to determine contact angles. All readings were performed immediately after sample preparation to minimize contamination. Average values and standard deviations (SDs) were obtained from 5 different measured values.

### 4.3. Results

#### 4.3.1 Surface roughness

The surface of the glass slide as a substrate for HR4-DOPA film was measured because the thin HR4-DOPA film follows the surface roughness of the glass. The average  $\pm$  SD surface roughness of the glass slides was  $446.00 \pm 128.06$  pm from 5 different points in 3 separate samples (see **Table 4.3**).

**Table 4.3:** Measured surface roughness (RMS) in a  $1 \times 1 \mu\text{m}^2$  area of the glass slide.

Glass slides	Sample 1	Sample 2	Sample 3
Point 1	729.00 pm	387.04 pm	545.23 pm
Point 2	770.59 pm	251.35 pm	452.73 pm
Point 3	600.15 pm	348.83 pm	298.30 pm
Point 4	346.69 pm	332.49 pm	538.78 pm
Point 5	377.35 pm	352.67 pm	358.83 pm

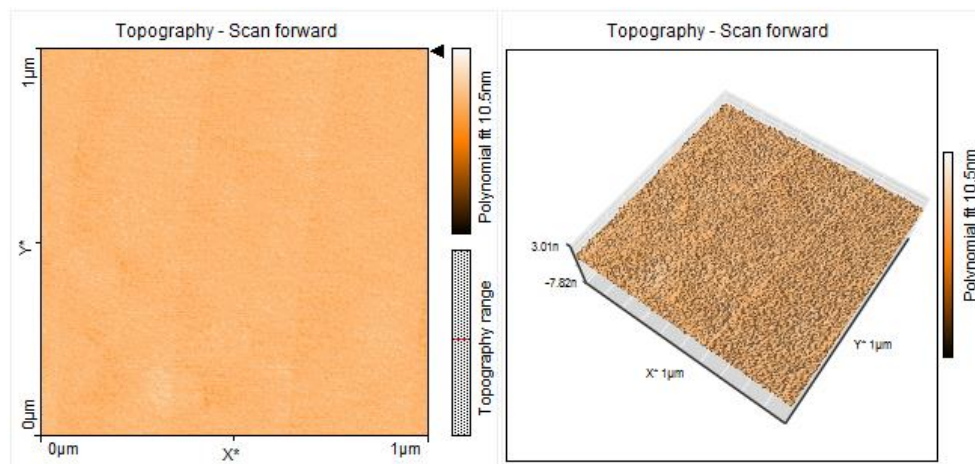


**Figure 4.4:** AFM images of pure white glass coverslips. The measured area was  $1 \times 1 \mu\text{m}^2$  in tapping and noncontact mode. The average ( $\pm$  SD) surface roughness was  $446.00 \pm 128.06$  pm.

The average ( $\pm$  SD) surface roughness of HR4-DOPA films coated on glass slides was  $789.35 \pm 141.56$  pm, as shown in **Table 4.4**. Surface roughnesses of HR4-DOPA remained below 1 nm despite being increased by 77.0% compared to the glass coverslip.

**Table 4.4:** Measured surface roughness (RMS) in a  $1 \times 1 \mu\text{m}^2$  area of the HR4-DOPA film.

HR4-DOPA	Sample 1	Sample 2	Sample 3
Point 1	795.71 pm	1295.1 pm	739.91 pm
Point 2	842.61 pm	1027.5 pm	719.94 pm
Point 3	835.96 pm	551.11 pm	588.45 pm
Point 4	795.45 pm	713.69 pm	994.79 pm
Point 5	690.87 pm	677.16 pm	568.01 pm

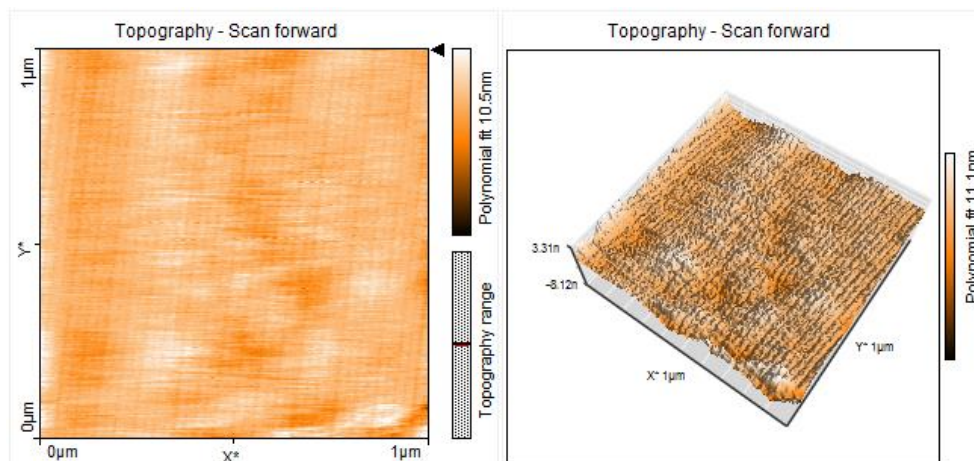


**Figure 4.5:** AFM images of the HR4-DOPA film on the glass coverslip. The measured area was  $1 \times 1 \mu\text{m}^2$  in tapping and noncontact mode. The average ( $\pm$  SD) surface roughness was  $789.35 \pm 141.56 \text{ nm}$ .

### 4.3.2 Water contact angle of HR4-DOPA film

The water contact angle of HR4-DOPA film was examined in order to determine whether the film was applicable for cell adhesion in terms of wettability. Since values can decrease gradually as water droplets evaporate, all measurements were conducted immediately (i.e.,  $< 10 \text{ s}$ ) after dropping the water droplet on the surface. The average ( $\pm$  SD) water contact angle was  $62.08^\circ \pm 1.90^\circ$  (see **Figure 4.6**). The value was similar to that of polydopamine [187] and demonstrated that HR4-DOPA has lower wettability than HR4 ( $49^\circ$ ) [158]. The wettability of HR4-DOPA was in the range of moderate wettability for cell adhesion: i.e.,  $40\text{--}70^\circ$  [51, 88].

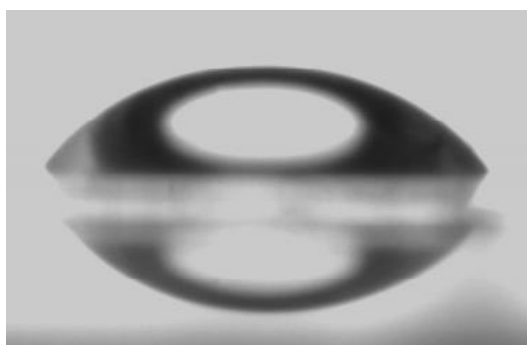


**Figure 4.6:** The water contact angle (sessile drop) of HR4-DOPA was  $62.08^\circ \pm 1.90^\circ$  at room temperature. The water volume was 10  $\mu\text{l}$ .

### 4.3.3 Long-term stability of HR4-DOPA

The stability of a silane coupling agent (MPTMS) in the different mesoporous inorganic-organic resins of HR4 and HR4-DOPA was observed for two years. **Figure 4.7** shows the different conditions for HR4 and HR4-DOPA, which contain catecholic salt and catecholic amine (dopamine), respectively, that were kept for two years at 8°C after synthesis. The formation of cross-linked silane aggregates – islands – was observed in HR4 (**Figure 4.7**, left) due to direct attachment by individual molecules to surface hydroxyl groups of MPTMS in HR4 [49]. However, HR4-DOPA exhibited a clear, stable state after long-term storage, suggesting that dopamine prevents MTPMS from forming cross-linked silane aggregates in HR4-DOPA.

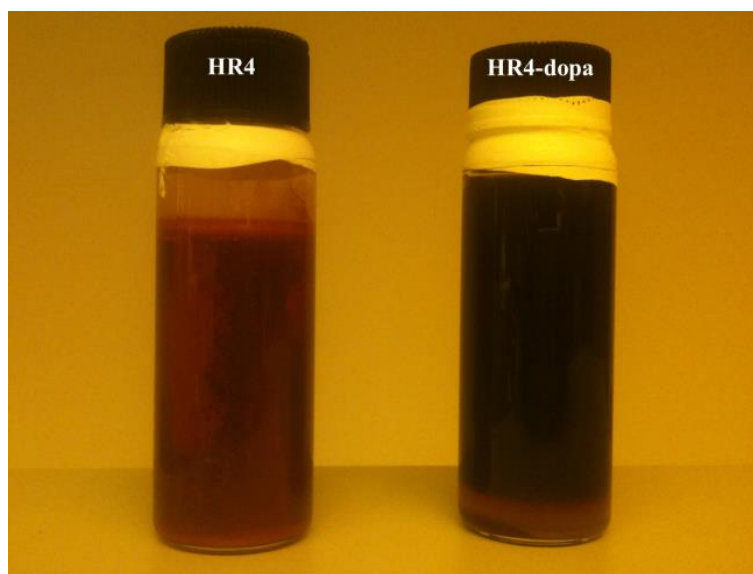


**Figure 4.7:** Comparison of the stability of MPTMS in HR4 and HR4-DOPA over time. Both resins were kept in vials at 8°C for two years after synthesis without being opened. The formation of cross-linked silane aggregates – islands – was observed in HR4 (left), while HR4-DOPA remained clear and stable for a long period of time.

## 4.4. Discussion

### 4.4.1 Surface roughness of HR4-DOPA

Surface roughness on the nanometer-scale regulates cell adhesion behaviors and cell

phenotypes [96, 188, 189]. The optimal surface roughness ranged from 10–30 nm (RMS) for cell adhesion [96, 188]. HR4-DOPA films appeared smooth, even on the subnanometer scale, indicating that the effect of HR4-DOPA surface roughness on cell adhesion was insignificant. In future applications, surface treatment with HR4-DOPA can be used to create the optimal surface roughness for cell adhesion.

#### **4.4.2 Long-term stability of HR4-DOPA**

Water, ethanol, and acid are essential for the sol-gel process in synthesizing silica-based inorganic-organic hybrid materials as well as HR4-DOPA [190]. Moreover, inorganic and organic components were hybridized by silane coupling agents, which are unstable in aqueous environments [181, 190]. Hamming *et al.* [191] utilized a DOPA-initiator instead of a silane coupling agent for improving the stability and interfacial adhesion of inorganic-polymer composites. Although a small amount of dopamine (1.03 mol%) was found in HR4-DOPA, the long-term stability of the resin was indicated by its ability to stabilize a silane coupling agent in an aqueous environment over a 2-year period. However, a more detailed chemical analysis is required to explain the effects of the dopamine found in HR4-DOPA on the long-term stability of the resin.

#### **4.5. Conclusion**

This study investigated the surface roughness and wettability of a dopaminergic mesoporous inorganic-organic hybrid resin (HR4-DOPA) to determine its capacity for cell adhesion. HR4-DOPA was also modified by dopamine instead of a catecholic salt in order to stabilize a silane coupling agent in previous mesoporous inorganic-organic hybrid resins. The average surface roughness of HR4-DOPA was 789.35 pm, indicating that this material is smooth and would exert insignificant effects on cell adhesion. Surface treatment with HR4-DOPA can be used to create the optimal surface roughness for cell adhesion. The water

contact angle of HR4-DOPA was  $62.08^\circ$ , indicating a moderate wettability for cell adhesion. The stability of a silane coupling agent in HR4-DOPA was observed over a long-term storage period of 2 years, but a more detailed chemical analysis is required in order to explain the effects of the dopamine found in HR4-DOPA on the long-term stability of the resin.

# Chapter 5. Biocompatibility of dopaminergic inorganic-organic hybrid resin film

## 5.1. Introduction

### 5.1.1 Cell adhesion assay

The analysis of cell adhesion is an essential part of cell biology. Cell survival is dependent on proliferation, migration, and communication via cell-cell and cell-matrix interactions, and cellular adhesion is the first step in these processes [192]. Cell adhesion is dominated by the chemical or/and physical properties of the substrates [193, 194], and thus, cell adhesion assays are utilized for studying cell-substrate interactions as well as the biocompatibility of new biomaterials for microcellular applications [52, 195, 196]. Quantification of cell adhesion can be performed using several methods: by manually counting the number of adhered cells per unit area [193, 197], by colorimetric or fluorometric detection [198], or by measuring the depletion of a variety of extracellular matrix proteins in the medium [199].

#### 5.1.1.1 Cell adhesion

Cells continually communicate with their extracellular environment and respond to specific signals. A large number of receptors, channels, and cell adhesion molecules (CAMs) that mediate specific cellular interactions are embedded in the phospholipid bilayer of the cell membrane [200], as shown in **Figure 5.1**, and these play a significant role in cell adhesion.

A transmembrane protein (TP), which is a specific CAM, is a protein that goes from one side of a membrane through to the other side. TPs include proteins such as integrins, cadherins, and selectins. They interact with their specific ligands, which are located either in the extracellular matrix (ECM) surrounding cells or are embedded in the cell membrane of

other cells and establish a close contact between them. Each of these adhesion molecules has a different function and recognizes different ligands. Cadherins are named for “calcium-dependent adhesion” molecules and mediate calcium ( $\text{Ca}^{2+}$ )-dependent homophilic cell-cell adhesion [201]. Selectins mediate the initial attachment of leukocytes to venular endothelial cells prior to their firm adhesion and diapedesis at sites of tissue injury and inflammation [202]. Integrins are heterodimers with variable  $\alpha$  and  $\beta$  subunits that usually mediate cell-matrix adhesions [203, 204], as shown in **Figure 5.2**.

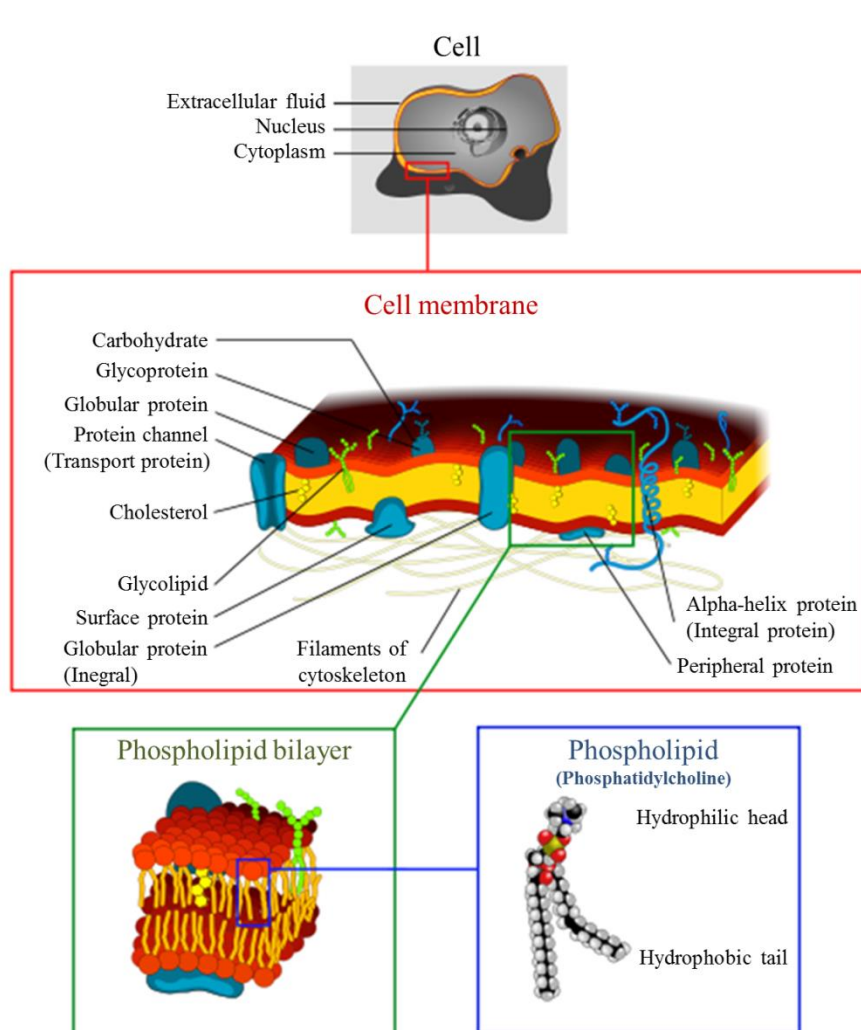


**Figure 5.1:** Structure of the cell membrane. The cell membrane is composed of a phospholipid bilayer, which is embedded with a large number of receptors, channels, and cell adhesion molecules. This depiction of the cell membrane was adapted from Wikipedia.

([http://commons.wikimedia.org/wiki/File:Cell\\_membrane\\_detailed\\_diagram\\_3.svg#filelinks](http://commons.wikimedia.org/wiki/File:Cell_membrane_detailed_diagram_3.svg#filelinks)).

The extracellular domains of integrin receptors bind to ECM glycoproteins (e.g., fibronectin, collagen, or laminin), whereas the intracellular domains of integrin receptors interact with the actin cytoskeleton [203].

Here, we will discuss two types of cell adhesion: focal adhesions and hemidesmosomes. Hemidesmosomes prefer keratin-associated adherence, while actin-associated adherence is observed in focal contacts.

### 5.1.1.1.1 Focal adhesion

Once the integrin is bound to fibronectin, the cell forms focal adhesions near the periphery. Focal adhesions are large and robust attachment sites containing a large number of proteins, and they serve to integrate the extracellular matrix with the actin cytoskeleton [205].

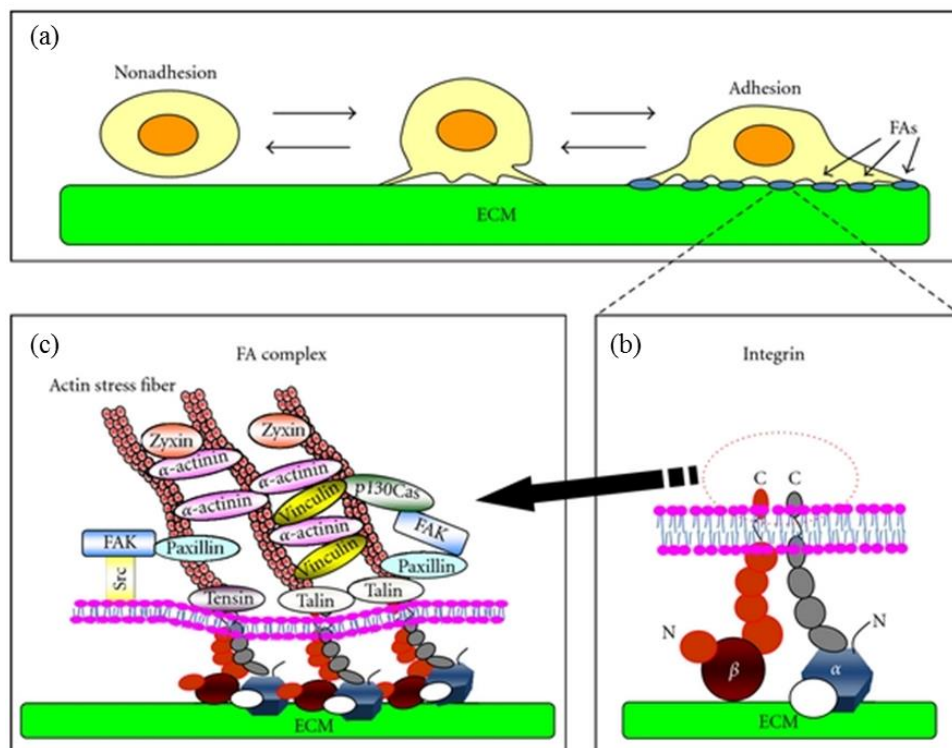


**Figure 5.2:** Integrin-mediated focal cell adhesion to the extracellular matrix (ECM) [204].

- (a) Suspended cells adhere to the surface of the ECM via integrins. Some of the nascent adhesion contacts grow and form mature focal adhesions.
- (b) Integrins function as a heterodimer composed of  $\alpha$ - and  $\beta$ -chains.
- (c) The cytoplasmic portions of integrins recruit multiple cellular proteins and form cross-linked platforms to regulate both the actin cytoskeleton and signal transduction.

Focal adhesion proteins act as linkers between the integrin receptors and the cytoplasmic actin cytoskeleton [206]. In addition, integrins recruit several structural and signaling molecules such as the focal adhesion kinase (FAK). The accumulated FAK is phosphorylated and initiates signal transduction cascades such as tyrosine phosphorylation, creating docking sites for other signaling proteins [203, 205]. After building these focal adhesions, the cells start spreading. Therefore, the integrin-mediated cell adhesions provide dynamic bidirectional links between the ECM and the cytoskeleton [207].

#### **5.1.1.1.2 Hemidesmosomal adhesion**

Hemidesmosomes are a type of specialized integrin-mediated adhesion. In contrast to desmosomes, which are cadherin-mediated cell-cell contacts, hemidesmosomes are cell-matrix contacts that connect the basal lamina (i.e., a special form of the ECM) with epithelial cells (**Figure 5.3**) [208, 209]. The basal lamina is composed of the lamina lucida and the underlying lamina densa, both of which mainly consist of proteins such as collagen and laminin. The anchoring filaments (i.e., sub-basal lamina fibrous components) connect the hemidesmosomes with the lamina densa. Additionally, anchoring fibrils spread from the basement membrane along the dermal edge of the lamina densa. These anchoring fibrils either (1) loop back and reinsert into the lamina densa or (2) extend perpendicularly from the basement membrane and insert into the anchoring plaques of the hemidesmosomes, which are electron-dense condensations at the ends of anchoring fibrils, together with other associated constituents of the basal lamina [210, 211]. The intracellular domains of integrin receptors embedded in the membrane of the epithelial cells connect with the keratin filament network, while their extracellular domains connect with laminin-anchoring filaments of the basal lamina to establish hemidesmosomes [212]. This hemidesmosomal adhesion, consisting of the hemidesmosomal plaque, anchoring filaments, and fibrils, provides stable adherence of the epithelial cell to the basal lamina [213].

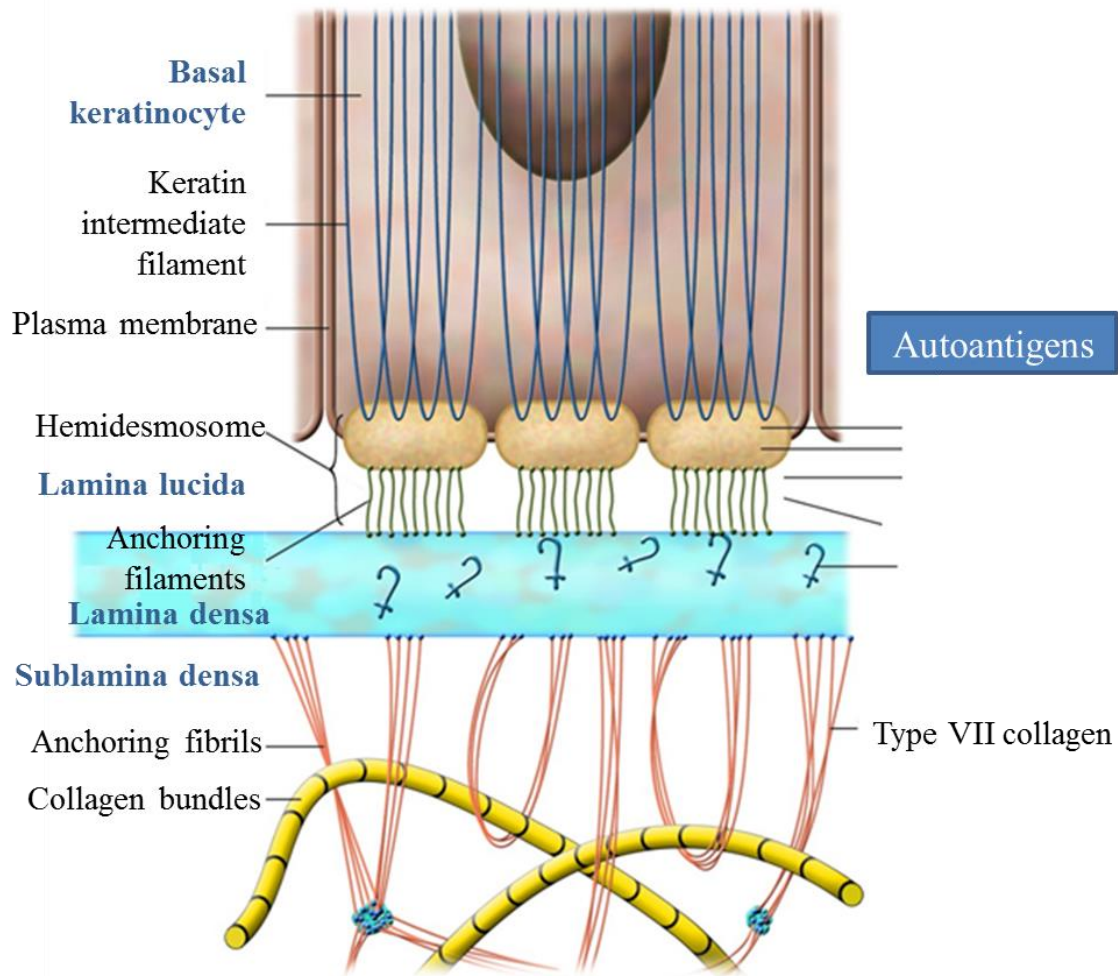


**Figure 5.3:** Schematic showing the major components of hemidesmosomes in epithelial cells [209].

Basal keratinocytes adhere to the basement membrane by the interaction of cytoplasmic and transmembranous components of hemidesmosomes, such as BP230, BP180, and  $\alpha_6\beta_4$  integrin, with ligands such as laminin 5 located in the lamina lucida and lamina densa of the dermoepidermal basement membrane.

### 5.1.1.2 Cell spreading and migration

Integrin-mediated signaling events in focal adhesions contribute to stable cell spreading, migration, survival, proliferation, and differentiation [214], while hemidesmosomes cause stable anchorage of epithelial cells to maintain a migration direction during wound healing [215]. **Figure 5.4** shows integrin-mediated cell spreading and migration.

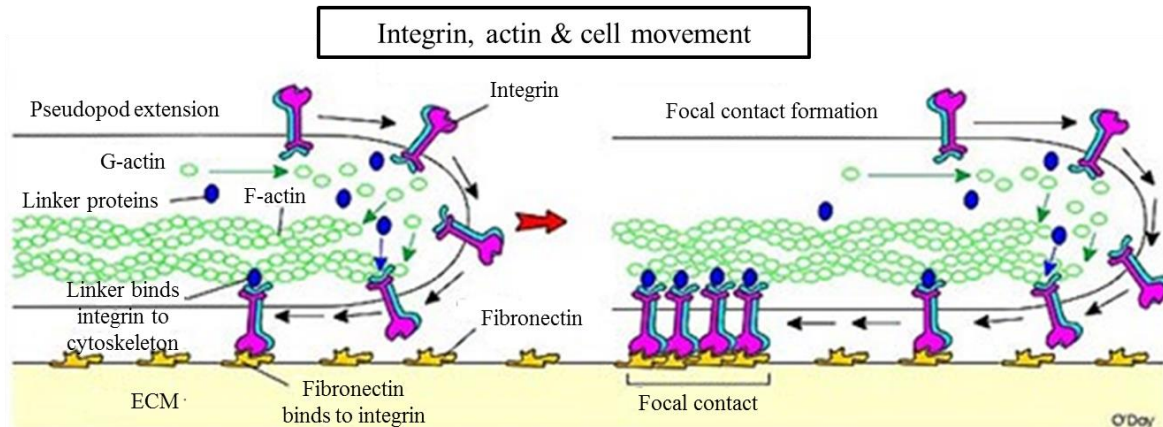


**Figure 5.4:** Integrin-mediated cell spreading and migration.

G-actin polymerizes to F-actin at the leading edge of the cell (pseudopod). Integrin-fibronectin binding allows linkers to bind integrins to F-actin. Clustering of integrin-fibronectin forms strong focal adhesion plaques. Contraction of actin (interacting with myosin) allows the cell to be pulled forward. The depiction was adapted from a web site of the University of Toronto. (<http://www.erin.utoronto.ca/~w3bio315/lecture13.htm>)

### 5.1.2 Cell viability assay

Cell viability assays are an essential tool for determining viable or dead cells in cell-based studies to evaluate the efficacy of anticancer compounds in drug screening or the effect of new biomaterials on cells. Cell viability is assessed by directly counting the number of healthy cells or by measuring a chemical indicator of healthy cells in cell populations [216-221]. The reagents widely used as chemical indicators are 3-(4,5-dimethylthiazol-2-yl)-2,5-diphenyl-2H-tetrazolium bromide (MTT), 2,3-bis-(2-methoxy-4-nitro-5-sulfo-phenyl)-2H-tetrazolium-5-carboxanilide (XTT), and 5-bromo-deoxyuridine (BrdU) [218]. The MTT assay is based on the metabolism of the yellow tetrazolium salt MTT by mitochondrial dehydrogenases of active cells into blue formazan crystals [219]. The XTT assay uses water-soluble orange XTT crystals whose optical density (OD) can be measured directly by an enzyme-linked immunosorbent assay (ELISA) reader, without any preceding solubilization [220]. The BrdU assay is based on the incorporation of BrdU as a pyrimidine analogue in place of thymidine into the newly synthesized DNA of proliferating cells. BrdU is then detected by a monoclonal anti-BrdU-antibody [221].

### **5.1.3 Biocompatibility of dopaminergic inorganic-organic hybrid resin films**

In this study, we analyzed the biocompatibility of dopaminergic inorganic-organic hybrid resin (HR4-DOPA) with respect to the growth and proliferation of HeLa cells. We used cell adhesion and cell viability assays to investigate the applicability of the HR4-DOPA film for an isolated single-cell array. The cell adhesion assay was performed by manually counting the adhered HeLa cells per unit area of 1 mm<sup>2</sup> in the time-lapse format for 6 h. The HeLa cell adhesion on HR4-DOPA was compared with the adhesion on mesoporous inorganic-organic hybrid resin (HR4), ECM proteins (i.e., collagen IV and fibronectin), and glass. The viability of HeLa cells on HR4-DOPA was measured using the XTT assay after 2-d incubation.

## **5.2. Materials and Methods**

### **5.2.1 Culture of HeLa cells**

HeLa cells (Deutsche Sammlung für Mikroorganismen und Zellkulturen GmbH [DSMZ], Germany) were cultivated in an incubator at 37°C and 5% CO<sub>2</sub>. In all the experiments, we used RPMI 1640 medium (PAN Biotech GmbH, Germany) supplemented with 10% FBS (Sigma-Aldrich) and 2% penicillin/streptomycin (Sigma-Aldrich). Confluent cultures of HeLa cells were passaged 1:3 (v/v) every 3 d, using a trypsin/EDTA solution (Sigma-Aldrich) for 5 min in an incubator at 37°C and 5% CO<sub>2</sub>. The cells were washed 3 times with 400 µl PBS to remove trypsin after centrifugation for 3 min at 200 × g. HeLa cells were subsequently resuspended in growth medium to achieve a seeding density of 1 × 10<sup>6</sup> cells/80 cm<sup>2</sup>..

### **5.2.2 Preparation of HR4-DOPA and HR4 film**

HR4-DOPA was kindly provided by Prof. Dong-Pyo Kim from Chungnam National University, South Korea. HR4-DOPA is a derivative of HR4 and is prepared by replacing

catecholic salt with dopamine during chemical synthesis. We used HR4-DOPA and HR4, which were from the series of HR-DOPAs (HR1-4-DOPA) and HRs (HR1-4), respectively, because they contained the largest amount of the organic compound (PEG-DMA), which lessens the brittleness and improves the microfabrication process. HR4-DOPA and HR4 had a TEOS:TiCl<sub>4</sub>:MPTMS:PEG-DMA:dopamine (for HR4-DOPA) or catecholic salt (for HR4) molar ratio, respectively, of 1:0.1:0.88:0.416:0.05 [158].

Borosilicate glass coverslips (Fisher Scientific, Germany; diameter, 22 mm) were cleaned by acetone and subsequently washed with ethanol and deionized water. The slides were then dried on a hotplate at 150°C for 10 min. HR4-DOPA was spun on the glass slide at 3000 rpm for 20 s by using a spin-coater (BLE Laboratory Equipment GmbH, Germany) after oxygen plasma treatment at 200 W and 30 mbar for 25 s (Diener Electronic GmbH, Germany). These films were cured on a hotplate at 50°C for 5 h and subjected to post-heat treatment at 100°C for 2 h, immersed in ethanol for 2 h to remove the surfactants incorporated in the material [158], and dried at room temperature (RT).

### **5.2.3 Cell adhesion assay**

In preparation for the cell adhesion assay, the adhered HeLa cells were first detached using trypsin/EDTA. The HeLa cell suspension was then washed 3 times with 400 µl PBS and diluted in PBS to achieve a concentration of  $5 \times 10^5$  cells/ml. The HeLa cell concentration was measured 3 times for each trial by using a CASY cell counter (CASYton; Schärfe System GmbH, Germany). The HeLa cell adhesion assay on HR4-DOPA was compared with HR4, rat-tail collagen IV (Sigma-Aldrich), human fibronectin (Sigma-Aldrich), and glass (Fisher Scientific, Germany). All the substrates had a diameter of 22 mm.

The glass slides were sterilized by immersion in ethanol for 5 min and drying at RT. The prepared substrates were put into an untreated polystyrene (PS) 6-well plate (BD Biosciences) and positioned at the center of the well. Subsequently,  $3.0 \times 10^6$  HeLa cells in 3 ml medium

were seeded into each well. The samples were cultured at 37°C and 5% CO<sub>2</sub> for 15 min, 30 min, 45 min, 1 h, 3 h, or 6 h. After incubation, non-adherent cells were carefully rinsed with PBS 3 times (see **Figure 5.5**).

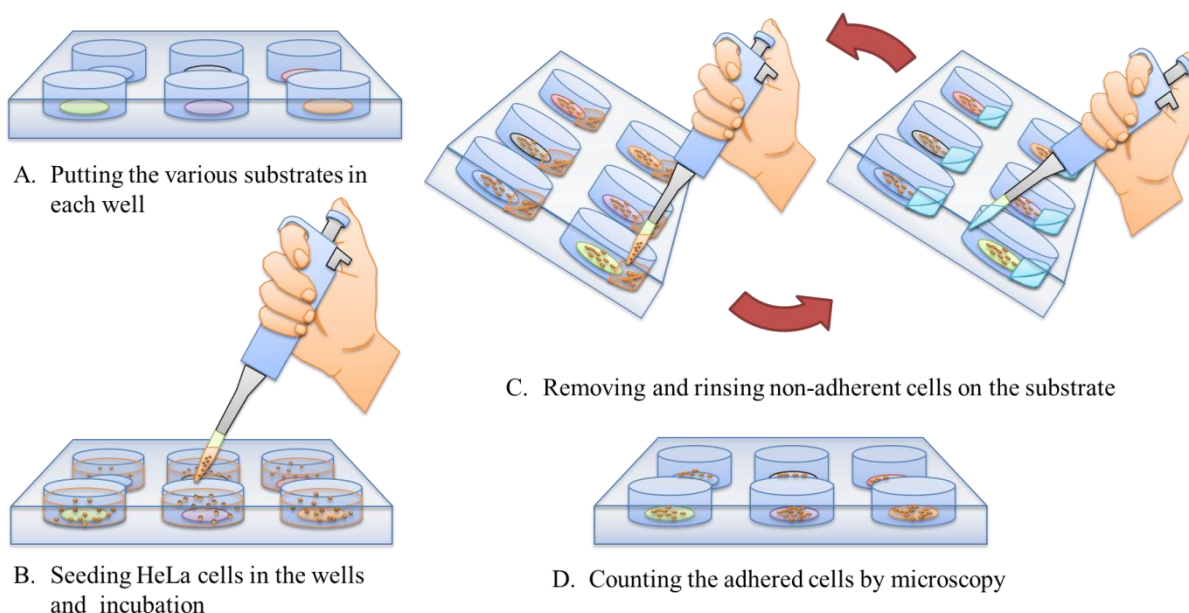


**Figure 5.5:** Procedure for the HeLa cell adhesion assay.

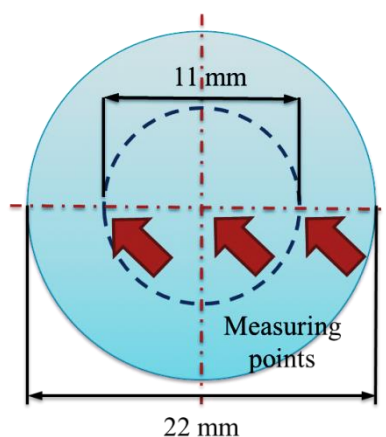


**Figure 5.6:** Observation points for the HeLa cell adhesion assay. The adhered HeLa cells were manually counted in 3 different view fields (0.48 mm<sup>2</sup>) from each sample using the grid function. The left/right observing point is 11 mm away from the center of the sample.

Images from 3 different view fields ( $\times 10$  objectives; area, 0.48 mm<sup>2</sup>) were acquired from each sample by using a semi-confocal microscope (IX70, Olympus) mounted with a CCD camera (Olympus soft imaging systems, F-View), using the grid function of the cell

software package (Olympus). The average number of adhered cells was calculated per millimeter square of the image area. All the values indicate the average and the standard error of the mean (SEM).

HeLa cell viability on HR4-DOPA was examined using an XTT cytotoxicity assay kit (Sigma-Aldrich), and the viability was compared with that on HR4. The HR4-DOPA- or HR4-coated substrates were put into an untreated PS 6-well plate. HeLa cells in 2 ml medium were seeded into each well at a cell concentration of  $2.0 \times 10^6$  cell/ml and were subsequently incubated for 48 h at 37°C and 5% CO<sub>2</sub>. After incubation, XTT reagent (400 µl) was added to each well, and the plate was incubated for 8 h. The XTT dye solution (200 µl) was transferred from each sample to a 96-well plate. The light absorbance of each sample was measured 3 times by using an ELISA reader (Tecan Sunrise Plate Reader; Tecan Group Ltd., Switzerland) at a wavelength of 450 nm. The XTT reagent is colorless but is converted to a brightly colored molecule by the cell's metabolism, and its light absorbance increases according to the cell viability. We used HeLa cells incubated in a well without any substrate as a control; any reduction in the light absorbance indicated reduction in cell viability.

#### **5.2.4 Statistical analysis**

All statistical computations were performed with the GraphPad Prism 5 software (GraphPad Software Inc., USA). We compared cell adhesion and cell viability on HR4-DOPA with that on other substrates. One-way analysis of variance (ANOVA) with  $P \leq 0.05$  was considered to be significant, and pairwise comparisons between the substrates were conducted using the Tukey-Kramer test with a significance level of 0.05.

### **5.3. Results**

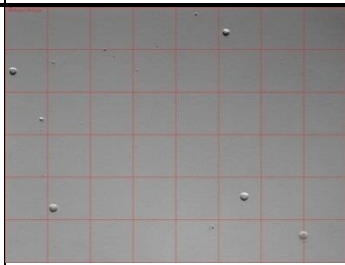
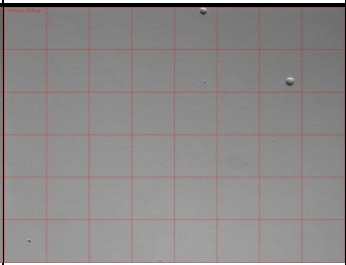
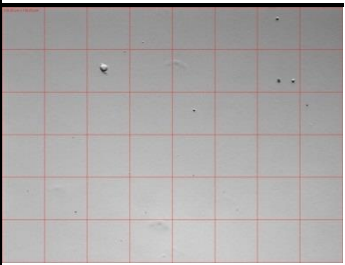
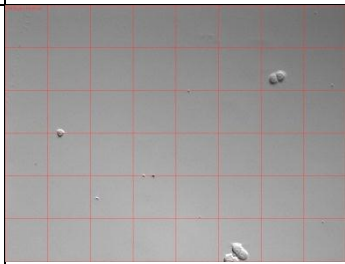
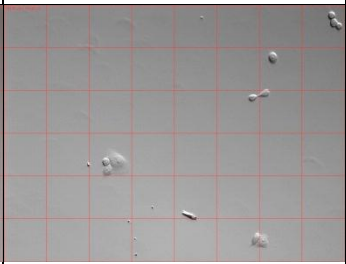
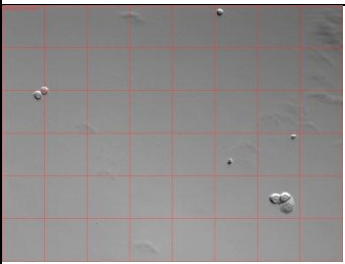
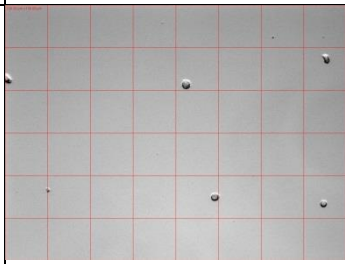
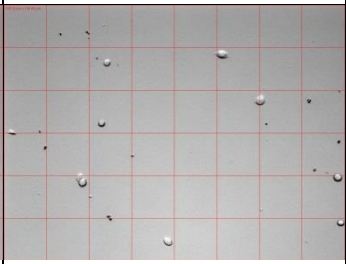
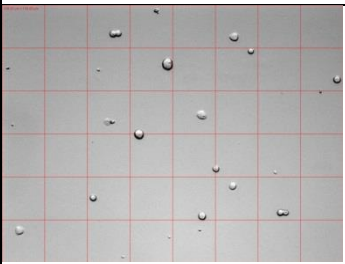
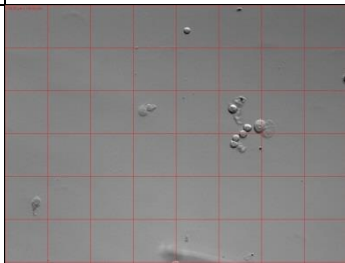
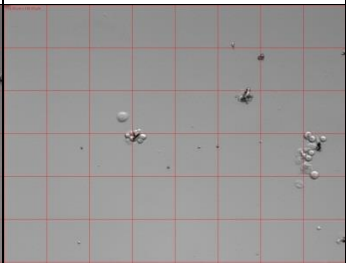
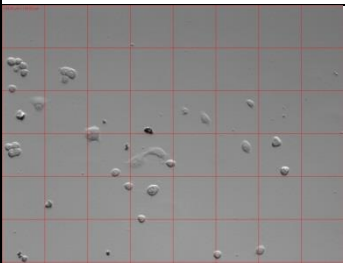
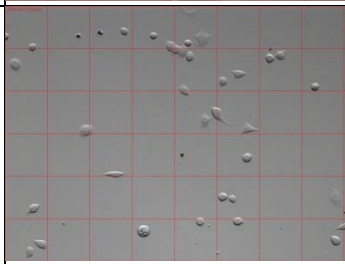
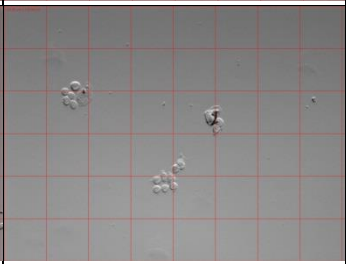
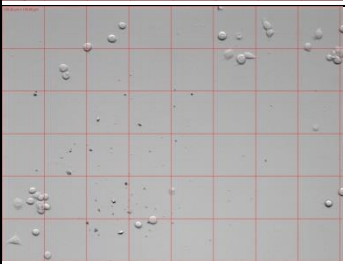
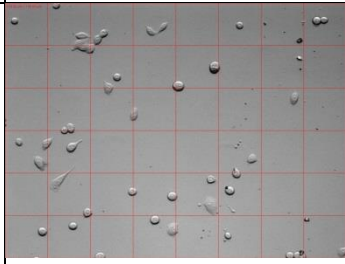
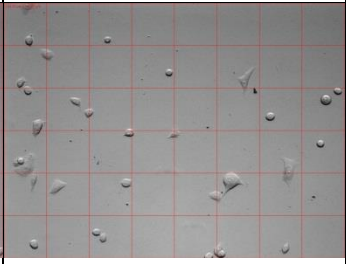
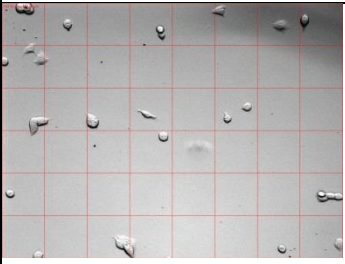
#### **5.3.1 HeLa cell adhesion assay**

HeLa cells were used to study the cell adhesion behaviors on the HR4-DOPA surface

because of their biological value for cancer treatment and their robust adherence to surfaces that are rendered hydrophilic through the use of microtechniques such as O<sub>2</sub> plasma treatment or deposition of self-assembled monolayers (SAMs) [39-42, 143]. HeLa cell adhesion was monitored by counting the cells adhered on HR4-DOPA in 3 different view fields after incubation for 15 min, 30 min, 45 min, 1 h, 3 h, and 6 h. The maximum incubation time was 6 h because HeLa cell populations exhibited insignificant growth for the first 6 h of incubation, with only a 9% increase in the number of cells. The cell morphological features at each time point are shown in **Table 5.1**. HeLa cells firmly adhered to HR4-DOPA and spread out on the surface. A larger number of adhered cells were observed as the incubation time increased.

The HeLa cell adhesion behavior on HR4-DOPA was compared with that on HR4 to determine the effect of dopamine versus catecholic salt on cell adhesion. ECM proteins (i.e., collagen IV and fibronectin) and glass were used as controls for cell adhesion. Collagen IV and fibronectin are cell-adhesive ECM proteins and have been used to biologically modify surfaces in order to control cell functions such as adhesion, proliferation, and differentiation [222]. Glass was also used as a control because it has been shown to have a low cell adhesion strength and is commonly used to verify the improved cell adhesive characteristics of a new biomaterial [223]. The choice of control substrates was based on the cell adhesion assay of Yamamoto *et al.* [223]. **Table 5.2** shows the morphological features of HeLa cells adhered on the controls after each time point. One of the 3 different view fields has been shown for each sample.

**Table 5.1:** Morphological features of the adhered HeLa cells on HR4-DOPA. The grid size is  $100 \times 100 \mu\text{m}^2$ .

HR4-DOPA	Left point	Center point	Right point
15 min			
30 min			
45 min			
1 h			
3 h			
6 h			

**Table 5.2:** Morphological features of HeLa cell adhered on the control substrates. The grid size is  $100 \times 10 \mu\text{m}^2$ .

	HR4	Collagen IV	Fibronectin	Glass
15 min				
30 min				
45 min				
1 h				
3 h				
6 h				

The average number ( $\pm$  SEM) of the HeLa cells adhering to the substrates is summarized in **Table 5.3** and graphically shown in **Figure 5.7**.

**Table 5.3:** The number of HeLa cells per millimeter square adhering to the various substrates. The values indicate the mean  $\pm$  SEM values from the 3 different view fields on the sample (n = 3).

Time	HR4-DOPA	HR4	Collagen IV	Fibronectin	Glass
15 min	5.56 $\pm$ 1.08	27.78 $\pm$ 4.48	15.97 $\pm$ 0.62	3.47 $\pm$ 0.31	0.69 $\pm$ 0.31
30 min	15.97 $\pm$ 1.54	54.17 $\pm$ 4.63	27.08 $\pm$ 0.46	4.86 $\pm$ 0.31	2.08 $\pm$ 0.46
45 min	20.19 $\pm$ 2.47	52.78 $\pm$ 6.17	53.47 $\pm$ 4.48	4.86 $\pm$ 0.77	2.78 $\pm$ 0.62
1 h	46.53 $\pm$ 4.48	60.42 $\pm$ 6.02	77.08 $\pm$ 5.09	10.42 $\pm$ 1.85	8.33 $\pm$ 1.39
3 h	61.81 $\pm$ 5.40	168.06 $\pm$ 14.04	216.67 $\pm$ 7.41	83.33 $\pm$ 2.78	44.44 $\pm$ 2.93
6 h	71.53 $\pm$ 4.94	313.20 $\pm$ 9.57	275.00 $\pm$ 8.80	377.08 $\pm$ 26.39	395.14 $\pm$ 34.41

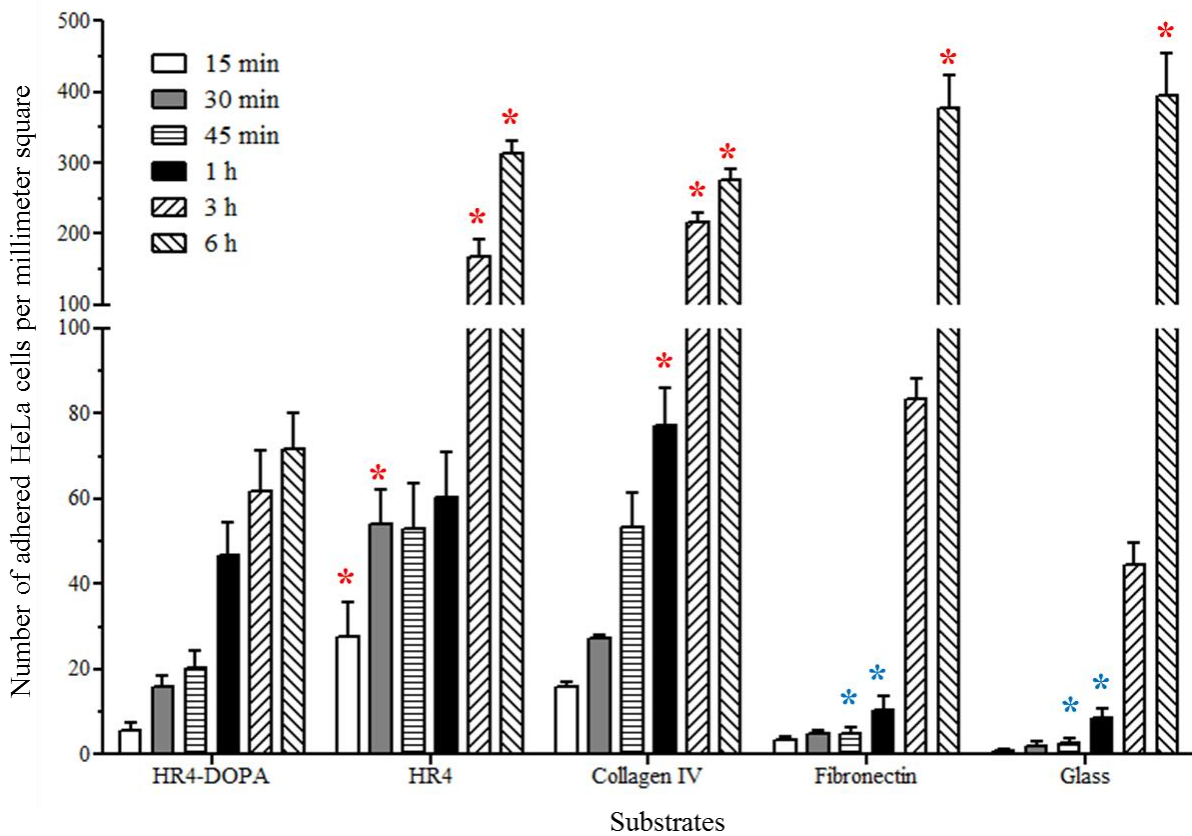


**Figure 5.7:** The number of adhered HeLa cells at various incubation times on dopaminergic mesoporous inorganic-organic hybrid resin (HR4-DOPA), mesoporous inorganic-organic hybrid resin (HR4), ECM protein layers (collagen IV and fibronectin), and glass. The cells were incubated at a concentration of  $1.0 \times 10^6$  cells/ml in 3 ml RPMI 1640 medium with 10% FBS at 37°C. The values indicate the average number of the adhered HeLa cells per millimeter square, and the vertical bars indicate the standard error of the mean (SEM). The asterisks (\*) indicates a significant (P value  $\leq$  0.05) difference between HR4-DOPA and the controls. The red asterisks show that cell adhesion on the indicated substrate is significantly higher than on HR4-DOPA, while the blue asterisks show that adhesion is significantly less than on HR4-DOPA.

HeLa cells began to adhere to all substrates even after a short period of incubation, and the population gradually increased over time. Comparison with the controls showed that both HR4 and collagen IV demonstrated a strong adhesion behavior at all time points, while the number of cells remained low for 1 h on fibronectin and for 3 h on glass, and then dramatically increased.

As a reference, HeLa cell harvest density – the maximum number of adhering and spreading HeLa cells in a unit area – is approximately 625 cells/mm<sup>2</sup>, based on the spreading area of 1600 ± 500 μm<sup>2</sup> of the cells when adhered to the substrate [146]. In cell adhesion assays, the HeLa cell concentration cannot exceed the harvesting density because over-proliferated cells are eliminated by self-destruction mechanisms like apoptosis, during which cells develop abnormal phenotypes [151]. Among all the substrates tested, the maximum number of adherent HeLa cells was ~395 cells/mm<sup>2</sup> (i.e., 60.7% of the harvest density) on the glass substrate after 6 h.

On the HR4-DOPA film, the number of adhered HeLa cells increased until 1 h, after which the growth rates remained low. Therefore, the HeLa cells on HR4-DOPA were significantly lower in number than on HR4 after 3 h, collagen IV after 1 h, and all controls at 6 h. HR4-DOPA and HR4 share the same chemical compositions, with dopamine in place of the catecholic salt in HR4; however, we found a significant difference between the number of cells adhered to HR4-DOPA and HR4 after 3 h of incubation ( $P \leq 0.05$ ). The number of cells adhered to HR4-DOPA was comparable to that for collagen IV at 45 min and fibronectin at 1 h ( $P > 0.05$ ). HR4-DOPA showed a better cell adhesion performance than glass until 3 h, but the result was only significant at 45 min and 1 h. In contrast, glass exhibited significantly higher cell adhesion than HR4-DOPA at 6 h.

### **5.3.2 HeLa cell viability assay**

The viability of HeLa cells on HR4-DOPA was assessed using XTT *in vitro* toxicology

assays after disturbance-free incubation for 48 h and was compared to viability on HR4, whose biocompatibility had been previously proved by implanting an HR4-coated poly(ethylene terephthalate) (PET) disc in mice for 12 weeks [158]. **Table 5.4** shows the light absorbance in the XTT assay of the samples. Average values and standard deviations (SDs) were obtained from 3 different measured values. The blank contained XTT reagent alone, without any cells in the well. The light absorbance of the control was 1.432, indicating 100% viability of the cells. The cell viability was 86.1% for HR4-DOPA and 134.3% for HR4, based on the control. In this experiment, HeLa cell viability was not negatively affected by HR4-DOPA. The difference between the light absorbance of HR4-DOPA and the control was not significant ( $P > 0.05$ ), despite a lower cell viability on HR4-DOPA. However, the viability of HeLa cells on HR4 was significantly higher than that on the others ( $P \leq 0.05$ ).

**Table 5.4:** Light absorbance of the XTT reagent for HeLa cell viability for HR4-DOPA and HR4. The blank contained XTT reagent alone, without any cells in the well. The positive control consisted of XTT reagent plus HeLa cells cultured in medium without substrate.

Sample	Light absorption (1)	Light absorption (2)	Light absorption (3)	Mean $\pm$ SD
Blank	0.204	0.142	0.229	0.192 $\pm$ 0.033
HeLa, control	1.421	1.455	1.420	1.432 $\pm$ 0.015
HeLa, HR4-DOPA	1.217	1.260	1.224	1.234 $\pm$ 0.018
HeLa, HR4	1.660	1.689	2.420	1.923 $\pm$ 0.331

## 5.4. Discussion

### 5.4.1 HeLa cell adhesion assay

In the HeLa cell adhesion assay, HR4 exhibited a better cell-adhesive performance than HR4-DOPA over the entire time range from 15 min to 6 h, whether the differences were significant or insignificant. Therefore, we studied the adhesion of HeLa cells in terms of the wettability of the substrate and the effect of dopamine on the substrate. We also examined the

effect of cell culture conditions and cell treatment methods on cellular adhesion.

#### 5.4.1.1 Effect of wettability on HeLa cell adhesion

The water contact angle, which is associated with wettability, of HR4-DOPA was  $62.08^\circ \pm 1.90^\circ$  (mean  $\pm$  SD,  $n = 5$ ), as described in **Chapter 4**. The wettability of HR4-DOPA is lower than that of HR4, which has a water contact angle of  $49^\circ$  [158], but it was in the range of moderate wettability for cell adhesion, i.e.,  $40\text{--}70^\circ$  [51, 88]. However, the optimal water contact angle is  $\sim 50^\circ$  for HeLa cell adhesion [51], which suggests that HR4-DOPA is inferior to HR4 for HeLa cell adhesion, at least with regard to wettability.

#### 5.4.1.2 Effect of dopamine on HeLa cell adhesion

In **Chapter 4**, we discussed the use of dopamine rather than catecholic salt in cellular substrates to achieve long-term stability of silane-coupling agents in aqueous environments. Although the dopamine-based polymer exhibited cell-adhesive characteristics for even non-adherent cells [186], HR4-DOPA demonstrated inferior adhesion of HeLa cells compared to that for HR4 and the controls used in this study. The disadvantage of using HR4-DOPA for cell adhesion might be caused by the dopamine in the medium. Moshkov *et al.* [224] verified that the dopamine in the cell culture medium highly regulated cell adhesion and viability in a dose-dependent manner. When the dopamine concentration in the medium was higher than  $10^{-4}$  M, there was a negative effect on cell adhesion due to changing the cytoplasmic globular actin of the cells as shown in **Figure 5.8**. The amount of dopamine in the medium, which may have been released from the HR4-DOPA film containing 1.03 mol% dopamine, should be investigated to better understand the negative effect of dopamine on cell adhesion. Changing the molar ratio of HR4-DOPA may improve the long-term stability of the substrate by controlling the concentration of dopamine in the cell culture medium (i.e.,  $\leq 10^{-5}$  M [224]).

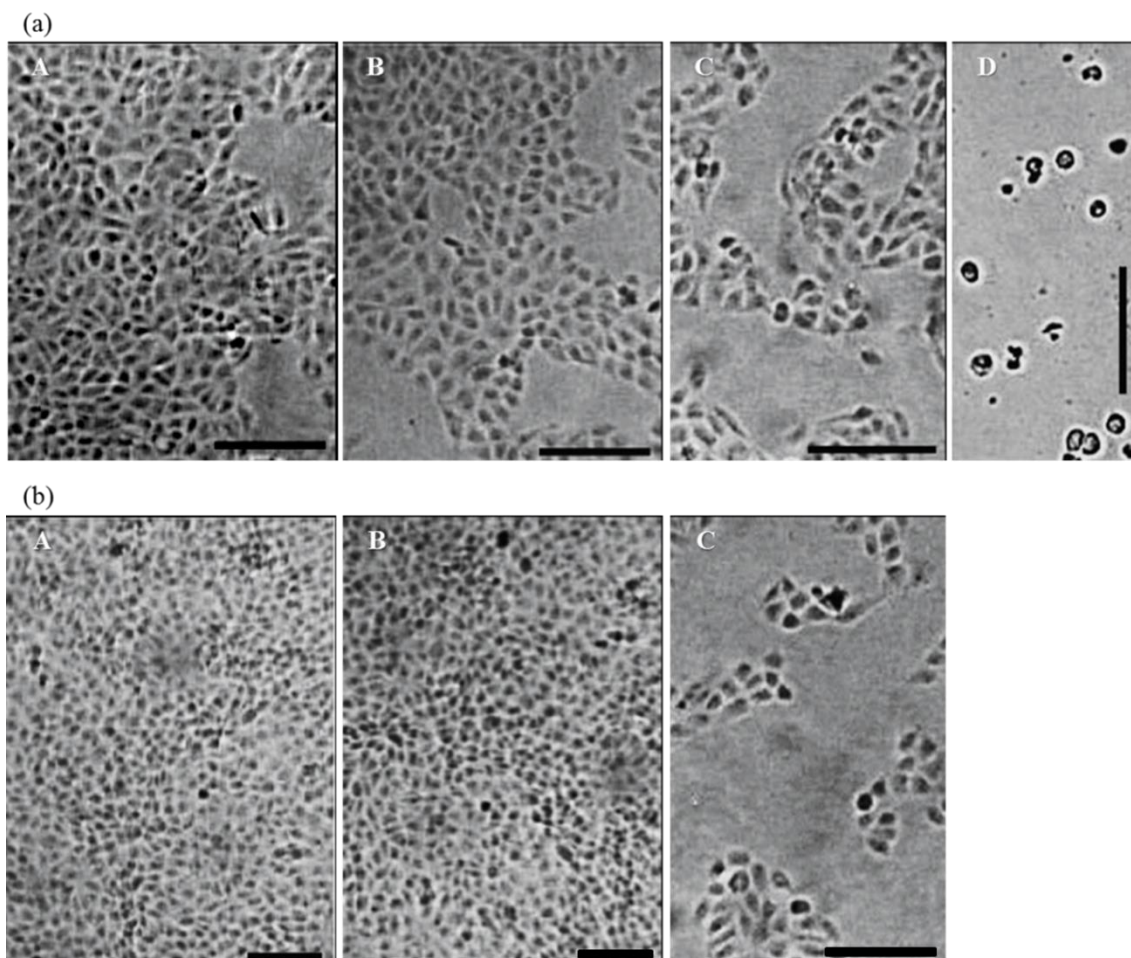


**Figure 5.8:** Morphological features of BHK-21 cells after treatment with various concentrations of dopamine [224].

- (a) Dopamine affects the cells adhering to the substrate for 48 h: [A] control, [B] 10<sup>-5</sup> M, [C] 10<sup>-4</sup> M, and [D] 10<sup>-3</sup> M. Scale bars, 100  $\mu$ m.
- (b) Dopamine affects the cells adhering to the substrate for 72 h: [A] control, [B] 10<sup>-5</sup> M, and [C] 10<sup>-4</sup> M. Scale bar, 100  $\mu$ m.

#### 5.4.1.3 Conditions of the cell culture medium

The adhesion behavior of the cells depends not only on the coated surfaces but also on the culture conditions [222]. The amount of serum in cell culture medium is one of the important parameters for regulating cellular behavior [88, 92, 163, 168, 172, 174-178, 180]. Serum (e.g., FBS or fetal calf serum [FCS]) is commonly used as a supplement to cell culture media at a concentration of 10% of the total volume and provides a broad spectrum of macromolecules, carrier proteins for lipid substances and trace elements, attachment and spreading factors, low molecular weight nutrients and hormones, and growth factors [225].

Moreover, ECM proteins in the serum – mainly fibronectin and vitronectin – are adsorbed in advance onto surfaces and these regulate cell adhesion, proliferation, and migration [88, 92, 163, 168, 172, 174-178, 180].

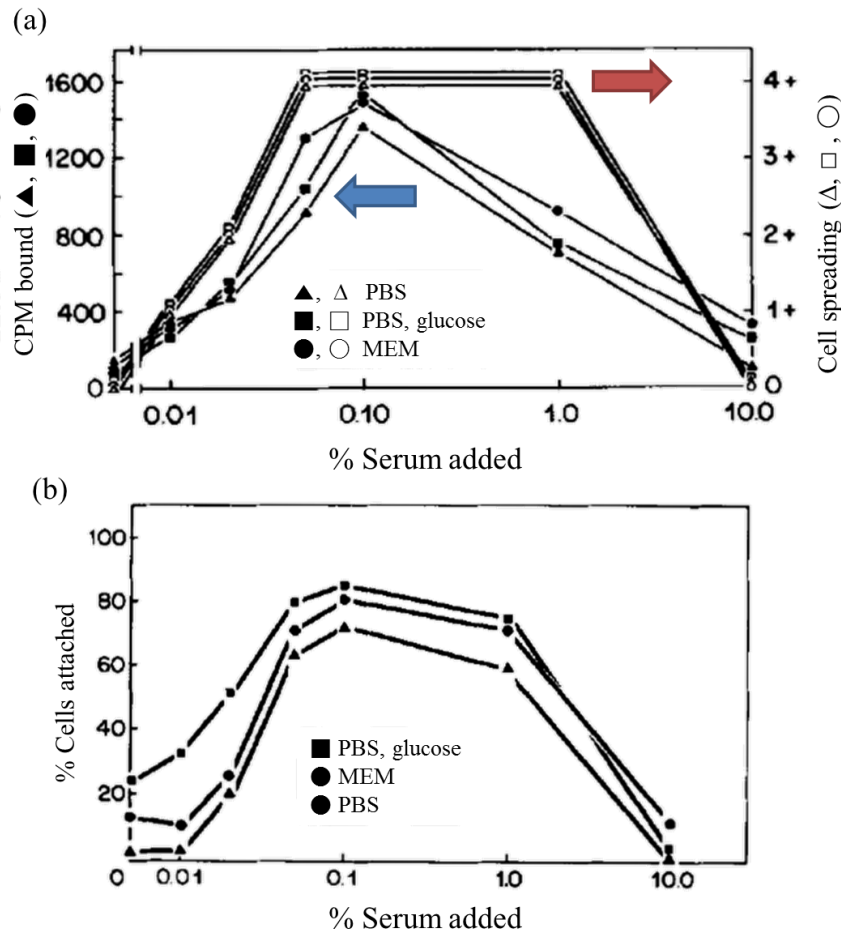


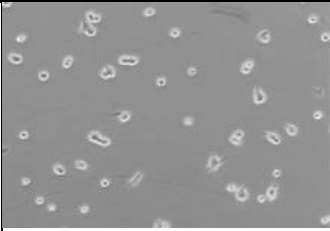
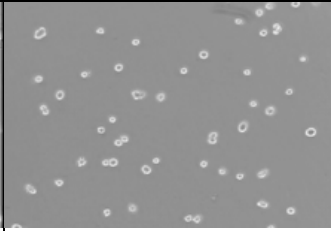
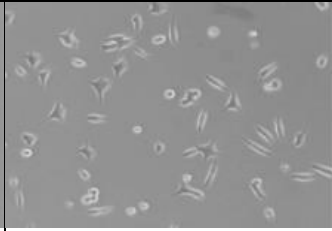
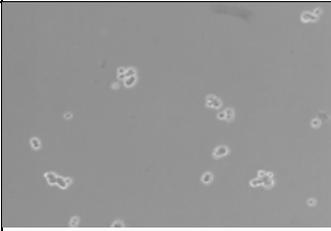
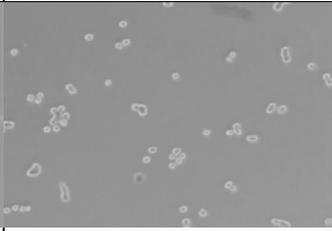
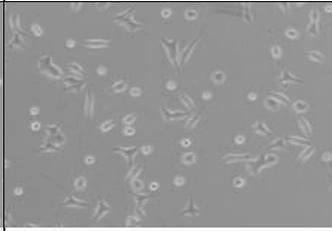
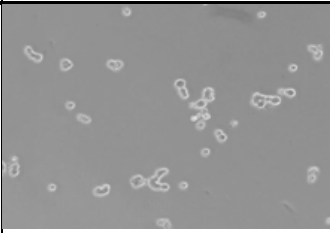
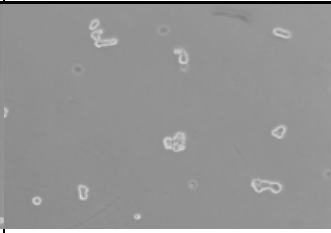
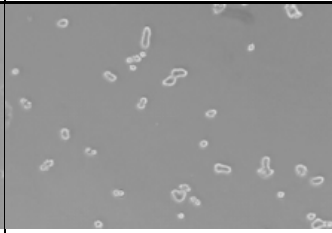
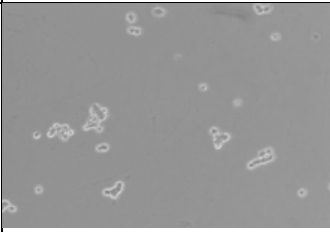
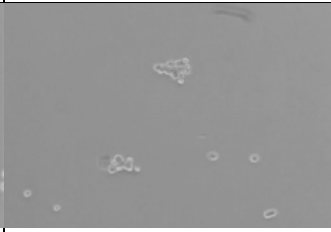
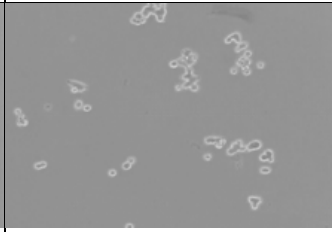
**Figure 5.9:** Adsorption of fibronectin from serum solutions in relation with cell-spreading activity and cell adhesion [165]. In all the experiments, pairs of tissue culture dishes were treated with human serum at the concentrations indicated in the buffers shown, for 10 min at 22°C. At the end of the incubations, the dishes were rinsed and fixed.

- (a) Fibronectin adsorption and cell-spreading activity with respect to serum concentration in media. The amount of plasma fibronectin adsorption was determined by the indirect antibody assay (left axis), and cell-spreading activity was determined by visually estimating the percentage of well-spread cells: 5–35% (1+), 40–60% (2+), 65–85% (3+), and 90–100% (4+) (right axis). The amount of adsorbed plasma fibronectin increased by 0.1% and later decreased as the serum concentration increased.
- (b) Cell adhesion with respect to serum concentration in media. The highest cell adhesion was seen in all media supplemented with 0.1% serum.

The process of cell adhesion occurs in two main steps: (1) serum proteins such as fibronectin and vitronectin are adsorbed onto the surface, as shown in **Figure 2.6 (b)**; and (2)

cells subsequently attach to the pre-adsorbed proteins by focal cell adhesion, as shown in **Figure 5.2**. However, the amount of serum in the medium plays a primary role in the pre-adsorption rate of the cell-adhesive ECM proteins, thereby affecting cell adhesion [165]. The optimal amount of serum in medium is 0.1% for fibronectin adsorption, cell spreading, and cell adhesion, as shown in **Figure 5.9**.

**Table 5.5:** Effect of the serum in the medium on the adhesion and proliferation of RIN-5F cells on various ECM proteins by comparing two different culture conditions: in serum-free medium (RPMI 1640) or in serum medium (RPMI 1640 with 10% FBS). The cells were cultured for 8 h at 37°C and 5% CO<sub>2</sub>.

	Fibronectin	Vitronectin	Laminin
Serum-free medium			
Serum medium			
	Collagen I	Collagen II	Collagen IV
Serum-free medium			
Serum medium			

Moreover, the existence of serum in the medium also regulates cell spreading and cell adhesion, even on the cell-adhesive ECM proteins. Proteins generally utilized for surface

modification of biomaterials are fibronectin, vitronectin, laminin, collagen I, collagen II, and collagen IV [222], as shown in **Table 5.5**. The serum in the medium regulated cell adhesion and cell proliferation on fibronectin; the fibronectin-coated surface had some positive effects on cell spreading only in serum-free medium. In contrast, the effect of laminin, collagen I, collagen II, and collagen IV on cell adhesion and proliferation was independent of the existence/absence of serum.

In conclusion, the serum in the culture medium regulates the adsorption of the cell-adhesive ECM proteins (i.e., fibronectin and vitronectin) and cell behaviors (i.e., cell adhesion, spread, and proliferation), even on fibronectin. Therefore, a more detailed investigation of the concentration of FBS in the medium is required to explain the effects of FBS on the cell adhesion to HR4-DOPA.

#### **5.4.1.4 Settling time of HeLa cells**

For the cell adhesion assay, HeLa cells were seeded at a cell density of  $1.0 \times 10^6$  cells/ml in a 6-well plate and cultivated in RPMI 1640 (3 ml) supplemented with 10% FBS at 37°C. The settling time of HeLa cells, that is, the time taken for the cells in suspension to completely settle onto the bottom of the plate and begin to adhere to the surface, was 316.7 s (i.e., ~5 min) under these culture conditions (see **Table 3.14**). Although the cell adhesion was postponed because of the settling time required, the cells still had sufficient time to adhere to the substrates, even for the minimum culture time of 15 min.

#### **5.4.1.5 Cell fixation**

While obtaining images in different view fields for a single sample, we noticed that the morphological features of the adhered HeLa cells in the other samples continuously changed. Therefore, only a few images (i.e., 3 per sample) could be acquired before this morphological change was noticed, due to the time required to load/unload the samples and position the

fields of view. We attempted to fix the cells by ethanol or paraformaldehyde at the end of the treatment time [226, 227] because this would give us enough time to obtain a larger number of images ( $\geq 100$ ); however, this method was inappropriate for our experiment because the cells died after fixation [226].

#### **5.4.2 HeLa cell viability assay**

The viability of HeLa cells was 86.1% on HR4-DOPA, and this value did not differ significantly on the control substrate. However, the minimum viability of HeLa cells on HR4-DOPA cannot be disregarded because dopamine can deplete various cancer cells and might play a role as an anti-tumor agent in clinical treatment [228-230]. Additionally, dopamine is a catecholamine neurotransmitter in humans and an important molecule bridging the nervous and immune systems by controlling movement; endocrine regulation; and cardiovascular, renal, and gastrointestinal functions [231-234]. HR4-DOPA should be additionally tested using a normal mammalian cell line in order to confirm the viability for the cells.

### **5.5. Conclusion**

The biocompatibility of dopaminergic inorganic-organic hybrid resin (HR4-DOPA) for HeLa cells was investigated using cell adhesion and cell viability assays.

The cell adhesion assay of HR4-DOPA was performed by manually counting the adhered HeLa cells per unit area in the time-lapse format for 6 h in RPMI 1640 supplemented with 10% FBS and compared with mesoporous inorganic-organic hybrid resin (HR4), ECM proteins (i.e., fibronectin, collagen IV), and glass. On the HR4-DOPA film, the number of adhered HeLa cells increased until 1 h, after which the growth rates remained low. Thus, HeLa cells adhering to HR4-DOPA were significantly less than those adhering to HR4 after 3 h, collagen IV after 1 h, and all controls at 6 h. Both HR4-DOPA and HR4 share the same chemical compositions, except that HR4-DOPA contains dopamine in place of the catecholic

salt in HR4. The dopamine in HR4-DOPA led to poor cell adhesion performance at all time points; however, the differences between HR4-DOPA and HR4 were not significant until after 3 h of incubation ( $P \leq 0.05$ ). During the initial phase of cell adhesion, the adhesion for HR4-DOPA was comparable to that for collagen IV for 45 min and fibronectin for 1 h ( $P > 0.05$ ).

The water-contact angle of HR4-DOPA ( $62.08^\circ$ ) was in the moderate wettability range for cell adhesion (i.e.,  $40\text{--}70^\circ$ ), but the optimal value for HeLa cell adhesion was  $\sim 50^\circ$ , which indicated that the HR4 film (water-contact angle,  $49^\circ$ ) was more suited for HeLa cell adhesion than HR4-DOPA. Dopamine helped achieve long-term stability of a silane-coupling agent in HR4-DOPA, but the dopamine in the medium, perhaps released from HR4-DOPA, might weaken the HeLa cell adhesion. The FBS in the medium also regulates not only the amount of the cell-adhesive ECM protein adsorption but also cell adhesion and proliferation on even the pre-adsorbed proteins. Therefore, a proper FBS concentration is required for optimal conditions in the cell adhesion assay on the HR4-DOPA film. HeLa cells required the settling time of  $\sim 5$  min for settling and adhering to the substrates, but the time was given to the cells enough time for adhesion, even for the minimum culture time of 15 min.

The HeLa cell viability for HR4-DOPA was assessed using XTT assays after 2-d incubation, and viability was compared to that on HR4. The HeLa cell viability of HR4-DOPA was 86.1% that for the control. While this cell viability is not significantly less, the minimum viability cannot be disregarded because dopamine might act as an antitumor agent.

Both the cell adhesion and viability assay results sufficiently support the biocompatibility of HR4-DOPA and demonstrate its applicability for an isolated single-cell array as a function of cell-adhesive material.



# Chapter 6. A Microwell Array Coated by Dopaminergic Mesoporous Inorganic-organic Hybrid Resin Film

## 6.1. Introduction

### 6.1.1 Requirement of a microwell array for drug discovery

Cell models in conventional *in vitro* cell-based screening continue to provide misleading data that are not necessarily representative of *in vivo* responses due to the presence of slightly different cellular environments in *in vitro* assays [8, 18-21]. Uniform cellular environments are required during the early discovery process in order to increase the reliability of cellular response analyses and to benefit economically from the small-scale nature of such assays [8, 19].

To allow highly accurate measurement of cellular responses to a drug, researchers have used microfabrication techniques to provide a uniform cellular environment and mimic *in vivo* functions [4, 8, 19, 27, 29, 30]. Moreover, microarrays of individual living cells may facilitate elucidation of the biological effects of a drug on a single cell by eliminating multiplexing and complicated cell-cell contact and communications interferences that conceal direct and accurate correlations between cells and stimuli, thereby providing large amounts of information regarding cellular chemistry at the molecular level [20, 24, 27]. By spatially arranging isolated single cells, a sufficient number of cells can be quantitatively analyzed to draw valid conclusions, rather than interpreting individual cell variation as noise due to cell population heterogeneity [23, 27, 28, 54, 55]. Since quantitative measurements of cellular responses rely on the number of cells exposed to external stimuli, small chip-to-chip variations in the arrayed isolated single cells may allow for more accurate quantification of

the effects of anticancer drugs on cancer cells [59].

Single-cell microarrays are generally developed using planar cell adhesive patterns; however, conventional 2D cultures are often subject to loss of native cell morphology and functionality [34, 35]. Compared to 2D cultures, 3D *in vitro* cell models provide a more realistic cellular environment and permit the reproduction of *in vivo* cellular phenotypes, such as those related to metabolism and function, including morphogenesis, gene expression, and differentiation [36, 37]. Therefore, microwells containing single cells are required in order to preserve the native cell morphology and functionality in 3D *in vitro* cell models for drug discovery.

### **6.1.2 Limitations of the previous microwell arrays**

Microwells to trap single cells are generally fabricated of poly(dimethylsiloxane) (PDMS) because this material enables numerous replications at both micro- and nanometer scales from micro- and nanofabricated molds with high precision [38, 112, 114, 117, 118]. However, the cytophobic properties of PDMS do not allow for cellular adhesion; this may adversely affect the natural behaviors of anchorage-dependent cells, which can survive only when they adhere to appropriate substrates, due to the absence of supporting cells, extracellular matrix, and growth factors [38]. Therefore, the ability of microwells to maintain the native 3D morphology of anchorage-dependent cells can only be achieved when the inner surface of the microwell is conducive for cell adhesion.

Ochsner *et al.* [111] fabricated a cell-adhesive surface inside microwells of plasma-treated PDMS adsorbed with cell-adhesive fibronectin. However, this methodology was problematic both because the PDMS surface should be immediately immersed in an aqueous solution (i.e., water, methanol, or trifluoroethanol) after plasma treatment to preserve its bioactive characteristics [62, 235], and because fibronectin can be easily degraded [236]. Additionally, Leong *et al.* [70] fabricated microwells coated with a cell-adhesive self-

assembled monolayer (SAM); however, only the bottom of the microwells, not the walls, were coated with the SAM, creating an unpredictable native 3D cellular morphology in anchorage-dependent cells. Broderick *et al.* [71] fabricated 3D polyurethane-based microwell cell culture arrays; the inside surfaces of the wells were functionalized to promote cell adhesion, while the plateaus of wells were functionalized to resist cell adhesion. Although this method appeared promising, the process for selectively functionalizing the inner surfaces of the microwells and plateaus proved to be quite complicated.

### **6.1.3 Dopaminergic mesoporous inorganic-organic hybrid resin**

A dopaminergic mesoporous inorganic-organic hybrid resin (HR4-DOPA) was modified from a mesoporous inorganic-organic resin (HR4) for long-term stability with the help of dopamine to preserve the fabricability of HR4 for micro- or nano-engineering [47, 237], as described in **Chapter 4**. Moreover, the biocompatibility of HR4-DOPA for HeLa cells was also demonstrated by cell adhesion and cell viability assays in **Chapter 5**. In this study, we used the biocompatible HR4-DOPA film to create an adhesive inner surface in microwells.

### **6.1.4 A microwell array coated by dopaminergic inorganic-organic hybrid resin film**

In this study, we sought to fabricate a microwell array for single cell analysis that could preserve the native 3D morphology and functionality of HeLa cells by creating microwells with a cell-adhesive inner surface. We designed square microwells (size,  $25 \times 25 \mu\text{m}^2$ ) with various depths (e.g., 10, 25, and  $40 \mu\text{m}$ ). The PDMS substrate containing the microwell arrays was fabricated by soft lithography, and the inner surfaces of the microwells were functionalized to promote cell adhesion using microcontact printing. Finally, we optimized the technology (i.e., cell concentration and physical dimensions of the microwells) for HeLa cells by examining single-cell occupancy of the microwells after live-cell staining, allowing us to comment on whether this technology may be developed further as a mimic *in vivo*

microfluidic device for high-throughput single-cell-based assays.

## 6.2. Materials and methods

### 6.2.1 Fabrication of a replica-micromolding master for soft lithography

Silicon wafers (diameter, 100 mm; Si-mat, Kaufering, Germany) were used as a substrate for construction of a replica-molding master. The wafers were baked on a hot plate at 160°C for 20 min to remove moisture and treated with oxygen plasma at 200 W for 180 s (Pico, Diener electronic GmbH, Ebhausen, Germany).

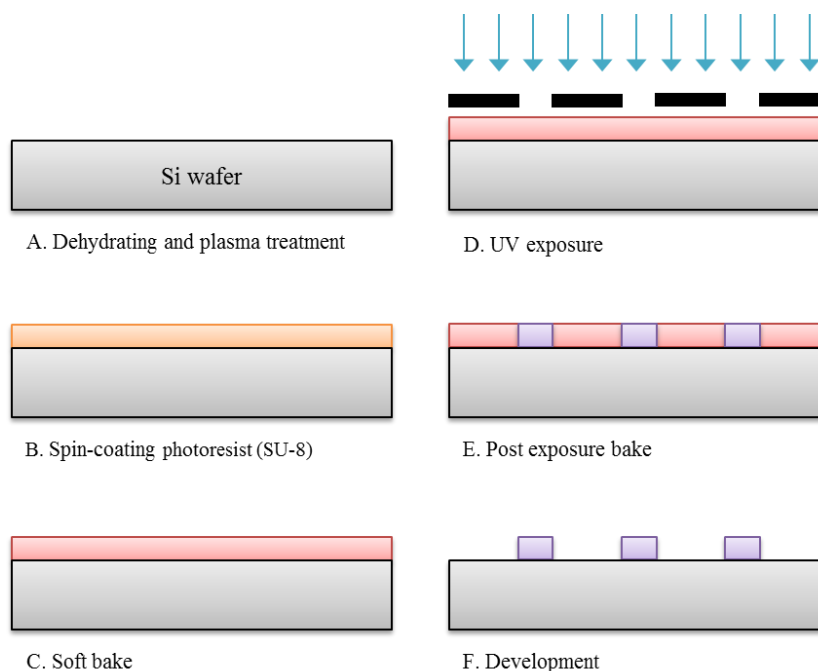


**Figure 6.1:** Fabrication process for the SU-8 micromolding master for soft-lithography.

A negative SU-8 10 photoresist (PR; MicroChem Corp., Newton, MA, USA) was used to construct a 10- or 25- $\mu\text{m}$  thick replica-molding master. SU-8 10 was spread at 500 rpm for 10 s and then spun at 3000 or 1160 rpm for 30 s to yield feature heights of 10 or 25  $\mu\text{m}$ , respectively. Immediately after spinning, each wafer was placed on a 65°C hot plate for 2 or 3 min, according to the feature height. The temperature of the hot plate was then increased to 95°C at 5°C/min, held at 95°C for 5 or 7 min, respectively, and lowered back to room

temperature. The wafers were then exposed to UV at  $375 \text{ mJ/cm}^2$  on a mask aligner (MA6, SUSS MicroTec AG, Garching, Germany) on a dark-field mask (Photo Data Ltd., Hitchin, UK), with high vacuum contact between the wafer and the mask, for 32 or 37.5 s, respectively. The wafers were placed on a  $65^\circ\text{C}$  hot plate for 1 min, and the temperature was raised to  $95^\circ\text{C}$  at  $5^\circ\text{C/min}$ , held at  $95^\circ\text{C}$  for 3 or 5 min, respectively, and cooled to room temperature (RT). Next, the substrates were immersed in SU-8 developer (mr-Dev 600, Micro Resist Technology GmbH, Berlin, Germany) for 3 or 5 min, respectively, to remove unexposed portions of the SU-8 10 PR.

A negative SU-8 2050 PR (MicroChem Corp.) was used to create a  $40\text{-}\mu\text{m}$ -thick replica-molding master. SU-8 2050 was spread at 500 rpm for 10 s and then spun at 4000 rpm for 30 s to yield feature heights of  $40 \mu\text{m}$ . Immediately after spinning, each wafer was placed on a hot plate at  $65^\circ\text{C}$  for 3 min, and the temperature was raised to  $95^\circ\text{C}$  at  $5^\circ\text{C/min}$ , held at  $95^\circ\text{C}$  for 7 min, and lowered back to RT. The wafers were then exposed to UV on the mask aligner on a dark-field mask, with high vacuum contact between the wafer and the mask, for 25.9 s. The wafers were placed on the hot plate at  $65^\circ\text{C}$  for 2 min, and the temperature was raised to  $95^\circ\text{C}$  at  $5^\circ\text{C/min}$ , held at  $95^\circ\text{C}$  for 5 min, and cooled to RT. Next, the substrates were immersed in SU-8 developer (mr-dev 600; Micro Resist Technology GmbH, Germany) for 5 min to remove unexposed portions of the SU-8 2050 PR.

**Table 6.1:** Fabrication specifications for construction of negative SU-8 photoresists with various thicknesses.

PR (thickness)	Spin-coat	Soft bake	UV exposure	Post bake	Development
SU-8 10 ( $10 \mu\text{m}$ )	500 rpm, 3 s 3000 rpm, 30 s	$65^\circ\text{C}$ , 2 min $95^\circ\text{C}$ , 5 min	$375 \text{ mJ/cm}^2$ 32 s	$65^\circ\text{C}$ , 1 min $95^\circ\text{C}$ , 3 min	3 min
SU-8 10 ( $25 \mu\text{m}$ )	500 rpm, 3 s 1160 rpm, 30 s	$65^\circ\text{C}$ , 3 min $95^\circ\text{C}$ , 7 min	$375 \text{ mJ/cm}^2$ 37.5 s	$65^\circ\text{C}$ , 2 min $95^\circ\text{C}$ , 5 min	5 min
SU-8 2050 ( $40 \mu\text{m}$ )	500 rpm, 3 s 3000 rpm, 30 s	$65^\circ\text{C}$ , 3 min $95^\circ\text{C}$ , 7 min	$375 \text{ mJ/cm}^2$ 25.9 s	$65^\circ\text{C}$ , 2 min $95^\circ\text{C}$ , 5 min	5 min

Images of the fabricated microstructures were obtained by scanning electron microscopy (JSM-6400F; JEOL GmbH, Germany) after deposition of a thin Pt film over the microstructure surface using a sputter coater (K675X; EMITech Inc., Fall River, MA, USA).

### **6.2.2 Fabrication of a microwell coated by dopaminergic mesoporous inorganic-organic hybrid resin**

The SU-8 microstructure masters were exposed to a trichloro (1H,1H,2H,2H-perfluorooctyl) silane ( $\text{CF}_3(\text{CF}_2)_5\text{CH}_2\text{CH}_2\text{SiCl}_3$ ; Sigma-Aldrich, St. Louis, MO, USA) vapor at 60 mbar for 3 h. This step rendered the exposed silicon surface highly inert, which facilitated the release of the PDMS mold (Sylgard 184; Dow Corning GmbH, Wiesbaden, Germany) after curing. Then, we used soft lithography methods to fabricate a microwell array of PDMS. Briefly, a PDMS oligomer was mixed with a cross-linker at a 10:1 volume ratio, degassed, and poured onto the master. PDMS was cured in a convection oven at 65°C for 3 h after a second degassing. The cured PDMS, shaped to the microwell array, was manually detached from the master.

HR4-DOPA, diluted with 5 wt% ethanol, was spun on the microwell array-shaped PDMS substrate at 3000 rpm for 30 s after oxygen plasma treatment at 7 W for 30 s. The coated film was cured on a hotplate at 50°C for 5 h and subjected to postheat treatment at 100°C for 2 h. To passivate the plateau of the microwell arrays with a cell-repellent PDMS layer, we used a microcontact printing method. The PDMS/cross-linker mixture was diluted to 10 wt% by tert-butyl alcohol (TBA;  $(\text{CH}_3)_3\text{COH}$ , Alfa Aesar GmbH, Karlsruhe, Germany) prewarmed at 35°C, subjected to thorough manual mixing, and spun on a glass slide (size,  $22 \times 40 \text{ mm}^2$ ; Carl Roth GmbH, Karlsruhe, Germany) at 6000 rpm for 5 min. The HR4-DOPA-coated PDMS microstructures were stamped upside down for 30 s on glass slide coated with the diluted PDMS layer and then immediately detached and cured on hot plate at 65°C for 3 h. This fabrication process for the single-cell microwell array is shown in **Figure**

**6.3.** The HR4-DOPA-coated microwells were arrayed in a  $500 \times 500 \mu\text{m}^2$  area, obtained by cutting the boundaries of an 8-array area ( $2 \times 2 \text{ mm}^2$ ) with a sharp knife, immersed in ethanol for 2 h in order to eliminate the incorporated surfactants [158], and dried at RT.

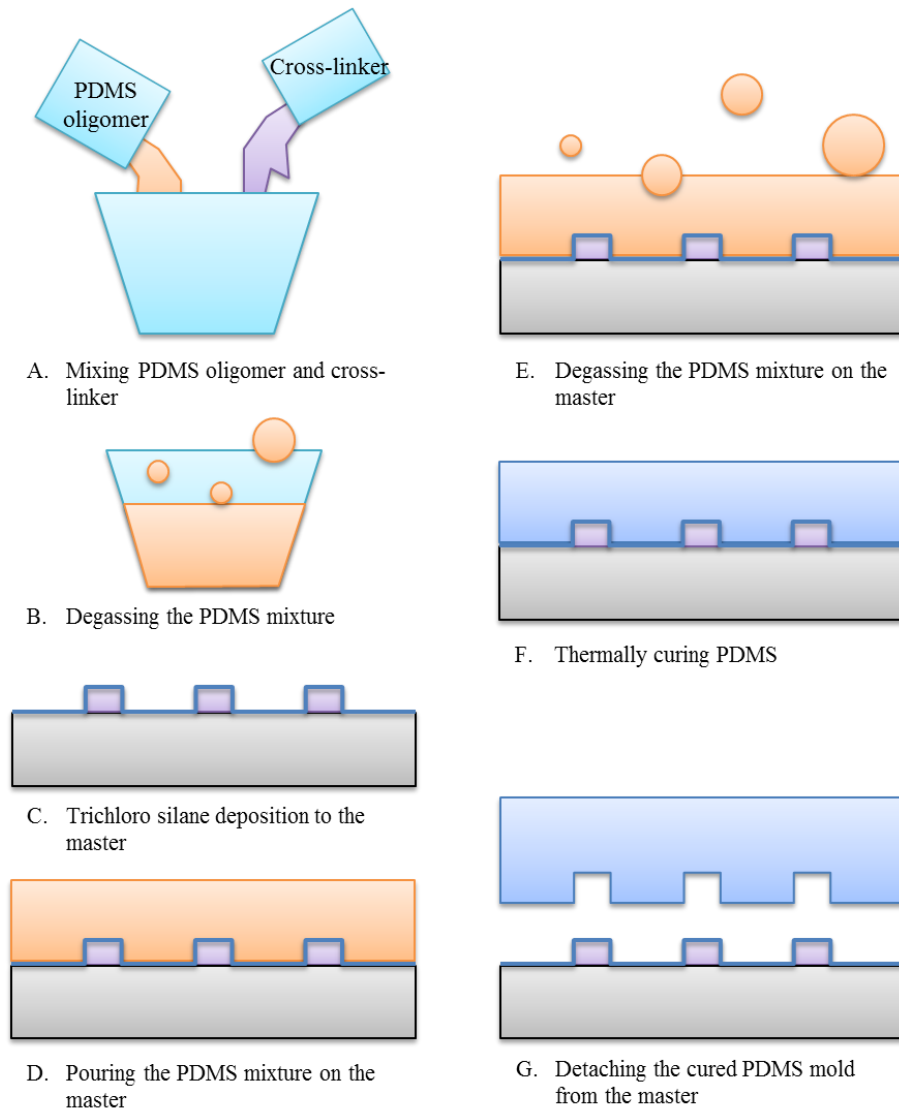


**Figure 6.2:** Fabrication process for the PDMS microwell array.

The depths of the microwells were profiled using a noncontact laser 3D scanning profilometer ( $\mu\text{scan explorer}$ ; Optoelektronische Messtechnik GmbH, Ismaning, Germany).

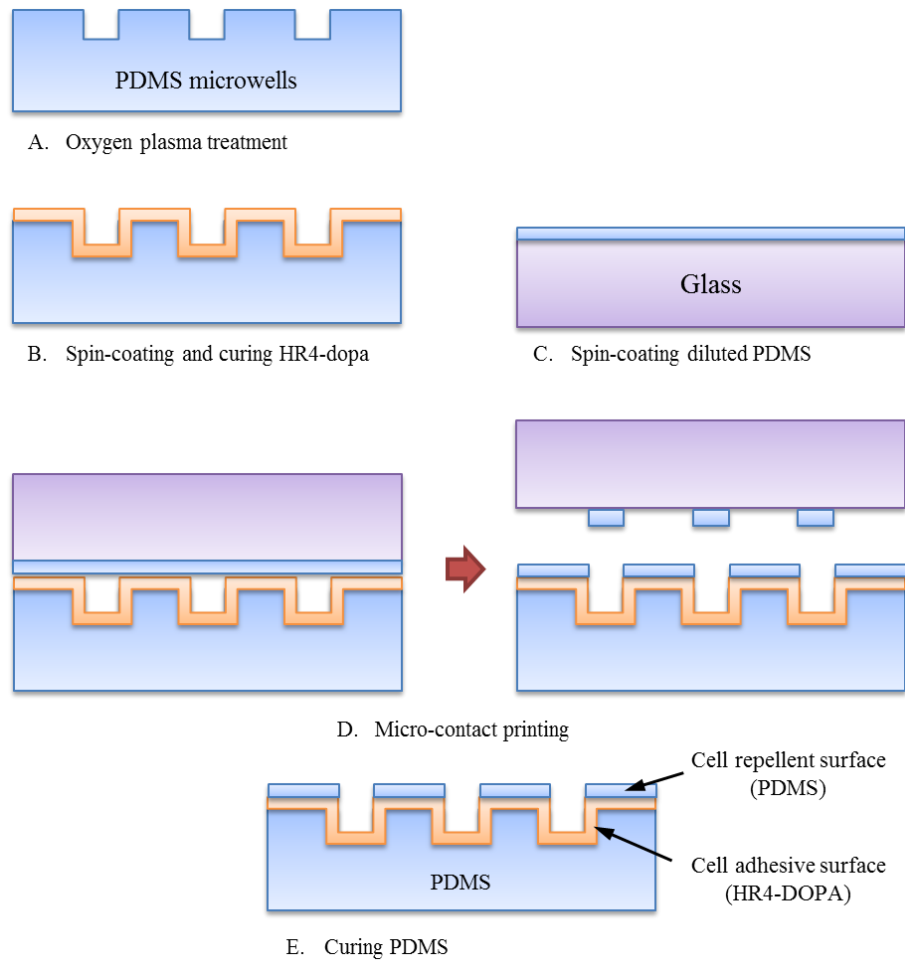


**Figure 6.3:** Fabrication process for the PDMS microwell array coated with cell-adhesive HR4-DOPA on the inner surface of the microwells.

### 6.2.3 Culture of HeLa cells

HeLa cells (Deutsche Sammlung für Mikroorganismen und Zellkulturen GmbH [DSMZ], Braunschweig, Germany) were cultivated in an incubator at 37°C and 5% CO<sub>2</sub>. In all experiments, we used RPMI 1640 medium (PAN Biotech GmbH, Aidenbach, Germany) supplemented with 10% fetal bovine serum (FBS, Sigma-Aldrich) and 2% penicillin/streptomycin (Sigma-Aldrich) without phenol red. Confluent cultures of HeLa cells were passaged every 3 days by treatment with a trypsin/EDTA solution (Sigma-Aldrich) for 5 min at 37°C with 5% CO<sub>2</sub>. Cells were centrifuged for 3 min at 200 × g and then washed 3 times with 400 μl PBS to remove residual trypsin. HeLa cells were subsequently resuspended in growth medium to achieve a seeding concentration of 1 × 10<sup>6</sup> cells/80 cm<sup>2</sup>.

#### 6.2.4 HeLa cell occupancy of a microwell array

For the preparation of single-cell occupancy in the microwell array, adhered HeLa cells were first detached using trypsin/EDTA as described above. The HeLa cell suspension was then washed 3 times with 400  $\mu$ l PBS and diluted in PBS to achieve a concentration of  $0.5 \times 10^6$ ,  $1.0 \times 10^6$ , or  $2.0 \times 10^6$  cells/ml. The HeLa cell concentration was measured 3 times for each trial using a CASY cell counter (CASYton, Schärfe System GmbH, Reutlingen, Germany).

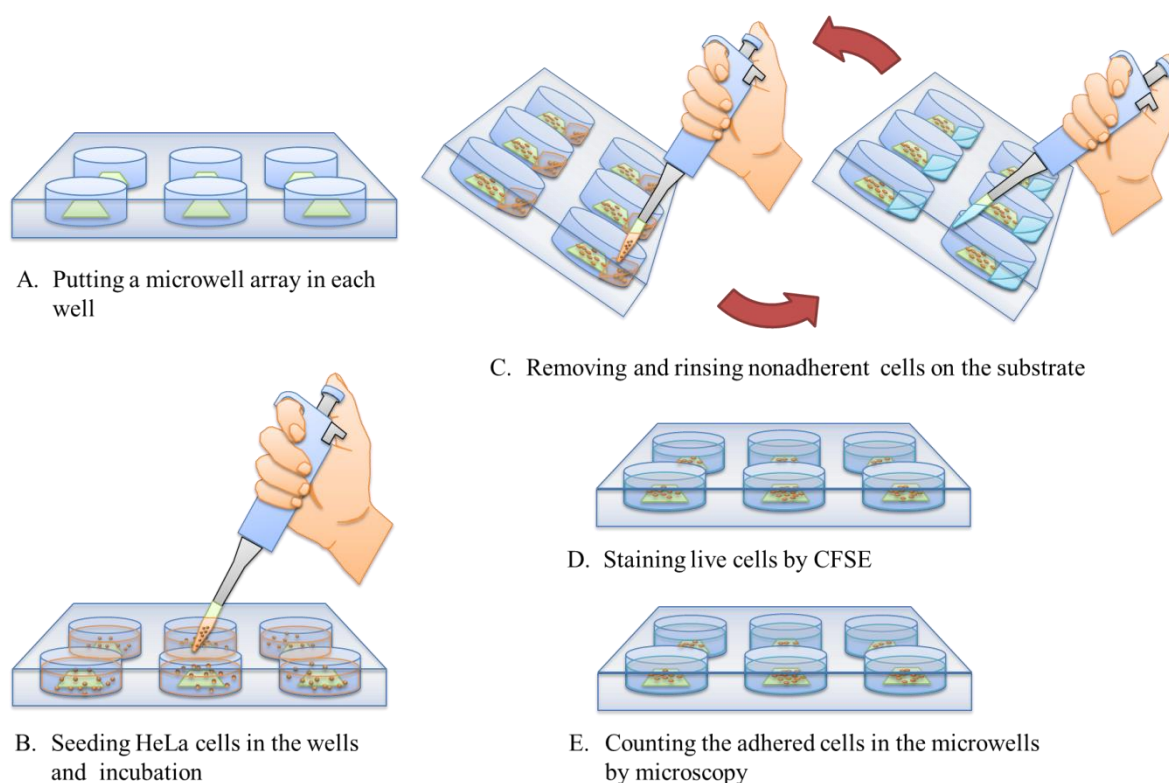


**Figure 6.4:** The HeLa cell occupancy experiment in the microwell array.

Next, HeLa cell occupancies were assessed at the various microwell depths (i.e., 10, 25, and 40  $\mu$ m). The microwell arrays were sterilized by immersion in ethanol for 5 min and then dried at RT. Each prepared array was placed into an untreated PS 6-well plate (BD Biosciences, San Jose, CA, USA) and positioned at the center of the well. Subsequently, HeLa cells in 3 ml medium were seeded into each well. All samples were cultured for 6 h at

37°C with 5% CO<sub>2</sub>. After incubation, nonadherent cells were carefully rinsed in PBS 3 times.

In order to identify adhered live cells in the microwells, the cells were stained with 10 μM 5(6)-carboxyfluorescein diacetate n-succinimidyl ester (CFSE; Molecular Probes, Invitrogen Detection Technologies, Karlsruhe, Germany) for 30 min at 37°C with 5% CO<sub>2</sub>. After staining, the cells were rinsed twice with PBS to remove excess CFSE that diffused out of the cells, and cell occupancy was analyzed by cell counting in 6 different microwell arrays using ImageJ software (version 1.45; <http://rsbweb.nih.gov/ij/>).

## 6.3. Results

### 6.3.1 Design of a microwell array

The physical dimensions of the microwells were designed to achieve high single-cell occupancy. Square microwells measured  $25 \times 25 \mu\text{m}^2$  in size, slightly larger (by approximately 10 μm) than the diameter of a HeLa cell ( $16.17 \pm 2.4 \mu\text{m}$ ) [38, 70, 80, 118-120], as previously described in **Chapters 2** and **3**. The depths of the microwells (i.e., 10, 25, and 40 μm) were also investigated in order to fully characterize the physical dimensions of the microwells.

The microwells were arranged in an array resembling a chess pattern in order to increase the microwell density per unit area since shorter distances and diffusion times for molecules and cells are more suitable for time-efficient, accurate analyses, especially in high-throughput applications [27, 55]. Moreover, cell number is critical for quantitative measurements; conventionally, 10,000 cells are used for single-cell analysis [54]; however, some single-cell analysis techniques have assessed as few as 1000 single cells to provide adequate sets of data [55]. Therefore, in our study, the total number of microwells on the 8 arrays was 1,600 (each array measured  $500 \times 500 \mu\text{m}^2$ , with a total area of  $2 \times 2 \text{ mm}^2$ ). In the array, 200 microwells were placed between passivated areas of the same size in order to facilitate easy calculation

of single-cell occupancy (see **Figure 6.5**). The passivation areas were positioned in such a way as to demonstrate the existence of the cell-adhesive HR4-DOPA film inside the microwells through comparison of two controls: one coated with the HR4-DOPA film on the entire surface and the other with an untreated PDMS surface.

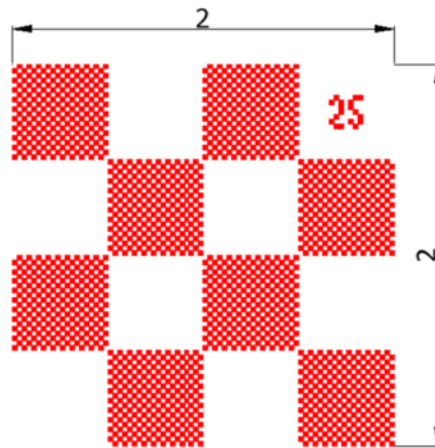


**Figure 6.5:** Microwell arrays in an area of  $2 \times 2 \text{ mm}^2$ . This area contained a total of 8 arrays, and each array (area,  $500 \times 500 \mu\text{m}^2$ ) contained 200 microwells (size,  $25 \times 25 \mu\text{m}^2$  each).

### 6.3.2 Fabrication of a microwell array

The PDMS substrate containing the microwell array was fabricated using soft lithography, and a cell-adhesive surface, coated with the HR4-DOPA film, was created using microcontact printing.

#### 6.3.2.1 Fabrication of a replica-micromolding master

We used oxygen plasma treatment to clean the silicon wafers by ashing organic contamination and to increase the surface contact strength between SU-8 PRs and substrates. Hexamethyldisilazane (HMDS) and MCC primer 80/20 (MicroChem Corp.) are widely used in the MEMS processes to improve the adhesion of SU-8 PRs to oxides, i.e., glass or silicon dioxide ( $\text{SiO}_2$ ); however, as shown in **Figure 6.6**, the SU-8 microstructures were easily detached when the microstructured wafers were overdeveloped by SU-8 developer or when the developed structures were rinsed with isopropyl alcohol in this study.

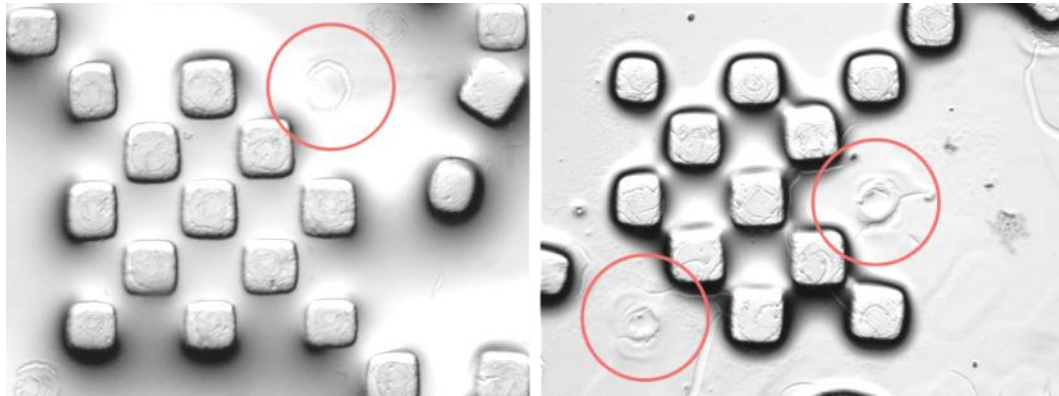


**Figure 6.6:** Detached SU-8 microstructures on the MCC primer 80/20-coated silicon substrate after development. Red circles show the locations of SU-8 microstructure detachment, which occurred despite their size ( $100 \times 100 \mu\text{m}^2$ ).

The fabricated replica-micromolding master containing 25- $\mu\text{m}$ -high SU8 microstructures is shown in **Figure 6.7**. The SU-8 films were spun and patterned on the oxygen plasma-treated silicon wafer.

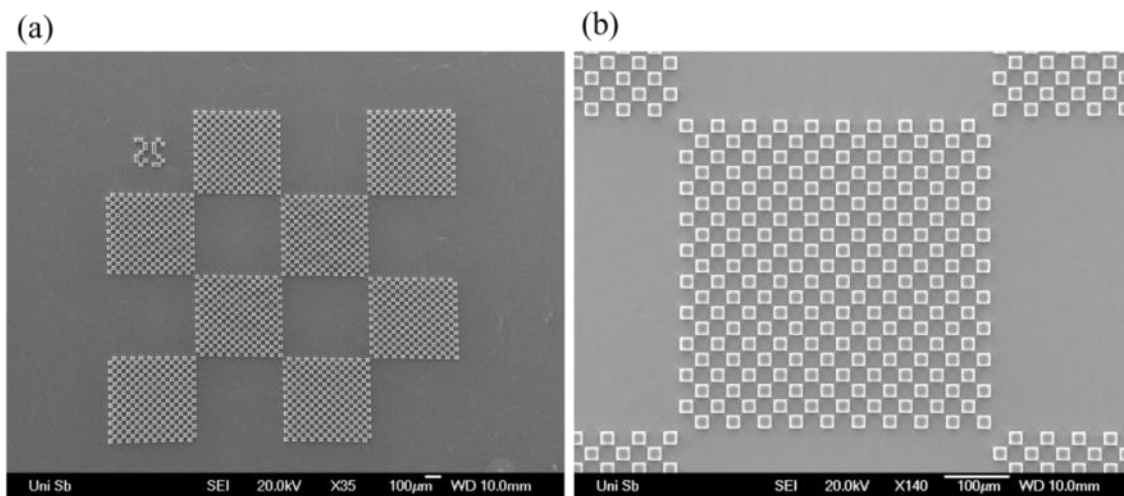


**Figure 6.7:** Scanning electron microscope images of the fabricated replica-micromolding master containing the array of 25- $\mu\text{m}$ -high SU-8 structures shaped in  $25 \times 25 \mu\text{m}^2$  squares.

### 6.3.2.2 Fabrication of a microwell array coated by dopaminergic inorganic-organic hybrid resin (HR4-DOPA) film

The PDMS substrate containing the microwell features had a thickness of approximately 1.3 mm after coating the wafer (100 mm in diameter) with 10 ml PDMS in order to increase

the softness and allow easy removal of air bubbles within the microwell plateau during microcontact printing passivation by a thin cytophobic PDMS layer. HR4-DOPA was diluted and spun on the oxygen plasma-treated PDMS substrate. Oxygen plasma treatment of PDMS was assessed for production of a silicate layer and the ability to react with the HR4-DOPA layer using covalent siloxane coupling [47]. HR4-DOPA was diluted to 5 wt% with ethanol in order to reduce the thickness of the spin-coated HR4-DOPA film on the surface to the nanometer scale (i.e., approximately 2 nm) and to decrease changes to the inner dimensions of the microwells [158].

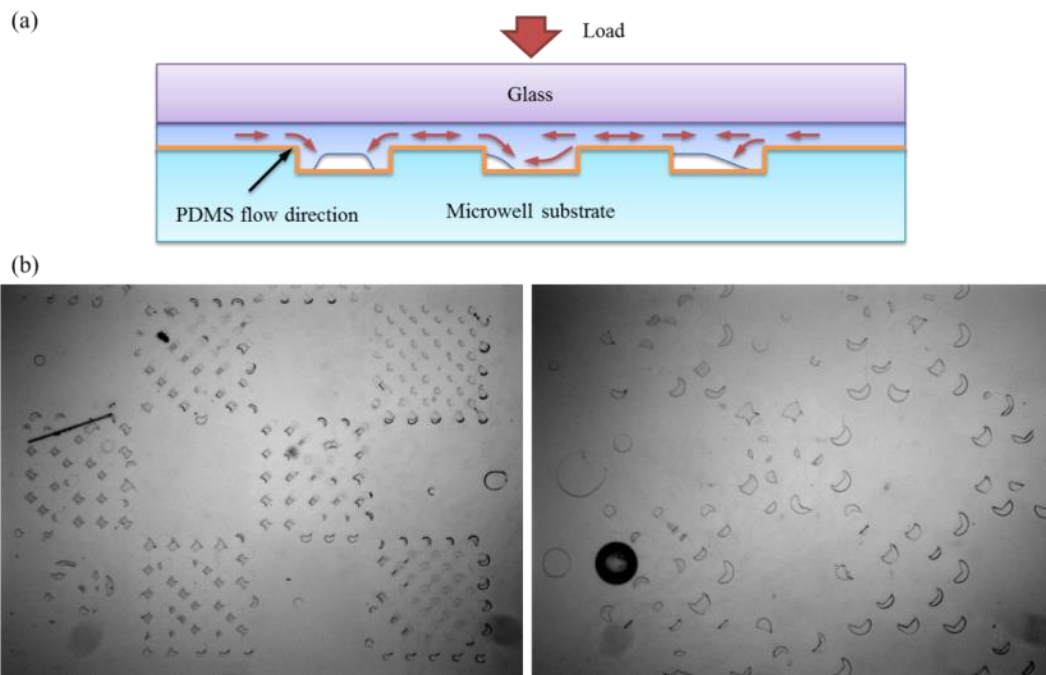


**Figure 6.8:** Pattern transfer failure of the liquid PDMS layer (thickness, 5  $\mu\text{m}$ ).

- (a) The pressure applied in microcontact printing caused the flow of the liquid PDMS layer into the microwells.
- (b) Photomicrographs of 25- $\mu\text{m}$ -deep microwell arrays filled with PDMS in microcontact printing.

The plateau of the microwell array was biologically passivated by the PDMS layer using the microcontact printing method. The liquid PDMS layer was sandwiched between the plateaus of the micromold and a flat substrate, and pressure was applied to the PDMS layer; the pressure applied caused the flow of the voluminous liquid PDMS layer (approximately

5  $\mu\text{m}$  thick, which was the minimum achievable thickness for 100% PDMS when spun at 6000 rpm for 5 min [238]) into the microwells (see **Figure 6.8**). Therefore, the thickness of the liquid PDMS layer should be reduced to permit high reproducibility of pattern transfer in microcontact printing.

When PDMS is diluted with TBA at different concentrations, the thicknesses of the spin-coated layers change as a function of spin speed [238], as shown in **Figure 6.9**. Therefore, we diluted PDMS by 10% with TBA to obtain a thickness of less than 1  $\mu\text{m}$ , thereby eliminating the formation of PDMS-filled microwells during microcontact printing. The melting point of TBA is 25 $^{\circ}\text{C}$ , and thus, the TBA solution should be prewarmed at 35 $^{\circ}\text{C}$  before use.

Photomicrographs of the HR4-DOPA film coated on the inside surface of the microwells, including both laser surface and line plot profiles, are shown in **Figure 6.10**; these data indicated that 25- $\mu\text{m}$ -deep microwells were formed from SU-8 10 PR spun at 1160 rpm.

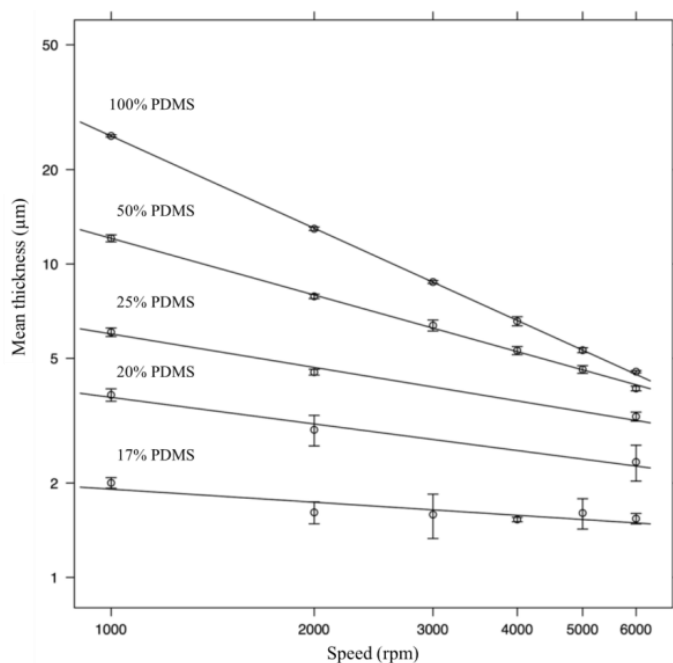


**Figure 6.9:** Thickness of the PDMS films at various concentrations of PDMS in tert-butyl alcohol (TBA) as a function of spin speed [238]. All substrates were spun for 5 min.

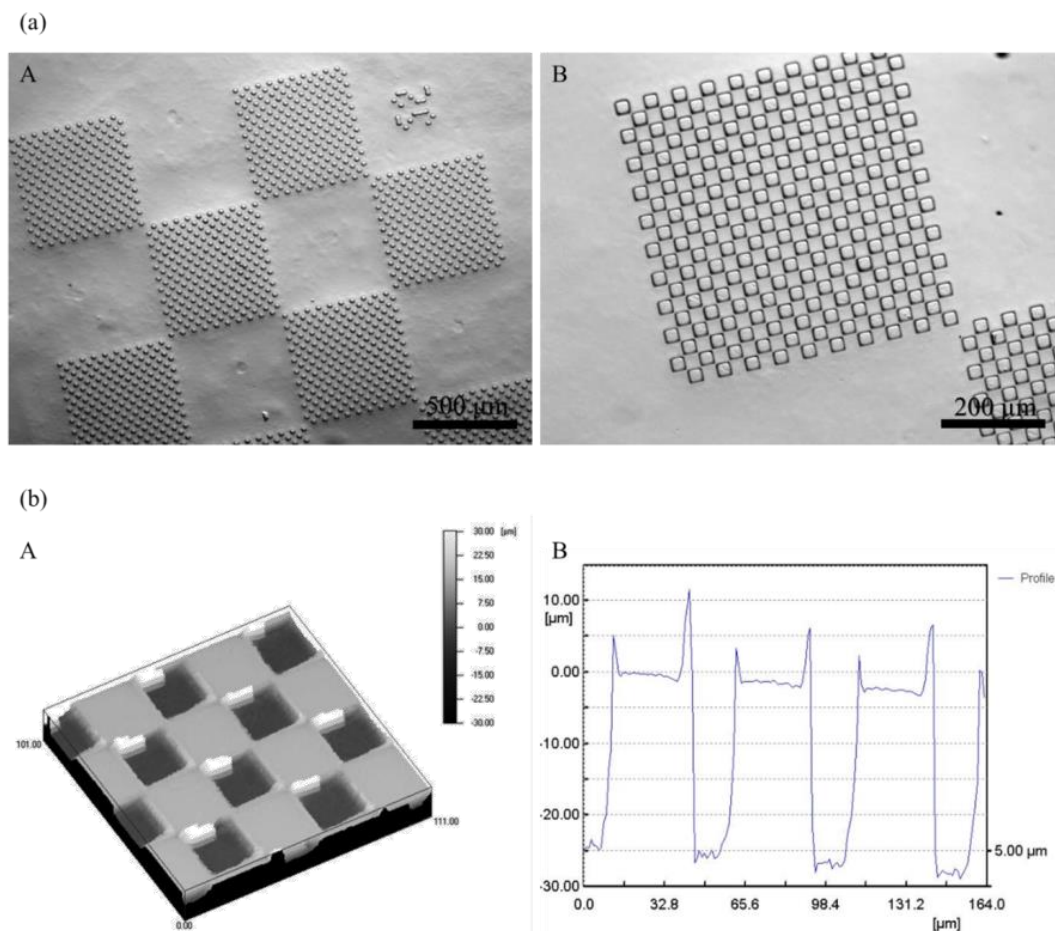


**Figure 6.10:** The fabricated microwell array coated with dopaminergic inorganic-organic hybrid resin (HR4-DOPA) on the inner surface of the microwells. The plateaus of the microwells were passivated by the cytophobic PDMS layer using microcontact printing.

- (a) Photomicrographs of the 25- $\mu\text{m}$ -deep microwell arrays coated with HR4-DOPA on the inner surface of the microwells.
- (b) Laser surface and line plot profiles indicate that the microwell array is 25  $\mu\text{m}$  deep. The sharp peak is noise from the boundary of the microwell and the plateau.

### 6.3.3 HeLa cell adhesion on the controls

In order to verify the fabrication processes, i.e., the deposition of HR4-DOPA film using spin coating and the passivation of microwell plateaus by the cytophobic PDMS layer using microcontact printing, we examined two controls. One was a positive control coated with HR4-DOPA film on the entire surface, while the other was a negative control having an untreated PDMS surface. Cell adhesion assays were conducted for both of the controls by seeding HeLa cells (cell density,  $1.0 \times 10^6$  cells/ml) and incubating for 3 h. For the positive

control, HeLa cells adhered to the plateaus coated with the HR4-DOPA film, as well as the inner microwells. In contrast, adhered HeLa cells were not observed on any surface in the negative control.

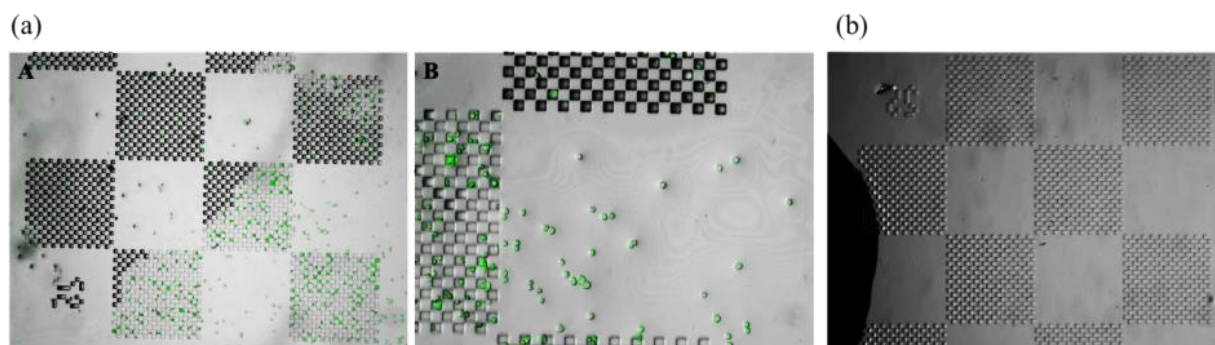


**Figure 6.11:** HeLa cell adhesion on the control surfaces. HeLa cells were cultured for 3 h at an initial seeding concentration of  $1.0 \times 10^6$  cell/ml. The cells were stained green with 5(6)-carboxyfluorescein diacetate n-succinimidyl ester (CFSE). All images depict overlapped fluorescent photomicrographs.

- (a) Photomicrographs of a positive control coated with HR4-DOPA on the entire PDMS surface after oxygen plasma treatment. [A] The image was taken at  $3\times$  magnification. [B] The image was taken at  $10\times$  magnification.
- (b) Photomicrograph of a negative control having an untreated PDMS surface. The image was taken at  $3\times$  magnification.

### 6.3.4 HeLa cell occupancy of a microwell array

To investigate the optimal cell density for preparation of the single-cell microwells, we used a narrow range of cell concentrations, testing  $0.5 \times 10^6$ ,  $1.0 \times 10^6$ , and  $2.0 \times 10^6$  cells/ml. A previous study suggested that a cell concentration of  $1.0 \times 10^6$  cells/ml was optimal for isolated single-cell arrays; however, 10-fold increments (i.e.,  $1 \times 10^5$ ,  $1 \times 10^6$ , and  $1 \times 10^7$  cells/ml) were used, rather than our 2-fold increments in the current study [114].

For all experiments, we used a cell incubation time of 6 h because these cell populations were shown to exhibit insignificant growth during the first 6 h of incubation, with only a 9% increase in the number of cells during this time, as described in **Chapter 3**. After this incubation, HeLa cell occupancies were investigated in terms of cell concentrations for each depth (i.e., 10, 25, and 40  $\mu\text{m}$ ).

**Table 6.2:** Microwell arrays (size,  $25 \times 25 \mu\text{m}^2$ ; depth,  $10 \mu\text{m}$ ) coated with the HR4-DOPA film for assaying HeLa cell occupancy of microwells.

Fluorescent photomicrographs of HeLa cells in the arrayed microwells coated with the HR4-DOPA layer after 6 h of culture at various initial cell concentrations ( $0.5 \times 10^6$ ,  $1.0 \times 10^6$ , or  $2.0 \times 10^6$  cells/ml) in untreated polystyrene 6-well plates containing RPMI 1640 medium with 10% FBS and 2% antibiotic solution at  $37^\circ\text{C}$ . The cells were stained green with 5(6)-carboxyfluorescein diacetate n-succinimidyl ester (CFSE). The images in the top row depict overlapped fluorescent photomicrographs, while those in the bottom row depict fluorescent photomicrographs of HeLa cells. All images were taken at  $3\times$  magnification.

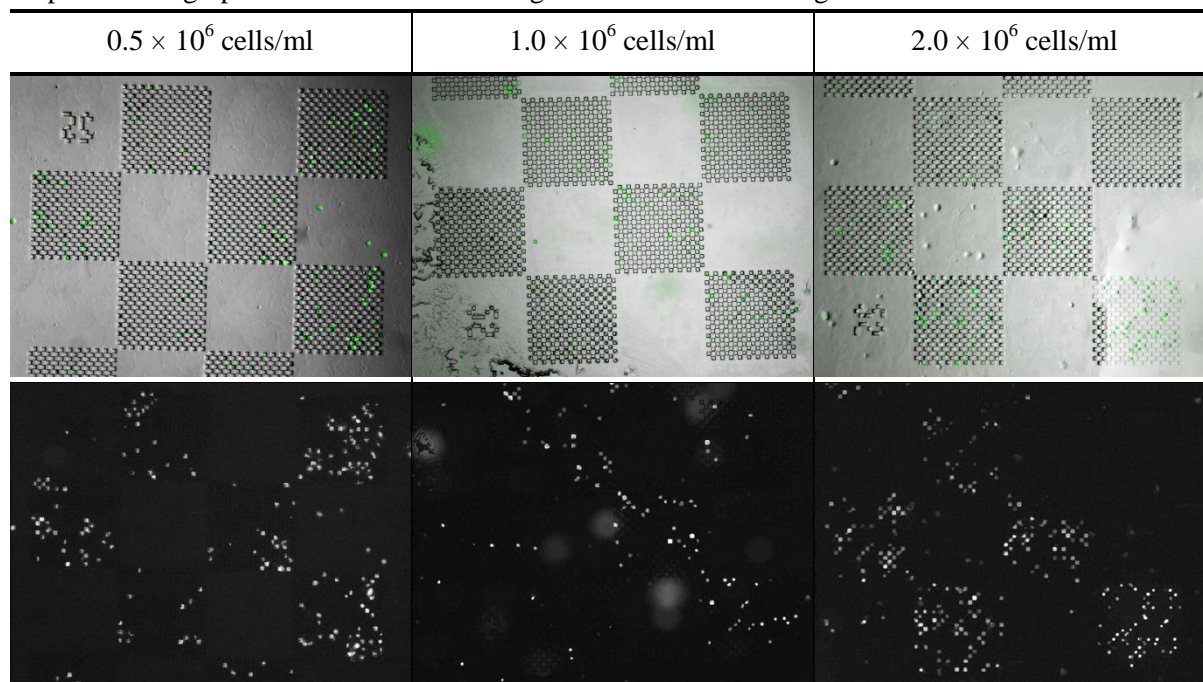


**Table 6.2** shows fluorescent photomicrographs of the HeLa cells adhering in the  $10\text{-}\mu\text{m}$ -deep microwells, and **Table 6.3** indicates the average number of cells ( $\pm$  standard deviation [SD]) found in microwells from 6 arrays, which contained 200 microwells each ( $n = 6$ ). For these measurements, occupancy was measured as single cell, 2 cells, 3 or more cells, or empty. Overall, the number of adhered HeLa cells was insufficient at all concentrations;  $174.8 \pm 9.5$  out of 200 microwells were empty at  $0.5 \times 10^6$  cells/ml,  $185.7 \pm 9.0$  were empty at  $1.0 \times 10^6$  cells/ml, and  $165.0 \pm 15.0$  were empty at  $2.0 \times 10^6$  cells/ml. Here,  $2.0 \times 10^6$  cells/ml yielded the highest single-cell occupancy of the microwells, and microwells containing 2 HeLa cells (i.e.,  $1.8 \pm 2.1$  wells) were also observed. Therefore,  $2.0 \times 10^6$  cells/ml was the optimal cell concentration for single-cell occupancy in the  $10\text{-}\mu\text{m}$ -

deep microwell array.

**Table 6.3:** The number of microwells (depth, 10  $\mu\text{m}$ ) occupied by different numbers of HeLa cells at various cell concentrations. The microwells measured  $25 \times 25 \mu\text{m}^2$  in size and were coated with the HR4-DOPA film. The initial seeding cell concentrations were  $0.5 \times 10^6$ ,  $1.0 \times 10^6$ , and  $2.0 \times 10^6$  cells/ml. The values indicate means  $\pm$  SDs.

Cell concentration (cells/ml)	1 cell	2 cells	3 or more cells	Empty
$0.5 \times 10^6$	$91.7 \pm 8.4$	$6.2 \pm 3.5$	$0.0 \pm 0.0$	$102.2 \pm 6.7$
$1.0 \times 10^6$	$134.8 \pm 11.8$	$4.3 \pm 2.1$	$0.0 \pm 0.0$	$60.8 \pm 9.8$
$2.0 \times 10^6$	$96.0 \pm 19.7$	$30.8 \pm 9.5$	$5.8 \pm 2.8$	$67.3 \pm 8.9$

**Table 6.4:** Microwell arrays (size,  $25 \times 25 \mu\text{m}^2$ ; depth, 25  $\mu\text{m}$ ) coated with the HR4-DOPA film for assaying HeLa cell occupancy of microwells.

Fluorescent photomicrographs of HeLa cells in the arrayed microwells coated with the HR4-DOPA layer after 6 h of culture at various initial cell concentrations ( $0.5 \times 10^6$ ,  $1.0 \times 10^6$ , and  $2.0 \times 10^6$  cells/ml) in untreated polystyrene 6-well plates containing RPMI 1640 medium with 10% FBS and 2% antibiotic solution at 37°C. The cells were stained green with 5(6)-carboxyfluorescein diacetate n-succinimidyl ester (CFSE). The images in the top row depict overlapped fluorescent photomicrographs, while those in the bottom row depict fluorescent photomicrographs of HeLa cells. All images were taken at 3 $\times$  magnification.

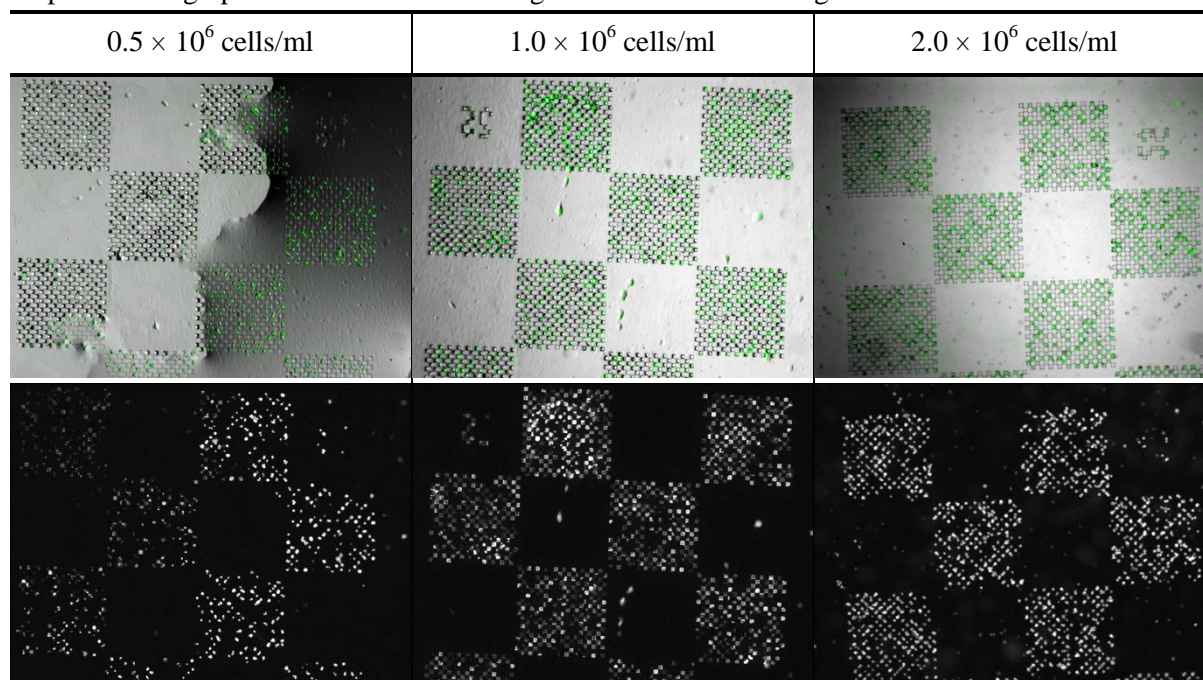


**Table 6.4** shows fluorescent photomicrographs of HeLa cells positioned in the 25- $\mu\text{m}$ -deep microwells, and **Table 6.5** indicates the average number of microwells occupied with

different numbers of HeLa cells (e.g., 0, 1, 2, or 3 or more cells) from 6 arrays, which contained 200 microwells each ( $n = 6$ ). Among the tested cell concentrations, the  $1.0 \times 10^6$  cells/ml concentration had the greatest number of singly occupied microwells (approximately 135) and the smallest number of empty microwells (approximately 61). Approximately 37 microwells contained 2 or more cells in the  $2.0 \times 10^6$  cell/ml array, which yielded a lower single-cell occupancy (96 microwells) than that of  $1.0 \times 10^6$  cell/ml. Thus, in the case of 25- $\mu$ m-deep microwells,  $1.0 \times 10^6$  cells/ml was the optimal cell concentration for single-cell analysis.

**Table 6.5:** The number of microwells (depth, 25  $\mu$ m) occupied by different numbers of HeLa cells at various cell concentrations. The microwells measured  $25 \times 25 \mu\text{m}^2$  in size and were coated with the HR4-DOPA film. The initial seeding cell concentrations were  $0.5 \times 10^6$ ,  $1.0 \times 10^6$ , and  $2.0 \times 10^6$  cells/ml. The values indicate means  $\pm$  SDs.

Cell concentration (cells/ml)	1 cell	2 cells	3 or more cells	Empty
$0.5 \times 10^6$	$91.7 \pm 8.4$	$6.2 \pm 3.5$	$0.0 \pm 0.0$	$102.2 \pm 6.7$
$1.0 \times 10^6$	$134.8 \pm 11.8$	$4.3 \pm 2.1$	$0.0 \pm 0.0$	$60.8 \pm 9.8$
$2.0 \times 10^6$	$96.0 \pm 19.7$	$30.8 \pm 9.5$	$5.8 \pm 2.8$	$67.3 \pm 8.9$

**Table 6.6** shows fluorescent photomicrographs of HeLa cells attached in the 40- $\mu$ m-deep microwells, and **Table 6.7** indicates the average number of microwells occupied with different numbers of HeLa cells (e.g., 0, 1, 2, or 3 or more cells) from 6 arrays, containing 200 microwells each ( $n = 6$ ). At the  $1.0 \times 10^6$  cells/ml concentration, an average of 18.0 microwells had 2 or more cells, while 41.0 microwells contained 2 or more cells at the  $2.0 \times 10^6$  cells/ml concentration. Thus, for 40- $\mu$ m-deep microwells,  $1.0 \times 10^6$  cells/ml was found to be the optimal cell concentration for cell occupancy. Moreover, an average of 96.8 microwells were occupied by single cells at the  $1.0 \times 10^6$  cells/ml concentration, which was greatest number of singly occupied microwells, but was still less than that of 25- $\mu$ m-deep microwells (134.8). Moreover, a cell concentration of  $1.0 \times 10^6$  cells/ml yielded the fewest

empty microwells (85.2), which also suggested less efficient cell occupancy in these 40- $\mu\text{m}$ -deep microwells than in the 25- $\mu\text{m}$ -deep microwells (60.8).

**Table 6.6:** Microwell arrays (size,  $25 \times 25 \mu\text{m}^2$ ; depth,  $40 \mu\text{m}$ ) coated with the HR4-DOPA film for assaying HeLa cell occupancy.

Fluorescent photomicrographs of HeLa cells in the arrayed microwells coated with the HR4-DOPA layer after 6 h of culture at various initial cell concentrations ( $0.5 \times 10^6$ ,  $1.0 \times 10^6$ , and  $2.0 \times 10^6$  cells/ml) in untreated polystyrene 6-well plates containing RPMI 1640 medium with 10% FBS and 2% antibiotic solution at  $37^\circ\text{C}$ . The cells were stained green with 5(6)-carboxyfluorescein diacetate n-succinimidyl ester (CFSE). The images in the top row depict overlapped fluorescent photomicrographs, while those in the bottom row depict fluorescent photomicrographs of HeLa cells. All images were taken at  $3\times$  magnification.

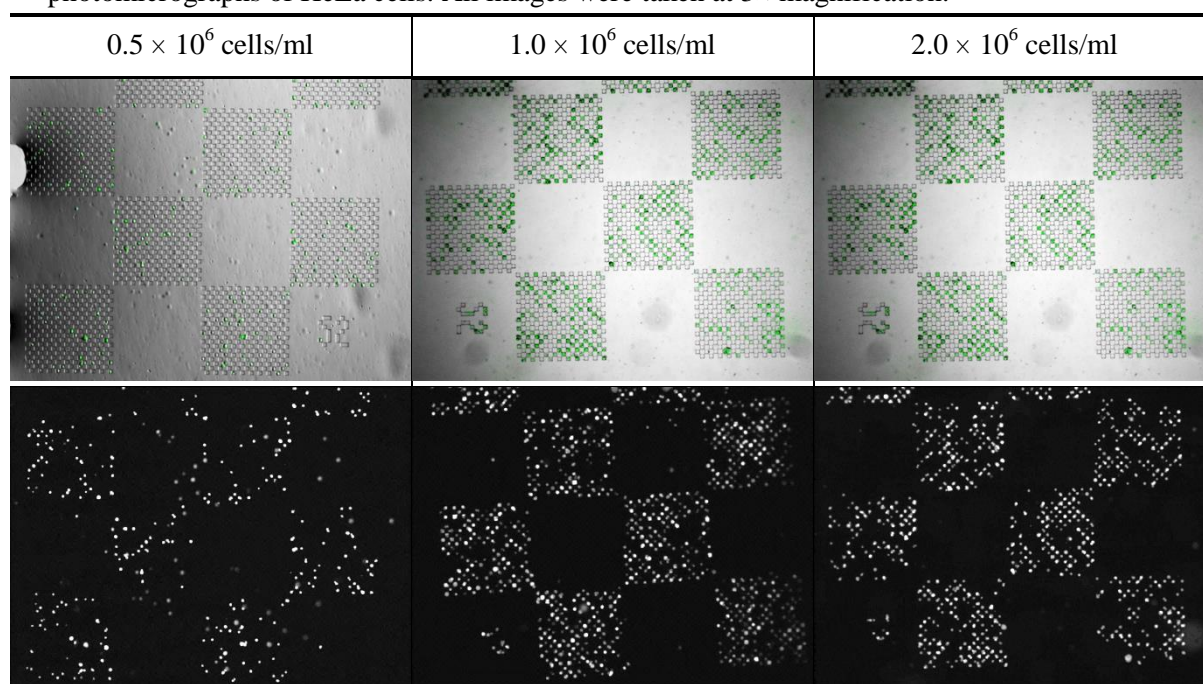


**Table 6.7:** The number of microwells (depth,  $40 \mu\text{m}$ ) occupied with different numbers of HeLa cells at various cell concentrations. The microwells measured  $25 \times 25 \mu\text{m}^2$  and were coated with the HR4-DOPA film. The initial seeding cell concentrations were  $0.5 \times 10^6$ ,  $1.0 \times 10^6$ , and  $2.0 \times 10^6$  cells/ml. The values indicate means  $\pm$  SDs.

Cell concentration (cells/ml)	1 cell	2 cells	3 or more cells	Empty
$0.5 \times 10^6$	$32.5 \pm 3.5$	$3.3 \pm 1.3$	$0.2 \pm 0.3$	$164.0 \pm 4.0$
$1.0 \times 10^6$	$96.8 \pm 5.9$	$16.5 \pm 6.3$	$1.5 \pm 1.3$	$85.2 \pm 8.2$
$2.0 \times 10^6$	$57.3 \pm 8.4$	$30.2 \pm 4.1$	$10.5 \pm 4.0$	$102.0 \pm 7.3$

Next, we graphically compared cell occupancies of the cuboidal microwells for the tested microwell depths (i.e., 10, 25, and 40  $\mu\text{m}$ ) and cell concentrations (i.e.,  $0.5 \times 10^6$ ,  $1.0 \times 10^6$ , or  $2.0 \times 10^6$  cells/ml), as depicted in **Figure 6.12**. Both of these conditions affected HeLa cell occupancy of the microwell array. Among the different cell concentrations tested in this study, the  $1.0 \times 10^6$  cells/ml concentration yielded the highest single-cell occupancy and lowest number of empty wells; additionally, the  $2.0 \times 10^6$  cells/ml concentration generally yielded the greatest number of multicell wells. The 25- $\mu\text{m}$ -deep microwells exhibited the highest level of single-cell occupancy for all cell concentrations. Among the 9 ( $3 \times 3$ ) different conditions, the highest single-cell occupancy (67.4%) was obtained at a HeLa cell concentration of  $1.0 \times 10^6$  cells/ml in 25- $\mu\text{m}$ -deep microwells, which we considered to be the most optimal conditions for single-cell analysis.

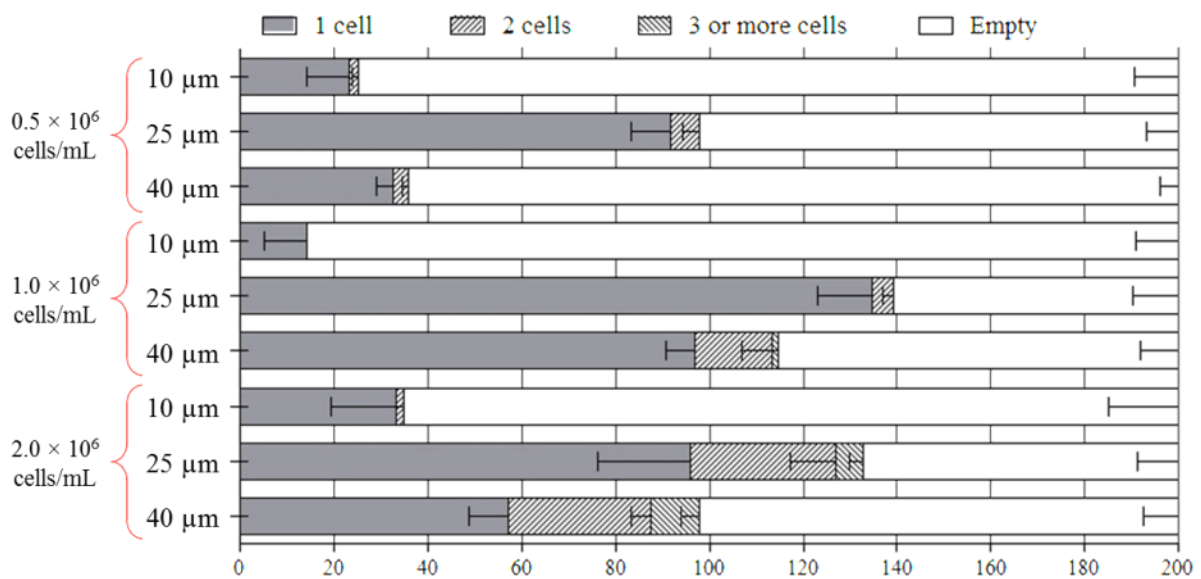


**Figure 6.12:** HeLa cell occupancy in 6 microwell arrays under two different experimental conditions: cell concentration and microwell depth.

Each arrays comprised 200 microwells. Cell occupancy was assessed in microwells of various depths (i.e., 10, 25, or 40  $\mu\text{m}$ ) and at various cell concentrations (i.e.,  $0.5 \times 10^6$ ,  $1.0 \times 10^6$ , or  $2.0 \times 10^6$  cells/ml). The horizontal bars indicate the average number of microwells occupied by different numbers of HeLa cells (i.e., 0, 1, 2, or 3 or more). The error bars indicate the SD.

## 6.4. Discussion

### 6.4.1 Physical dimension of the microwell array

#### 6.4.1.1 Microwell size for HeLa cells

In a previous **chapter 3**, we investigated the percentage of HeLa cells smaller than the microwell size (diameter,  $\leq 25 \mu\text{m}$ ) from the cell size distribution, as measured by CASY cell counter (see **Figure 3.4**) using Image J software as a function of stack analysis. Viable HeLa cells ranged in size from 12 to 30  $\mu\text{m}$ , and the percentage of HeLa cells measuring between 12 and 25  $\mu\text{m}$  was 93.6%. Therefore, we expected that most HeLa cells were able to be loaded into the microwells in this study.

#### 6.4.1.2 Surface area of the microwells

The areal size of a cell-adhesive surface strongly regulates cell behaviors, such as cell growth, migration, proliferation, and viability. A surface area larger than 3000  $\mu\text{m}^2$  was suggested to be optimal for long-term cell culture, providing cells with adequate space to spread, increasing cell growth, and minimizing apoptosis [45, 72]. The surface areas of the microwells (size,  $25 \times 25 \mu\text{m}$ ) coated with the cell adhesive HR4-DOPA film differed for the various microwell depths, i.e., 1625  $\mu\text{m}^2$  for the 10  $\mu\text{m}$  depth, 3125  $\mu\text{m}^2$  for the 25  $\mu\text{m}$  depth, and 4625  $\mu\text{m}^2$  for the 40  $\mu\text{m}$  depth. Therefore, the microwells should be deeper than 25  $\mu\text{m}$  in order to permit the maintenance of the native 3D cellular morphology and promote normal cell function during single cell analysis.

#### 6.4.1.3 Volume of the microwells

Total volumes were 6250  $\mu\text{m}^3$  for 10- $\mu\text{m}$ -deep microwells, 15,625  $\mu\text{m}^3$  for 25- $\mu\text{m}$ -deep microwells, and 25,000  $\mu\text{m}^3$  for 40- $\mu\text{m}$ -deep microwells. The measured HeLa cell volume was 2385  $\mu\text{m}^3$  (see **Chapter 3**); therefore, microwells of 10, 25, and 40  $\mu\text{m}$  depths could theoretically contain 2.63, 6.55, and 10.48 HeLa cells, respectively. Thus, we were able to

observe the presence of multiple HeLa cells per microwell (see **Figure 6.13**).

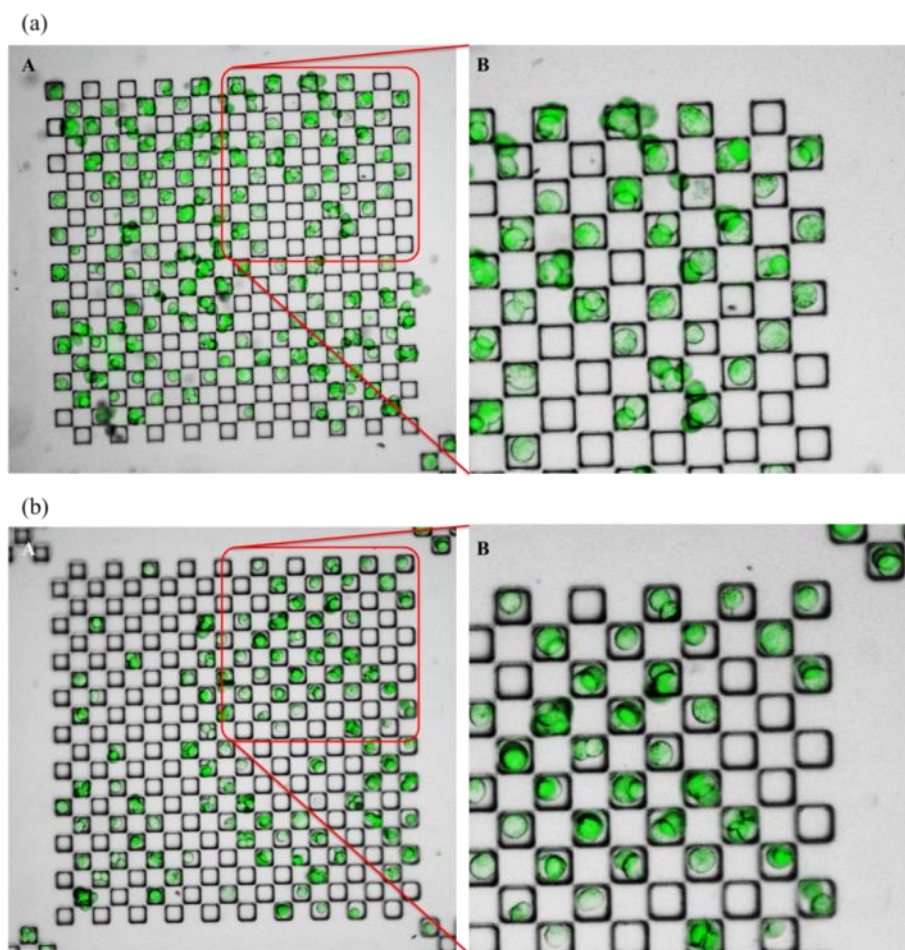


**Figure 6.13:** Microwells containing 2 or more HeLa cells at the seeding cell concentration of  $2.0 \times 10^6$  cells/ml.

- (a) Fluorescent photomicrographs of HeLa cells in arrayed square microwells (depth, 25  $\mu\text{m}$ ) coated with HR4-DOPA. Photomicrographs were taken at 10 $\times$  magnification [A] and 20 $\times$  magnification [B].
- (b) Fluorescent photomicrographs of HeLa cells in arrayed square microwells (depth, 40  $\mu\text{m}$ ) coated with HR4-DOPA. Photomicrographs were taken at 10 $\times$  magnification [A] and 20 $\times$  magnification [B].

The microwell size of  $25 \times 25 \mu\text{m}^2$ , which was about 10  $\mu\text{m}$  larger than the size of a HeLa cell [38, 70, 80, 118-120], was optimal for single-cell arrays using HeLa cells; however, the square shape was unsuitable in terms of the volumetric analysis of the microwell. Therefore, in future studies, the microwell shape should be redesigned to meet the following criteria: (1) the surface area should be larger than  $3000 \mu\text{m}^2$ , and (2) the volume of each microwell should not exceed the volume of two target cells.

#### **6.4.1.4 Depth of the microwells**

The 25- $\mu\text{m}$ -deep microwells showed the highest single-cell occupancy of all tested cell concentrations, indicating that 25  $\mu\text{m}$  was the ideal depth for the  $25 \times 25 \mu\text{m}^2$  microwells. These results were supported by previous studies demonstrating that the optimal ratio of size to depth was approximately 1 [38, 117]. Rettig and Folch [38] demonstrated that single-cell occupancy increased dramatically as the ratio of size to depth increased up to 1, after which single-cell occupancy decreased slightly; this tendency was also observed in our current study.

#### **6.4.1.5 Number of microwells in the arrays**

The highest single-cell occupancy obtained in this study was  $134.8 \pm 11.8$  microwells per array; this occurred in the 25- $\mu\text{m}$ -deep microwells at a concentration of  $1.0 \times 10^6$  cells/ml. From these data, we can expect to achieve single-cell occupancy with HeLa cells in 1072 microwells from 8 microwell arrays in the  $2 \times 2 \text{ mm}^2$  area. Thus, since the single-cell occupancy achieved in this study satisfied the requirement for adequate sets of data (i.e., 1000 single cells) in advanced single-cell analysis techniques [55] and since the array-to-array variation, i.e., the SD of the number of microwells containing single cells relative to the total number of microwells, was 5.9%, we can conclude that this microwell array had the capacity for use in quantitative analyses in advanced single-cell analysis techniques. Moreover, after the elimination of passivated areas, the density of microwells can be doubled and the technique becomes more suitable for high-throughput applications.

### **6.4.2 Cell conditions**

#### **6.4.2.1 Cell concentration**

A seeding cell concentration of  $1.0 \times 10^6$  cells/ml is commonly used for static culture [70, 110, 114, 116, 117]. Liu *et al.* [114] showed the effect of cell concentration on single-cell occupancy by varying cell concentrations from  $1 \times 10^5$  to  $1 \times 10^7$  cells/ml. At cell

densities of  $1 \times 10^6$  and  $1 \times 10^5$  cell/ml, single-cell occupancies of 90% and 84%, respectively, were achieved in Ramos cells. Higher cell seeding densities (exceeding  $1 \times 10^6$  cells/ml) did not have an obvious effect on cell occupancy. Thus, their results indicated that  $1.0 \times 10^6$  cells/ml was the optimal concentration for isolated single-cell arrays.

For this reason, we used  $1.0 \times 10^6$  cell/ml as the standard cell concentration, but performed a more detailed investigation of the effects of cell concentration on single-cell occupancy of the microwell array, using a narrower range of concentrations (from  $0.5 \times 10^6$  to  $2.0 \times 10^6$  cells/ml). Among these tested cell concentrations, the optimal HeLa cell concentration was  $1.0 \times 10^6$  cells/ml, while  $2.0 \times 10^6$  cells/ml exhibited adverse effects on single-cell occupancy, often yielding multiple cells per microwell.

#### **6.4.2.2 Washing the non-adherent cells**

Cell occupancy, i.e., the number of microwells occupied with any number of HeLa cells, was expected to be highest at  $2.0 \times 10^6$  cells/ml because a greater number of cells would have the chance to settle into the microwells. However, while this hypothesis was correct when we compared  $0.5 \times 10^6$  and  $1.0 \times 10^6$  cells/ml, cell occupancy at  $2.0 \times 10^6$  cells/ml (132.6 microwells) was lower than that at  $1.0 \times 10^6$  cells/ml (139.2 microwells).

This result may be due to the strong cell-cell interactions of HeLa cells, a cell line that is derived from epithelial cells, which are known to pack densely to form the epithelium, interacting and attaching to each other [157]. At  $2.0 \times 10^6$  cells/ml, HeLa cells attached to each other and formed cell aggregates, with balls of cells observed and single cells anchored on the microwell surface; this may have created tremendously increased shear stress through fluid flow during washing-off of nonadherent HeLa cells, a step included in our protocol. This strong shear stress may detach these balls of cells, even when the cells were adhered to the cell-adhesive HR4-DOPA surface on the microwells.

### 6.4.2.3 Cell types

Interactions between cells placed in the microwell and the surface of the microwell are strongly dependent on the characteristics of the cells, whether adherent or nonadherent. Given the cell adhesive surface of the microwell, adherent cells firmly adhere to the microwell while nonadherent cells are mechanically trapped inside the microwell. Because of this, higher single-cell occupancy is expected for adherent cells than for nonadherent cells.

However, single-cell occupancy of nonadherent cells is often higher than that of adherent cells [38, 114, 118]; for example, the single-cell occupancy of nonadherent Ramos cells reached at 90% [114], while adherent HeLa cells showed single-cell occupancy of 83.19% [118]. This difference in single-cell occupancy between adherent and nonadherent cells may be due to the different shapes of these cells. The morphological features of adherent versus nonadherent cells are compared in **Figure 6.14**.

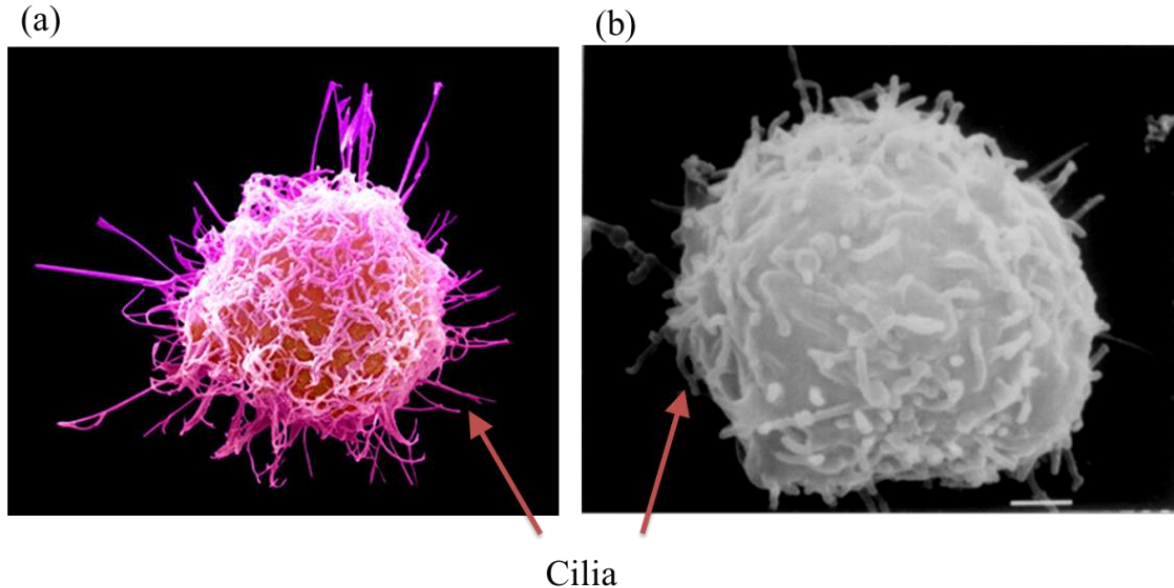


**Figure 6.14:** Different morphologies of adherent (anchorage-dependent) and nonadherent (anchorage-independent) cells.

- (a) Scanning electron microscope image of an adherent HeLa cell. HeLa cells have long, narrow cilia on their surfaces (<http://www.smithsonianmag.com>).
- (b) Scanning electron microscope image of a nonadherent Jurkat cell [239]. Jurkat cells have short, thick cilia on their surfaces.

Adherent cells have long and narrow cilia on their surfaces in order to interact with and attach to each other or survive by attaching to the surface [157], while nonadherent cells have short, thick cilia on their surfaces. The long cilia of adherent cells may interfere with cell loading into the microwells. Therefore, we can conclude that the achievement of 67.5% single-cell occupancy (the highest value we obtained) was an acceptable result for adherent HeLa cells in this experiment.

## 6.5. Conclusion

In this study, we fabricated a microwell array for single-cell analysis that was expected to preserve the native 3D morphology and functionality of HeLa cells through construction of microwells with a cell-adhesive inner surface using soft lithography and microcontact printing. Microwells were shaped as squares (size,  $25 \times 25 \mu\text{m}^2$ ) according to the physical dimensions of HeLa cells (diameter,  $16.17 \pm 2.4 \mu\text{m}$ ). We fabricated 8 arrays, with each array containing 200 microwells, in a  $2 \times 2 \text{ mm}^2$  area.

We also investigated the optimal conditions for achievement of single-cell occupancy with HeLa cells, defining optimal microwell depth (i.e., 10, 25, or  $40 \mu\text{m}$ ) and cell concentration (i.e.,  $0.5 \times 10^6$ ,  $1.0 \times 10^6$ , or  $2.0 \times 10^6$  cells/ml). Microwells deeper than  $25 \mu\text{m}$  provided cell-adhesive surface areas larger than  $3000 \mu\text{m}^2$ , which has been suggested to improve long-term cell culture by helping cells adequately spread, increasing cell growth, and minimizing apoptosis. However, the volumes of all microwells was large enough to allow multiple HeLa cells to adhere (i.e., 2.63–10.48 cells), and a change in the shape of the microwell may be necessary in order to achieve less than 2 cells per microwell.

HeLa cells are adherent cells that exhibit strong cell-cell interactions due to their long, narrow cilia. Therefore, the densest cell concentration ( $2.0 \times 10^6$  cells/ml) did not yield the highest single-cell occupancy due to HeLa cell aggregation, which increased shear stress

during the washing process, and disturbance of the cilia.

In various microwell depths and cell concentrations, the highest single-cell occupancy achieved in this study was 67.5% in 25- $\mu\text{m}$ -deep microwells at  $1.0 \times 10^6$  cells/ml; these data indicated that we could achieve adequate data (i.e., 1072 singly occupied microwells) for advanced single-cell analysis techniques. Moreover, the presence of only 5.9% array-to-array variation demonstrated the suitability of this microwell array for accurate quantification in single-cell analyses. Therefore, a microwell size of  $25 \times 25 \mu\text{m}^2$ , with a 25  $\mu\text{m}$  depth, and a cell density of  $1.0 \times 10^6$  cells/ml were optimal conditions for single-cell occupancy with HeLa cells and verified the applicability of this technique as a high-throughput single-cell-based assay.

## Chapter 7. Discussion

In this study, the microwell array was coated with a cell-adhesive dopaminergic mesoporous inorganic-organic hybrid resin (HR4-DOPA) film on the inner surface to control HeLa cell shape and maintain native cell morphology and functionality. In order to obtain the optimal biological conditions and physical dimensions of the microwells, various biological/physical parameters used in previous studies were reviewed.

### 7.1. Biological conditions used in the cellular experiments

For assessing cell adhesion, viability, and single-cell occupancy of the microwell array for drug discovery, HeLa cells (cancerous cell line) were used at a density of  $1.0 \times 10^6$  cells/ml, and the medium used was RPMI 1640 medium supplemented with 10% FBS and 2% penicillin/streptomycin.

#### 7.1.1 HeLa cells

In this study, we chose HeLa cells among the potential mammalian cell models for microengineering because of their biological relevance to cancer treatment and their ability to adhere to hydrophilic surfaces created by microtechniques [39-42, 143]; HR4-DOPA was used as cell- adhesive material because its water contact angle (wettability,  $62^\circ$ ) is within the range for cell adhesion ( $40\text{--}70^\circ$ ).

HeLa cells, derived from epithelial cells, pack densely to form the epithelium, interact with and attach to each other [157], and have long, narrow cilia on the plasma membrane. Moreover, the measured diameter of HeLa cells could not be used to accurately predict the volume, and vice versa, due to the spheroidal shape of normal HeLa cells undergoing mitosis. Therefore, these biological characteristics, morphological features, and physical dimensions of HeLa cells provided unexpected results such as inconstant settling velocity, prolonged

settling time, and less than 70% single cell occupancy.

#### **7.1.1.1 Settling velocity of HeLa cells**

The strong interactions between HeLa cells and their long cilia violate the assumptions of Stokes' law for calculating the settling velocity of HeLa cells: (1) particles do not interfere with each other, and (2) particles have a smooth surface. The spheroidal shape (eccentricity, 0.507) also violates the assumptions of Stokes' law in which particles are spheres. These violations of the assumptions of Stokes' law caused the inconstant settling velocity to function as a Boltzmann sigmoidal curve and prolonged settling time by 46.1% of the mathematically expected value.

#### **7.1.1.2 Single-cell occupancy in the microwells**

The biological characteristics of HeLa cells may interfere with cell loading into the microwells; the achievement of 67.5% single-cell occupancy (the highest value we obtained) was an acceptable result for adherent HeLa cells, although this value is less than that for nonadherent cells ( $\geq 90\%$ ) with short cilia [114]. HeLa cells attached to each other and formed cell aggregates, with balls of cells and single cells anchored to the microwell surface; this may have tremendously increased shear stress during washing to remove nonadherent cells. This strong shear stress may detach these balls of cells, even when the cells were adhered to the HR4-DOPA surface.

#### **7.1.1.3 Cell concentration**

We investigated the effect of cell concentration on single-cell occupancy in microwell arrays. Liu *et al.* [114] demonstrated that the concentration of  $1.0 \times 10^6$  cells/ml was optimal for an isolated single-cell array by using cell concentrations varying from  $1 \times 10^5$  to  $1 \times 10^7$  cells/ml (10-fold increments), but we performed a more detailed investigation of the effects of cell concentration on single-cell occupancy of the microwell array by using a narrower

range of concentrations (from  $0.5 \times 10^6$  to  $2.0 \times 10^6$  cells/ml; 2-fold increments). However, we also obtained the highest single cell occupancy for the microwell array at a HeLa cell density of  $1.0 \times 10^6$  cells/ml.

### **7.1.2 FBS concentration in the medium**

Serum, e.g., fetal bovine serum (FBS) or fetal calf serum (FCS), is a common supplement in cell culture media and is used at a concentration of 10% of the total volume [225]; we also used RPMI 1640 medium supplemented with 10% FBS in all the experiments. However, the amount of serum in the medium plays a primary role in pre-adsorption of cell-adhesive ECM proteins, thereby regulating cellular behavior [88, 92, 163, 165, 168, 172, 174-178, 180]. The optimal amount of serum in medium is 0.1% for fibronectin adsorption, cell spreading, and cell adhesion [165]. Therefore, a more detailed investigation of FBS concentration is required to explain the effects of FBS on cell adhesion to HR4-DOPA.

## **7.2. Dopaminergic mesoporous inorganic-organic hybrid resin**

We used the HR4-DOPA film, modified from a previous mesoporous inorganic-organic hybrid resin (HR4) [47, 158], as a cell-adhesive surface with long-term stability in aqueous environments and good adhesive characteristics. HR4-DOPA demonstrated the ability of dopamine to stabilize a silane-coupling agent, which is unstable and aggregated in an aqueous environment, over a 2-year period.

### **7.2.1 HeLa cell adhesion on HR4-DOPA**

In the HeLa cell adhesion assay, HR-DOPA exhibited worse adhesive performance than HR4 over 6 h; the differences were not significant at some time points despite the long-term stability of HR4-DOPA. The results may be caused by the fact both that the optimal water contact angle for HeLa cells is  $\sim 50^\circ$  and that dopamine concentrations greater than  $10^{-4}$  M have a negative effect on cell adhesion due to changes in cytoplasmic globular actin [224].

HR4-DOPA (water contact angle,  $62^\circ$ ) is inferior to HR4 (water contact angle,  $49^\circ$ ) for HeLa cell adhesion, although it is in the range of moderate wettability, i.e.,  $40\text{--}70^\circ$  [51, 88, 158]. Moreover, the disadvantage of HR4-DOPA may be due to dopamine in the medium, released from the HR4-DOPA film, which contains 1.03 mol% dopamine.

### **7.2.2 HeLa cell viability of HR4-DOPA**

HeLa cell viability was 86.1% on HR4-DOPA and did not differ significantly from the control, which consisted of XTT reagent plus HeLa cells cultured in substrate-free medium. However, the minimum viability of HeLa cells on HR4-DOPA cannot be disregarded because dopamine can deplete various cancer cells and might serve as an anti-tumor agent in clinical treatment [228-230]. HR4-DOPA should be tested using a normal mammalian cell line in order to confirm cell viability.

## **7.3. Physical dimensions of the microwell array**

### **7.3.1 Physical dimensions of the microwell**

The physical dimensions of the HR4-DOPA film-coated microwells were designed to achieve high single-cell occupancy. The dimensions of the square microwells were  $25 \times 25 \mu\text{m}^2$ , that is, slightly larger than the diameter of HeLa cells ( $16.17 \pm 2.4 \mu\text{m}$ ) [38, 70, 80, 118-120]. The highest single cell occupancy was provided by microwells with a depth of  $25 \mu\text{m}$ , supported by the fact that the optimal size: depth ratio was  $\sim 1$  in previous studies [38, 117]. The cell-adhesive surface of the cuboidal microwells ( $25 \times 25 \times 25 \mu\text{m}^3$ ) was  $3125 \mu\text{m}^2$ , which is larger than the minimum area suggested for long-term cell culture in order to ensure adequate spreading; adequate spreading is important for increasing cell growth and thereby minimizing apoptosis [45, 72].

However, microwells of 10, 25, and 40  $\mu\text{m}$  depths could theoretically contain 2.63, 6.55, and 10.48 HeLa cells, respectively. Thus, we were able to observe the presence of multiple

HeLa cells per microwell. In future studies, the microwell shape should be redesigned to meet the following criteria: (1) the surface area should be larger than  $3000 \mu\text{m}^2$  and (2) the volume of each microwell should not exceed the volume of 2 target cells.

### **7.3.2 Physical dimensions of the microwell array for single-cell occupancy**

After testing various microwell depths and cell concentrations, the highest single-cell occupancy achieved in this study was 67.5% (i.e., 1072 singly occupied microwells) in 25- $\mu\text{m}$ -deep microwells at  $1.0 \times 10^6$  cells/ml; these data indicated that we could achieve adequate throughput: 1000 single cells for advanced single-cell analysis techniques [55]. Moreover, the 5.9% array-to-array variation demonstrated the ability of this microwell array to be used for accurate quantification. Therefore, a microwell size of  $25 \times 25 \mu\text{m}^2$ , with a 25- $\mu\text{m}$  depth and a density of  $1.0 \times 10^6$  cells/ml were optimal for single-cell occupancy with HeLa cells and verified the feasibility of this technique for high-throughput single-cell-based assays.

## **7.4. System integration**

### **7.4.1 Microfluidic biochip**

Microfluidic biochips are designed for immobilizing single cells, mimicking the *in vivo* microenvironment, and application to high-throughput drug screening with cellular analysis. The microwell array is essential to maintain the native morphology and functionality of experimental cells and provide results that predict *in vivo* responses during drug discovery.

### **7.4.2 Cell-based biosensors**

Cell-based biosensors are portable sensing devices that contain living cells and detect physiological changes that are induced in biological components (i.e., enzyme, antibody, animal or plant cell, oligonucleotide, lipid, and microorganisms) by exposure to environmental stimuli (i.e., toxicants, pathogens, or other chemical/biological agents), and

assess these changes in real-time by using physical transducers (i.e., an electrode, an optical fiber, or a vibrating quartz) [240-243].

The single-cell microwell array for 3D cell culture can increase the feasibility of cell-based biosensors for high-throughput screening of bioprocess-produced antibodies and candidate drug screening, including target identification, ligand fishing, assay development, lead selection, and manufacturing quality control [240-243], and provides remarkable real-time information regarding cellular chemistry at the molecular level [20, 27].

## Chapter 8. Conclusion

In this study, we fabricated a microwell array for isolated single-cell analysis that maintains native cell morphology and functionality for 3D *in vitro* models for high-throughput drug discovery using HeLa cells and dopaminergic mesoporous inorganic-organic hybrid resin (HR4-DOPA). HeLa cells are widely used for their biological relevance to cancer and their ability to adhere to hydrophilic surfaces created by microtechniques; HR4-DOPA stabilizes a silane-coupling agent through its dopamine modification.

The physical properties of HeLa cells were investigated for potential application in microbiochips. HeLa cell populations exhibited only a 9% increase in the number of cells in the first 6 h of incubation. We could assess cell adhesion on HR4-DOPA in the absence of apoptosis due to overproliferation; single-cell occupancy in the microwells inhibited cell growth in the wells. This may explain their spheroidal shape during cell division. These measurements were used to theoretically analyze and measure the settling velocity and time. Stokes law was used to calculate the theoretical Stokes velocity of the HeLa cells, and experiments to investigate settling velocity were performed in a PS cuvette (internal dimensions,  $10 \times 10 \times 20 \text{ mm}^3$ ) at  $23^\circ\text{C}$ . This timed study showed that the settling velocity developed slowly during the initial phase and decreased exponentially during the final phase, leading to a Boltzmann sigmoid-shaped curve, and prolonged the settling time by 46.1% from the theoretical time. Although the assumptions of Stokes' law were violated by several conditions, that is, the presence of cilia, the non-perfect spherical shape of the HeLa cells, and cell-cell interactions, the measured Stokes velocity exhibited only an 11.1% deviation as compared to the theoretical velocity.

The applicability of the dopaminergic mesoporous inorganic-organic hybrid resin (HR4-DOPA) for the construction of cell-adhesive microwells was proven by the stability of a

silane-coupling agent over long-term storage (2 years); the average surface roughness of 789.35 pm, indicating that the material is smooth and should have little effect on cell adhesion; and the water contact angle of 62.08°, indicating moderate wettability for cell adhesion (i.e., 40–70°). The biocompatibility of HR4-DOPA with HeLa cells was assessed by cell adhesion and viability assays. In the cell adhesion assay, the number of adhered HeLa cells on the HR4-DOPA film initially increased within the first hour, after which growth rates remained low. Thus, significantly fewer HeLa cells adhered to HR4-DOPA than to HR4 after 3 h, collagen IV after 1 h, and all controls at 6 h. The dopamine in HR4-DOPA led to poor cell adhesion at all time points; however, the differences between HR4-DOPA and HR4 were not significant until after 3 h of incubation. During the initial phase of adhesion, HR4-DOPA was comparable to collagen IV for 45 min and fibronectin for 1 h. The optimal water contact angle for HeLa cell adhesion was ~50°, suggesting the HR4 film (49°) was better suited for HeLa cell adhesion than HR4-DOPA (62.08°). Dopamine helped achieve long-term stability of a silane-coupling agent in HR4-DOPA, but the dopamine in the medium, perhaps released from HR4-DOPA, might weaken cell adhesion. The HeLa cell viability was 86.1% that of the control because dopamine might act as an antitumor agent.

We fabricated a microwell array comprising 8 arrays – each containing 200 microwells in a  $2 \times 2\text{-mm}^2$  area – for single-cell analysis that was expected to preserve the native 3D morphology and functionality of HeLa cells through construction of microwells with an adhesive inner surface using soft lithography and microcontact printing. Microwells were shaped as squares according to the diameter of HeLa cells. After testing various microwell depths and cell concentrations, the highest single-cell occupancy achieved in this study was 67.5% in 25- $\mu\text{m}$ -deep microwells at  $1.0 \times 10^6$  cells/ml. This provided sufficient cell-adhesive surface area for long-term cell culture ( $\geq 3000 \mu\text{m}^2$ ) enabling adequate spread, increasing cell growth, and minimizing apoptosis. The presence of 1072 singly occupied microwells and

only 5.9% array-to-array variation indicated that we could achieve adequate throughput for accurate quantification in advanced single-cell analysis techniques.

We determined that microwells coated with HR4-DOPA are feasible for use in a high-throughput single-cell-based assay for drug discovery. Given that the microwell arrays are integrated in a microfluidic biochip, they can mimic the *in vivo* microenvironment; we can thus predict *in vivo* responses through high-throughput, isolated single-cellular analysis. Additionally, the single-cell array of microwells for 3D cell culture can increase the feasibility of cell-based biosensors for high-throughput screening of bioprocess-produced antibodies and candidate drug screening including target identification, ligand fishing, assay development, lead selection, and manufacturing quality control, and provide remarkable real-time information regarding cellular chemistry at the molecular level.



## Chapter 9. Future Work

### 9.1. Integration of cell-based biosensors in microwells

Cell-based biosensors are portable sensing devices that contain living cells and detect physiological changes of biological components (i.e., enzyme, antibody, animal or plant cell, oligonucleotide, lipid, or microorganisms) induced by exposure to environmental stimuli (i.e., toxicants, pathogens, or other chemical/biological agents) in real time by using physical transducers (i.e., electrode, optical fiber, or vibrating quartz) [240-243].

The development of 3D cell culture technologies increases the feasibility of cell-based biosensors for high-throughput screening of bioprocess-produced antibodies and for candidate drug screening including target identification, ligand fishing, assay development, lead selection, and manufacturing quality control [240-243].

In this study, microwell arrays demonstrated significant biological functions as they maintained native 3D morphologies and cellular functions of anchorage-dependent cells. Therefore, given that the microwells for individual single cells array are integrated with cell-based biosensors, they can provide remarkable real-time information regarding cellular chemistry at the molecular level [20, 27].

### 9.2. Mimic *in vivo* microenvironments

A potential application for this research is a bio-cell processor for drug discovery, integrated with novel platforms such as microfluidic chips and biochips. Microfluidic chips are designed to introduce nutrient cell media and drugs via microvalves and mixers. Biochips are designed to immobilize single cells for mimicking the *in vivo* microenvironment and for application to high-throughput drug screening. A single-cell array is essential to the bio-cell processor for maintaining the native morphology and functionality of experimental cells and

providing results that better predict *in vivo* responses during drug discovery.

We planned to construct the biochip (see **Figure 9.1**) for high-throughput drug screening with microcomponents: (1) a micro cell-incubation chamber for individual cells to mimic *in vivo* environments, (2) 2 inlet ports for cell loading with vertical sheath flow to shorten settling time and for injecting anti-cancer drugs, and (3) an outlet port for waste (dead or non-adherent target cells) or to transport biological components (i.e., enzyme, antibody, animal or plant cell, oligonucleotide, lipid, or microorganisms) to biosensors.

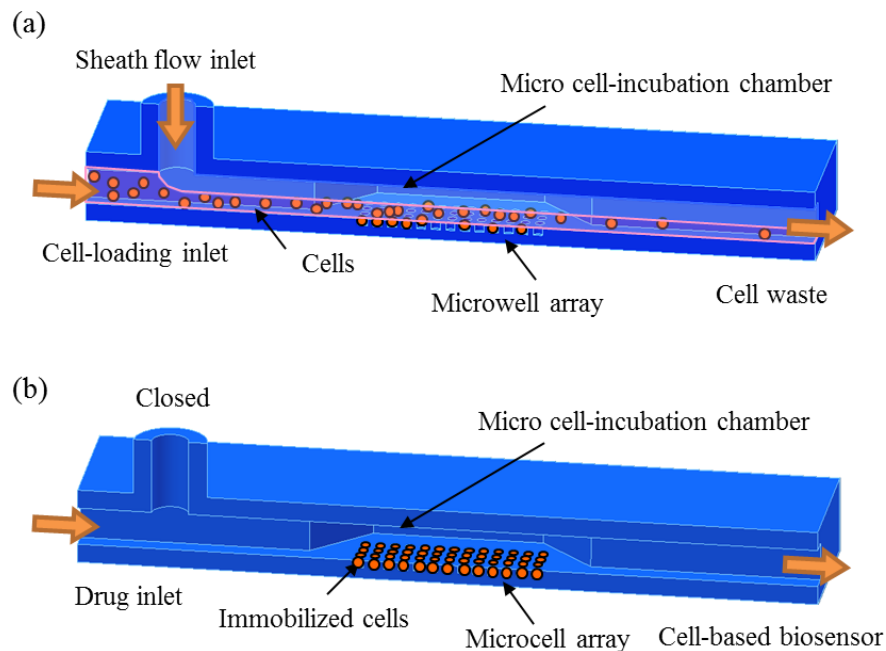


**Figure 9.1:** Microbiochip for mimicking *in vivo* microenvironments in a bio-cell processor for application to high-throughput drug screening with cellular analysis.

## References

- [1] M. Dickson and J. Gagnon, "The cost of new drug discovery and development," *Discovery medicine*, vol. 4, pp. 172-179, 2004.
- [2] "Drug Discovery and Development: Understanding the R&D Process," [http://www.innovation.org/drug\\_discovery/objects/pdf/RD\\_Brochure.pdf](http://www.innovation.org/drug_discovery/objects/pdf/RD_Brochure.pdf).
- [3] S. Morgan, P. Grootendorst, J. Lexchin, C. Cunningham, and D. Greyson, "The cost of drug development: A systematic review," *Health policy*, vol. 100, pp. 4-17, 2011.
- [4] P. Dittrich and A. Manz, "Lab-on-a-chip: microfluidics in drug discovery," *Nature Reviews Drug Discovery*, vol. 5, pp. 210-218, 2006.
- [5] J. Drews and S. Ryser, *Human disease - from genetic causes to biochemical effects: proceedings of the symposium "The Genetic Basis of Human Disease" held to celebrate the 100th anniversary of the founding of F. Hoffmann-La Roche Ltd. October 2-3, 1996, Basel*: Blackwell Science, 1997.
- [6] A. Dove, "Drug screening - beyond the bottleneck," *Nat Biotech*, vol. 17, pp. 859-863, 1999.
- [7] K. Giese, J. Kaufmann, G. J. Pronk, and A. Klippel, "Unravelling novel intracellular pathways in cell-based assays," *Drug Discovery Today*, vol. 7, pp. 179-186, 2002.
- [8] D. Falconnet, G. Csucs, H. Michelle Grandin, and M. Textor, "Surface engineering approaches to micropattern surfaces for cell-based assays," *Biomaterials*, vol. 27, pp. 3044-3063, 2006.
- [9] J. W. Gardner, V. K. Varadan, and O. O. Awadelkarim, *Microsensors, Mems, and Smart Devices*: Wiley, 2001.
- [10] F. Yang, "Electromechanical contact of microelectromechanical structure," *Journal of applied physics*, vol. 100, p. 124511, 2006.

- [11] H. Baltes and O. Brand, "CMOS-based microsensors and packaging," *Sensors and Actuators A: Physical*, vol. 92, pp. 1-9, 2001.
- [12] B. H. Weigl, R. L. Bardell, and C. R. Cabrera, "Lab-on-a-chip for drug development," *Advanced Drug Delivery Reviews*, vol. 55, pp. 349-377, 2003.
- [13] C. Monat, P. Domachuk, and B. Eggleton, "Integrated optofluidics: A new river of light," *Nature Photonics*, vol. 1, pp. 106-114, 2007.
- [14] A. Romani, *et al.*, "Capacitive sensor array for localization of bioparticles in CMOS lab-on-a-chip," *IEEE International Solid-State Circuits Conference*, vol. 1, pp. 224-225, 2004.
- [15] S. P. FitzGerald, J. V. Lamont, R. I. McConnell, and E. O. Benchikh, "Development of a high-throughput automated analyzer using biochip array technology," *Clinical chemistry*, vol. 51, pp. 1165-1176, 2005.
- [16] O. P. Kallioniemi, "Biochip technologies in cancer research," *Annals of medicine*, vol. 33, pp. 142-147, 2001.
- [17] R. Simon and G. Sauter, "Tissue microarrays for miniaturized high-throughput molecular profiling of tumors," *Experimental hematology*, vol. 30, pp. 1365-1372, 2002.
- [18] R. M. Walmsley and N. Billinton, "How accurate is in vitro prediction of carcinogenicity?," *British Journal of Pharmacology*, vol. 162, pp. 1250-1258, 2011.
- [19] K. Bhadriraju and C. S. Chen, "Engineering cellular microenvironments to improve cell-based drug testing," *Drug Discov Today*, vol. 7, pp. 612-620, 2002.
- [20] W.-H. Huang, F. Ai, Z.-L. Wang, and J.-K. Cheng, "Recent advances in single-cell analysis using capillary electrophoresis and microfluidic devices," *Journal of Chromatography B*, vol. 866, pp. 104-122, 2008.
- [21] Z. Palková, L. Váchová, M. Valer, and T. Preckel, "Single-cell analysis of yeast,

- mammalian cells, and fungal spores with a microfluidic pressure-driven chip-based system," *Cytometry Part A*, vol. 59A, pp. 246-253, 2004.
- [22] D. D. Carlo and L. P. Lee, "Dynamic single-cell analysis for quantitative biology," *Analytical chemistry*, vol. 78, pp. 7918-7925, 2006.
- [23] M. E. Lidstrom and D. R. Meldrum, "Life-on-a-chip," *Nature Reviews Microbiology*, vol. 1, pp. 158-164, 2003.
- [24] D. Di Carlo, L. Y. Wu, and L. P. Lee, "Dynamic single cell culture array," *Lab Chip*, vol. 6, pp. 1445-1449, 2006.
- [25] P. C. Arck, "Stress and pregnancy loss: role of immune mediators, hormones and neurotransmitters," *American Journal of Reproductive Immunology*, vol. 46, pp. 117-123, 2001.
- [26] E. W. K. Young and D. J. Beebe, "Fundamentals of microfluidic cell culture in controlled microenvironments," *Chem. Soc. Rev.*, vol. 39, pp. 1036-1048, 2010.
- [27] S. Lindstrom and H. Andersson-Svahn, "Overview of single-cell analyses: microdevices and applications," *Lab Chip*, vol. 10, pp. 3363-3372, 2010.
- [28] J. L. Spudich and D. Koshland Jr, "Non-genetic individuality: chance in the single cell," *Nature*, vol. 262, pp. 467-471, 1976.
- [29] A. Folch and M. Toner, "Microengineering of cellular interactions," *Annual review of biomedical engineering*, vol. 2, pp. 227-256, 2000.
- [30] M. Goto, T. Tsukahara, K. Sato, and T. Kitamori, "Micro-and nanometer-scale patterned surface in a microchannel for cell culture in microfluidic devices," *Analytical and Bioanalytical Chemistry*, vol. 390, pp. 817-823, 2008.
- [31] S. Ishii, K. Tago, and K. Senoo, "Single-cell analysis and isolation for microbiology and biotechnology: methods and applications," *Applied Microbiology and Biotechnology*, vol. 86, pp. 1281-1292, 2010.

- [32] E. Brouzes, *et al.*, "Droplet microfluidic technology for single-cell high-throughput screening," *Proceedings of the National Academy of Sciences*, vol. 106, pp. 14195-14200, 2009.
- [33] J. J. Agresti, *et al.*, "Ultrahigh-throughput screening in drop-based microfluidics for directed evolution," *Proceedings of the National Academy of Sciences*, vol. 9, pp. 4004-4009, 2010.
- [34] W. Mueller-Klieser, "Three-dimensional cell cultures: from molecular mechanisms to clinical applications," *American Journal of Physiology-Cell Physiology*, vol. 273, pp. C1109-C1123, 1997.
- [35] S. Yang, X. Zhang, and Y. Wen, "Microbioreactors for high-throughput cytotoxicity assays," *Current Opinion in Drug Discovery and Development*, vol. 11, pp. 111-127, 2008.
- [36] H. Kobayashi, *et al.*, "Acquired multicellular-mediated resistance to alkylating agents in cancer," *Proceedings of the National Academy of Sciences*, vol. 90, pp. 3294-3298, 1993.
- [37] E. Smitskamp-Wilms, H. Pinedo, G. Veerman, V. Ruiz van Haperen, and G. Peters, "Postconfluent multilayered cell line cultures for selective screening of gemcitabine," *European journal of cancer*, vol. 34, pp. 921-926, 1998.
- [38] J. R. Rettig and A. Folch, "Large-Scale Single-Cell Trapping And Imaging Using Microwell Arrays," *Analytical Chemistry*, vol. 77, pp. 5628-5634, 2005.
- [39] W. F. Scherer, J. T. Syverton, and G. O. Gey, "Studies on the propagation in vitro of poliomyelitis viruses. IV. Viral multiplication in a stable strain of human malignant epithelial cells (strain HeLa) derived from an epidermoid carcinoma of the cervix," *J Exp Med*, vol. 97, pp. 695-710, 1953.
- [40] J. R. Masters, "HeLa cells 50 years on: the good, the bad and the ugly," *Nat Rev*

- Cancer*, vol. 2, pp. 315-319, 2002.
- [41] B. Lu, M. Hu, K. liu, and J. Peng, "Cytotoxicity of berberine on human cervical carcinoma HeLa cells through mitochondria, death receptor and MAPK pathways, and in-silico drug-target prediction," *Toxicology in Vitro*, vol. 24, pp. 1482-1490, 2010.
- [42] H. M. L. Tan, H. Fukuda, T. Akagi, and T. Ichiki, "Surface modification of poly (dimethylsiloxane) for controlling biological cells' adhesion using a scanning radical microjet," *Thin Solid Films*, vol. 515, pp. 5172-5178, 2007.
- [43] J. A. Hubbell, "Bioactive biomaterials," *Current Opinion in Biotechnology*, vol. 10, pp. 123-129, 1999.
- [44] S. Zhang, *et al.*, "Biological surface engineering: a simple system for cell pattern formation," *Biomaterials*, vol. 20, pp. 1213-1220, 1999.
- [45] L. Bacakova, E. Filova, F. Rypacek, V. Svorcik, and V. Stary, "Cell adhesion on artificial materials for tissue engineering," *Physiol Res*, vol. 53, pp. S35-S45, 2004.
- [46] G. Kim, *et al.*, "The biocompatibility of mesoporous inorganic–organic hybrid resin films with ionic and hydrophilic characteristics," *Biomaterials*, vol. 31, pp. 2517-2525, 2010.
- [47] B.-Y. Kim, L.-Y. Hong, Y.-M. Chung, D.-P. Kim, and C.-S. Lee, "Solvent-Resistant PDMS Microfluidic Devices with Hybrid Inorganic/Organic Polymer Coatings," *Advanced Functional Materials*, vol. 19, pp. 3796-3803, 2009.
- [48] D. J. Kim, J. M. Lee, J.-G. Park, and B. G. Chung, "A self-assembled monolayer-based micropatterned array for controlling cell adhesion and protein adsorption," *Biotechnology and Bioengineering*, vol. 108, pp. 1194-1202, 2011.
- [49] M. H. Lee, D. A. Brass, R. Morris, R. J. Composto, and P. Ducheyne, "The effect of non-specific interactions on cellular adhesion using model surfaces," *Biomaterials*, vol. 26, pp. 1721-1730, 2005.

- [50] Y. Jiao and F. Cui, "Surface modification of polyester biomaterials for tissue engineering," *Biomedical Materials*, vol. 2, p. R24, 2007.
- [51] Y. Arima and H. Iwata, "Effect of wettability and surface functional groups on protein adsorption and cell adhesion using well-defined mixed self-assembled monolayers," *Biomaterials*, vol. 28, pp. 3074-3082, 2007.
- [52] G. Kotzar, *et al.*, "Evaluation of MEMS materials of construction for implantable medical devices," *Biomaterials*, vol. 23, pp. 2737-2750, 2002.
- [53] Z. Ma, Z. Mao, and C. Gao, "Surface modification and property analysis of biomedical polymers used for tissue engineering," *Colloids and Surfaces B: Biointerfaces*, vol. 60, pp. 137-157, 2007.
- [54] A. L. Givan, "Flow cytometry: first principles," p. 41, 2001.
- [55] S. Lindström and H. Andersson-Svahn, "Miniaturization of biological assays—Overview on microwell devices for single-cell analyses," *Biochimica et Biophysica Acta (BBA)-General Subjects*, vol. 1810, pp. 308-316, 2011.
- [56] A. Author, "Single cells or large populations?," *Lab Chip*, vol. 7, pp. 544-546, 2007.
- [57] D. D. Carlo, L. Y. Wu, and L. P. Lee, "Dynamic single cell culture array," *Lab Chip*, vol. 6, pp. 1445-1449, 2006.
- [58] A. M. Skelley, O. Kirak, H. Suh, R. Jaenisch, and J. Voldman, "Microfluidic control of cell pairing and fusion," *Nature methods*, vol. 6, pp. 147-152, 2009.
- [59] D. Wlodkovic, S. Faley, M. Zagnoni, J. P. Wikswo, and J. M. Cooper, "Microfluidic single-cell array cytometry for the analysis of tumor apoptosis," *Analytical chemistry*, vol. 81, pp. 5517-5523, 2009.
- [60] J. Chung, Y. J. Kim, and E. Yoon, "Highly-efficient single-cell capture in microfluidic array chips using differential hydrodynamic guiding structures," *Applied physics letters*, vol. 98, p. 123701, 2011.

- [61] W. H. Tan and S. Takeuchi, "A trap-and-release integrated microfluidic system for dynamic microarray applications," *Proceedings of the National Academy of Sciences*, vol. 104, pp. 1146-1151, 2007.
- [62] J. P. Frimat, *et al.*, "A microfluidic array with cellular valving for single cell co-culture," *Lab Chip*, vol. 11, pp. 231-237, 2011.
- [63] M. Hosokawa, *et al.*, "High-density microcavity array for cell detection: single-cell analysis of hematopoietic stem cells in peripheral blood mononuclear cells," *Analytical chemistry*, vol. 81, pp. 5308-5313, 2009.
- [64] K. Terao, *et al.*, "Localized substance delivery to single cell and 4D imaging of its uptake using a flow channel with a lateral aperture," *Microfluidics and Nanofluidics*, pp. 1-7, 2012.
- [65] J. J. Agresti, *et al.*, "Ultrahigh-throughput screening in drop-based microfluidics for directed evolution," *Proceedings of the National Academy of Sciences*, vol. 107, pp. 4004-4009, 2010.
- [66] H. Shintaku, *et al.*, "Micro cell encapsulation and its hydrogel-beads production using microfluidic device," *Microsystem technologies*, vol. 13, pp. 951-958, 2007.
- [67] J. F. Edd, *et al.*, "Controlled encapsulation of single-cells into monodisperse picolitre drops," *Lab Chip*, vol. 8, pp. 1262-1264, 2008.
- [68] C. Kim, *et al.*, "Generation of core-shell microcapsules with three-dimensional focusing device for efficient formation of cell spheroid," *Lab Chip*, vol. 11, pp. 246-252, 2011.
- [69] J. Meredith Jr, B. Fazeli, and M. Schwartz, "The extracellular matrix as a cell survival factor," *Molecular biology of the cell*, vol. 4, pp. 953-961, 1993.
- [70] K. Leong, A. K. Boardman, H. Ma, and A. K. Y. Jen, "Single-cell patterning and adhesion on chemically engineered poly (dimethylsiloxane) surface," *Langmuir*, vol.

- 25, pp. 4615-4620, 2009.
- [71] A. H. Broderick, S. M. Azarin, M. E. Buck, S. P. Palecek, and D. M. Lynn, "Fabrication and Selective Functionalization of Amine-Reactive Polymer Multilayers on Topographically Patterned Microwell Cell Culture Arrays," *Biomacromolecules*, vol. 12, pp. 1998-2007, 2011.
- [72] C. S. Chen, "Geometric Control of Cell Life and Death," *Science*, vol. 276, pp. 1425-1428, 1997.
- [73] S. A. Jadhav, "Self-assembled monolayers (SAMs) of carboxylic acids: an overview," *Central European Journal of Chemistry*, vol. 9, pp. 369-378, 2011.
- [74] F. Mastrangelo, G. Fioravanti, R. Quaresima, R. Vinci, and E. Gherlone, "Self-Assembled Monolayers (SAMs): Which Perspectives in Implant Dentistry?," *Journal of Biomaterials and Nanobiotechnology*, vol. 2, pp. 533-543, 2011.
- [75] Y. Arima and H. Iwata, "Effects of surface functional groups on protein adsorption and subsequent cell adhesion using self-assembled monolayers," *Journal of Materials Chemistry*, vol. 17, pp. 4079-4087, 2007.
- [76] D. R. Schmidt, H. Waldeck, and W. J. Kao, "Protein adsorption to biomaterials," *Biological Interactions on Materials Surfaces*, pp. 1-18, 2009.
- [77] M. Ni, *et al.*, "Cell Culture on MEMS Platforms: A Review," *International Journal of Molecular Sciences*, vol. 10, pp. 5411-5441, 2009.
- [78] B. G. Keselowsky, D. M. Collard, and A. J. García, "Surface chemistry modulates fibronectin conformation and directs integrin binding and specificity to control cell adhesion," *Journal of Biomedical Materials Research Part A*, vol. 66, pp. 247-259, 2003.
- [79] R. Inaba, A. Khademhosseini, H. Suzuki, and J. Fukuda, "Electrochemical desorption of self-assembled monolayers for engineering cellular tissues," *Biomaterials*, vol. 30,

- pp. 3573-3579, 2009.
- [80] G. Jing, S. F. Perry, and S. Tatic-Lucic, "Precise cell patterning using cytophobic self-assembled monolayer deposited on top of semi-transparent gold," *Biomedical Microdevices*, vol. 12, pp. 935-948, 2010.
- [81] A. Ron, G. H. Lee, L. Amar, S. Ghassemi, and J. Hone, "Adjacent assembly of self-assembled monolayers for the construction of selective bio-platforms," *Sensors and Actuators B: Chemical*, pp. 75-81, 2011.
- [82] J. Voldman, "Electrical forces for microscale cell manipulation," *Annu. Rev. Biomed. Eng.*, vol. 8, pp. 425-454, 2006.
- [83] G. B. Schneider, *et al.*, "The effect of hydrogel charge density on cell attachment," *Biomaterials*, vol. 25, pp. 3023-3028, 2004.
- [84] K. J. Luebke, D. E. Carter, H. R. Garner, and K. C. Brown, "Patterning adhesion of mammalian cells with visible light, tris (bipyridyl) ruthenium (II) chloride, and a digital micromirror array," *Journal of Biomedical Materials Research Part A*, vol. 68, pp. 696-703, 2004.
- [85] M. Ozkan, *et al.*, "Electro-optical platform for the manipulation of live cells," *Langmuir*, vol. 19, pp. 1532-1538, 2003.
- [86] H. Yasuda, A. K. Sharma, and T. Yasuda, "Effect of orientation and mobility of polymer molecules at surfaces on contact angle and its hysteresis," *Journal of Polymer Science: Polymer Physics Edition*, vol. 19, pp. 1285-1291, 1981.
- [87] I. Beaulieu, M. Geissler, and J. Mauzeroll, "Oxygen plasma treatment of polystyrene and Zeonor: substrates for adhesion of patterned cells," *Langmuir*, vol. 25, pp. 7169-7176, 2009.
- [88] Y. Tamada and Y. Ikada, "Effect of Preadsorbed Proteins on Cell Adhesion to Polymer Surfaces," *Journal of Colloid and Interface Science*, vol. 155, pp. 334-339,

- 1993.
- [89] D. L. Elbert and J. A. Hubbell, "Surface Treatments of Polymers for Biocompatibility," *Annual Review of Materials Science*, vol. 26, pp. 365-294, 1996.
- [90] H. Lodish, *et al.*, "Molecular cell biology," *New York*, p. 1616, 1995.
- [91] E. Tziampazis, J. Kohn, and P. V. Moghe, "PEG-variant biomaterials as selectively adhesive protein templates: model surfaces for controlled cell adhesion and migration," *Biomaterials*, vol. 21, pp. 511-520, 2000.
- [92] C. J. Wilson, R. E. Clegg, D. I. Leavesley, and M. J. Percy, "Mediation of biomaterial-cell interactions by adsorbed proteins: A review," *Tissue Engineering*, vol. 11, pp. 1-18, Jan 2005.
- [93] Q. Cheng and K. Komvopoulos, "Integration of plasma-assisted surface chemical modification, soft lithography, and protein surface activation for single-cell patterning," *Applied physics letters*, vol. 97, p. 043705, 2010.
- [94] T. G. V. Kooten and A. F. V. Recum, "Cell adhesion to textured silicone surfaces: the influence of time of adhesion and texture on focal contact and fibronectin fibril formation," *Tissue Engineering*, vol. 5, pp. 223-240, 1999.
- [95] C. S. Ranucci and P. V. Moghe, "Substrate microtopography can enhance cell adhesive and migratory responsiveness to matrix ligand density," *Journal of Biomedical Materials Research*, vol. 54, pp. 149-161, 2001.
- [96] J. Lim, J. Hansen, C. Siedlecki, J. Runt, and H. Donahue, "Human foetal osteoblastic cell response to polymer-demixed nanotopographic interfaces," *Journal of The Royal Society Interface*, vol. 2, pp. 97-108, 2005.
- [97] H. Zhang and K. K. Liu, "Optical tweezers for single cells," *Journal of The Royal Society Interface*, vol. 5, pp. 671-690, 2008.
- [98] E. Eriksson, *et al.*, "A microfluidic device for reversible environmental changes

- around single cells using optical tweezers for cell selection and positioning," *Lab Chip*, vol. 10, pp. 617-625, 2010.
- [99] F. Arai, *et al.*, "On chip single-cell separation and immobilization using optical tweezers and thermosensitive hydrogel," *Lab Chip*, vol. 5, pp. 1399-1403, 2005.
- [100] G. Carmon and M. Feingold, "Rotation of single bacterial cells relative to the optical axis using optical tweezers," *Optics Letters*, vol. 36, pp. 40-42, 2011.
- [101] M. Suwa and H. Watarai, "Magnetoanalysis of micro/nanoparticles: A review," *Analytica Chimica Acta*, vol. 690, pp. 137-147, 2011.
- [102] E. Al-Hetlani, *et al.*, "Sorting and Manipulation of Magnetic Droplets in Continuous Flow," *AIP Conf. Proc.*, vol. 1311, pp. 167-175, 2010.
- [103] J. Kim, H. H. Lee, U. Steinfeld, and H. Seidel, "Fast Capturing on Micromagnetic Cell Sorter," *Sensors Journal, IEEE*, vol. 9, pp. 908-913, 2009.
- [104] W. Liu, *et al.*, "A novel permalloy based magnetic single cell micro array," *Lab Chip*, vol. 9, pp. 2381-2390, 2009.
- [105] Q. Ramadan, "Reversible assembly of magnetized particles: Application to water-borne pathogen enumeration," *Journal of applied physics*, vol. 106, p. 124701, 2009.
- [106] B. M. Taff and J. Voldman, "A scalable addressable positive-dielectrophoretic cell-sorting array," *Analytical chemistry*, vol. 77, pp. 7976-7983, 2005.
- [107] D. S. Gray, J. L. Tan, J. Voldman, and C. S. Chen, "Dielectrophoretic registration of living cells to a microelectrode array," *Biosensors and Bioelectronics*, vol. 19, pp. 771-780, 2004.
- [108] J. Voldman, M. Toner, M. L. Gray, and M. A. Schmidt, "A dielectrophoresis-based array cytometer," 2001, pp. 322-325.
- [109] J. Voldman, M. Toner, M. Gray, and M. Schmidt, "Design and analysis of extruded quadrupolar dielectrophoretic traps," *Journal of electrostatics*, vol. 57, pp. 69-90,

- 2003.
- [110] M. Deutsch, *et al.*, "A novel miniature cell retainer for correlative high-content analysis of individual untethered non-adherent cells," *Lab Chip*, vol. 6, pp. 995-1000, 2006.
- [111] M. Ochsner, *et al.*, "Micro-well arrays for 3D shape control and high resolution analysis of single cells," *Lab Chip*, vol. 7, pp. 1074-1077, 2007.
- [112] Y. Sasuga, *et al.*, "Single-cell chemical lysis method for analyses of intracellular molecules using an array of picoliter-scale microwells," *Analytical chemistry*, vol. 80, pp. 9141-9149, 2008.
- [113] T. W. Molter, *et al.*, "A microwell array device capable of measuring single-cell oxygen consumption rates," *Sensors and Actuators B: Chemical*, vol. 135, pp. 678-686, 2009.
- [114] C. Liu, J. Liu, D. Gao, M. Ding, and J. M. Lin, "Fabrication of microwell arrays based on two-dimensional ordered polystyrene microspheres for high-throughput single-cell analysis," *Analytical chemistry*, vol. 82, pp. 9418-9424, 2010.
- [115] N. Ferrell, *et al.*, "Vacuum-Assisted Cell Seeding in a Microwell Cell Culture System," *Analytical chemistry*, vol. 82, pp. 2380-2386, 2010.
- [116] J. Y. Park, *et al.*, "Single cell trapping in larger microwells capable of supporting cell spreading and proliferation," *Microfluidics and Nanofluidics*, vol. 8, pp. 263-268, 2009.
- [117] Y. Wang, P. Shah, C. Phillips, C. E. Sims, and N. L. Allbritton, "Trapping cells on a stretchable microwell array for single-cell analysis," *Analytical and Bioanalytical Chemistry*, pp. 1-8, 2012.
- [118] C. P. Jen, J. H. Hsiao, and N. A. Maslov, "Single-Cell Chemical Lysis on Microfluidic Chips with Arrays of Microwells," *Sensors*, vol. 12, pp. 347-358, 2011.

- [119] L. Zhao, *et al.*, "Intracellular water-specific MR of microbead-adherent cells: the HeLa cell intracellular water exchange lifetime," *NMR in Biomedicine*, vol. 21, pp. 159-164, 2008.
- [120] J. Dai, H. P. Ting-Beall, and M. P. Sheetz, "The secretion-coupled endocytosis correlates with membrane tension changes in RBL 2H3 cells," *The Journal of general physiology*, vol. 110, pp. 1-10, 1997.
- [121] F. Q. Schafer and G. R. Buettner, "Singlet Oxygen Toxicity Is Cell Line-dependent: A Study of Lipid Peroxidation in Nine Leukemia Cell Lines," *Photochemistry and photobiology*, vol. 70, pp. 858-867, 1999.
- [122] M. Chabert and J. L. Viovy, "Microfluidic high-throughput encapsulation and hydrodynamic self-sorting of single cells," *Proceedings of the National Academy of Sciences*, vol. 105, pp. 3191-3196, 2008.
- [123] G. Ghosh, L. G. Bachas, and K. W. Anderson, "Biosensor incorporating cell barrier architectures for detecting Staphylococcus aureus alpha toxin," *Analytical and Bioanalytical Chemistry*, vol. 387, pp. 567-574, 2007.
- [124] J. Ramalho-Santos, S. Nir, N. Duzgunes, A. Pato de Carvalho, and M. C. Pedroso de Lima, "A common mechanism for influenza virus fusion activity and inactivation," *Biochemistry*, vol. 32, pp. 2771-2779, 1993.
- [125] T. D. Perroud, *et al.*, "Microfluidic-Based Cell Sorting of Francisella tularensis Infected Macrophages Using Optical Forces," *Analytical chemistry*, vol. 80, pp. 6365-6372, 2008.
- [126] S. S. Kay, A. M. Bilek, K. C. Dee, and D. P. Gaver III, "Pressure gradient, not exposure duration, determines the extent of epithelial cell damage in a model of pulmonary airway reopening," *Journal of Applied Physiology*, vol. 97, pp. 269-276, 2004.

- [127] S. Suresh, *et al.*, "Connections between single-cell biomechanics and human disease states: gastrointestinal cancer and malaria," *Acta Biomaterialia*, vol. 1, pp. 15-30, 2005.
- [128] D. Kirk, M. F. Szalay, and M. E. Kaighn, "Modulation of growth of a human prostatic cancer cell line (PC-3) in agar culture by normal human lung fibroblasts," *Cancer research*, vol. 41, p. 1100, 1981.
- [129] I. Murillo and L. M. Henderson, "Expression of gp91phox/Nox2 in COS-7 cells: cellular localization of the protein and the detection of outward proton currents," *Biochemical Journal*, vol. 385, pp. 649-657, 2005.
- [130] J. N. Weinstein, "Drug discovery: Cell lines battle cancer," *Nature*, vol. 483, pp. 544-545, 2012.
- [131] J. Barretina, *et al.*, "The cancer cell line encyclopedia enables predictive modelling of anticancer drug sensitivity," *Nature*, vol. 483, pp. 603-307, 2012.
- [132] R. Shoemaker, *et al.*, "Human tumor xenograft models for use with an in vitro-based, disease-oriented antitumor drug screening program," *Human Tumor xenografts in Anticancer Drug Development*. Springer-Verlag, Berlin, pp. 115-120, 1988.
- [133] L. M. Shi, *et al.*, "Mining and visualizing large anticancer drug discovery databases," *Journal of chemical information and computer sciences*, vol. 40, pp. 367-379, 2000.
- [134] T. Yamori, "Panel of human cancer cell lines provides valuable database for drug discovery and bioinformatics," *Cancer Chemotherapy and Pharmacology*, vol. 52, pp. 74-79, 2003.
- [135] Gey GO, Coffman WD, and K. MT, "Tissue culture studies of the proliferative capacity of cervical carcinoma and normal epithelium," *Cancer Res*, vol. 12, pp. 264-265, 1952.
- [136] J. R. W. Masters, "OPINION: Human cancer cell lines: fact and fantasy," *Nature*

- Reviews Molecular Cell Biology*, vol. 1, pp. 233-236, 2000.
- [137] J. R. W. Masters, *et al.*, "UKCCCR Guidelines for the Use of Cell Lines in Cancer Research," *British Journal of Cancer*, vol. 82, pp. 1495-1509, 2000.
- [138] M. Macville, *et al.*, "Comprehensive and definitive molecular cytogenetic characterization of HeLa cells by spectral karyotyping," *Cancer Res*, vol. 59, pp. 141-150, 1999.
- [139] P. Brodwin, *Biotechnology and Culture: Bodies, Anxieties, Ethics*. Bloomington, IN: Indiana University Press, 2000.
- [140] H. Harris and J. F. Watkins, "Hybrid Cells Derived from Mouse and Man: Artificial Heterokaryons of Mammalian Cells from Different Species," *Nature*, vol. 205, pp. 640-646, 1965.
- [141] H. Harris, "Review Lecture: Hybrid Cells from Mouse and Man: A Study in Genetic Regulation," *Proceedings of the Royal Society of London. Series B, Biological Sciences*, vol. 166, pp. 358-368, 1966.
- [142] P. J. Maddon, *et al.*, "The T4 gene encodes the AIDS virus receptor and is expressed in the immune system and the brain," *Cell*, vol. 47, pp. 333-348, 1986.
- [143] H. Kaji, T. Yokoi, T. Kawashima, and M. Nishizawa, "Directing the flow of medium in controlled cocultures of HeLa cells and human umbilical vein endothelial cells with a microfluidic device," *Lab Chip*, vol. 10, pp. 2374-2379, 2010.
- [144] L. S. Cohen and G. P. Studzinski, "Correlation between cell enlargement and nucleic acid and protein content of HeLa cells in unbalanced growth produced by inhibitors of DNA synthesis," *Journal of Cellular Physiology*, vol. 69, pp. 331-339, 1967.
- [145] K. Monier, J. C. Gonzalez Armas, S. Etteldorf, P. Ghazal, and K. F. Sullivan, "Annexation of the interchromosomal space during viral infection," *Nature Cell Biology*, vol. 2, pp. 661-665, 2000.

- [146] T. T. Puck, P. I. Marcus, and S. J. Cieciura, "Clonal growth of mammalian cells in vitro," *The Journal of experimental medicine*, vol. 103, pp. 273-284, 1956.
- [147] K. Park, *et al.*, "'Living cantilever arrays' for characterization of mass of single live cells in fluids," *Lab on a Chip*, vol. 8, pp. 1034-1041, 2008.
- [148] A. Christopoulos and M. J. Lew, "Beyond eyeballing: fitting models to experimental data," *Critical Reviews in Biochemistry and Molecular Biology*, vol. 35, pp. 359-391, 2000.
- [149] M. Tsukamoto, *et al.*, "Cell separation by an aqueous two-phase system in a microfluidic device," *Analyst*, vol. 134, pp. 1994-1998, 2009.
- [150] R. Wolkowicz and G. Nolan, "Gene therapy progress and prospects: novel gene therapy approaches for AIDS," *Gene therapy*, vol. 12, pp. 467-476, 2005.
- [151] K. Sone, *et al.*, "hScrib, a human homologue of *Drosophila* neoplastic tumor suppressor, is a novel death substrate targeted by caspase during the process of apoptosis," *Genes to Cells*, vol. 13, pp. 771-785, 2008.
- [152] A. A. Aleksandrov and M. S. Trakhtengerts, "Viscosity of water at temperatures of  $-20$  to  $150^{\circ}\text{C}$ ," *Journal of Engineering Physics and Thermophysics*, vol. 27, pp. 1235-1239, 1974.
- [153] S. B. Mutyala, "Development of Efficient Pancreatic Islet Isolation System: Redesign of Critical Components and Analysis of Process Variables," *Master thesis, University of Cincinnati*, 2008.
- [154] U. Richter, *et al.*, "Adhesion of small cell lung cancer cells to E- and P-Selectin under physiological flow conditions: implications for metastasis formation," *Histochemistry and Cell Biology*, vol. 135, pp. 499-512, 2011.
- [155] J. Rejman, G. Tavernier, N. Bavarsad, J. Demeester, and S. C. De Smedt, "mRNA transfection of cervical carcinoma and mesenchymal stem cells mediated by cationic

- carriers," *Journal of Controlled Release*, vol. 147, pp. 385-391, 2010.
- [156] É. Guazzelli and J. Hinch, "Fluctuations and instability in sedimentation," *Annual Review of Fluid Mechanics*, vol. 43, pp. 97-116, 2011.
- [157] E. N. Marieb, *Human Anatomy and Physiology*, 3th ed.: Benjamin/Cummings, 1995.
- [158] G. Kim, *et al.*, "The biocompatibility of mesoporous inorganic-organic hybrid resin films with ionic and hydrophilic characteristics," *Biomaterials*, vol. 31, pp. 2517-2525, 2010.
- [159] D. J. Kim, J. M. Lee, J.-G. Park, and B. G. Chung, "A self-assembled monolayer-based micropatterned array for controlling cell adhesion and protein adsorption," *Biotechnology and Bioengineering*, pp. 1194-1202, 2010.
- [160] A. Revzin, R. G. Tompkins, and M. Toner, "Surface Engineering with Poly(ethylene glycol) Photolithography to Create High-Density Cell Arrays on Glass," *Langmuir*, vol. 19, pp. 9855-9862, 2003.
- [161] L. Kam, W. Shain, J. N. Turner, and R. Bizios, "Correlation of astroglial cell function on micro-patterned surfaces with specific geometric parameters," *Biomaterials*, vol. 20, pp. 2343-2350, 1999.
- [162] I. Degasne, *et al.*, "Effects of Roughness, Fibronectin and Vitronectin on Attachment, Spreading, and Proliferation of Human Osteoblast-Like Cells (Saos-2) on Titanium Surfaces," *Calcified Tissue International*, vol. 64, pp. 499-507, 1999.
- [163] T. Collier, C. Jenney, K. DeFife, and J. Anderson, "Protein adsorption on chemically modified surfaces," *Biomedical sciences instrumentation*, vol. 33, pp. 178-183, 1997.
- [164] N. Faucheux, R. Schweiss, K. Lutzow, C. Werner, and T. Groth, "Self-assembled monolayers with different terminating groups as model substrates for cell adhesion studies," *Biomaterials*, vol. 25, pp. 2721-2730, 2004.
- [165] F. Grinnell and M. Feld, "Fibronectin adsorption on hydrophilic and hydrophobic

- surfaces detected by antibody binding and analyzed during cell adhesion in serum-containing medium," *Journal of Biological Chemistry*, vol. 257, pp. 4888-4893, 1982.
- [166] F. Grinnell, C. Ho, and A. Wysocki, "Degradation of fibronectin and vitronectin in chronic wound fluid: analysis by cell blotting, immunoblotting, and cell adhesion assays," *The Journal of investigative dermatology*, vol. 98, pp. 410-416, 1992.
- [167] M. Horie, *et al.*, "Protein Adsorption of Ultrafine Metal Oxide and Its Influence on Cytotoxicity toward Cultured Cells," *Chemical Research in Toxicology*, vol. 22, pp. 543-553, 2009.
- [168] C. R. Jenney and J. M. Anderson, "Adsorbed serum proteins responsible for surface dependent human macrophage behavior," *Journal of Biomedical Materials Research*, vol. 49, pp. 435-447, 2000.
- [169] P. Kingshott, H. Thissen, and H. J. Griesser, "Effects of cloud-point grafting, chain length, and density of PEG layers on competitive adsorption of ocular proteins," *Biomaterials*, vol. 23, pp. 2043-2056, 2002.
- [170] L. Koo, D. Irvine, A. Mayes, D. Lauffenburger, and L. Griffith, "Co-regulation of cell adhesion by nanoscale RGD organization and mechanical stimulus," *Journal of cell science*, vol. 115, pp. 1423-1433, 2002.
- [171] J. H. Lee, G. Khang, J. W. Lee, and H. B. Lee, "Interaction of Different Types of Cells on Polymer Surfaces with Wettability Gradient," *Journal of Colloid and Interface Science*, vol. 205, pp. 323-330, 1998.
- [172] B. Rezek, *et al.*, "Adsorption of fetal bovine serum on H/O-terminated diamond studied by atomic force microscopy," *Diamond and Related Materials*, vol. 18, pp. 918-922, 2009.
- [173] M. Shen, I. Garcia, R. Maier, and T. Horbett, "Effects of adsorbed proteins and surface chemistry on foreign body giant cell formation, tumor necrosis factor alpha

- release and procoagulant activity of monocytes," *Journal of Biomedical Materials Research Part A*, vol. 70, pp. 533-541, 2004.
- [174] J. G. Steele, B. A. Dalton, G. Johnson, and P. A. Underwood, "Adsorption of fibronectin and vitronectin onto Primaria and tissue culture polystyrene and relationship to the mechanism of initial attachment of human vein endothelial cells and BHK-21 fibroblasts," *Biomaterials*, vol. 16, pp. 1057-1067, 1995.
- [175] J. G. Steele, *et al.*, "Roles of Serum Vitronectin and Fibronectin in Initial Attachment of Human Vein Endothelial-Cells and Dermal Fibroblasts on Oxygen-Containing and Nitrogen-Containing Surfaces Made by Radiofrequency Plasmas," *Journal of Biomaterials Science-Polymer Edition*, vol. 6, pp. 511-532, 1994.
- [176] J. G. Steele, G. Johnson, W. D. Norris, and P. A. Underwood, "Adhesion and growth of cultured human endothelial cells on perfluorosulphonate: role of vitronectin and fibronectin in cell attachment," *Biomaterials*, vol. 12, pp. 531-539, 1991.
- [177] J. G. Steele, G. Johnson, and P. A. Underwood, "Role of Serum Vitronectin and Fibronectin in Adhesion of Fibroblasts Following Seeding onto Tissue-Culture Polystyrene," *Journal of Biomedical Materials Research*, vol. 26, pp. 861-884, 1992.
- [178] N. Tani, *et al.*, "Effects of fibronectin cleaved by neuropsin on cell adhesion and migration," *Neuroscience Research*, vol. 39, pp. 247-251, 2001.
- [179] B. Wesslén, M. Kober, C. Freij-Larsson, Å. Ljungh, and M. Paulsson, "Protein adsorption of poly(ether methacrylate) surfaces modified by amphiphilic and hydrophilic polymers," *Biomaterials*, vol. 15, pp. 278-284, 1994.
- [180] C. R. Wittmer, J. A. Phelps, W. M. Saltzman, and P. R. Van Tassel, "Fibronectin terminated multilayer films: Protein adsorption and cell attachment studies," *Biomaterials*, vol. 28, pp. 851-860, 2007.
- [181] S. Marcinko and A. Y. Fadeev, "Hydrolytic Stability of Organic Monolayers

- Supported on TiO<sub>2</sub> and ZrO<sub>2</sub>," *Langmuir*, vol. 20, pp. 2270-2273, 2004.
- [182] J. H. Waite, "Reverse Engineering of Bioadhesion in Marine Mussels," *Annals of the New York Academy of Sciences*, vol. 875, pp. 301-309, 1999.
- [183] V. V. Papov, T. V. Diamond, K. Biemann, and J. H. Waite, "Hydroxyarginine-containing polyphenolic proteins in the adhesive plaques of the marine mussel *Mytilus edulis*," *Journal of Biological Chemistry*, vol. 270, p. 20183, 1995.
- [184] H. Lee, B. P. Lee, and P. B. Messersmith, "A reversible wet/dry adhesive inspired by mussels and geckos," *Nature*, vol. 448, pp. 338-341, 2007.
- [185] X. Fan, L. Lin, J. L. Dalsin, and P. B. Messersmith, "Biomimetic anchor for surface-initiated polymerization from metal substrates," *Journal of the American Chemical Society*, vol. 127, pp. 15843-15847, 2005.
- [186] D. S. Hwang, Y. Gim, D. G. Kang, Y. K. Kim, and H. J. Cha, "Recombinant mussel adhesive protein Mgfp-5 as cell adhesion biomaterial," *Journal of Biotechnology*, vol. 127, pp. 727-735, 2007.
- [187] H. Lee, S. M. Dellatore, W. M. Miller, and P. B. Messersmith, "Mussel-Inspired Surface Chemistry for Multifunctional Coatings," *Science*, vol. 318, pp. 426-430, 2007.
- [188] Y. W. Fan, *et al.*, "Culture of neural cells on silicon wafers with nano-scale surface topograph," *Journal of Neuroscience Methods*, vol. 120, pp. 17-23, 2002.
- [189] A. Thapa, D. C. Miller, T. J. Webster, and K. M. Haberstroh, "Nano-structured polymers enhance bladder smooth muscle cell function," *Biomaterials*, vol. 24, pp. 2915-2926, 2003.
- [190] F. Hoffmann, M. Cornelius, J. Morell, and M. Fröba, "Silica-Based Mesoporous Organic-Inorganic Hybrid Materials," *Angewandte Chemie International Edition*, vol. 45, pp. 3216-3251, 2006.

- [191] L. M. Hamming, X. W. Fan, P. B. Messersmith, and L. C. Brinson, "Mimicking mussel adhesion to improve interfacial properties in composites," *Composites Science and Technology*, vol. 68, pp. 2042-2048, 2008.
- [192] D. J. Kim, J. M. Lee, J. G. Park, and B. G. Chung, "A self-assembled monolayer-based micropatterned array for controlling cell adhesion and protein adsorption," *Biotechnol Bioeng*, vol. 108, pp. 1194-1202, 2011.
- [193] M. H. Lee, D. A. Brass, R. Morris, R. J. Composto, and P. Ducheyne, "The effect of non-specific interactions on cellular adhesion using model surfaces," *Biomaterials*, vol. 26, pp. 1721-1730, May 2005.
- [194] Y. P. Jiao and F. Z. Cui, "Surface modification of polyester biomaterials for tissue engineering," *Biomed Mater*, vol. 2, pp. R24-37, Dec 2007.
- [195] Z. Ma, Z. Mao, and C. Gao, "Surface modification and property analysis of biomedical polymers used for tissue engineering," *Colloids Surf B Biointerfaces*, vol. 60, pp. 137-157, Nov 15 2007.
- [196] M. Gardel and U. Schwarz, "Cell-substrate interactions," *J Phys Condens Matter*, vol. 22, p. 190301, 2010.
- [197] Y. Arima and H. Iwata, "Effect of wettability and surface functional groups on protein adsorption and cell adhesion using well-defined mixed self-assembled monolayers," *Biomaterials*, vol. 28, pp. 3074-3082, Jul 2007.
- [198] E. Tziampazis, J. Kohn, and P. V. Moghe, "PEG-variant biomaterials as selectively adhesive protein templates: model surfaces for controlled cell adhesion and migration," *Biomaterials*, vol. 21, pp. 511-520, Mar 2000.
- [199] J. G. Steele, G. Johnson, H. J. Griesser, and P. A. Underwood, "Mechanism of initial attachment of corneal epithelial cells to polymeric surfaces," *Biomaterials*, vol. 18, pp. 1541-1551, Dec 1997.

- [200] M. Benoit and C. Selhuber-Unkel, "Measuring cell adhesion forces: theory and principles," *Methods Mol Biol*, vol. 736, pp. 355-377, 2011.
- [201] D. Ivanov, M. Philippova, and V. Tkachuk, "Structure and functions of classical cadherins," *Biochemistry (Moscow)*, vol. 66, pp. 1174-1186, 2001.
- [202] T. Tedder, D. Steeber, A. Chen, and P. Engel, "The selectins: vascular adhesion molecules," *The FASEB journal*, vol. 9, pp. 866-873, 1995.
- [203] S. K. Akiyama, "Integrins in cell adhesion and signaling," *Hum Cell*, vol. 9, pp. 181-186, 1996.
- [204] M. Nagano, D. Hoshino, N. Koshikawa, T. Akizawa, and M. Seiki, "Turnover of Focal Adhesions and Cancer Cell Migration," *International Journal of Cell Biology*, p. 310616, 2012.
- [205] K. Webb, V. Hlady, and P. A. Tresco, "Relative importance of surface wettability and charged functional groups on NIH 3T3 fibroblast attachment, spreading, and cytoskeletal organization," *J Biomed Mater Res*, vol. 41, pp. 422-430, 1998.
- [206] L. Bacakova, E. Filova, F. Rypacek, V. Svorcik, and V. Stary, "Cell adhesion on artificial materials for tissue engineering," *Physiol Res*, vol. 53 Suppl 1, pp. S35-45, 2004.
- [207] B. Geiger, A. Bershadsky, R. Pankov, and K. M. Yamada, "Transmembrane crosstalk between the extracellular matrix--cytoskeleton crosstalk," *Nat Rev Mol Cell Biol*, vol. 2, pp. 793-805, Nov 2001.
- [208] K. J. Green and J. C. Jones, "Desmosomes and hemidesmosomes: structure and function of molecular components," *FASEB J*, vol. 10, pp. 871-881, Jun 1996.
- [209] M. Hertl, R. Eming, and C. Veldman, "T cell control in autoimmune bullous skin disorders," *The Journal of Clinical Investigation*, vol. 116, pp. 1159-1166, 2006.
- [210] R. E. Burgeson and A. M. Christiano, "The dermal-epidermal junction," *Curr Opin*

- Cell Biol*, vol. 9, pp. 651-658, 1997.
- [211] P. Rousselle, G. P. Lunstrum, D. R. Keene, and R. E. Burgeson, "Kalinin: an epithelium-specific basement membrane adhesion molecule that is a component of anchoring filaments," *J Cell Biol*, vol. 114, pp. 567-576, 1991.
- [212] J. Dowling, Q. C. Yu, and E. Fuchs, "Beta4 integrin is required for hemidesmosome formation, cell adhesion and cell survival," *J Cell Biol*, vol. 134, pp. 559-572, Jul 1996.
- [213] L. Borradori and A. Sonnenberg, "Structure and function of hemidesmosomes: more than simple adhesion complexes," *J Invest Dermatol*, vol. 112, pp. 411-418, 1999.
- [214] M. A. Schwartz, "Integrin signaling revisited," *Trends Cell Biol*, vol. 11, pp. 466-470, 2001.
- [215] Y. Kitajima, "Cross-talk between hemidesmosomes and focal contacts: understanding subepidermal blistering diseases," *J Invest Dermatol*, vol. 130, pp. 1493-1496, 2010.
- [216] P. Twentyman and M. Luscombe, "A study of some variables in a tetrazolium dye (MTT) based assay for cell growth and chemosensitivity," *British journal of cancer*, vol. 56, pp. 279-285, 1987.
- [217] J. Carmichael, W. G. DeGraff, A. F. Gazdar, J. D. Minna, and J. B. Mitchell, "Evaluation of a tetrazolium-based semiautomated colorimetric assay: assessment of chemosensitivity testing," *Cancer research*, vol. 47, p. 936, 1987.
- [218] U. Wagner, E. Burkhardt, and K. Failing, "Evaluation of canine lymphocyte proliferation: comparison of three different colorimetric methods with the-thymidine incorporation assay," *Veterinary immunology and immunopathology*, vol. 70, pp. 151-159, 1999.
- [219] T. Mosmann, "Rapid colorimetric assay for cellular growth and survival: application to proliferation and cytotoxicity assays," *Journal of immunological methods*, vol. 65,

- pp. 55-63, 1983.
- [220] D. A. Scudiero, *et al.*, "Evaluation of a soluble tetrazolium/formazan assay for cell growth and drug sensitivity in culture using human and other tumor cell lines," *Cancer research*, vol. 48, p. 4827, 1988.
- [221] J. Magaud, I. Sargent, and D. Mason, "Detection of human white cell proliferative responses by immunoenzymatic measurement of bromodeoxyuridine uptake," *Journal of immunological methods*, vol. 106, pp. 95-100, 1988.
- [222] G. Chen, N. Kawazoe, and T. Tateishi, "Effects of ECM Proteins and Cationic Polymers on the Adhesion and Proliferation of Rat Islet Cells," *Open Biotechnology Journal*, vol. 2, pp. 133-137, 2008.
- [223] A. Yamamoto, S. Mishima, N. Maruyama, and M. Sumita, "Quantitative evaluation of cell attachment to glass, polystyrene, and fibronectin-or collagen-coated polystyrene by measurement of cell adhesive shear force and cell detachment energy," *Journal of Biomedical Materials Research*, vol. 50, pp. 114-124, 2000.
- [224] D. Moshkov, *et al.*, "Effect of Dopamine on Viability of BHK-21 Cells," *Bulletin of experimental biology and medicine*, vol. 149, pp. 359-363, 2010.
- [225] G. Gstraunthaler, "Alternatives to the use of fetal bovine serum: serum-free cell culture," *Altex*, vol. 20, pp. 275-281, 2003.
- [226] D. Gusnard and R. H. Kirschner, "Cell and organelle shrinkage during preparation for scanning electron microscopy: effects of fixation, dehydration and critical point drying," *Journal of microscopy*, vol. 110, pp. 51-57, 1977.
- [227] W. Schönhuber, B. Fuchs, S. Juretschko, and R. Amann, "Improved sensitivity of whole-cell hybridization by the combination of horseradish peroxidase-labeled oligonucleotides and tyramide signal amplification," *Applied and environmental microbiology*, vol. 63, pp. 3268-3273, 1997.

- [228] P. S. Wang, *et al.*, "Dopamine antagonists and the development of breast cancer," *Archives of general psychiatry*, vol. 59, pp. 1147-1154, 2002.
- [229] M. M. Wick, "Dopamine: a novel antitumor agent active against B-16 melanoma in vivo," *Journal of Investigative Dermatology*, vol. 71, pp. 163-164, 1978.
- [230] D. Chakroborty, *et al.*, "Depleted Dopamine in Gastric Cancer Tissues," *Clinical cancer research*, vol. 10, pp. 4349-4356, 2004.
- [231] S. BASU, P. S. DASGUPTA, and J. R. CHOWDHURY, "Altered plasma level and uptake of dopamine by platelets in some human malignant tumors," *Biogenic amines*, vol. 11, pp. 31-38, 1995.
- [232] O. HORNYKIEWICZ, "DOPAMINE (3-HYDROXYTYRAMINE) AND BRAIN FUNCTION," *Pharmacological Reviews*, vol. 18, pp. 925-964, 1966.
- [233] D. Chakroborty, *et al.*, "Dopamine regulates endothelial progenitor cell mobilization from mouse bone marrow in tumor vascularization," *The Journal of Clinical Investigation*, vol. 118, pp. 1380-1389, 2008.
- [234] E. Mezey, *et al.*, "Non-neuronal dopamine in the gastrointestinal system," *Clinical and experimental pharmacology & physiology. Supplement*, vol. 26, pp. S14-22, 1999.
- [235] J. R. Anderson, *et al.*, "Fabrication of topologically complex three-dimensional microfluidic systems in PDMS by rapid prototyping," *Analytical chemistry*, vol. 72, pp. 3158-3164, 2000.
- [236] F. Grinnell, C. H. Ho, and A. Wysocki, "Degradation of Fibronectin and Vitronectin and Vitronectin in Chronic Wound Fluid: Analysis by Cell Blotting, Immunoblotting, and Cell Adhesion Assays," *Journal of Investigative Dermatology*, vol. 98, pp. 410-416, 1992.
- [237] B. K. Lee, L.-Y. Hong, H. Y. Lee, D.-P. Kim, and T. Kawai, "Replica Mold for Nanoimprint Lithography from a Novel Hybrid Resin," *Langmuir*, vol. 25, pp. 11768-

11776, 2009.

- [238] J. H. Koschwanetz, R. H. Carlson, and D. R. Meldrum, "Thin PDMS films using long spin times or tert-butyl alcohol as a solvent," *PLoS One*, vol. 4, p. e4572, 2009.
- [239] C. Zhang, Y. Xu, J. Gu, and S. F. Schlossman, "A cell surface receptor defined by a mAb mediates a unique type of cell death similar to oncosis," *Proceedings of the National Academy of Sciences*, vol. 95, pp. 6290-6295, 1998.
- [240] D. A. Stenger, *et al.*, "Detection of physiologically active compounds using cell-based biosensors," *Trends in Biotechnology*, vol. 19, pp. 304-309, 2001.
- [241] F. Asphahani and M. Zhang, "Cellular impedance biosensors for drug screening and toxin detection," *Analyst*, vol. 132, pp. 835-841, 2007.
- [242] D. Yu, B. Blankert, J. C. Viré, and J. M. Kauffmann, "Biosensors in drug discovery and drug analysis," *Analytical letters*, vol. 38, pp. 1687-1701, 2005.
- [243] M. A. Cooper, "Optical biosensors in drug discovery," *Nature Reviews Drug Discovery*, vol. 1, pp. 515-528, 2002.

## Abbreviations

AFM	atomic force microscopy
AP	alkaline phosphatase
APTES	amino-silane
BPAECs	bovine pulmonary artery endothelial cells
BPEI	branched polyethyleneimine
BrdU	5-bromo-deoxyuridine
CAMs	cell adhesion molecules
CDC	the Centers for Disease Control and Prevention
CFSE	5(6)-carboxyfluorescein diacetate n-succinimidyl ester
CR	cell retainers
CVD	cardiovascular disease
DEP	dielectrophoresis
DETA	3-trimethoxysilyl propyl-diethylenetriamine
E. coli	escherichia coli
ECM	extracellular matrix
ELISA	enzyme-linked immunosorbent assay
EP	electrophoresis
FAK	focal adhesion kinase
FBS	Fetal bovine serum
FCS	fetal calf serum
FDA	Food and Drug Administration
Fn	fibronectin
GFP	green fluorescent protein

HDT	1-hexadecanethiol
HEMA	2-hydroxyethylmethacrylate
hFOBs	human fetal osteoblastic cells
HMDS	hexamethyldisilazane
HR	mesoporous inorganic-organic hybrid resin
HR-DOPA	dopaminergic mesoporous inorganic-organic hybrid resin
IND	investigational new drug
ITO	indium tin oxide
LPP	line plot profile
MA	microwell array
MEMS	microelectromechanical systems
MFG	large-scale manufacturing
MMAAPA	(10-mercaptomethyl-9-anthyl)(4-aldehydephenyl)acetylene
MPTMS	3-(methacryloyloxy) propyltrimethoxysilane
MTT	3-(4,5-dimethylthiazol-2-yl)-2,5-diphenyl-2H-tetrazolium bromide
NCEs	new chemical entities
NDA	new drug application
ORLD	optimized rapid lifetime determination
OTS	octadecyltrichlorosilane
PBS	phosphate buffered saline
p-DEP	positive dielectrophoretic
PDMS	poly(dimethylsiloxane)
PEG	poly(ethylene glycol)
PEG-DMA	poly(ethylene glycol)-dimethacrylate

PET	poly(ethylene terephthalate)
PGLA	poly(glycolic-co-lactic)acid
PR	photoresist
PS	polystyrene
PVDMA	poly(2-vinyl-4,40-dimethylazlactone)
PW	picoliter well
RMS	root-mean square
RT	room temperature
SAMs	self-assembled monolayers
SD	standard deviation
SEM	standard error of the mean
SPP	surface plot profile
TBA	tert-butyl alcohol
TEOS	tetraethylorthosilicate
TP	transmembrane protein
Vn	vitronectin
XPS	X-ray photoelectron spectroscopy
XTT	2,3-bis-(2-methoxy-4-nitro-5-sulfophenyl)-2H-tetrazolium-5-carboxanilide
μCS	microcapillary system



## Remarks

### Financial Support

The study was performed as a part of research in the project, “Bio Cell Processor for Drug Discovery,” funded by Korea Institute of Science and Technology, Seoul, South Korea and Government of Saarland, Germany from 2008 to 2011.

### Paper publishing

1. **Park J**, Müller M, Kim J, Kim D-P, Seidel H, “Single Cell Array of Microwells coated with Dopaminergic Organic-inorganic Hybrid Resin”, The 5th Int. Conf. on Nano/Molecular Medicine and Engineering (IEEE-Nanomed 2011), Jeju, Nov., 2011
2. Krause H, Kim J-Y, **Park J**, Müller M, Kim J, Lim G and Seidel H, “Electrode Design for High Impedance Change of Coulter Based Cell Counter”, Lab-on-a-chip World Congress, San Diego, Oct., 2010.
3. **Park J**, Müller M, Jang E, Hong L-Y, Kim J, Koh W-G, Kim D-P and Seidel H, “Effect of Dimension of Micro Cell Wells Coated with Inorganic-organic Hybrid Resin on Cell Attachment”, Lab-on-a-chip World Congress, San Diego, Oct., 2010.
4. **Park J**, Müller M, Jang E, Kim J, Hong L-Y, Kim D-P, Seidel H and Koh W-G, “Fast Cell Immobilization by Using Non-immunological Method for Cell Based Biosensor”, The 9th Annual IEEE Conference on SENSORS, Hawaii, Nov., 2010
5. Kim J, **Park J**, Müller M, Lee H-H and Seidel H, “Uniform magnetic mobility in a curved magnetophoretic channel”, The 8th Annual IEEE Conference on SENSORS, Newzealand, Oct., 2009.
6. Müller M, **Park J** and Kim J, “Capture Probability Analysis and Experimental Evaluation of Short-Time Immune Binding Processes for Superparamagnetic Microparticles and T-Lymphocytes”, Lab-on-a-chip European Congress, Stockholm, May, 2009.
7. Kim J, **Park J**, Müller M, Lee H-H and Seidel H, “Curved channels of immune-magnetophoretic micro cell sorter for uniform magnetic mobility”, The 13th

International Conference on Miniaturized Systems for Chemistry and Life Sciences (MicroTAS), Jeju, Nov., 2009.

8. **Park J**, Park S, Müller M, Kim J, Hong L-Y, Jung S-H, Kim D-P, Lee H-H, and Seidel H, “Micro Cell Adhesive Patch Array with Super Hydrophilic Resin for Drug Discovery”, The 13th International Conference on Miniaturized Systems for Chemistry and Life Sciences (MicroTAS), Jeju, Nov., 2009.
9. Mueller M, Dahmke IN, **Park J**, Kim J T, Steinfeld U and Lee H-H, “Capture Probability Analysis of Short-Time Immune-Binding Processes for Simag-CD3 Microparticles and T-Lymphocytes”, 4th Int. Conf. on Bioengineering and Nanotechnology, Dublin, July, 2008.

**Via**

## **Jihwang Park**

Lehrstuhl für Mikromechanik, Mikrofluidik/Mikroaktorik

Jihwang Park was born in Seoul, South Korea on Jan. 26 1975. He earned his Bachelor of Science degree in Mechanical Engineering from Yonsei University, Seoul, South Korea, in 1998. He received his Master of Science degree in Mechancial Science in 2001 from Yonsei University, Seoul, South Korea. In 2007, he joined Professor Helmut Seidel's group at Saarland University, Saarbrücken, Germany, in the doctoral program.

While pursuing his degree, Dr. –Ing. Park worked as a research associate for Bio-MEMS team at Korea Institute of Science and Technology Europe Forschungsgesellschaft mbH, Saarbrücken, Germany from 2007 to 2012. He joined Nano Manufacturing Research Center at Yonsei University, Seoul, South Korea, in 2012 and is currently a full-time research staff member.



## Acknowledgements

First of all, I would like to gratefully and sincerely appreciate Univ.-Prof. Dr. rer. nat. Helmut Seidel at University of Saarland and PhD, FRSC, Prof. Dr. Andreas Manz at Korea Institute of Science and Technology Europe Forschungsgesellschaft mbH for their guidance, understanding, patience, and most importantly their thoughtful consideration during my graduate studies at University of Saarland and at Korea Institute of Science and Technology Europe Forschungsgesellschaft mbH. They have encouraged me to not only grow as a researcher and an engineer but also as an independent scholar.

I would also like to thank Dr. -Ing. Jooseok Lee, Dr. rer. nat. Young Jun Kim, Dipl. BioChem. André René Blaudszun, and Dipl. Bio. Michael Müller for their great collaboration and helpful discussion. I would like to also thank to Dr. -Ing. Jungtae Kim and Dr. -Ing. Hyeck-Hee Lee for showing a good example: what I must do as a PhD student and what I will have to do as a supervisor in the future.

Finally, and most importantly, I would like to thank my parents; Their support, encouragement, quiet patience and unwavering love were helpful to complete and build my works and to be “Humble themselves, therefore, under God’s mighty hand [Peter 5:5]”.